

# **CONFORMATIONAL MOBILITY IN THE ACTIVE SITE OF A HEME PEROXIDASE**

Thesis submitted for the degree of Doctor of Philosophy at the  
University of Leicester

by

Sandip Kaur Badyal

MChem Biological Chemistry (Joint Hons), University of Leicester

Department of Chemistry

Faculty of Science

University of Leicester

March 2008

***To respected Baba ji,  
Dad, Mum and in the memory of Uncle ji***

## STATEMENT

Unless otherwise acknowledged, the experimental work described in this thesis has been carried out by the author in the department of Chemistry and Henry Wellcome laboratories for Structural Biology, at the University of Leicester between October 2004 and March 2008. The work has not been submitted and is not presently being submitted for any other degree at this or any other university.

Signed:

Date:

Department of Chemistry  
University of Leicester  
University Road  
Leicester  
United Kingdom  
LE1 7RH

# CONFORMATIONAL MOBILITY IN THE ACTIVE SITE OF A HEME PEROXIDASE

Sandip Kaur Badyal

## ABSTRACT

Site-directed mutagenesis in recombinant soybean ascorbate peroxidase (rsAPX) has been performed to probe structure/function relationships in this and other heme proteins.

In Chapter Two, we present mechanistic, spectroscopic, and structural evidence for peroxide- and ligand-induced conformational mobility of the distal histidine (His-42) in the W41A variant of ascorbate peroxidase. In this variant, His-42 binds “on” to the heme in the oxidised form, duplicating the active site structure of the cytochromes *b* but, in contrast to cytochromes *b*, is able to swing “off” the iron during catalysis. Contrary to the widely adopted view of heme enzyme catalysis, these data indicate that strong coordination of the distal histidine to the heme iron does not automatically undermine catalytic activity.

In Chapter Three, we have shown that conformational rearrangement in W41A, discussed above, can also be triggered upon reduction of the heme iron. We present structural, spectroscopic and ligand binding data that support dissociation of His-42 from the iron in the ferrous form of W41A. Structural studies provide evidence for formation of a reduced, bis-histidine-ligated species that subsequently decays by dissociation of His-42 from the heme. Collectively, the data provide clear evidence that conformational movement within the same heme active site can be controlled by both ligand binding and metal oxidation state.

In Chapter Four, we present evidence for heme oxygenase reactivity in the W41A variant of rsAPX. Crystallographic, spectroscopic, HPLC and MS techniques reveal that the heme is modified on reaction of W41A with *tert*-butyl hydroperoxide to yield a *tert*-butyl derivative of biliverdin. Evidence for formation of a hydroperoxo, Compound 0, intermediate is also presented. A common intermediate for the two heme enzymes is proposed.

In Chapter Five, we examined the affect of disruption of the conserved distal histidine-asparagine hydrogen bond on active site mobility by formation of a series of asparagine-71 (Asn-71) variants. The spectroscopic data presented provide clear evidence that the conserved distal histidine-asparagine bond is required to maintain the correct orientation of distal histidine in the active site of rsAPX.

## ACKNOWLEDGEMENTS

I would like to thank my supervisor Professor Emma L. Raven for her guidance, support and help throughout my PhD research. I gratefully acknowledge the BBSRC and University of Leicester for funding.

Special thanks go to Dr Jaswir Basran for her advice, encouragement and support. I owe much to Jaswir, for her friendship, for sharing her expertise and for proof-reading this thesis.

I am very grateful to Dr Gordon M. Joyce for collection and interpretation of the W41A crystallographic data presented in Chapter Two and for spending endless evenings helping me understand the process of crystallographic data interpretation and refinement. I am also grateful to Dr Peter C. E. Moody for his assistance in determination of all structures presented in this thesis. I would like to thank Dr Katherine H. Sharp for crystallographic data of cyanide and nitric oxide bound derivatives of rsAPX, Dr Klaus Futterer for collection of the ferrous W41A crystal data and Professor John W. R. Schwabe for collection of the high resolution *tert*-butylhydroperoxide W41A crystal data. Thanks should also be extended to Dr John McGeehan for support in using the microspectrophotometer at the ESRF, Dr Clive L. Metcalfe for assistance in refinement of W41A crystal structures presented in Chapter Three and to Dr Louise Fairall, Dr Alexandre R. Gingras and Mr Nicholas Putz for assistance with graphics.

I am very grateful to Dr Igor Efimov for sharing his expertise in redox potentiometry and for many helpful discussions. I would like to thank Dr Graham Eaton for ESI-mass spectrometry, Dr Sharad C. Mistry, Dr Andrew R. Bottrill and Mrs Shairbanu Ashra for their expertise in HPLC and assistance in MALDI-TOF mass spectrometry. I would also like to thank Dr Harriet E. Seward for obtaining EPR data on W41A and Professor Andrew J. Thomson and Dr Myles R. Cheesman for the use of EPR facilities at University of East Anglia, Norwich. I would also like to thank Professor Paul M. Cullis for useful discussions.

I am also grateful to Miss Nishma Chauhan, Dr Zoi Pipirou, Mrs Nina Bhanji and Mrs Zimna Wazeer for their friendship and encouragement. Finally, I would like to thank my parents and brothers, Jatinder and Jagdish for their constant support and encouragement.

# CONTENTS

STATEMENT.....	i
ABSTRACT.....	ii
ACKNOWLEDGEMENTS.....	iii
TABLE OF CONTENTS.....	iv
ABBREVIATIONS.....	xiv
<b>CHAPTER ONE</b>	
<i>INTRODUCTION.....</i>	<b>1</b>
<b>CHAPTER TWO</b>	
<i>CONFORMATIONAL MOBILITY IN THE ACTIVE SITE OF A HEME PEROXIDASE.....</i>	<b>72</b>
<b>CHAPTER THREE</b>	
<i>IRON OXIDATION STATE MODULATES ACTIVE SITE STRUCTURE IN A HEME PEROXIDASE.....</i>	<b>108</b>
<b>CHAPTER FOUR</b>	
<i>HEME OXYGENASE ACTIVITY IN ASCORBATE PEROXIDASE....</i>	<b>139</b>
<b>CHAPTER FIVE</b>	
<i>THE CONSERVED DITSAL HISTIDINE-ASPARAGINE BOND IN ASCORBATE PEROXIDASE.....</i>	<b>179</b>
<b>CHAPTER SIX</b>	
<i>MATERIALS AND METHODS.....</i>	<b>202</b>
APPENDIX A.....	xix
APPENDIX B.....	xxiii
PUBLICATIONS.....	xxiv

## CHAPTER ONE

INTRODUCTION	1
<hr/>	
1.1 OVERVIEW	1
1.2 HEME PROSTHETIC GROUP	2
1.3 HEME PROTEINS: An overview on the active roles of heme in biological systems	5
1.4 HEME PEROXIDASES	7
1.5 PLANT PEROXIDASES	8
1.5.1 Classification of plant peroxidases	8
1.5.1.1 <i>Class I</i>	8
1.5.1.2 <i>Class II</i>	9
1.5.1.3 <i>Class III</i>	9
1.5.2 Structural studies of plant peroxidases	10
1.5.2.1 <i>The active site of plant peroxidases</i>	11
1.5.3 Mechanism of peroxidase catalysis	12
1.5.3.1 <i>Anomalies in peroxidase catalysis</i>	15
1.5.4 Role of active site residues	16
1.6 ASCORBATE PEROXIDASE	18
1.6.1 Introduction	18
1.6.2 Isolation of APX	20
1.6.3 APX cDNA sequences and bacterial expression	21
1.6.4 Structural studies on APX	22
1.6.4.1 <i>Overall structure</i>	22
1.6.4.2 <i>Active site structure</i>	23
1.6.4.3 <i>Metal ion site</i>	24
1.6.5 Catalysis in APX	25
1.6.5.1 <i>Compound I intermediate of APX</i>	26
1.6.5.2 <i>Compound II intermediate of APX</i>	29
1.6.5.3 <i>Steady state catalysis in APX</i>	30
1.6.6 Substrate binding in APX	31
1.7 ELECTRON TRANSFER HEME PROTEINS	34
1.8 MONOOXYGENASES	35

1.9	HEME OXYGENASE	37
1.10	HEME PROTEINS: An overview on the passive roles of heme in biological systems	41
1.10.1	The passive roles of heme in biological systems	41
	1.10.1.1 <i>Heme and gene expression</i>	41
	1.10.1.2 <i>Heme-based sensors</i>	42
1.11	THESIS AIMS	48
1.12	REFERENCES	49

## CHAPTER TWO

# CONFORMATIONAL MOBILITY IN THE ACTIVE SITE OF A HEME PEROXIDASE

72

---

2.1	INTRODUCTION	72
2.2	RESULTS	75
2.2.1	Expression and purification of W41A	75
2.2.2	Analysis of the purity of W41A	75
	2.2.2.1 <i>SDS-PAGE electrophoresis</i>	75
	2.2.2.2 <i>Mass spectrometric analysis</i>	76
2.2.3	Spectroscopic characterisation of W41A	77
	2.2.3.1 <i>Electronic absorption spectra</i>	77
	2.2.3.2 <i>Pyridine hemochromagen assay</i>	77
	2.2.3.3 <i>Binding of non-catalytic ligands</i>	78
	2.2.3.4 <i>EPR spectroscopy</i>	80
2.2.4	Crystallography of W41A	81
	2.2.4.1 <i>Interpretation and refinement of crystallographic data</i>	81
	2.2.4.2 <i>Overall crystal structure of W41A and                     ligand bound derivatives</i>	82
	2.2.4.3 <i>Active site of W41A</i>	84
	2.2.4.4 <i>Cyanide and nitric oxide derivatives of rsAPX and W41A</i>	85
	2.2.4.5 <i>Structural evidence for mobility of His-42 during                     catalysis in W41A</i>	87
2.2.5	Steady state kinetics of W41A	90
	2.2.5.1 <i>Ascorbate assays</i>	90
	2.2.5.2 <i>Guaiacol assays</i>	91
2.2.6	Transient state kinetics	92
	2.2.6.1 <i>Spectra of rsAPX and W41A oxidised intermediates                     Compound I and II</i>	92
	2.2.6.2 <i>Formation of Compound I</i>	93
	2.2.6.3 <i>Reduction of Compound I</i>	94
	2.2.6.4 <i>Reduction of Compound II</i>	95

2.3	DISCUSSION	96
2.3.1	Heme electronic structure in W41A	96
2.3.2	Crystallography: Evidence for displacement of His-42 by (a) Exogenous ligands and (b) H <sub>2</sub> O <sub>2</sub>	97
	<i>(a) Displacement of His-42 by exogenous ligands</i>	97
	<i>(b) Displacement of His-42 by H<sub>2</sub>O<sub>2</sub></i>	98
2.3.3	Evidence for mobility of His-42 during catalysis	99
	<i>(a) Steady state kinetics: oxidation of ascorbate and aromatic substrates</i>	99
	<i>(b) Transient state kinetics</i>	100
2.4	SUMMARY	102
2.5	REFERENCES	104

## CHAPTER THREE

# IRON OXIDATION STATE MODULATES ACTIVE SITE STRUCTURE IN A HEME PEROXIDASE 108

---

3.1	INTRODUCTION	108
3.2	RESULTS	111
3.2.1	Electronic absorption spectra of ferric and ferrous W41A	111
3.2.2	Ligand binding studies on W41A	112
3.2.2.1	<i>Ligand binding in the ferric form of W41A</i>	112
3.2.2.2	<i>Ligand binding in the ferrous form of W41A</i>	115
3.2.3	Crystallography	116
3.2.3.1	<i>Interpretation and refinement of crystallographic data</i>	116
3.2.3.2	<i>Structure of ferrous W41A</i>	117
3.2.3.3	<i>Reduction of ferric W41A crystals during X-ray data collection</i>	118
3.2.3.4	<i>Transient state kinetics for detection of bis-histidine intermediate observed during X-ray data collection</i>	121
3.2.4	Electrochemistry	122
3.2.4.1	<i>Xanthine/xanthine oxidase assay for determination of the ferric/ferrous reduction potential</i>	122
3.2.4.2	<i>Reduction potential of the ferric-cyanide/ferrous-cyanide couple</i>	125
3.3	DISCUSSION	126
3.3.1	Heme electronic structure and ligand binding	126
3.3.2	Electrochemistry	128
3.3.3	Crystallographic evidence for mobility of His-42 on reduction of heme in W41A	129
3.4	SUMMARY	132
3.5	REFERENCES	134

## CHAPTER FOUR

### HEME OXYGENASE ACTIVITY IN ASCORBATE PEROXIDASE **139**

---

4.1	INTRODUCTION	139
4.2	RESULTS	144
4.2.1	Reaction of W41A and rsAPX with <i>tert</i> -butyl hydroperoxide: spectroscopic analysis	144
4.2.1.1	<i>Absence of a ferryl intermediate in W41A on reaction with tert-butyl hydroperoxide: addition of ascorbate</i>	146
4.2.1.2	<i>Absence of a ferryl intermediate in W41A on reaction with tert-butyl hydroperoxide: stopped-flow analysis</i>	147
4.2.2	Identification of the species formed on reaction of W41A with <i>tert</i> -butyl hydroperoxide: mass spectrometry and HPLC analysis	149
4.2.3	Detection of a modified-heme species in W41A on reaction with <i>tert</i> -butyl hydroperoxide: crystallographic analysis	158
4.2.3.1	<i>Data interpretation and refinement</i>	158
4.2.3.2	<i>Structure of the tert-butyl-modified heme species in W41A</i>	158
4.3	DISCUSSION	163
4.3.1	Spectroscopic analysis of the reaction of W41A with <i>tert</i> -butyl hydroperoxide	163
4.3.2	Mass spectrometry and HPLC analysis of the reaction of W41A with <i>tert</i> -butyl hydroperoxide	164
4.3.3	Evidence for formation of a hydroperoxo species in reaction of W41A with <i>tert</i> -butyl hydroperoxide: crystallographic analysis	165
4.3.3.1	<i>The tert-butyl hydroperoxide-soaked W41A crystal structure</i>	165
4.3.3.2	<i>Evidence for formation of a hydroperoxo species</i>	165
4.3.3.3	<i>Mechanism for formation of tert-butyl-biliverdin</i>	168
4.4	SUMMARY	171
4.5	REFERENCES	173

## CHAPTER FIVE

### THE CONSERVED DISTAL HISTIDINE-ASPARAGINE BOND IN ASCORBATE PEROXIDASE

179

---

5.1	INTRODUCTION	179
5.2	RESULTS	181
5.2.1	Expression and purification of the Asn-71 variants	181
5.2.2	Mass spectrometric analysis of the Asn-71 variants	182
5.2.3	Spectroscopic characterisation of the Asn-71 variants	183
	5.2.3.1 <i>Electronic absorption spectra</i>	183
	5.2.3.2 <i>Equilibrium binding experiments</i>	183
5.2.4	Crystal screen trials of the Asn-71 variants	187
5.2.5	Electrochemistry of the Asn-71 variants	187
5.2.6	Kinetic analysis of the Asn-71 variants	188
5.3	DISCUSSION	192
5.3.1	Heme electronic structure of the Asn-71 variants and ligand binding studies	192
5.3.2	Electrochemistry and steady state kinetics of the Asn-71 variants	194
5.3.3	Conclusions	194
5.3.4	Disruption of the conserved distal histidine-asparagine bond in HRP, CcP and KatG	195
	5.3.4.1 <i>Mutation of the conserved His-Asn bond in HRP</i>	196
	5.3.4.2 <i>Mutation of the conserved His-Asn bond in CcP</i>	197
	5.3.4.3 <i>Mutation of the conserved His-Asn bond in KatG</i>	197
5.4	SUMMARY	199
5.5	REFERENCES	200

## CHAPTER SIX

MATERIALS AND METHODS	202
6.1 MATERIALS	202
6.1.1 Chemicals and reagents	202
6.2 RECOMBINANT DNA TECHNIQUES	203
6.2.1 Oligonucleotides	203
6.2.2 Site-directed mutagenesis	203
6.2.3 Transformation into XI1-Blue super-competent cells	207
6.2.4 Isolation of DNA	208
6.2.5 DNA sequencing	209
6.2.6 Agarose gel electrophoresis	209
6.2.7 Transformation of the recombinant DNA into competent <i>E.coli</i> cells	209
6.3 PREPARATION OF RECOMBINANT SOYBEAN APX AND VARIANTS	210
6.3.1 Protein expression	210
6.3.2 Protein expression and purification of soybean APX and variants	210
6.3.3 Fast Performance Liquid Chromatography (FPLC) of protein samples	212
6.4 METHODS FOR PROTEIN ANALYSIS AND CHARACTERISATION	212
6.4.1 Buffers and solution preparation	212
6.4.2 SDS-PAGE electrophoresis	213
6.4.3 UV-visible spectroscopy	213
6.4.4 Determination of absorption coefficients	214
6.4.5 Ligand-bound derivative spectra	215
6.4.6 Ligand binding studies	216
6.4.7 Electronic Paramagnetic Resonance (EPR) Spectroscopy	217
6.5 STEADY STATE KINETICS	218
6.5.1 Measurement of ascorbate and guaiacol activity	218
6.6 TRANSIENT STATE KINETICS	220
6.6.1 Formation of Compound I	220
6.6.2 Reduction of Compound I	221
6.6.3 Reduction of Compound II	221

6.6.4	Data analysis of kinetic transients	223
6.6.5	Analysis of Photodiode array (PDA) data	223
6.7	XANTHINE/XANTHINE OXIDASE METHOD FOR DETERMINATION OF THE FERRIC/FERROUS REDUCTION POTENTIAL	224
6.8	X-RAY CRYSTALLOGRAPHY	225
6.8.1	Crystallisation of W41A	225
6.8.2	Crystal screen trials of Asparagine-71 variants	226
6.8.3	Crystal soaks of W41A	226
6.8.4	Crystallographic data collection and interpretation	227
	6.8.4.1 Crystallographic <i>data collection and interpretation of ferric W41A, H<sub>2</sub>O<sub>2</sub><sup>-</sup>, cyanide- and nitric oxide-W41A derivatives</i>	227
	6.8.4.2 Crystallographic <i>data collection and interpretation of ferrous W41A and single-crystal microspectrophotometry</i>	228
	6.8.4.3 Crystallographic <i>data collection and interpretation of <sup>t</sup>BuO<sub>2</sub>H-W41A and single-crystal microspectrophotometry</i>	229
6.9	HIGH PERFORMANCE LIQUID CHROMATOGRAPHY (HPLC)	230
6.10	MASS SPECTROMETRY	230
	6.10.1 Matrix-Assisted Laser Desorption/Ionisation-Time of Flight (MALDI-TOF) mass spectrometry	230
	6.10.2 Electro Spray Ionisation (ESI) mass spectrometry	231
6.11	REFERENCES	232

## ABBREVIATIONS

Amino acids are abbreviated to three-letter codes recommended by the I. U. P. A. C. Joint Commission on Biochemical nomenclature (1985).

### ENZYMES

APX	Ascorbate peroxidase
rpAPX	Recombinant cytosolic pea ascorbate peroxidase
rsAPX	Recombinant cytosolic soybean ascorbate peroxidase
ARP	<i>Arthromyces ramosus</i> peroxidase
BP1	Barley peroxidase
KatG	Catalase peroxidase
CcP	Cytochrome <i>c</i> peroxidase
CPO	Chloroperoxidase
EPO	Eosinophil peroxidase
HRP	Horseradish peroxidase
LPO	Lactoperoxidase
LiP	Lignin peroxidase
MnP	Manganese peroxidase
MPO	Myeloperoxidase
PnP	Peanut peroxidase
TPO	Thyroid peroxidase
DNase	Deoxyribonuclease
HO	Heme oxygenase
RNase	Ribonuclease

### AMINO ACIDS

Ala	A	Alanine
Arg	R	Arginine
Asn	N	Asparagine
Asp	D	Aspartate
Cys	C	Cysteine
Gln	Q	Glutamine
Glu	E	Glutamic acid

Gly	G	Glycine
His	H	Histidine
Ile	I	Isoleucine
Leu	L	Leucine
Lys	K	Lysine
Met	M	Methionine
Phe	F	Phenylalanine
Pro	P	Proline
Ser	S	Serine
Thr	T	Threonine
Trp	W	Tryptophan
Tyr	Y	Tyrosine
Val	V	Valine

### **BASES**

A	Adenine
C	Cytosine
G	Guanine
T	Thymine

### **CHEMICALS**

dNTPs	Deoxynucleotide triphosphates
DTT	Dithiothreitol
EDTA	Ethylenediamine tetraacetic acid
DNTB	5,5'-dithiobis(2-nitrobenzoic acid) – Ellman's reagent
Hepes	<i>N</i> -2-Hydroxyethylpiperazine- <i>N'</i> -2-ethanesulphonic acid
IPTG	Isopropyl- $\beta$ -D thiogalactopyranoside
LB	Luria-Bertani broth
NTA	Nitrilotriacetic acid
PEG	Polyethylene glycol
SDS	Sodium dodecyl sulphate
TEMED	<i>N,N,N',N'</i> -Tetramethylethylenediamine
TFA	Trifluoroacetic acid
PMSF	Phenylmethylsulphonyl fluoride

## TECHNIQUES

ESI	Electrospray Ionisation
EPR	Electron Paramagnetic Resonance
ENDOR	Electron Nuclear DOuble Resonance
EXAFS	Extended X-ray Absorption Fine Structure
FPLC	Fast Protein Liquid Chromatography
HPLC	High Performance Liquid Chromatography
IR	Infra-red
MALDI-TOF	Matrix-Assisted Laser Desorption/Ionisation - Time Of Flight
MCD	Magnetic Circular Dichroism
OTTLE	Optically Transparent Thin-Layer Electrode
NMR	Nuclear Magnetic Resonance
PAGE	Polyacrylamide gel electrophoresis
PCR	Polymerase Chain Reaction
RR	Resonance Raman
R <sub>z</sub>	Reinheitzahl
SHE	Standard Hydrogen Electrode
UV	Ultra-Violet
Vis	Visible

## UNITS/SYMBOLS

A	Absorption
$\epsilon$	Absorption coefficient
Å	Angstroms (1 Å = 10 <sup>-10</sup> m)
K <sub>a</sub>	Association constant
amu	Atomic mass unit
CT	Charge transfer
Da	Daltons
°C	degrees Celsius
°	degrees
K <sub>d</sub>	Dissociation constant
g	grams
Hz	Hertz
$\mu$	Ionic strength

K	Kelvin
kDa	kiloDaltons
kb	kilobases
l	litres
m	metres
ms	milliseconds
min	minutes
M	Molar
MW	Molecular weight
m/z	mass to charge ratio
OD	Optical density
rpm	revolutions per minute
s	seconds
T	Tesla
V	Volts
$\lambda$	Wavelength
v/v	volume per volume
n	Whole number
W	Watt

### **CRYSTALLOGRAPHY-RELATED SYMBOLS**

CCD	Charge-coupled device
CCP4	Collaborative Computational Project No. 4
DESY	Deutsches Elektronen Synchrotron
ESRF	European Synchrotron Radiation Facility
$F_o$ ( $F_{obs}$ )	Amplitude of observed structure factor
$F_c$ ( $F_{calc}$ )	Amplitude of calculated structure factor
PDB	Protein Data Bank
RMSD	Root-mean-square deviation

### **MISCELLANEOUS**

C	Carboxyl terminal
CRP	Catabolite repressor protein
cAMP	cyclic adenine monophosphate

cGMP	cyclic guanine monophosphate
cDNA	complementary Deoxyribonucleic acid
DNA	Deoxyribonucleic acid
<i>E.coli</i>	<i>Escherichia coli</i>
FAD	Flavin adenine dinucleotide
FFQ	Fast flow Q Sepharose
HAP1	Heme activator protein
HRI	Heme-regulated eIF1 $\alpha$ kinase
<i>EcDOS</i>	Heme-regulated phosphodiesterase from <i>Escherichia coli</i>
I.U. P. A. C.	International Union of Pure and Applied Chemistry
N	Amino terminal
NADP(H)	Nicotinamide adenine dinucleotide phosphate
NPAS2	Neuronal PAS domain protein 2
PAS-	
domain	Per-ARNT-Sim motif
PNACL	Protein and Nucleic Acid Chemistry Laboratory



***CHAPTER ONE***

**INTRODUCTION**

## CHAPTER ONE

### INTRODUCTION

---

#### 1.1 OVERVIEW

Metal ions are used extensively in nature, in functional as well as structural roles, and thus are of crucial importance in a range of reactions in biological systems. Molecular evolution has selected iron to carry out a wide array of biological functions due to its rich and subtle chemical properties and also because of its abundance in the earth's crust (1). Iron, when in appropriately tailored macromolecular environments, is responsible for quite distinct activities ranging from electron transfer, catalysis, oxygen transport and storage, ligand binding, signal transduction, and control of gene expression (2). Two major factors control the properties of iron and other metal ions in biological systems: (a) the structure of the metal centre, including the geometry and structure of the metal complex and the nature of the ligands attached to the metal; and (b) the environment of the metal complex, including the polarity of the immediate surroundings and steric constraints on the accessibility of substrates to the metal and of the metal to the solvent. In order to partially address the general question of how these factors can influence the function in a metalloprotein system this Chapter as well as providing a background on heme peroxidases and a review on ascorbate peroxidase focuses on the diverse range of functions displayed by heme-containing proteins.

## 1.2 HEME PROSTHETIC GROUP

The common feature of heme proteins (e.g. hemoglobin, myoglobin, catalase, most peroxidases, the *b*-type cytochromes and the cytochromes P450) is that they harbour the same prosthetic group at their active site, namely that of iron protoporphyrin IX (Figure [1.1A]). Iron protoporphyrin IX also known as heme *b*, can be described as a partially unsaturated tetradentate macrocyclic ligand, which in its deprotonated form can bind to metal ions. Iron protoporphyrin IX consists of an organic component and an iron atom. Technically, ferriprotoporphyrin IX (iron III) is hemin and ferroprotoporphyrin (iron II) is heme; however since the heme iron used in proteins can have many oxidation states, any form of iron-containing protoporphyrin IX is usually denoted “heme” for any given oxidation state (3). Accordingly iron protoporphyrin IX is referred to as “heme” in this thesis. The organic component of the heme group, protoporphyrin, is made up of four pyrrole rings linked by methene bridges to form the tetrapyrrole ring. This tetrapyrrole ring is decorated with four methyl (at positions 1, 3, 5 and 8), two vinyl (at positions 2 and 4) and two propionate side chains (at positions 6 and 7) (Figure [1.1B]). The iron atom binds to the four pyrrole nitrogens in the centre of the protoporphyrin ring, giving rise to square planar structure; the net charge on the heme with four-coordinate iron (III) is +1 (Figure [1.1A]). The iron can form two additional bonds, one on either side of the heme plane and are termed as fifth (or proximal) and sixth (or distal) coordination sites (Figure [1.2]). The nature of the two axial ligands varies between heme proteins, although in many cases the proximal ligand is a histidine.

There are several variables that are known to influence the function of heme proteins, including altering the substituents on the heme, *i.e.* by a covalent link to the protein (myeloperoxidase) or by modification of the porphyrin structure. For example cytochrome *c* oxidase, which is responsible for the reduction of oxygen to water during the terminal electron transfer step in mitochondrial respiratory chains, contains a heme *a* prosthetic group, (Figure [1.1C]). This heme group has a hydroxyethylfarnesyl side chain (at position 2) and a formyl group (at position 8) of the porphyrin ring.

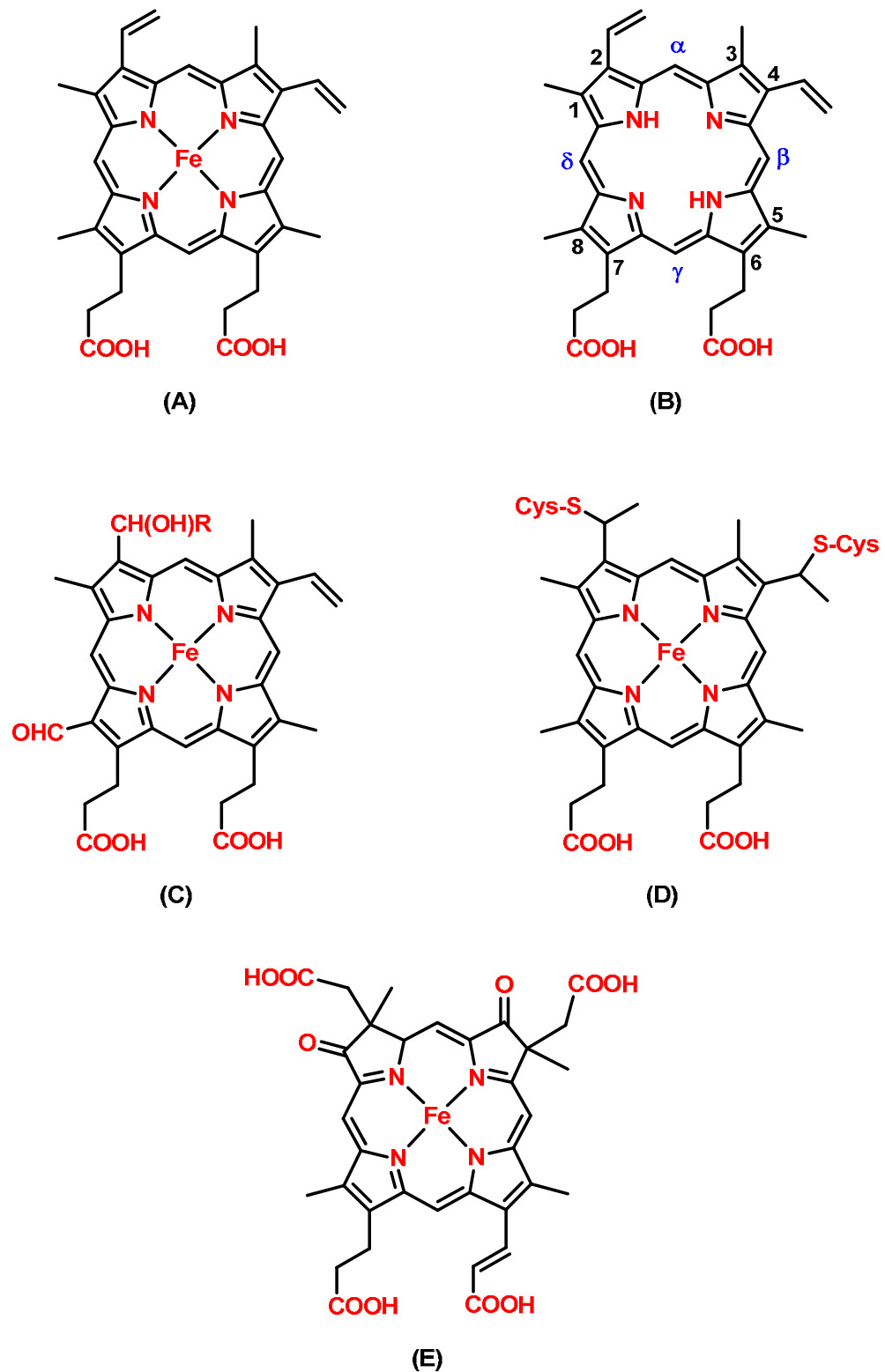
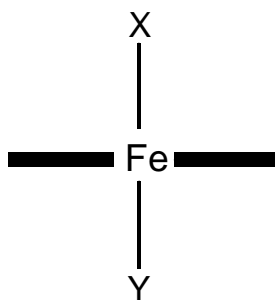


Figure [1.1]: The structures of (A) iron protoporphyrin IX, as found in the cytochromes *b*, globins, monooxygenases and some peroxidases, (B) protoporphyrin IX, (C) heme *a*, where  $R = [(CH_2)_2CH=C(CH_3)]_3CH_3$ , found in cytochrome *c* oxidase, (D) heme *c*, as found in the cytochromes *c*, and (E) heme *d*<sub>1</sub>, as found in cytochromes *cd*<sub>1</sub> nitrite reductase. Figure adapted from (4).

The electron transfer proteins cytochromes *c*, contain a type *c* heme group (Figure [1.1D]), in which the porphyrin is covalently linked to the surrounding protein matrix via two thioether linkages at positions 2 and 4. The bi-functional enzyme cytochrome *cd*<sub>1</sub> nitrite reductase, which catalyses both the one electron reduction of nitrite to nitric oxide and the four electron reduction of oxygen to water, contains, both type *c* and *d*<sub>1</sub> heme (Figure [1.1D,E]). This heme group is decorated with two acetate groups (at positions 2 and 4) and two carbonyl groups (at positions 1 and 3).

The functionality of heme proteins is also affected by the identity of the axial ligands that occupy the distal and proximal coordination sites of the iron (Figure [1.2]). The nature of the distal ligand can affect the spin state of the iron: strong field ligands (e.g. imidazole) lead to low-spin heme, whereas weak field ligands (e.g. water) exhibit high-spin heme. In addition, the solvent accessibility, the polarity of the heme environment, and the coordination number of the iron also influence the functionality of heme proteins.

The heme complex is clearly one of the most versatile redox centres in biology (5) and is an omnipresent prosthetic group found in many heme proteins and enzymes. Despite these proteins sharing a common or very similar porphyrin structure, they display a very wide range of biological functions, which are discussed in the following sections.



**Figure [1.2]: Schematic heme pocket architecture. The block lines represent the heme moiety (viewed along the plane). The axial ligands X and Y refer to the distal and proximal sites, respectively.**

### 1.3 HEME PROTEINS: An overview on the active roles of heme in biological systems

Historically, heme proteins attracted special attention because of the pioneering work on the structure determination of myoglobin and hemoglobin (6,7). However, heme proteins are amongst the most ancient metalloproteins known in biochemistry, and are contained and utilised in almost all living cells, both prokaryotic and eukaryotic. The wide spectrum of functions observed in heme-containing proteins, reviewed extensively (8-13), is a consequence of the versatility of the heme group whose properties are modulated by its molecular environment (2). The general coordination geometry of the iron in heme proteins, as shown in Table [1.1] is five or six; where the identity of the distal and proximal ligands (Figure [1.2]) can vary between proteins. The nature of the distal ligand, as well as the coordination chemistry and reduction-oxidation properties of the heme iron - which themselves are controlled by a number of variables imposed upon the molecule by the surrounding protein structure - can influence the function of the metalloprotein.

**Table [1.1]: The diversity of heme protein structure and function.**

<b>Protein</b>	<b>Coordination Number</b>	<b>Coordinating Ligand(s) (X/Y)</b>	<b>Function</b>
<b>Hemoglobin</b>	6	H <sub>2</sub> O/His	Oxygen binding
<b>Myoglobin</b>	6	H <sub>2</sub> O/His	Oxygen storage
<b>Cytochrome c</b>	6	His/Met	Electron transfer
<b>Cytochrome P450</b>	6	H <sub>2</sub> O/Cys	Monooxygenase
<b>Cytochrome c peroxidase</b>	5	-/His	Peroxidase

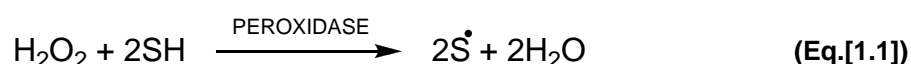
Traditionally, heme-containing proteins have been categorised into oxygen transport proteins (the globins), the electron transfer proteins (the cytochromes) and the catalytic heme-containing enzymes (*e.g.* the P450's, peroxidases and heme oxygenases *etc*), dependent on their biological function (Table [1.1]). However despite this traditional categorisation, over several years, a few examples of heme

proteins have emerged in the literature that did not fit this categorisation. Examples include the heme proteins which switch their heme coordination geometry through conformational rearrangements of the protein structure like cytochrome *c* (14), cytochrome *cd<sub>1</sub>* (15), the di-heme cytochrome *c* peroxidase (16) and the heme chaperone protein CcmE (17) and leghemoglobin (18). The trigger for these conformational rearrangements appeared to be, variously, pH, oxidation state of the iron, and the binding of ligands, substrate or other (non-catalytic) metal ions. Although these documented examples were significant in their own right, their collective significance was not immediately apparent. This was partly because a functional basis for the ligand switch could not be identified in all cases. Later on, further examples were published of conformational rearrangements in other regulatory heme proteins linked to, for example, gas-sensing processes, signalling and gene transcription (examples include the regulatory heme proteins that bind heme resulting in downstream signalling processes Hap1 (1), the various gas sensing proteins like guanylate cyclase, FixL and CoxA discussed Section 1.10). It was only then that it started to become clear that conformational rearrangements associated with the heme group, its ligands/substrates and its oxidation state might actually be used more widely as a means of regulation and/or sensing in biology. In light of these findings Poulos (1) classified heme as having two faces (*i.e.* being Janus-like): one face being “passive” and the other “active”. In some heme proteins, the porphyrin plays no functional role and the heme operates merely as a carrier of a metal that performs a function of biological importance and thus is “passive” (*e.g.* the globins, FixL, CoxA). In other heme proteins, both the metal and porphyrin play an “active” role in chemical transitions and undergo electronic/or chemical transformations (*e.g.* heme oxygenase, cytochrome P450 and heme peroxidases). Hence, the double-sided nature of heme (1).

The following section aims to summarise how the versatility in function of different heme proteins in which heme plays an “active” role is made possible. The Chapter begins with an introduction to heme peroxidases and then focuses on ascorbate peroxidase, the heme peroxidase extensively investigated in this thesis. A discussion on the “active” role of heme in context of the electron transfer proteins, cytochrome P450s and heme oxygenase is provided. This chapter ends with a brief overview on the emerging “passive” role of heme proteins in cell signalling and gene expression.

## 1.4 HEME PEROXIDASES

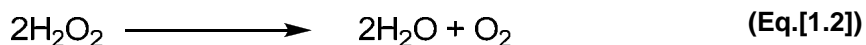
Perhaps the most well understood class of heme proteins where the heme “actively” participates in the required chemistry is the peroxidases (1). Heme peroxidases use the two oxidising equivalents in  $\text{H}_2\text{O}_2$  to oxidise various organic and inorganic biological substrates (3,19-22) (Equation [1.1]) where SH is the reducing substrate and  $\text{S}^\bullet$  the oxidised product.



Peroxidase enzymes have been isolated from a variety of biological sources and are known to perform several diverse roles in nature, such as aiding the development of processes which are environmentally clean, oxidation of dyes and/or toxic phenolic molecules (23,24) and degradation of lignin (25,26). Removal of  $\text{H}_2\text{O}_2$  in eye disease or in plants (ascorbate peroxidase) and synthesis of antibacterial compounds (myeloperoxidase and lactoperoxidase) and hormones (thyroid peroxidase) are a few examples of the role of peroxidases in nature.

Welinder developed a classification system for peroxidases and catalases based on structure and function so that the three-dimensional structure of an enzyme could be approximated from its primary sequence (27). This system was based on the yeast cytochrome *c* peroxidase (CcP) structure (28,29) and was further validated on obtaining the structure of horseradish peroxidase (HRP) (30,31), and later by the structure of other peroxidases. Welinder grouped these heme proteins, with a characteristic protein fold consisting of a central heme group sandwiched between a distal and proximal domain, into three super-families: catalases, animal and plant peroxidases.

Catalases are efficient catalysts for the catalytic reaction shown in Equation [1.2]. Catalases occur in both the plant and animal kingdoms and harbour a similar heme prosthetic group to that found in peroxidases. Similarly, catalases are able to catalyse some of the same reactions (peroxidatic reactions) catalysed by peroxidases and peroxidases are also able to catalyse some catalytic reactions. Despite such similarity to peroxidases, the crystal structure of two catalases (32,33) and primary sequence analysis show that catalases should form a separate super-family.



The animal peroxidase super-family includes myeloperoxidase (MPO), lactoperoxidase (LPO), thyroid peroxidase (TPO) and eosinophil peroxidase (EPO) (34). In spite of the heme binding region in animal peroxidases containing similar helices to the plant peroxidases, the crystal structures of myeloperoxidase (35) and prostaglandin H synthase (36) as well as sequence correlations (37) indicate that animal and plant peroxidases form distinct super-families. The remaining super-family is that of the plant peroxidases, which will be discussed in detail in the following section.

## 1.5 PLANT PEROXIDASES

### 1.5.1 Classification of plant peroxidases

The plant peroxidase super-family, which comprises of the fungal, bacteria and plant peroxidases (3), catalyse the oxidation of a wide variety of substrates, from small inorganic ions (*e.g.* manganese peroxidase) to large proteins (*e.g.* CcP). On the basis of protein sequence homologies, Welinder proposed a classification of the plant peroxidase super-family that sub-divided the enzymes into three peroxidase families (27).

#### 1.5.1.1 Class I

Class I constitutes of the intracellular peroxidases of prokaryotic origin. Examples of the Class I peroxidases for which crystal structures are available include yeast CcP (28), bacterial catalase-peroxidase (KatG) (38) and chloroplastic (39,40) and cytosolic (41,42) ascorbate peroxidase (APX). Bacterial catalase-peroxidases are approximately double the molecular weight of CcP due to gene duplication. Class I peroxidases have no carbohydrate, no cysteine bridges, no signal peptide for secretion, and no calcium ion; However unlike CcP, APX is known to harbour a metal binding site near the proximal tryptophan (Trp) residue, apparently occupied by a potassium ion (43). The Class I enzymes are distinguished from other peroxidases in

the super-family by the presence of distal and proximal tryptophan residues in the heme active site.

### **1.5.1.2 Class II**

Class II consist of the secretory fungal peroxidases. Lignin (LiP) (44) and manganese (MnP) (45) peroxidases from *Phanerochaete chrysosporium* and the ink cap mushroom peroxide from *Coprinus cinereus* (alternative name *Arthromyces ramosus*, ARP) (46) are examples of peroxidases in this class, for which there are crystal structures available. The fungal secretory peroxidases have an amino terminal (N-terminal) signal peptide sequence for secretion through the endoplasmic reticulum and contain ~5 % carbohydrate, two calcium ions and four disulphide bridges (47). The proximal tryptophan residue, conserved in the class I peroxidases, is replaced by phenylalanine (Phe) or leucine (Leu) in class II. One of the calcium binding sites, close to the proximal phenylalanine of lignin peroxidase, corresponds approximately to the potassium site in APX (3).

### **1.5.1.3 Class III**

Class III is comprised of the classical secretory plant peroxidases. The most extensively studied example of a class III peroxidase is HRP isoenzyme C, and there is structural data available for HRP (48), peanut (PnP) (49) and barley (BP) (50) peroxidases. These class III peroxidases posses an N-terminal signal peptide for secretion, two calcium ions, four disulphide bridges, which are in different locations from those in class II peroxidases, and extra helices that play a role in access to the heme edge. Glycosylation ranges from 0-25 % and some proteins may have a carboxyl terminal (C-terminal) pro-peptide that may target them for vacuoles (27).

### 1.5.2 Structural studies of plant peroxidases

The lack of carbohydrate attachments and the ease with which the enzyme itself precipitates out of solution, meant that CcP became the first heme peroxidase to have its crystal structure solved (1980) (28). As a result of extensive glycosylation the structure of HRP, the most studied peroxidase, was not solved (48) until almost a century after its discovery (51). Over a decade passed before crystal structures of other peroxidases emerged, thus CcP along with HRP became something of a paradigm for the peroxidase enzymes. However, neither is ideal as a general model for peroxidases, since CcP utilizes a large protein as its substrate and has an atypical Compound I structure (discussed later Section 1.5.3.1), and HRP contains disulphide bonds, calcium ions as well as being glycosylated. The biological function of HRP is not yet known and neither is its biological substrate. Once the lag in structural data was overcome, by using cloned enzymes expressed in *Escherichia coli* (*E. coli*) which prevents glycosylation, an explosion of structural data occurred in the early 1990s with the publication of crystal structures for manganese peroxidase (45), lignin peroxidase (44), peanut peroxidase (49), *Arthromyces ramosus* peroxidase (52), chloroperoxidase (53), barley peroxidase (54), soybean seed coat peroxidase (55), *Mycobacterium tuberculosis* alkylhydroperoxidase (3), *Mycobacterium tuberculosis* catalase-peroxidase (56) and ascorbate peroxidase (37,41,42,57). All of these peroxidases contain heme ligated with a proximal histidine ligand (Figure [1.3]); the exception being chloroperoxidase (CPO) which has a cysteine as a proximal ligand, and the overall folding pattern for these peroxidases is quite similar.

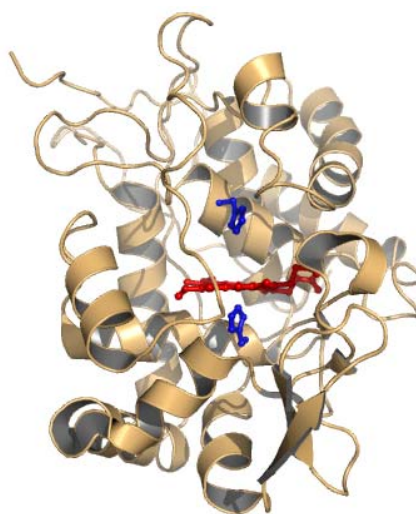


**Figure [1.3]:** The overall structure of CcP (PDB code: 2CYP) (58), showing the heme (red) and active site (distal and proximal) histidine residues (blue).

### 1.5.2.1 The active site of plant peroxidases

Although the three classes show less than 20 % amino acid sequence identity, examination of the crystal structures of these peroxidases reveal that they all contain some residues in the heme cavity that are invariant and considered catalytically relevant, as predicted on the basis of amino acid alignment. The distal histidine (His) and arginine (Arg) are the conserved residues in the distal pocket of peroxidases and the distal aromatic residue, tryptophan for class I peroxidases and phenylalanine for class II peroxidases, has been hypothesised to play a structural role in the distal cavity. Despite the distance from the heme, the distal asparagine (Asn) residue forms a hydrogen bond with distal histidine, an interaction which is conserved through out the plant peroxidase family. On the proximal side of the heme the axial histidine is hydrogen bonded to a buried carboxylate group of an aspartate (Asp) residue and an aromatic (tryptophan for class I and phenylalanine for class II) residue. In addition to the various conserved amino acids (Figure [1.4]), as reported in Table [1.2], a common characteristic appears to be a hydrogen bonding network extending from the distal functional residues (His, Arg, Asn) to the functional residues (His, Asp) of the proximal side of the heme through various water molecules present in the active site. It has been suggested that the extensive conserved hydrogen bonding networks in the active site of heme peroxidases function to stabilise the different charges at the redox centre that develop during peroxidase catalysis (59). The role of the conserved active site residues during catalysis will be discussed in Section 1.5.4.

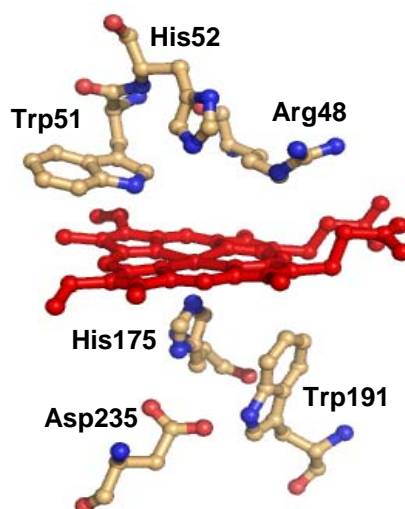


**Figure [1.4]:** The active site of CcP (PDB code: 2CYP) (58), showing the heme (red) and various active site residues.

**Table [1.2]: Catalytic residues in heme cavity of representative peroxidases from three classes (60).**

<b><i>Class I</i></b>							
<b>CcP</b>	Arg48	Trp51	His52	Asn82	His175	Trp191	Asp235
<b>APX</b>	Arg38	Trp41	His42	Asn71	His163	Trp179	Asp208
<b>KatG</b>	Arg104	Trp107	His108	Asn138	His270	Trp321	Asp381
<b><i>Class II</i></b>							
<b>CIP</b>	Arg51	Phe54	His55	Asn92	His183	Leu200	Asp245
<b>LIP</b>	Arg43	Phe46	His47	Asn84	His176	Phe193	Asp238
<b>MnP</b>	Arg42	Phe45	His46	Asn80	His173	Phe190	Asp242
<b><i>Class III</i></b>							
<b>HRP-C</b>	Arg38	Phe41	His42	Asn70	His170	Phe221	Asp247
<b>BP1</b>	Arg45	Phe48	His49	Asn77	His179	Leu224	Asp250

### 1.5.3 Mechanism of peroxidase catalysis

The goal of peroxidase chemistry is to use the two oxidising equivalents in  $H_2O_2$  to oxidise various biological substrates in a multi step reaction sequence, which proceeds through two detectable intermediates, Compound I and Compound II, which are represented in Equations [1.3 - 1.5] and are shown schematically in Figure [1.5], where SH and  $S^*$  are reduced and oxidised forms of the substrate.

The first step in peroxidase catalysis is the reaction of the resting ferric protein with  $H_2O_2$  to generate a transient hydroperoxide adduct, Compound 0 (a species also observed in heme oxygenase and cytochrome P450 catalysis), which leads to formation of a two-electron oxidised intermediate termed Compound I. Poulos and Kraut (28) proposed a mechanism for the formation of Compound I based upon the initial structure of CcP. As shown schematically in Figure [1.5],  $H_2O_2$  diffuses into the heme pocket and, in a concerted fashion, binds to the ferric iron with the concomitant donation of a proton to the distal histidine (His-52 in Figure [1.5]) from the  $\alpha$ -oxygen atom.

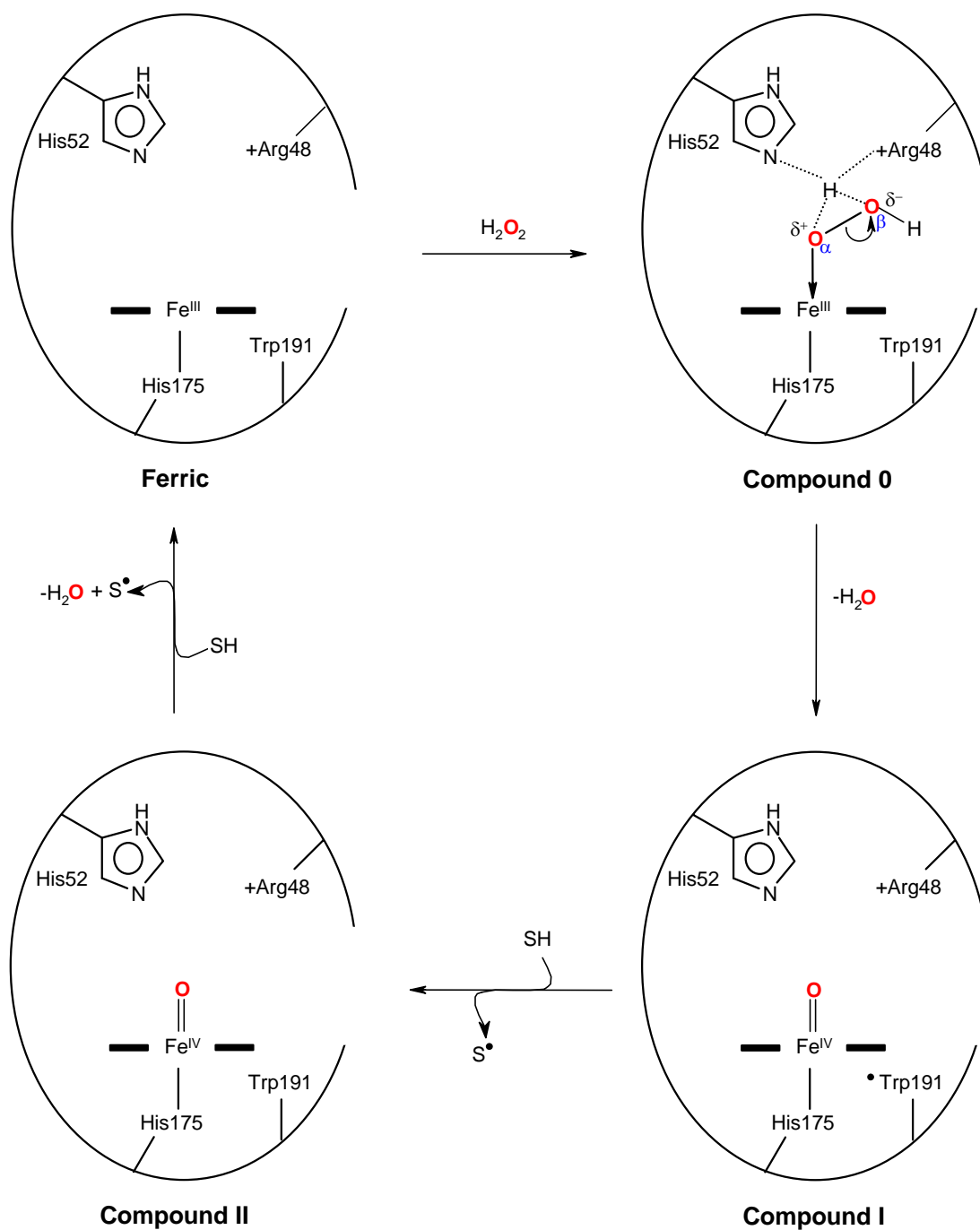


Figure [1.5]: Schematic representation of the catalytic mechanism of CcP (58). The thick black line represents the heme ring and S<sup>•</sup> and SH refer to the oxidised and reduced forms of the substrate, respectively.

The positively charged guanidinium side chain of the distal arginine (Arg-48 in Figure [1.5]) is proposed to interact directly with the anionic ligand, thus promoting the build-up of negative charge on the  $\beta$ -oxygen atom. Reorientation of the arginine, coupled with proton transfer from the distal histidine to the terminal oxygen of the peroxide ( $\beta$ -oxygen), results in the general acid-catalysed heterolytic (24,61) cleavage of the oxygen-oxygen bond, and formation of a ferryl ( $\text{Fe}^{\text{IV}}$ ) intermediate (Compound I) and a molecule of water. Extensive spectroscopic and kinetic evidence (24), including Mössbauer (62-64), EXAFS (Extended X-ray Absorption Fine Structure) (65), MCD (Magnetic Circular Dichroism) (66,67), ENDOR (Electron Nuclear Double Resonance) (68), magnetic susceptibility (69) and resonance Raman (70-73) supports formulation of the iron as a ferryl intermediate. Peroxidases can also utilise organic hydroperoxides, peracids and other oxygen-atom donors in place of  $\text{H}_2\text{O}_2$  to generate Compound I. The next step involves reduction of Compound I by an electron-rich substrate (SH) to generate Compound II and a radical of substrate ( $\text{S}^{\bullet}$ ). A second molecule of substrate (SH) reduces Compound II in the final step of the mechanism to regenerate the ferric resting state, and results in the protonation and subsequent release of the ferryl oxygen as a second molecule of water, Figure [1.5] (28).

The two substrate radical molecules ( $\text{S}^{\bullet}$ ) disproportionate non-enzymatically to form a two-electron-oxidised-molecule (S) and a regenerated substrate molecule (SH), (74) see Equation [1.6]:



The rate of substrate oxidation by Compound I is usually 10-100-fold faster than that by Compound II (75). This may be due to reorganisational energy differences between the two processes. The reduction of Compound I to Compound II merely requires the delivery of an electron to the ferryl-cation-radical species. However, reduction of Compound II to the ferric state requires the delivery of an electron and two protons, so that water can be released. In this process, the heme undergoes reorganisation from a six-coordinate to a five-coordinate iron (74), and thus normally represents the rate-limiting step in the overall peroxidase catalytic mechanism.

### 1.5.3.1 Anomalies in peroxidase catalysis

The oxygen atom which remains linked to the iron atom, upon heterolytic cleavage of the oxygen-oxygen bond, is a potent oxidant that removes one electron from the iron to give ferryl ( $\text{Fe}^{\text{IV}}$ ) iron and in the case of many peroxidases, bar CcP, one electron from the porphyrin to give a porphyrin  $\pi$ -cation radical (Figure [1.6A]) (76). The porphyrin thus plays an “active” role by storing one peroxide derived oxidising equivalent (1). The peroxidase-protein environment is designed to stabilise Compound I and peroxidases have, indeed, proven to be a rich source of understanding on how protein-heme interactions control heme reactivity (77). Evidence for a porphyrin  $\pi$ -cation radical in HRP Compound I, (Figure [1.6A]) came from Electron Paramagnetic Resonance (EPR) (76,78), ENDOR (68), Nuclear Magnetic Resonance (NMR) (79), resonance Raman spectroscopy (80), and self-consistent-field theoretical calculations (81). The same level of chemistry, as for Compound I of HRP, can be achieved with a single iron atom and a suitably stabilised protein centred radical (1), as observed for Compound I of CcP (Figure [1.6B]). In the Compound I species of CcP, one electron comes from the iron, as seen generally with the other peroxidases, and the second oxidising equivalent is stored in the form of a protein-based radical, which from site-directed mutagenesis (82) and ENDOR studies (83,84) was found to reside on the proximal tryptophan residue (Trp-191) (58,85-87).

Hence, the properties of the catalytic intermediates of the two benchmark proteins, CcP and HRP, were found to differ. This difference was initially accounted for based on amino acid sequence comparisons. CcP contains an oxidisable amino acid (Trp-191) (Figure [1.6B]) close to the heme that is used in Compound I formation, where as most other peroxidases lack an oxidisable residue at this position and instead have a phenylalanine residue at this position (Figure [1.6A]). The oxidation of phenylalanine is known to be energetically less favourable than that of tryptophan due to its high reduction potential and thus a porphyrin  $\pi$ -cation radical is used instead (88). However, studies performed on ascorbate peroxidase, which forms a porphyrin  $\pi$ -cation Compound I intermediate despite harbouring a proximal tryptophan (see Section 1.6.5) contradicted this hypothesis (88).

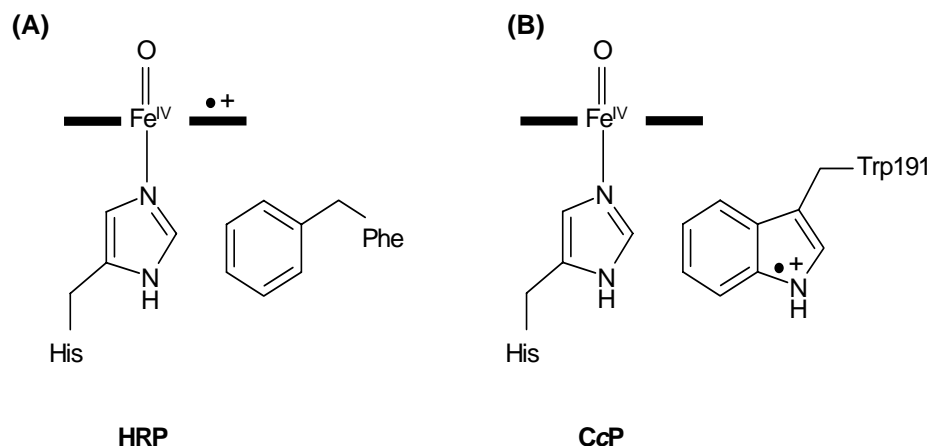


**Figure [1.6]:** The structures of the Compound I derivatives in (A) HRP and (B) CcP. The thick black line represents the heme ring and the axial histidine ligand is shown. For HRP, the second oxidising equivalent resides on the porphyrin ring (porphyrin  $\pi$ -cation radical); for CcP, an aromatic tryptophan residue, Trp191, adjacent to the heme is used (Trp $^{+\bullet}$  radical). Adapted from (89).

#### 1.5.4 Role of active site residues

Mutagenic studies on peroxidases, namely CcP and HRP, followed the successful cloning, expression of large amounts of recombinant protein and availability of crystallographic data and facilitated the detailed characterisation of heme peroxidases. An understanding on how peroxidase catalysis is controlled at an intermolecular level came from detailed characterisation studies on recombinant CcP and HRP active site variants. The conserved active site residues, shown in Figure [1.4]), have been thoroughly investigated using a combination of mutagenic, kinetic and spectroscopic techniques (the area has been reviewed (3,19,90-94).

Residues on the distal side of the heme are known to play a crucial role in the reaction of peroxidases with  $\text{H}_2\text{O}_2$ ; the most important being the distal site histidine and arginine residues. The distal histidine is known to perform several diverse roles. Firstly, it serves as a general base removing the  $\alpha$ -proton of  $\text{H}_2\text{O}_2$  facilitating binding of the peroxy anion to the ferric iron, and second, acting as a general acid stabilising the developing negative charge on the  $\beta$ -oxygen during heterolytic oxygen-oxygen bond cleavage through transferral of the  $\alpha$ -proton. Replacement of the distal histidine in studies performed on CcP (94-97) and HRP (98-101) essentially diminishes the

rate of Compound I formation, thus demonstrating the importance of this residue in peroxidase activity. The general base character of the distal histidine is maintained by a strong hydrogen bond to the distal asparagine. This histidine-asparagine bond, conserved throughout the peroxidase family (48,49,54), maintains the N<sup>ε</sup> of the distal histidine in a deprotonated form (102-105). Replacement of this distal asparagine in HRP with a valine or aspartate lead to a significant decrease in the rate of Compound I formation, indicating that the strong hydrogen bond is influential in peroxide activation (102-104).

Heterolytic cleavage of oxygen-oxygen bond and stabilisation of the resulting oxy-ferryl species is mainly attributed to the electron pull of the distal arginine and the push of the proximal histidine. Replacement of the distal arginine group with a lysine or leucine residue in CcP (95) had rather a modest effect on formation of Compound I, indicating that it is not essential for catalysis. On the other hand, when the distal arginine was mutated to a lysine in HRP (106) a 500-fold decrease in Compound I formation was observed. Therefore the removal of the positively charged guanidinium group in the active site is more critical in HRP than in CcP. Various site-directed studies on the distal arginine in HRP (99,107,108) revealed that arginine is essential for peroxidase catalysis because arginine and histidine are base partners and arginine plays a role in binding and heterolytically cleaving the peroxide bond (109).

The tryptophan residue in the class I peroxidase, CcP (Trp-51), is not critical for function although there is some evidence that it influences the stability of Compound I (110). Replacing Trp-51 in CcP with an alanine or phenylalanine residue effects the rate of Compound I formation, decreasing the rate to about 60 % and 40 %, respectively (111), and also makes the coordination of the heme iron sensitive to environmental effects, especially in the alanine variant (112). The analogous site in class II and class III peroxidases is occupied by a phenylalanine. In HRP the distal phenylalanine was found to act as a hydrophobic barrier between the distal site arginine and histidine and this hydrophobicity was found to be crucial in enzymatic catalysis (109).

On the proximal side of the heme, an aspartate-histidine-iron triad is present, with the proximal histidine forming a strong hydrogen bond with the buried charge of the aspartate. It is believed that this triad influences many of the biochemical and biophysical properties of the peroxidases such as the reduction potential and electronic properties (91,92,113). The carboxylate of the aspartate is thought to

stabilise the positive charge on the heme iron by partial (or complete) deprotonation of the histidine, resulting in a stronger histidine-iron bond (113). However, replacement of the proximal aspartate of CcP with an asparagine only leads to a 5-fold decrease in the rate of Compound I formation indicating that the electronic donation to the heme by the aspartate is not influential in peroxide activation (114). Additionally, the strong interaction between the proximal histidine and heme iron is responsible for a decreased affinity of the resting state for ligands at the sixth coordination site (99,109,115,116). Imidazolate character of the proximal histidine has also been proposed to stabilise the ferryl intermediate due to its electron-donating properties (117).

Replacement of the proximal tryptophan, Trp-191 the site of radical formation in Compound I of CcP, with a phenylalanine results in formation of an unstable classic peroxidase Compound I intermediate, a ferryl ( $\text{Fe}^{\text{IV}}$ ) porphyrin  $\pi$ -cation radical species (82,118). Thus in CcP the proximal tryptophan is required for formation of protein-based radical Compound I species. On the other hand in the class II and III peroxidases, which utilise a ferryl porphyrin  $\pi$ -cation radical species, harbour a phenylalanine at the analogous site to Trp-191 of CcP. In HRP, this aromatic residue (Phe-179) was found to be crucial for aromatic substrate binding (115).

## 1.6 ASCORBATE PEROXIDASE

Ascorbate-dependent peroxidase activity was first reported in 1979 (119,120), however detailed information did not emerge until the late 1990s when the availability of recombinant expression systems, for site-directed mutagenesis, and new structural information made structure-function studies on ascorbate peroxidase (APX) feasible for the first time.

### 1.6.1 Introduction

In cells,  $\text{H}_2\text{O}_2$  is an inevitable intermediate of dioxygen reduction. Being a stable oxygen radical form,  $\text{H}_2\text{O}_2$  will accumulate to toxic levels unless removed (121). Scavenging of  $\text{H}_2\text{O}_2$  in plants, algae and certain cyanobacteria is

accomplished by APX by reduction of the potentially damaging  $\text{H}_2\text{O}_2$  to water using ascorbate (Figure [1.7]) as a reductant, Equation [1.7]:

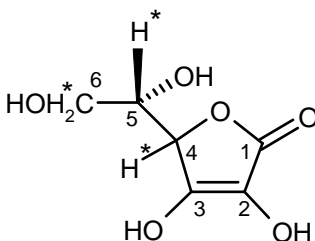


**Figure [1.7]:** The structure of L-ascorbic acid (vitamin C), showing the L configuration at C<sup>5</sup>. Non-exchangeable protons are indicated with a \*. The pK<sub>a</sub>s of the 2-OH and 3-OH groups are 11.3 and 4.0, respectively; (122) at neutral pH. The 3-OH group is deprotonated and the molecule exists as the anionic form.



Under physiological conditions, the immediate product of the reaction, the monodehydroascorbate radical, Figure [1.8A], is reduced back to ascorbate in a NAD(P)H-dependent reaction catalysed by monodehydroascorbate reductase (123-130). However, in the absence of a reductase, two monodehydroascorbate radicals can disproportionate rapidly to dehydroascorbic acid and ascorbate (131), Figure [1.8B]. Ascorbate can be regenerated from dehydroascorbic acid, formed from the spontaneous disproportionation reaction, using a glutathione-dependent dehydroascorbate reductase (132).

APX enzymes are class I heme peroxidases that show high specificity for ascorbate as an electron donor, but are somewhat indiscriminate in their choice of redox partner. Thus, the class I peroxidase, APX, will oxidise non-physiological (usually organic) substrates that are characteristic of the class III peroxidases, in some cases at rates comparable to that of ascorbate itself (89). Due to this broad substrate specificity it appears more sensible to classify a peroxidase as an APX when the specific activity of the enzyme for ascorbate is higher than that for other substrates (89). Using this classification system discrimination between APXs and other classical peroxidases that are, coincidentally also able to catalyse oxidation of ascorbate becomes possible.

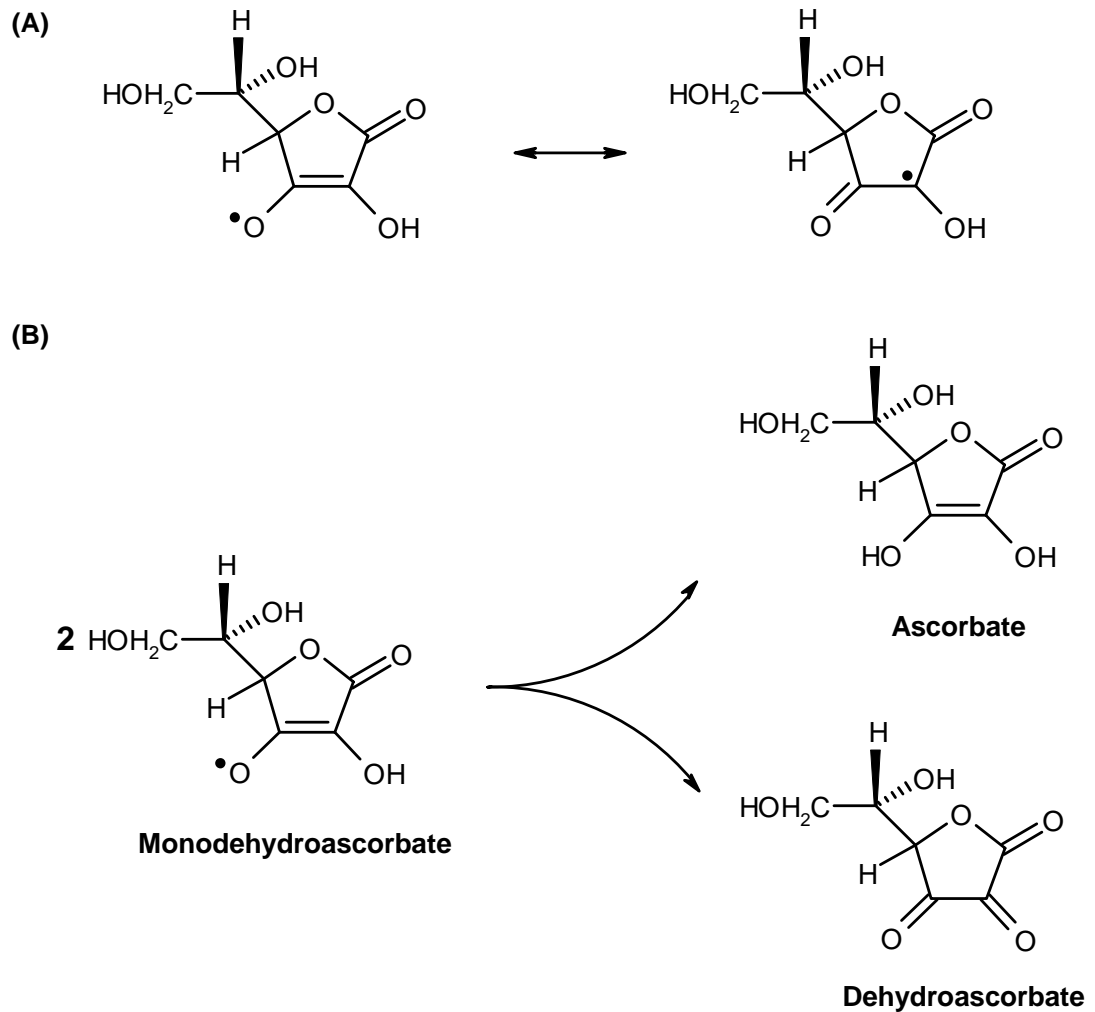


Figure [1.8]: (A) The structure of protonated monodehydroascorbate radical. This molecule is very acidic ( $pK_a = 0.45$  (122,133)). (B) Schematic diagram showing the disproportionation of the free radical, monodehydroascorbate, to dehydroascorbate and ascorbate.

### 1.6.2 Isolation of APX

APXs have been isolated and purified from a number of sources including plant chloroplasts, plant cytosol and nitrogen-fixing root nodules; However in most cases the yields are low and there is only limited functional information available (134,135). Chloroplastic APX enzymes have been isolated and purified from spinach (136-139), pea (140,141), wheat (142), tobacco (40) and tea (135,143-146). Cytosolic APX has been purified from pea (119-121,147), Japanese radish (148), soybean (149), wheat (150,151), potato tubers (152), maize (153), komatsuna (154), tea (135,144,155), cucumber (156), spinach (136,137), bean (*Phaseolus vulgaris*) (157) and rice (130). Glyoxysomal enzymes have been identified in cotton (158),

pumpkin (159) and spinach (160,161); peroxisomal enzymes have been identified in cucumber (162), pea (163,164) and pumpkin (159). APXs have also been identified from several algal sources, namely *Galdieria partita* (165,166), *Selenastrum capricornutum* (167), *Chlorella vulgaris* (168), *Chlamydomonas* sp. W80 (169) and *Euglena gracilis* (170,171), in cyanobacteria (172,173), insects (174) and in mitochondria from potato tuber (175). A mammalian APX has been found in bovine eye (176), raising the intriguing possibility that APX may have a functional role in mammalian systems.

### 1.6.3 APX cDNA sequences and bacterial expression

Since the publication of the first APX cDNA sequence from pea cytosolic APX in 1991 (121) a plethora of cDNA sequences for APX enzymes from various sources have appeared. These include: (a) the soluble cytosolic enzymes from soybean (177,178), spinach (160,179), *Arabidopsis* (180), carrot (181), radish (182,183), maize (184), potato (185), tobacco (186), rice (187,188), strawberry (189), tomato (190), pepper (bell pepper (191) and hot pepper (192)) and *Pimpinella brachycarpa* (193); (b) the stromal (chloroplastic) enzymes from *Arabidopsis* (194,195), spinach (196) and pumpkin (197); (c) the thylakoid-bound (chloroplastic) enzymes from *Arabidopsis* (194,195), spinach (196) and pumpkin (197,198); and (d) the glyoxysomal/peroxisomal (microbody-bound) enzymes from *Arabidopsis* (194,195,199), spinach (161), pumpkin (200), cotton (201), barley (202) and *M. crystallinum* (203). cDNA sequences are also available for algal APX enzymes (166,168,204). The potassium binding site was found to be a conserved feature of the above mentioned APX proteins.

Although a variety of cloned genes for various APXs are now available, expression of these genes in *E. coli* to generate workable amounts for structure/function studies has been less successful (51). Recombinant expression systems have been reported in few cases. Pea cytosolic APX was first over-expressed in *E. coli* as a fusion product with the *E. coli* maltose binding protein (89,205). This expression system was, however, later modified to use a more efficient histidine-tag expression vector (206) which delivered greater amounts of workable protein than the previous methods of APX expression. Expression of cytosolic APX enzymes from soybean (177,207) and spinach, (137) have also been reported and

the authenticity of the recombinant wild type pea (rpAPX) and soybean (rsAPX) enzymes has been confirmed using a variety of spectroscopic and crystallographic techniques (41,208-212). Alignment of the amino acid sequences of rpAPX and rsAPX, shows a 90 % backbone homology (Figure [1.9]). Bacterial expression of two chloroplastic (stromal and thylakoid-bound) (40,137,213) enzymes, a glyoxysomal APX enzyme (161) from spinach, and for algal APX (169) have been reported.

```

Soybean APX
Pea APX

1
MGKSYATVSADYQKAVEKAKKKL
-GKSYPTVSADYQKAI EKAKRKL

61
RGFIAEKRCAPLMLRLAWHSAGTFDKGKTGGPFATIKHPAELAHSANGLDIAVRLLEP
RGFIAEKRCAPLILRLAWHSAGTFDSKTGKTGGPFATIKHQAE LAHGANNGLDIAVRLLEP

121
LKA EFPILSYADFYQLAGVVAVEVTGGPEVPPFHPGREDKPEPPP EGRLPDATKGS DHLRD
I KEQFP I VSYADFYQLAGVVAVEITGGPEVPPFHPGREDKPEPPP EGRLPDATKGS DHLRD

181
VFGKAMGLTDQDIVALSGGHTIGAAHKERSGFEGPWTSNPLIFDNSYFTELLS GEKEG LLL
VFGKAMGLSDQDIVALSGGHTIGAAHKERSGFEGPWTSNPLIFDNSYFTELLTGEKDGLL

241
QLPSDKALLSDPVFRPLVDKYAADEDAFFADYAEAHQKLS E L G F A D A
QLPSDKALLTDSVFRPLVEKYAADEDVFFADYAE AHLKLS E L G F A E A

```

**Figure [1.9]: Sequence alignment of rpAPX and rsAPX with the differences underlined. The two sequences are 90 % identical. The active site residues are highlighted in red. Residues involved in ascorbate binding are highlighted in green and residues involved in potassium binding are highlighted in blue.**

## 1.6.4 Structural studies on APX

### 1.6.4.1 Overall structure

The crystal structure rpAPX was reported in 1995 (41) which provided a platform whereupon structure/function studies were launched. rpAPX was found to crystallise as pair of homodimers, where the dimer interface was found to consist of a series of electrostatic interactions. The monomeric structure of the rpAPX, shown in Figure [1.10], was found to be very similar to that of CcP (58), Figure [1.10], comprising of 12 helices (as for CcP) but contained less  $\beta$ -sheet structure than CcP. The overall arrangement of the recently solved structure of rsAPX, Figure [1.10], which has 91 % sequence identity with rpAPX, was found to be very similar to

that of rpAPX (r.m.s. deviation between C $\alpha$  positions of 0.443 Å) (89). Although, APX has high sequence identity with CcP structural alignment of CcP with rpAPX and rsAPX (89) revealed differences between the two class I peroxidases: (a) APX was found to be truncated at the C-terminus; (b) the loop containing residues 34 - 41 in CcP was found to be missing in APX and; (c) CcP was found to harbour an additional  $\beta$ -sheet structure that is missing in APX. The functional consequences of these differences are discussed later.

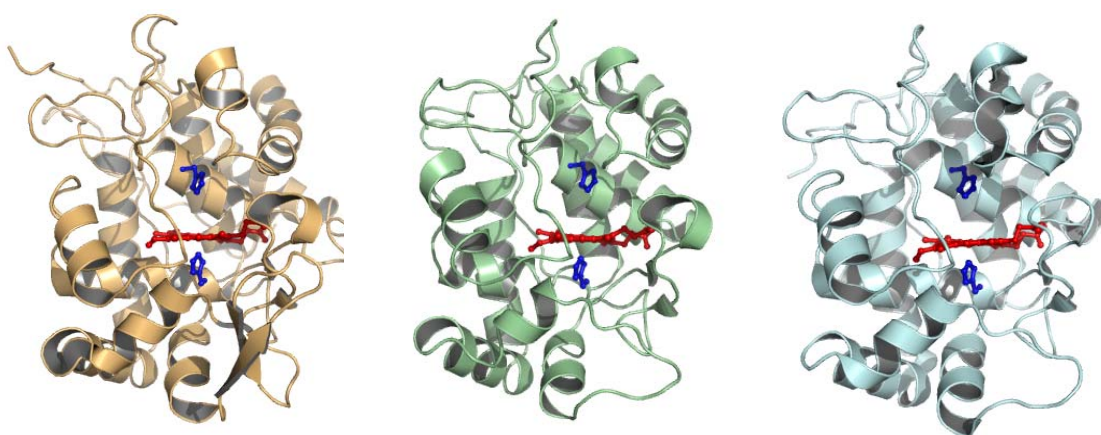


**Figure [1.10]:** The overall structures of (*left*) CcP (58) , (*middle*) rpAPX (41) and (*right*) rsAPX (42) (PDB code: 2CYP, 1APX, 1OAG, respectively), showing the heme (red) and active site (distal and proximal) histidine residues (blue).

#### 1.6.4.2 Active site structure

The active site structure of rsAPX (214), shown in Figure [1.11], is essentially identical to that of rpAPX (41) and very similar to that of CcP Figure [1.11]. The heme is anchored in the protein through a coordinate bond from proximal histidine (His-163) to the iron and the residues present in the distal cavity of APX (Arg-38, Trp-41, His-42) are also observed in the distal pocket of CcP (Arg-48, Trp-51, His-52). On the proximal side, the catalytic His-Asp-Trp triad present in CcP (His-175, Asp-235, Trp-191) is also apparent in APX (His-163, Asp-208, Trp-179).

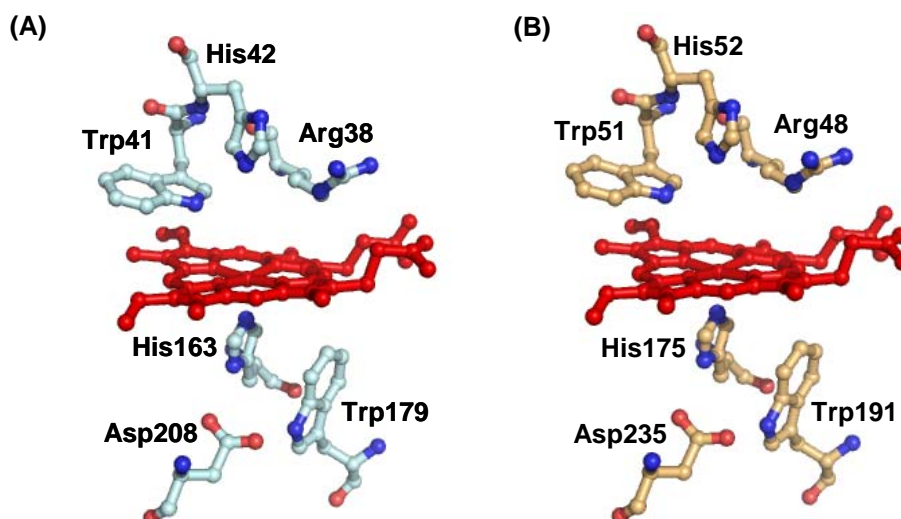
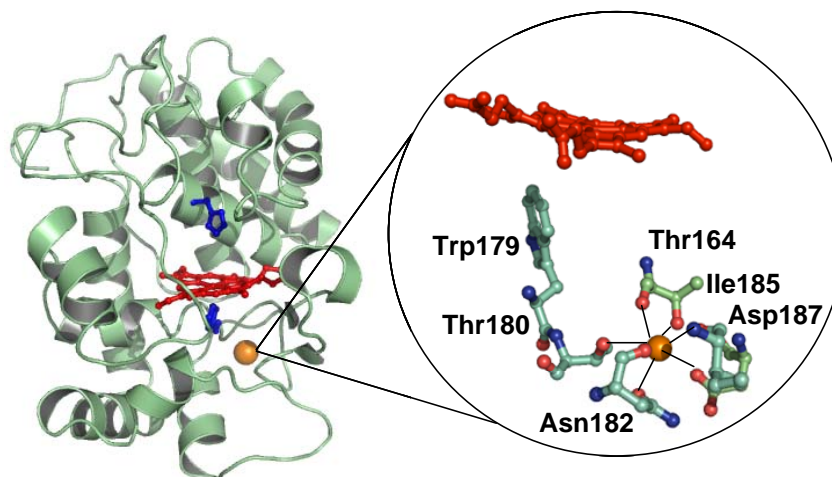


Figure [1.11]: The active site of (A) rsAPX (42) and (B) CcP (58) (PDB code: 1OAG and 2CYP, respectively) showing the heme (red) and various active site residues.

#### 1.6.4.3 Metal ion site

A metal binding site, assigned as a potassium ion binding site, close to the heme porphyrin was identified in the rpAPX structure, Figure [1.12]. The potassium ion is found to be coordinated, with ligands provided from Asp-187 ( $O^\delta$ ), Thr-164 ( $O^\gamma$ ), Thr-180 ( $O^\gamma$ ), Asn-182 ( $O^\delta$ ) and three main chain carbonyl oxygens (Asn-182, Ile-185 and Thr-164). The metal ion is also linked through an extensive array of hydrogen bonds to the distal histidine itself, and is only  $\sim 8$  Å from the  $\alpha$ -carbon of the Trp-179 residue. The metal was assigned as a monovalent potassium ion ( $K^+$ ), because it was only bound by one charged ligand (Asp-187), whereas two charged ligands are normally found for divalent ions, such as calcium ions ( $Ca^{2+}$ ) found in the class II and class III peroxidases. Crystallographic data for rsAPX (42) are consistent with occupation of the equivalent site in rsAPX by a water molecule and not a metal site. However, in the structure of the rsAPX-ascorbate complex the presence of a sodium ion, almost certainly introduced during soaking of rsAPX crystals with sodium ascorbate, was observed. The sodium ion in rsAPX was ligated by similar ligands (Thr-164, Asn-182, Ile-185 and hydrogen bonded to Asp-187) as the potassium ion in rpAPX. The presence of a metal site in rpAPX was not expected and its exact role, if there is one, is unclear at this stage (89). However, removal of the metal ligands in rpAPX by site-directed mutagenesis resulted in large conformational changes and formation of a new low-spin form of the enzyme that had electronic and MCD

spectroscopic properties similar to those observed for bis-histidine ligated proteins, such as cytochrome  $b_5$  (206,207). Although the exact nature of the axial ligands in the low-spin derivative were not assigned, it is clear that the potassium site plays a structural role in rpAPX.



**Figure [1.12]:** The overall structure of potassium bound rpAPX, showing the heme (red), potassium ion (orange) and distal and proximal histidine residues (blue). *Inset:* shows the metal-ligand interactions. Adopted from (87) (PDB code: 1APX).

### 1.6.5 Catalysis in APX

Publication of the rpAPX crystal structure in 1995 provided a prominent contribution to the APX research field and made structure-function studies feasible. The structure provided a dichotomy of ideas: (a) on one hand, APX, as expected, had a high sequence identity with the well-characterised class I peroxidase CcP and was found to contain the same active site (proximal) tryptophan residue (Trp-179, Figure [1.11]) that in the Compound I derivative of CcP is the site of the protein-based radical (Trp-191, Figure [1.11]); (b) on the other hand, unlike the benchmark peroxidase CcP, which utilises an atypical macromolecular protein substrate, APX was found to be representative of the classical class III enzymes in that it oxidises small aromatic substrates. The substrate binding properties of APX place it at the interface between the class I and class III peroxidases (89). Therefore due to the high sequence identity of APX with CcP and the class III-peroxidase type substrate specificity, APX was identified as a useful model for understanding the more general aspects of peroxidase catalysis.

The catalytic oxidation of ascorbate by APX is analogous to the description of peroxidase catalysis provided in Section 1.5.3, Equations [1.3 - 1.5] and is discussed in detail in the following sections.

#### **1.6.5.1 Compound I intermediate of APX**

The reaction of  $\text{H}_2\text{O}_2$  with APX, which is known to be pH-dependent (212), proceeds rapidly to form Compound I and the second-order rate constant for this process has been determined for various APX enzymes (146,211,212,215-218). Surface mutations in APX, designed to probe substrate binding, don't affect the rate of Compound I formation (212,216-218). However, replacement of the distal histidine (His-42) with an alanine (H42A) essentially eliminates reactivity towards  $\text{H}_2\text{O}_2$  (212). While, replacement of the distal histidine with a glutamic acid residue yields a variant (H42E) that can also act as the acid-base catalyst during Compound I formation in place of His-42 in APX (212). Similar observations were made in CcP and HRP on mutation of the distal histidine (3,8,11,12,20-22,219-221) and the role of the distal histidine has been reviewed extensively (3,21,93,94,222,223).

Formation of Compound I (discussed in Section 1.5.3) is known to involve binding of neutral peroxide, concomitant proton transfer from peroxide to the distal histidine, followed by O-O bond cleavage and release of water, Figure [1.13]; Yet, there is only limited information in support of formation of a transient Compound 0 (hydroperoxo) intermediate in heme peroxidases. The H42A variant of APX, however, provided kinetic evidence for the presence of the transient Compound 0 intermediate during Compound I formation, because the rate constant for cleavage of the O-O bond becomes rate-limiting in the variant. The transient spectra, in this case, suggest neutral ferric peroxide ( $\text{Fe}^{\text{III}}\text{-HOOH}$ ) rather than a hydroperoxo ( $\text{Fe}^{\text{III}}\text{-OOH}$ ) structure for this intermediate. Transient intermediates have also been detected for HRP in polyethylene glycol (224) and under cryogenic conditions (225-227) and in variants of HRP (H42L, R38L, R38G) (107,228).

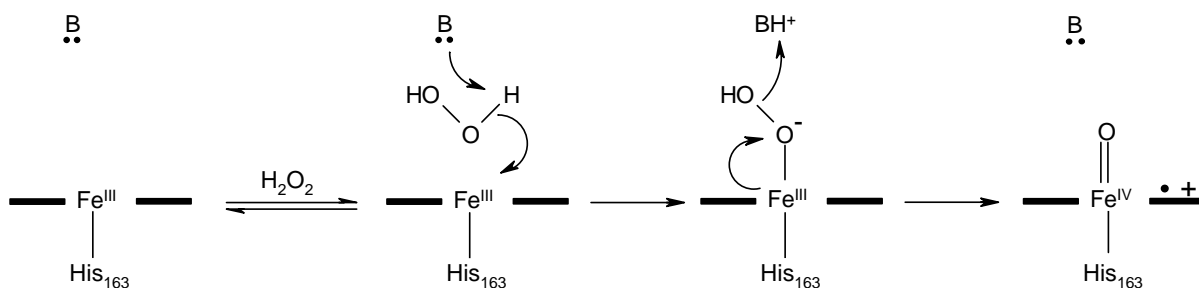


**Figure [1.13]: Proposed mechanism for formation of Compound I in APX, showing formation of the neutral peroxide-bound and anionic peroxide-bound intermediates. The distal histidine residue that acts as the acid-base catalyst is indicated (B). Adapted from (212).**

Despite the high sequence identity of APX and CcP and presence of the same active site tryptophan residue (Trp-179, Figure [1.11]), that is used in CcP (Trp-191, Figure [1.11]) as the site of radical formation on reaction with peroxide, the Compound I intermediate of rpAPX, however, was identified as a porphyrin  $\pi$ -cation radical using EPR spectroscopy (210) (Figure [1.14]). Spectroscopic studies (146,155,211,212,215) from various laboratories confirmed the origin as assignment of a porphyrin  $\pi$ -cation radical Compound I intermediate for several other APX enzymes, including rsAPX (211). Also the wavelength maxima for Compound I derivatives of various APX enzymes are consistent with those observed for HRP, in which porphyrin  $\pi$ -cation radical formation has been established (229). In the absence of substrate, migration of the radical from the porphyrin to the protein is known to occur in APX (230-232).

Compound I of APX is very short-lived ( $t_{1/2}$  ~seconds) (210), which contrasts with the stability of the protein radical formed in CcP ( $t_{1/2}$  ~2 hours) (233) on reaction with H<sub>2</sub>O<sub>2</sub>. However, on replacement of the proximal tryptophan residue in CcP with a phenylalanine (W191F) a transient porphyrin  $\pi$ -cation radical Compound I intermediate (analogous to APX) is formed in the W191F variant, which is similarly unstable (82,118). The proximal tryptophan in CcP (Trp-191) is also found to be absolutely essential for cytochrome *c* oxidation (234), whereas removal of Trp-179 in APX (W179F variant) has only a marginal effect on the ability of the enzyme to oxidise ascorbate (217).

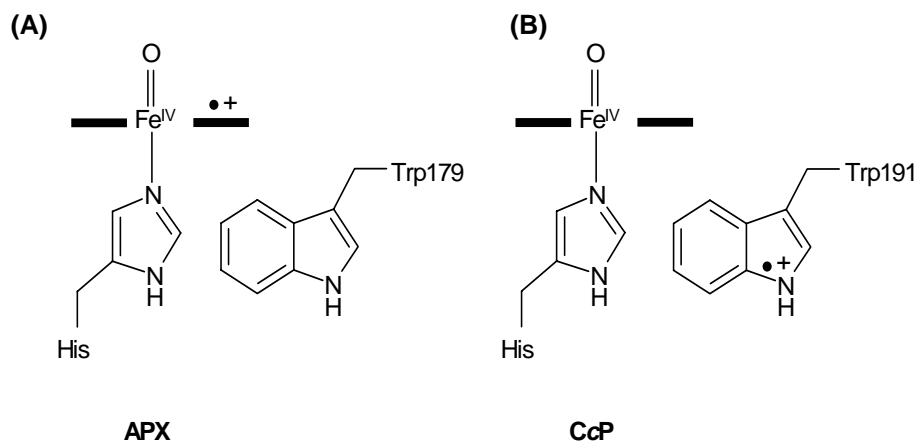


**Figure [1.14]:** The structures of the Compound I derivatives in (A) APX and (B) CcP. The thick black line represents the heme ring and the axial histidine ligand is shown. For APX, the second oxidising equivalent resides on the porphyrin ring (porphyrin  $\pi$ -cation radical); for CcP, an aromatic tryptophan residue, Trp191, adjacent to the heme is used (Trp<sup>•+</sup> radical). Adapted from (89).

It was initially proposed that the potassium ion, which is known to play structural role in APX (see Section 1.6.4.3), located  $\sim 8$  Å of Trp-179 in rpAPX but not present in CcP might destabilise radical cation formation at Trp-179 on electrostatic grounds (89). Thus a corresponding potassium ion binding site was engineered, by iterative mutations, in CcP and the new metal site was found to destabilise protein radical formation at Trp-191 (87,235,236). In more recent studies, the Trp-191 radical in CcP is found to be stabilised by three methionine residues (1). Converting these three methionine residues to the corresponding residues in APX was found to decrease the stability of the Trp-191 cation radical (237). Furthermore, the reverse experiment where the three methionine residues were engineered into the proximal cavity of APX lead to formation of Trp-179 cation radical and a decrease in the stability of the porphyrin radical (77). Contradictory to these results, formation of a porphyrin  $\pi$ -cation radical Compound I intermediate was observed in a variant of APX where a single methionine residue was introduced to the proximal cavity (231). In light of these results, it appears electrostatics is the key feature controlling how the radical is distributed within the heme pocket and this view is supported by theoretical calculations (77,87,238-242). However, the electrostatic arguments do not account for the failure to observe a radical at Trp-179 in rsAPX, which contains no metal site (42) and yet still uses a porphyrin  $\pi$ -cation radical (211).

However, a new hypothesis that is emerging in the field is that the site of substrate binding may influence the site of delocalisation of the second oxidising equivalent (88). In CcP the binding site for substrate, cytochrome *c*, is close to protein radical at Trp-191 meaning that efficient electron transfer can occur during catalysis (Figure [1.15]) (56); Whereas in APX, which has a porphyrin  $\pi$ -cation based Compound I, ascorbate is found to interact near the  $\gamma$ -heme edge (42) (see Section 1.6.6) which enables rapid hydrogen abstraction by the porphyrin radical (1).

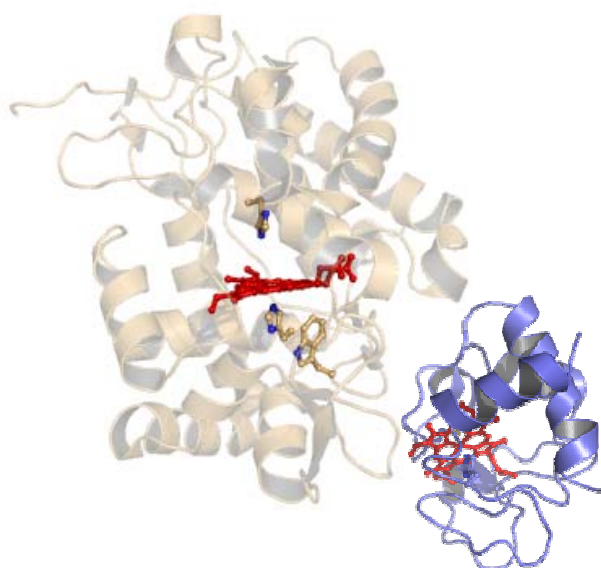


**Figure [1.15]:** The crystal structure of the noncovalent complex between CcP (shown in yellow) and cytochrome *c* (shown in blue) (PDB code: 2PCB) (56). The heme (red), proximal tryptophan, distal and proximal histidine of CcP and the heme (red) and proximal histidine of cytochrome *c* are indicated.

### 1.6.5.2 Compound II intermediate of APX

The short-lived Compound I intermediate is rapidly reduced by ascorbate, to form Compound II, and the rate constants for various APX enzymes have been reported (89,146,211,212,215-218). Compound II is a relatively stable ferryl ( $\text{Fe}^{\text{IV}}=\text{O}$ ) heme species, which can be observed by conventional electronic spectroscopy. Reduction of Compound II by ascorbate is the rate-limiting step of the APX mechanism, and has been shown to be biphasic at high ascorbate concentrations (211). This biphasic behaviour was eliminated when the APX was modified with Ellman's reagent (5,5'-dithiobis(2-nitrobenzoic acid)), which specifically modifies cysteine amino acids. The structure of Cys-32-modified rpAPX derivative (216)

revealed that Ellman's reagent selectively blocked binding of ascorbate close to the Cys-32. This data (211) provided evidence for distinct high- and low-affinity binding sites for ascorbate in APX, which built upon previous NMR data (243) that suggested the presence of more than one substrate binding site (89). The existence of more than one binding site has been prevalent in peroxidase literature and has also been identified under certain conditions for cytochrome *c*-CcP (reviewed in Ref. (223) and references therein) and manganese (II)/MnP interactions (244), and discrete binding sites (89) for many different substrates have been proposed in LiP (40) and CcP (245).

### **1.6.5.3 Steady state catalysis in APX**

Steady state oxidation of aromatic substrates by APX enzymes became a widespread feature in the APX literature before development of recombinant expression systems (89). Consistent with the idea of more than one binding site in APX, ascorbate turnover by rpAPX and rsAPX (121,149,205,207,246) exhibited a non-hyperbolic (sigmoidal) dependence of the rate on substrate concentration. However, sigmoidal kinetics is not a feature of all APX enzymes (89). This non-hyperbolic dependence on ascorbate was thought to arise from cooperativity in the homodimeric structure of rpAPX and rsAPX enzymes; however site-directed mutagenesis studies in which the dimer interface was destabilised did not support this (246). Recently a cooperative model, in which substrate binding at one site induces conformational changes that affect binding of substrate at another site, has been used to analyse the sigmoidal kinetics exhibited by rpAPX and rsAPX enzymes (211). A complex dependence of rate on substrate concentration under various conditions has also been observed during steady state oxidation of cytochrome *c* by CcP (reviewed in reference (90,94)).

On the other hand, oxidation of non-physiological aromatic substrates (*e.g.* guaiacol and salicylhydroxamic acid (Figure [1.16]) by rpAPX and rsAPX, is known to occur at rates comparable to ascorbate turnover and exhibits Michaelis-Menten (hyperbolic) kinetics. The binding site for ascorbate and aromatic substrates was found to be in different locations and is discussed in detail in the following section.

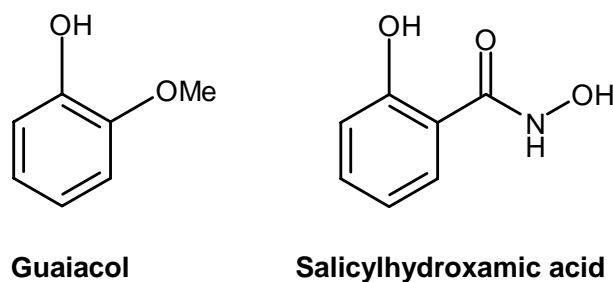


**Figure [1.16]:** The structure of guaiacol and salicylhydroxamic acid, examples of the aromatic substrates oxidised by APX.

### 1.6.6 Substrate binding in APX

Although structures of peroxidases bound with substrate were available in the literature for complexes of cytochrome *c*/CcP (56), manganese (II)/MnP (45), benzhydroxamic acid/HRP (50,247), ferulic acid/HRP (247,248), halide/MPO (249), benzhydroxamic acid/ARP (250) and iodide/ARP (251). Nonetheless, these structures provided limited generic information (89) because the substrate was either not representative of peroxidases in general (e.g. cytochrome *c*, manganese (II), halide ion), had no known physiological role or was not the true biological substrate of the peroxidase in question. Thus assignment of the binding site in APX became an interesting target due to the substrate binding properties of APX that place it at the interface between class I and class III peroxidases (89). Based on spectroscopic, site-directed mutagenesis and chemical modification studies (50,147,216,218,243,248,252) the binding site in APX was hypothesised to be located at the  $\gamma$ - or  $\delta$ -meso heme edge. Publication of the ascorbate/rsAPX crystal structure (42) (Figure [1.17A]) resolved and validated the predictions from previous studies and confirmed  $\gamma$ -heme position as the site of ascorbate oxidation. The bound ascorbate is stabilised (Figure [1.17B]) by hydrogen bonds between 2-OH and 3-OH groups of ascorbate, (Figure [1.7]), and Arg-172. The hydrogen bond between the 2-OH group of ascorbate and the (deprotonated) heme 6-propionate was also found to stabilise ascorbate binding in rsAPX. Additional hydrogen bond stabilisation is provided to 6-OH of ascorbate from Lys-30, which swings in from solvent on substrate binding (42). The contributions of these hydrogen bonds were dissected using site-directed mutagenesis, kinetics, crystallographic and modified substrate analogues (253). The hydrogen bonds to Arg-172 and the heme 6-propionate were

found to play a major part in stabilisation of the bound ascorbate, whereas interaction with Lys-30 was found to play a minor contribution (253).

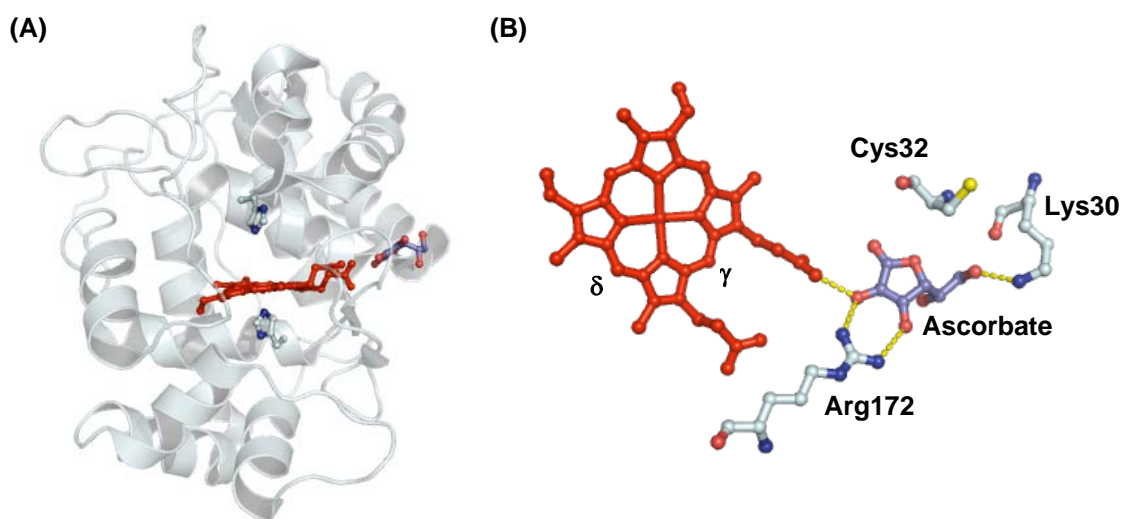


**Figure [1.17]: (A) The ascorbate/rsAPX complex (PDB code: 1OAF) (42). The heme (red), the proximal and distal histidine residues and the bound ascorbate molecule are indicated. (B) The ascorbate binding site in the ascorbate/rsAPX complex. Hydrogen bonds are shown as yellow dashed lines.**

Arg-172 is fully conserved in all APX enzymes, except in the membrane-bound enzyme from *M. crystallinum*, where it is replaced by an isoleucine residue. The N-terminal region is less well-conserved overall in APX enzymes (89). The presence of a lysine residue at position 30 (Lys-30) is not fully conserved, although there is a lysine present in *M. crystallinum* enzyme. A lysine residue at position 29 or 31 is found in enzymes where Lys-30 is absent (89). The membrane-bound enzyme from spinach is the only example of an APX enzyme where a lysine residue is completely absent. Although Arg-172 is present in the spinach APX enzyme, like the *M. crystallinum* enzyme it also curiously lacks Trp-41 and Trp-179 (replaced by phenylalanine residues) (89).

The use of heme propionates for binding substrate is not just unique to APX; the first crystallographic indication that the heme propionates may be active players in redox transformations came from the manganese (II)/MnP structure (45), in which the manganese (II) ion was ligated by the heme propionate. The use of heme propionates in substrate binding was also found to be evident in nitric oxide synthase (254-256) and in di-heme CcP (16). Thus the structure-function studies on these four

examples provides a clear indication that the heme propionates serve as electron transfer conduit from the substrate to the porphyrin radical and the ferryl iron (1).

The structure of the salicylhydroxamic acid (SHA)/rsAPX complex confirmed the  $\delta$ -heme edge (Figure [1.18]) as the site for oxidation of aromatic substrates (214). The SHA molecule (Figure [1.16]) was found to be bound close to the  $\delta$ -heme edge, stabilised by hydrogen bonds between the phenolic hydroxide of SHA and the main chain carbonyl of Pro-132, between the carbonyl oxygen of SHA and the side chain guanidinium group of Arg-38, and between the hydroxamic acid group and the indole nitrogen of Trp-41.

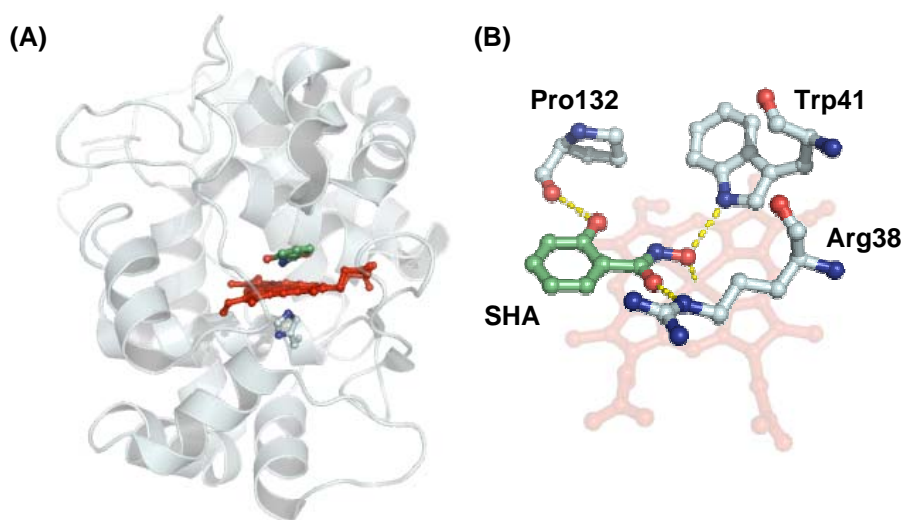


**Figure [1.18]: (A) The SHA/rsAPX complex (PDB code: 1VOH) (214). The heme (red), the proximal histidine and the bound SHA molecule are indicated. (B) The SHA binding site in the SHA/rsAPX complex. Hydrogen bonds are shown as yellow dashed lines.**

The crystal structures of ARP and HRP in complex with SHA (250) and its analogue benzylhydroxamic acid (BHA) (50,250) also revealed the  $\delta$ -heme edge as the binding site for aromatic substrates. The oxidation of guaiacol (Figure [1.16]) was found to be inhibited in the presence of SHA and BHA, thus the  $\delta$ -heme edge is the binding site for guaiacol also (214). The following section provides a brief discussion of the “active” role of heme in electron transfer, cytochrome P450 and heme oxygenase heme proteins.

## 1.7 ELECTRON TRANSFER HEME PROTEINS

Electron transfer heme proteins perform the reversible reduction-oxidation (redox) reactions essential in biological processes such as photosynthesis and respiration. The iron in these “active” heme proteins undergoes an electronic transformation (shuttles between the ferric and ferrous oxidation state) during the electron transfer reaction. The ability of these heme proteins (and other electron transfer systems in general) to carry out electron transfer reactions is dependent on a number of factors. Firstly, the distance between redox centres during the transfer process and the nature of the intervening medium, *i.e.* whether the electron travels through a bond or through space, is vitally important. Secondly, the rates of electron transfer within physiological systems are influenced by the differences in reduction potential between the electron donor and acceptor. This factor contributes to the driving force for the reaction. In addition, the re-organisation energy associated within the protein also affects the efficiency of electron transfer.

Heme is found to be ideally suited for electron transfer reactions, since the extended  $\pi$ -system of the porphyrin ring delocalises the electron/electrons over a wide surface, thereby reducing the necessity for re-organisation in the local atomic structure and the surrounding protein environment during electron transfer (change in oxidation state). Cytochromes, one of the electron transfer heme proteins found in nature, capitalise on these advantages by minimising the required re-organisation energy associated with electron transfer within the rigid hydrophobic heme environment. Thus for cytochromes, which are associated with simple electron transfer reactions, the heme is usually found to be six-coordinate, low-spin (where methionine and histidine act as the fifth and sixth ligands) (Figure [1.19]) and encapsulated within a hydrophobic crevice (257). Therefore, delocalisation of the electron can be easily achieved over the porphyrin ring  $\pi$ -system.

The reduction potential of the heme can be modulated over a wide range (-400 mV to +400 mV) by the surrounding protein environment. The rate of electron transfer, as mentioned above, is dependent on the reduction potential of the electron donor and electron acceptor (4). Site-directed mutagenesis has facilitated quantification of the effect that the heme-iron ligation has upon heme protein reduction potentials (134,258-262). Factors that are known to also affect reduction potentials include (a) orientation of the heme (263), (b) the orientation of the heme

vinyl groups (220), (c) the identity and hydrogen bonding to the proximal and distal ligands (221,264,265). The exact structural factors controlling the reduction potential in heme proteins is still unfortunately not clearly defined, because isolation of only one of the above variable factors, whilst keeping all other factors constant has proved difficult.

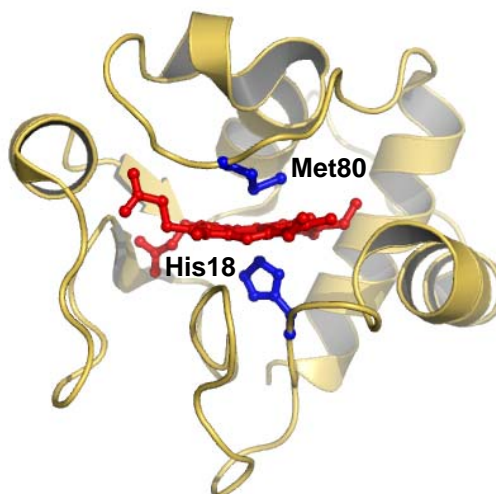
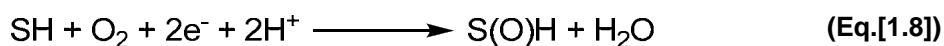


Figure [1.19]: The structure of yeast cytochrome *c* (PDB code: 2YCC) (257). The heme group is shown in red together with the axial histidine and methionine ligands which are shown in blue.

## 1.8 MONOOXYGENASES

Heme-containing monooxygenases are remarkably versatile oxygen-activating catalysts that can incorporate one of the two oxygen atoms of oxygen into a broad variety of substrates with concomitant reduction of the other oxygen atom by two electrons to water (8) Equation [1.8]:



Cytochrome P450s, which have been isolated from numerous mammalian tissues, insects, plants, yeasts and bacteria, are a well known examples of the heme-containing monooxygenase family of heme proteins (266-268). Cytochrome P450 is a heme *b* containing monooxygenase where the proximal site is occupied by a cysteine (Cys) residue, leaving the distal site vacant to bind and activate molecular oxygen (Figure [1.20]). The heme in this “active” redox protein requires electrons, for activation of oxygen, that are transferred to the enzyme by electron transfer proteins

and insertion of one of the oxygen atoms necessitates that the substrate to be bound within the vicinity of the heme iron.

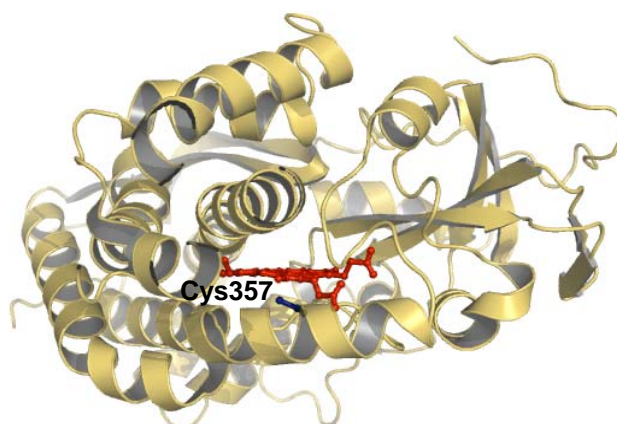


**Figure [1.20]: The structure of cytochrome P450cam (PDB code: 2CPP) (269). The heme group is shown in red together with the thiolate axial ligand in blue.**

The catalytic reaction cycle of cytochrome P450, Figure [1.21] (57,270), involves: (a) binding of the substrate to the heme iron which is associated with a change in the heme-iron reduction potential (from -270 mV to -170 mV) (271) and reduction of the heme from ferric to the ferrous state; (b) binding of molecular oxygen to generate the dioxygen complex; (c) protonation and transfer of a second electron to this complex to give a ferric hydroperoxo intermediate (also known as Compound 0); (d) cleavage of the O-O bond with concurrent incorporation of the distal oxygen atom into a molecule of water and the formation of a reactive ferryl species (the reactive ferryl species can also be formed by addition of  $\text{H}_2\text{O}_2$  in the presence of substrate) (272,273); (e) oxygen atom transfer from this ferryl species to the bound substrate; and (f) dissociation of the product.

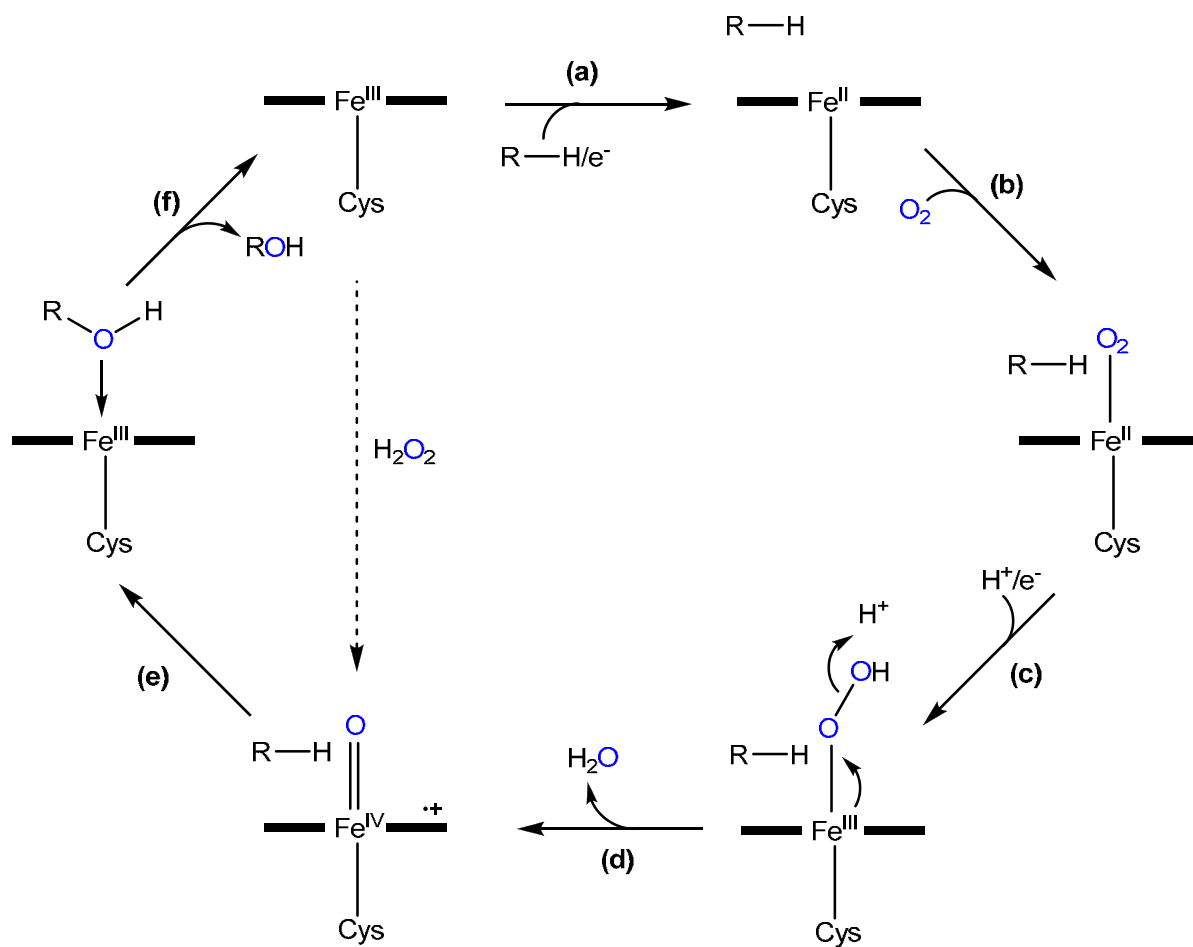
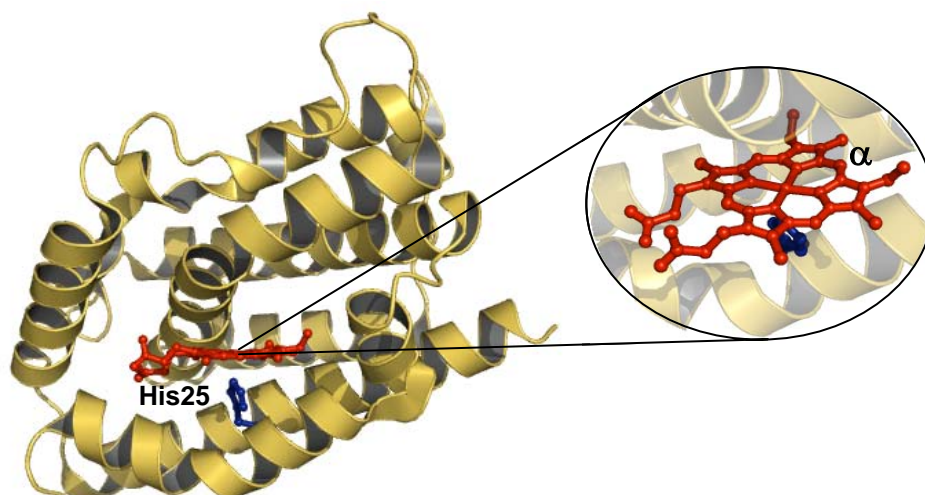


Figure [1.21]: A scheme showing the catalytic mechanism of cytochrome P450. R-H represents substrate. Adapted from (57).

## 1.9 HEME OXYGENASE

The heme group in heme oxygenases (HO) is tightly sandwiched between the proximal and distal helices with a neutral imidazole of histidine as an axial ligand (Figure [1.22]). Heme oxygenase, in the presence of dioxygen and NADPH-dependent cytochrome P450 reductase (274-276), catalyses the oxygen-dependent regiospecific conversion of heme to biliverdin, carbon monoxide and free iron (II) as shown in Figure [1.23]. The degradation product biliverdin, formed on oxidative degradation of heme an important catabolic step in biology, is a precursor of the potent antioxidant bilirubin (277) and carbon monoxide is thought to share some of the biological properties of nitric oxide in signal transduction and communication (278-280) and the free iron released by heme oxygenase activity is known to regulate genes, including that of nitric oxide synthase (276) (see Section 1.10.1.1).



**Figure [1.22]:** The structure of heme oxygenase (PDB code: 1N45) (281). The heme group is shown in red together with the axial histidine ligand in blue. *Inset:* shows close-up of heme pocket and the  $\alpha$ -meso-carbon is indicated.

Heme oxygenase is unique in the sense that it employs heme as both the prosthetic group and substrate, and is also a prime example of the “active” heme proteins category in that both the porphyrin and iron undergo electronic and chemical transformations during the degradation of heme. The catalytic mechanism of heme oxygenase (Figure [1.23]) involves: (a) reduction of the heme from ferric to the ferrous state; (b) binding of molecular oxygen to generate the dioxygen complex, oxy species; (c) transfer of a second electron to this complex to give a ferric hydroperoxo heme complex; (d) proton transfer activates the ferric hydroperoxo complex, which leads to the selective hydroxylation of the heme  $\alpha$ -meso-carbon to yield  $\alpha$ -meso-hydroxyheme; (e) loss of carbon monoxide, by reaction of  $\alpha$ -meso-hydroxyheme with oxygen and another electron, leads to formation of ferrous verdoheme; and (f) further reaction with oxygen and concomitant reduction to form biliverdin.

The catalytic mechanism of heme oxygenase includes many interesting aspects, the most striking of all being the fact that the ferric hydroperoxo ( $\text{Fe}^{\text{III}}\text{-OOH}$ ) species self-hydroxylates the  $\alpha$ -meso-carbon of the porphyrin ring to generate  $\alpha$ -meso-hydroxyheme in heme oxygenase (Figure [1.24]). The ferric hydroperoxo ( $\text{Fe}^{\text{III}}\text{-OOH}$ ) species is a common intermediate not only in the catalytic cycle of heme oxygenases but also in the catalytic cycles of cytochrome P450s and peroxidases; where the O-O bond in the identical hydroperoxo ( $\text{Fe}^{\text{III}}\text{-OOH}$ ) species is

heterolytically cleaved to generate an actively hydroxylating Compound I, a ferryl species coupled with a porphyrin  $\pi$ -cation radical.

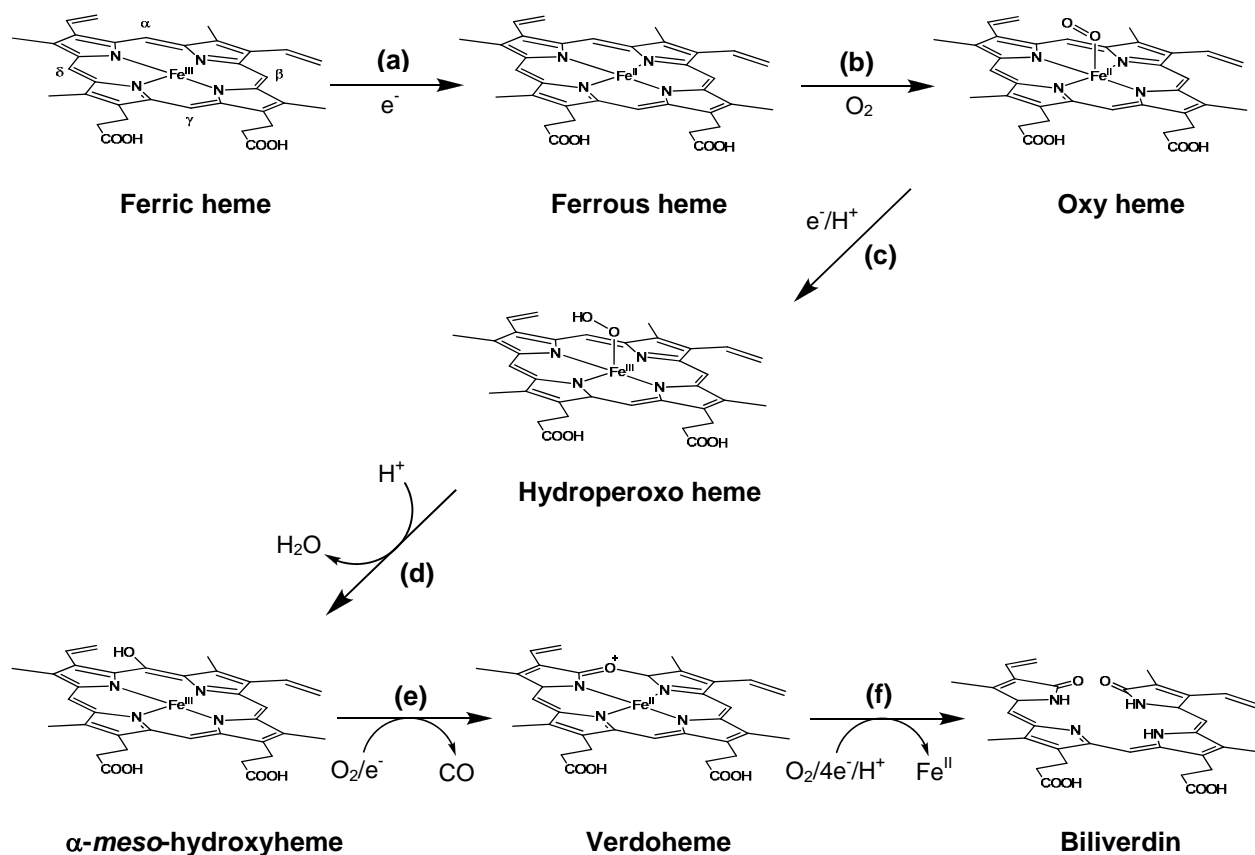


**Figure [1.23]:** A scheme showing the catalytic mechanism of heme oxygenase. Adapted from (282).

The proteins (heme peroxidases, electron transfer proteins, cytochrome P450s and heme oxygenases) discussed so far are prime examples of “active” heme proteins, in which the iron and the porphyrin both play a functional role in chemical transitions and also undergo electronic or chemical transformations (1). Considering that much of heme enzyme catalysis involves electrostatic stabilisation of transition states, it comes as no surprise that the negative charges on the heme propionates have an effect on redox chemistry (1).

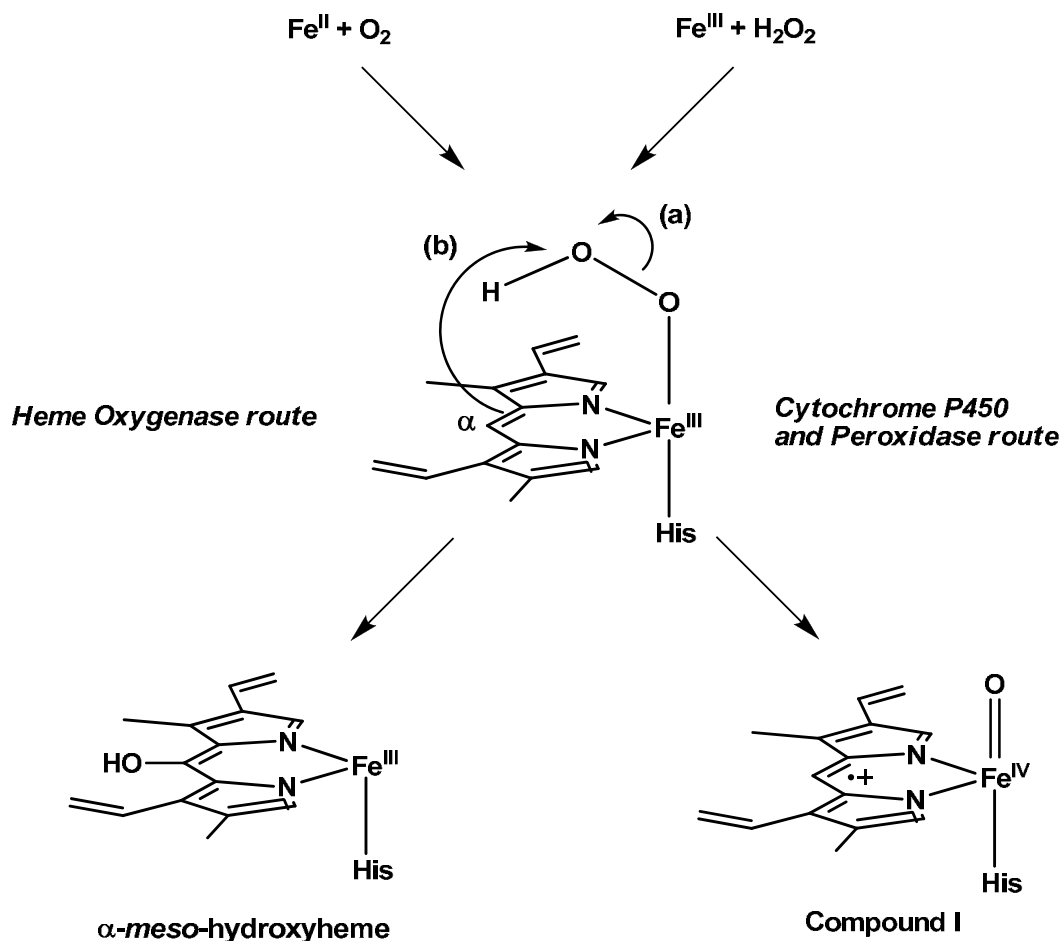


Figure [1.24]: Comparison of the fate of the common catalytic hydroperoxo intermediate in cytochrome P450, peroxidases and heme oxygenase. One-electron reduction and protonation of the ferrous-oxygen complex in heme oxygenase or in the case of heme peroxidases and cytochrome P450 reaction with hydrogen peroxide yields a ferric hydroperoxo species ( $\text{Fe}^{\text{III}}\text{-OOH}$ ). (a) In cytochrome P450 and the peroxidases, the O-O bond of  $\text{Fe}^{\text{III}}\text{-OOH}$  is heterolytically cleaved to afford a reactive oxo-ferryl species (Compound I); (b) Whereas in heme oxygenase, the terminal oxygen of  $\text{Fe}^{\text{III}}\text{-OOH}$  is attacked by the porphyrin  $\alpha$ -meso-carbon to form  $\alpha$ -meso-hydroxyheme. Adapted from (282).

Thus Poulos (1) has referred to the role of the heme propionate to range from purely “passive”, as in the case of heme oxygenase where the primary role appears to be orientation of the heme in the active site so the correct *meso*-carbon is oxidised (283), to a more “active” role as seen in the peroxidases and P450s (1). The following section provides an overview on the emerging “passive” roles of heme in various heme proteins.

## **1.10 HEME PROTEINS: An overview on the passive roles of heme in biological systems**

The following section provides a brief overview on the emerging “passive” role of heme proteins in cell signalling and gene expression.

### **1.10.1 The passive roles of heme in biological systems**

Despite fitting into the traditional heme protein categorisation, the globins are the most obvious example of proteins where heme plays a “passive” role. Hemoglobin, a oxygen transport and binding protein, provides the most classical example of heme signalling to the surrounding protein environment (2). Structural changes triggered by the shift of the iron atom into the heme plane upon oxygen binding provide a mechanism of heme-heme interaction (cooperativity) thus resulting in a heme environment with enhanced ligand affinity.

#### ***1.10.1.1 Heme and gene expression***

Recently heme has been shown to serve as a regulatory molecule whose binding to specific targets alters function including gene transcription. Biological evolution has adapted heme to function as a signalling trigger in the yeast heme activator protein, Hap1. Hap1 is a transcription factor consisting of various sub-domains including heme- and DNA-binding motifs, which regulates expression of genes required for respiration and for controlling oxidative damage (284). Hap1, in the absence of heme, is present as a high molecular weight aggregate which has poor affinity for DNA (1). Heme synthesis in the mitochondria requires oxygen, and as the heme concentration rises, heme binds to HAP1 and the Hap1-associated proteins are released; thus increasing the DNA affinity of Hap1 and increasing gene transcription of the many enzymes required for oxidative phosphorylation (284).

Heme also serves as regulatory molecule, controlling translation of the globin genes. When the heme concentration is low the heme-regulated eIF2 $\alpha$  kinase (HRI) phosphorylates the  $\alpha$ -subunit of the translation initiation factor 2 which blocks protein synthesis thus shutting down the translation of globin genes (1). Heme binds to two different sites in HRI. In the N-terminal heme binding domain heme binds forming a

stable complex with carbon monoxide but not with oxygen (285,286). In the second heme-binding site of HRI the heme moiety has been found to be hexa-coordinate with histidine and cysteine as axial ligands (287,288). The kinase activity is increased about five-fold when nitric oxide is bound at the N-terminal heme binding site. These studies show that the precise coordination environment of the heme is connected to the catalytic domains most likely by long-range conformational changes similar to some of the heme-sensor proteins which are discussed below (1).

### **1.10.1.2 Heme-based sensors**

All living organisms respond to changes in the atmospheric levels of diatomic gases (oxygen, carbon monoxide and nitric oxide) that are physiologically essential but can sometimes also be toxic to living organisms. Therefore, mechanisms for sensing these gases and responding to them are essential for survival (288). Recently, the heme-containing sensor proteins, a new class of heme proteins, have been identified as sensing these diatomic molecules. Generally, the heme-sensor proteins are composed of an N-terminal heme-containing sensor domain and a C-terminal effector domain. Guanylate cyclase, FixL and CooA (discussed below) are examples of heme-sensor (also known as gas-sensor) proteins that function through an effector ligand (nitric oxide, oxygen and carbon monoxide, respectively) binding to the heme-ferrous iron which leads to conformational changes that trigger activation in a catalytic or DNA-binding domain (Figure [1.25]). Thus heme serves to bind the ligand but the heme itself does not undergo any chemical changes, but the local perturbation is transduced over a long distance within the protein.

From the limited spectroscopic and biochemical data available on guanylate cyclase, it appears that binding of the small regulatory molecule nitric oxide to the heme-iron activates guanylate cyclase activity, which leads to cyclic GMP formation, and sets in motion a signalling cascade (for example, by regulation of calcium homeostasis or calcium-dependent ion channels) (2). There are still a number of questions about guanylate cyclase that remain to be addressed: (a) how does the binding of nitric oxide affect heme and the surrounding environment, (b) how is the nitric oxide binding event translated into increased catalytic activity and (c) how is guanylate cyclase deactivated (289).

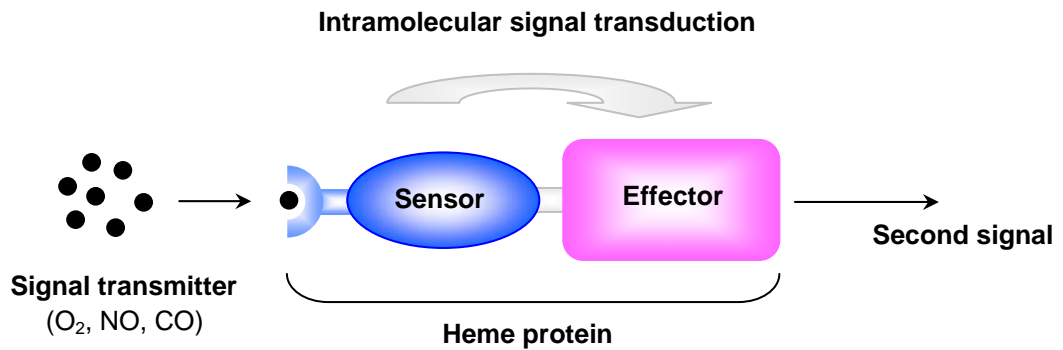


**Figure [1.25]:** The cellular signal transduction system mediated by heme sensor proteins. Binding of gases to the sensor domain induces structural changes in these proteins, which are transmitted to the effector domain, eliciting cellular signal transduction. Adapted from (288).

Unlike guanylate cyclase, there is vast amount of structural as well as spectroscopic and biochemical literature available on CooA (2,290) and FixL (291), which provide insights into the mechanism of action of the heme-based sensors. For majority of the heme-based sensor proteins only structural information on the heme domain alone is available, except for CooA where the crystal structure of the holo protein has been solved (1). The protein CooA is a transcription factor that belongs to the classic helix-turn-helix catabolite repressor protein (CRP) family of transcription factors which are regulated by cyclic AMP (cAMP). CooA regulates carbon monoxide metabolism in various bacteria (292) by binding to the 5' regulatory region of the CooA operon when in complex with carbon monoxide and helps recruit RNA polymerase and hence stimulate gene transcription of the carbon monoxide oxidising enzymes (1). From structural studies, CooA has been found to be a homodimeric molecule with a similar fold to the CRP protein (290) although the effector region in CooA binds heme while in CRP the effector domain binds cAMP. Dimerisation probably contributes to the allosteric switch between the active "on", carbon monoxide-bound and the inactive "off", ligand-free forms. The two heme groups, positioned across the dimer interface, are ligated by histidine residue in the proximal cavity; however the distal site, the binding site for carbon monoxide, in both heme groups is occupied by a proline residue in the "off" form. Interestingly, the N-terminal proline (Pro-2) of one monomer coordinates the heme of the other monomer and *vice versa* (Figure [1.26A]).

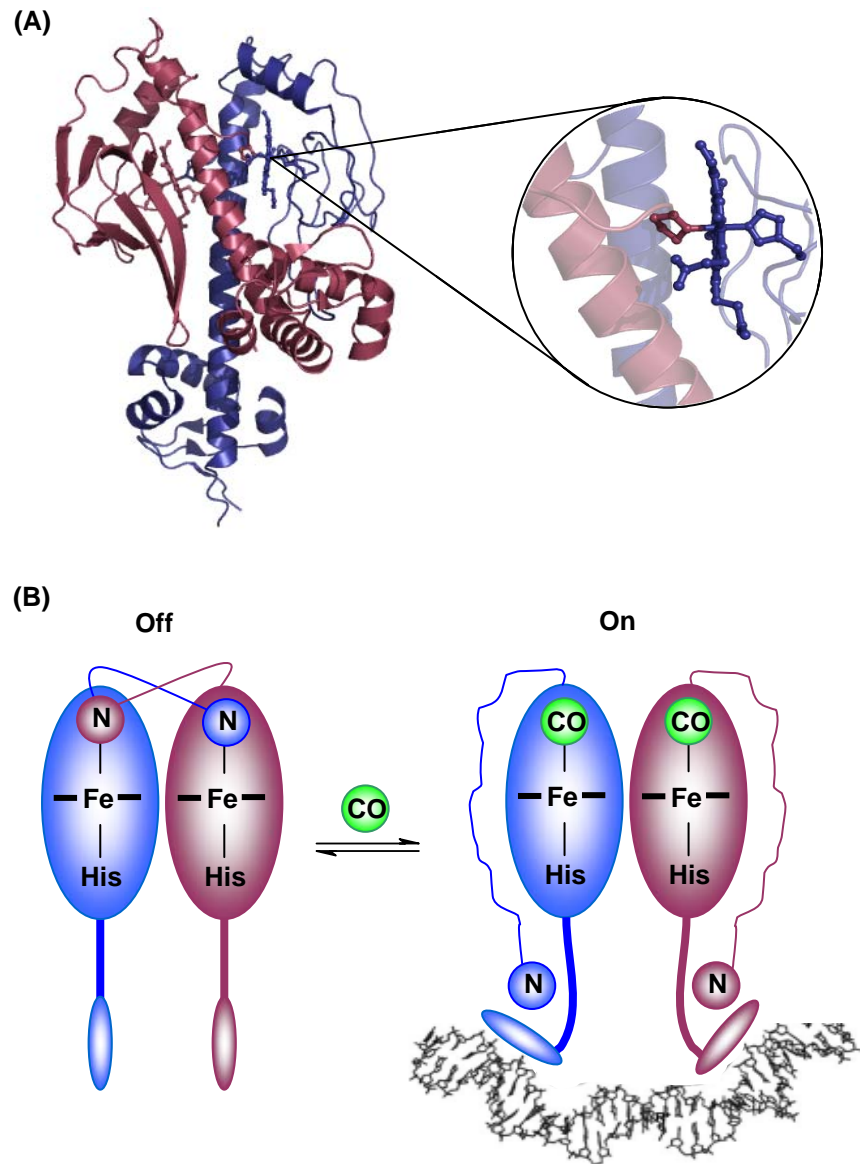


Figure [1.26]: (A) The overall structure of CooA from *Rhodospirillum rubrum* (RrCooA) (PDB code: 1FT9) (290) showing the bound heme for each monomer. *Inset*: The heme pocket of RrCooA, in which a proline (Pro-2) residue of monomer A coordinates the heme iron of monomer B and *vice versa*. Activation involves replacing the proline-iron bond with a carbon monoxide CO-iron bond. (B) Proposed mechanism for CO sensing and activation by the CooA family of transcription factors. CooA is an equilibrium mix between the "off" and "on" states. In the "off" state the N-terminus of monomer A coordinates the heme iron of monomer B. In the "on" state the N-terminus dissociates thus enabling CO to bind. The freed N-terminus undergoes a large repositioning that enables the N-terminal segment to provide a bridge between the heme- and DNA-binding domains effectively holding the DNA-binding domain in the orientation required for DNA binding. These changes involve motion at the C-helical interface and heme which tightens the CO binding pocket thus providing additional stabilisation to CO binding. Adapted from (1).

Hence, conversion from the “off” form (where the heme groups are ligated by proline and histidine) to the “on” form involves displacement of the distal proline thus freeing the axial coordination site for carbon monoxide binding which leads to the large reorientation of the DNA-binding domain (Figure [1.26B]).

Before discussion of FixL, an overview of the Per-Arnt-Sim (PAS) domain in heme-based sensors is fundamental. The PAS domain, which have been identified in over 1100 proteins in all three kingdoms of life (293) is an important structural motif, that has a characteristic protein fold with several  $\alpha$ -helices flanking a five- or six-stranded anti-parallel  $\beta$ -sheet scaffold (288). The PAS domains convert various input stimuli (changes in small ligands, light, gases and redox potential) into signals that propagate to downstream components by altering intra- and intermolecular protein-protein interactions (294). PAS-sensor proteins often have bound cofactors, such as chromophores, flavin adenine dinucleotide (FAD), [2Fe2S] clusters, and heme (293). A heme-bound PAS domain is included in several important sensor proteins, such as FixL, neural PAS domain protein 2 (NPAS2) and a heme-regulated phosphodiesterase from *E. coli* (*EcDOS*) (295).

FixL is an oxygen-sensing protein from *Rhizobium* that contains a heme-bound PAS domain as a sensor (291,296,297). The FixL protein works along with FixJ to form a classical two-component regulatory system that accomplishes signal transduction by phosphoryl transfer (Figure [1.27]) (296,298-300). The sensory PAS domain of FixL protects the nitrogenase enzyme from oxygen, so that gene expression is activated only in anaerobic conditions. In the absence of oxygen, the PAS heme domain of FixL activates the neighbouring protein kinase domain (effector domain), which undergoes auto-phosphorylation. The phosphoryl group is rapidly transferred from phospho-FixL to the transcription factor FixJ, which regulates the expression of the nitrogen fixation genes: *nif* and *fix*.

*EcDOS*, originally identified on the basis of sequence homology to the FixL protein (301), is a unique heme-based sensor in that it responds to changes in redox state/oxygen levels. *EcDOS* is a homo-dimer that contains a heme-bound PAS and non-heme PAS domain and a C-terminal phosphodiesterase domain that degrades cAMP in a redox dependent manner, thus indirectly alters the transcription of specific proteins. In the ferric form the heme-bound PAS domain is ligated by a proximal histidine and the distal cavity is occupied by a water molecule which is displaced by a methionine residue upon reduction of the heme. It's only in the reduced form that

*EcDOS* has cAMP phosphodiesterase activity. This type of ligand displacement is rare in other well-characterised heme-sensor proteins; therefore, it may be a key aspect of the overall mechanism of *EcDOS*, including redox sensing, intramolecular signal transduction, and catalytic activation.

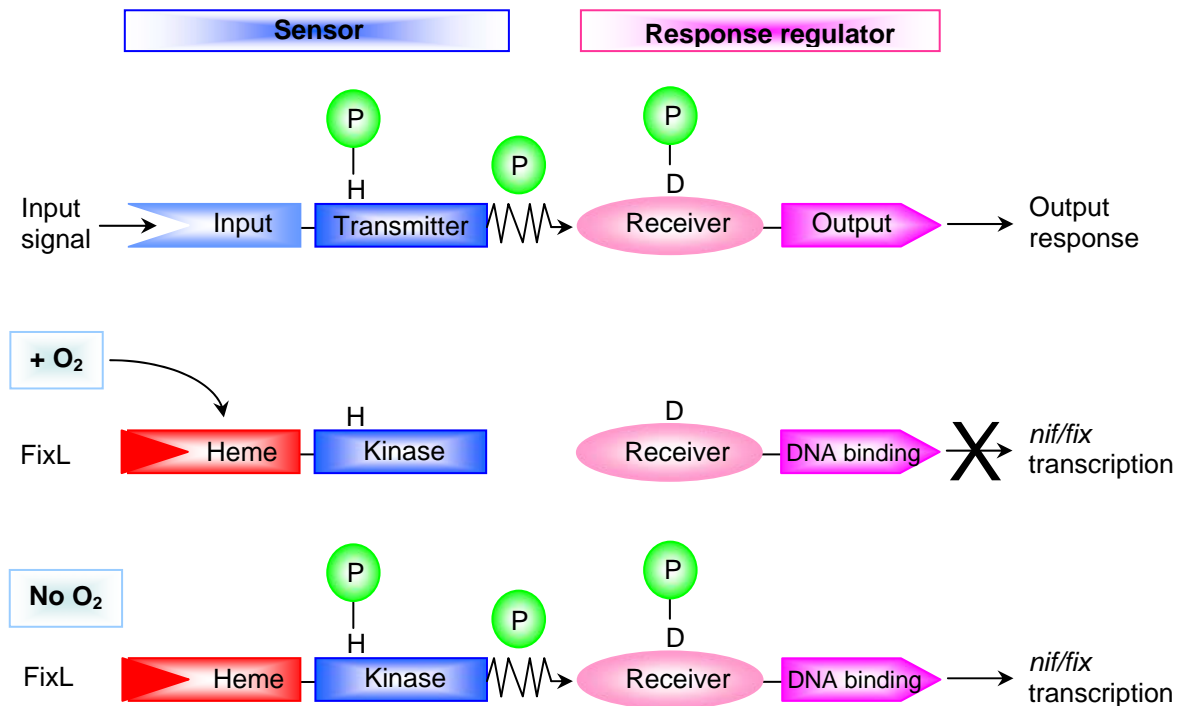


**Figure [1.27]:** The FixL/FixJ two-component regulatory system. In two-component regulatory systems, the inputs and outputs are variable, but the transmitter and receiver domains from unrelated systems share ~2 % identity. The input of the sensor FixL is a heme-binding domain that inhibits autophosphorylation when oxygen binds and permits enzyme activity when oxygen dissociates. The output response is transcriptional activation at nitrogen fixation promoters for only hypoxic conditions. The phosphorylation-site histidine in FixL and aspartate in FixJ are denoted “H” and “D”, respectively. Adapted from (302).

NPAS2 is a carbon monoxide-sensing transcription factor but unlike CooA has two heme-bound PAS domains in its N-terminus. NPAS2 binds to DNA along with the protein BMAL1 and regulates the circadian rhythm (303). The recently discovered Hem-At is the first heme-sensor protein identified with a myoglobin-like fold. It acts as an aero-taxis transducer by sensing atmospheric oxygen through its myoglobin-like N-terminal domain in bacteria and archaea (304-306). The N-terminal domain controls the activity of the signalling C-terminal domain, which has been found to have

significant sequence similarity with signalling bacterial chemoreceptors involved in chemotaxis.

This section has provided a brief overview on the role of heme as both a regulatory molecule and as a gas sensor; however the key question which remains unanswered is how binding of heme leads to important conformational, occasionally long range, changes involved in cell signalling and gene expression. There is no doubt that future structural and functional studies on heme proteins will reveal more interesting aspects of the multipurpose, widespread prosthetic group heme (2).

## 1.11 THESIS AIMS

The Raven laboratory has a long-standing interest in structure-function relationships in heme peroxidases. The remit of this thesis was to examine the individual role of key active site residues and their role in catalysis. As part of this, we observed that mutation of the conserved Trp-41 residue in APX to an alanine residue (W41A) affected the conformational mobility within the active site. Conformational mobility has been observed in a number of heme proteins *e.g.* cytochrome *cd*<sub>1</sub>, the di-heme cytochrome *c* peroxidase, *Chlamydomonas* hemoglobin, CooA and FixL are a few examples. The aims of this project were therefore to characterise the conformational changes in the W41A variant in detail. This involved:

- Determination of the crystal structure of W41A variant and examination of the catalytic mechanism and conformational mobility in the presence of hydrogen peroxide (Chapter 2).
- Examination of the conformational changes associated with reduction of the heme in the W41A variant (Chapters 3).
- Examination of the reactivity of W41A with tertiary butyl hydroperoxide and an examination of the products of this reaction in terms of heme oxygenase chemistry (Chapter 4).
- Examination of the conformational changes in the distal cavity on disruption of the conserved hydrogen bonding interaction between the distal histidine (His-42) and asparagine (Asp-171) residues (Chapter 5).

These results are discussed in terms of the emerging ideas on the role of heme in gene expression and cell signalling where conformational mobility, in some cases long range, is required.

**1.12 REFERENCES**

1. Poulos, T. L. (2007) *Natural Product Reports* **24**, 504-510
2. Paoli, M., Marles-Wright, J., and Smith, A. (2002) *DNA and Cell Biology* **21**, 271-280
3. Dunford, H. B. (1999) *Heme Peroxidases*, Wiley-VCH, New York, Chichester, Weinheim, Brisbane, Singapore, Toronto
4. Patel, N. (2002) in *Phd Thesis in Chemistry*, University of Leicester, Leicester
5. Chapman, S. K., Daff, S., and Munro, A. W. (1997) *Metal Sites in Proteins and Models* **88**, 39-70
6. Kendrew, J. C., Bodo, G., Dintzis, H. M., Parrish, R. G., Wickoff, H. M., and Phillips, D. C. (1958) *Nature* **181**, 662-666
7. Perutz, M. F., Rossmann, M. G., Cullis, A. F., Muirhead, H., Will, G., and North, A. C. T. (1960) *Nature* **185**, 422-427
8. Dawson, J. H. (1988) *Science* **240**, 433-439
9. Sykes, A. G. (2001) *Advances in Inorganic Chemistry* (Sykes, A. G., and Mauk, A. G., Eds.), 51, Academic Press, London
10. Springer, B. A., Sligar, S. G., Olson, J. S., and Phillips, G. N. (1994) *Chemical Reviews* **94**, 699-714
11. Ortiz de Montellano, P. R. (1987) *Accounts of Chemical Research* **20**, 289-294
12. Gray, H. B., and Winkler, J. R. (1996) *Annual Review of Biochemistry* **65**, 537-561
13. Raven, E. L., and Ortiz de Montellano, P. R. (2007) *Natural Product Reports* **24**, Special Edition: The chemistry and biochemistry of heme proteins, 489-644
14. Rosell, F. I., Ferrer, J. C., and Mauk, A. G. (1998) *Journal of the American Chemical Society* **120**, 11234-11245

15. Williams, P. A., Fulop, V., Garman, E. F., Saunders, N. F. W., Ferguson, S. J., and Hajdu, J. (1997) *Nature* **389**, 406-412
16. Dias, J. M., Alves, T., Bonoifacio, C., Pereira, A. S., Trincao, J., Bougeois, D., Moura, I., and Romano, M. (2004) *Structure* **12**, 961-973
17. Uchida, T., Stevens, J. M., Daltrop, O., Harvat, E. M., Hong, L., Ferguson, S. J., and Kitagawa, T. (2004) *Journal of Biological Chemistry* **279**, 51981-51988
18. Patel, N., Jones, A. D., Cheesman, M. R., Thomson, A. J., and Raven, E. L. (2002) *Inorganic Chimica Acta*, 303-309
19. English, A. M., and Tsaprailis, G. (1995) *Advances in Inorganic Chemistry* **43**, 79-125
20. Frew, J. E., and Jones, P. (1984) *Advances in Inorganic and Bioinorganic Mechanisms* (Sykes, A. G., Ed.), 3, Academic Press, New York
21. English, A. M. (1994) *Encyclopaedia of inorganic chemistry: Iron heme proteins, peroxidases and catalysis* (King, R. B., Ed.), 4, Wiley, Chichester
22. Dunford, H. B. (1991) *Peroxidases in chemistry and biology* (Everse, J., and Grisham, M. B., Eds.), 2, CRC Press, Boca Raton
23. Ator, M. A., and Ortiz de Montellano, P. R. (1987) *Journal of Biological Chemistry* **263**
24. Ortiz de Montellano, P. R. (1992) *Annual Review of Pharmacology and Toxicology* **32**, 89-107
25. Wariishi, H. (1990) *Journal of Biological Chemistry* **265**, 11137-11142
26. Kirk, T. K., and Farrell, R. (1987) *Annual Review of Microbiology* **41**, 465-505
27. Welinder, K. G. (1995) *Current Opinion in Structural Biology* **2**, 388-393
28. Poulos, T. L., Freer, S. T., Alden, R. A., Edwards, S. L., Skogland, U., Takio, K., Eriksson, B., Xuong, N., Yontani, T., and Kraut, J. (1980) *Journal of Biological Chemistry* **255**, 575-584

29. Welinder, K. G., and Norskov-Lauritsen, L. (1986) (Greppin, H., Penel, C., and Gaspar, T., eds), University of Geneva, Geneva
30. Morita, Y., Mikami, B., Yamashita, H., Lee, J. Y., Aibara, S., Sato, M., Katsube, Y., and Tanaka, N. (1991) *Biochemical, Molecular, and Physiological Aspects of Plant Peroxidases* (Greppin, H., Penel, C., and Gaspar, T., Eds.), Univeristy of Geneva, Geneva
31. Morita, Y., Funatsu, J., and Mikami, B. (1993) *Plant Peroxidases, Biochemistry and Physiology* (Welinder, K. G., Rasmussen, S. K., Penel, C., and Greppin, H., Eds.), University of Geneva, Geneva
32. Vainshtein, B. K., Melik-Adamyanyan, W. R., Barynin, V. V., Vagin, A. A., Grenbenko, A. I., Borisov, V. V., Bartels, K. S., Fita, I., and Rossman, M. G. (1986) *Journal of Molecular Biology* **188**, 49-61
33. Murthy, M. R. N., Reid III, T. J., Sicignano, A., Tanaka, N., and Rossman, M. G. (1981) *Journal of Molecular Biology* **152**, 465-499
34. Kimura, S., and Ikeda-Saito, M. (1988) *Proteins-Structure Function and Genetics* **3**, 113-120
35. Zeng, J., and Fenna, R. (1992) *Journal of Molecular Biology* **226**, 185-207
36. Picot, D., Loll, P. J., and Garavito, R. M. (1994) *Nature* **367**, 243-249
37. Poulos, T. L., and Fenna, R. E. (1994) *Metal Ions in Biological Systems*, 30, H. Siegel, New York
38. Bertrand, T., Eady, N. A. J., Jones, J. N., Bodiguel, J., Jesmin, Nagy, J. M., Raven, E. L., Jamart-Gregoire, B., and Brown, K. A. (2004) *Journal of Biological Chemistry* **279**, 38991-33899
39. Wada, K., Tada, T., Nakamura, Y., Ishkawa, T., Yabuta, Y., Yoshimura, H., Shigeoka, S., and Nishimura, K. (2003) *Journal of Biological Chemistry* **134**, 239-244

40. Wada, K., Tada, T., Nakamura, K., Yabuta, Y., Yoshimura, K., Takeda, T., Shigeoka, S., and Nishimura, K. (2002) *Acta Crystallographica Section D-Biological Crystallography* **58**, 559-561
41. Patterson, W. R., and Poulos, T. L. (1995) *Biochemistry* **34**, 4331-4341
42. Sharp, K. H., Mewies, M., Moody, P. C. E., and Raven, E. L. (2003) *Nature Structural Biology* **10**, 303-307
43. Carlstrom, A. (1969) *Acta Chemica Scandinavica* **23**, 185-202
44. Edwards, S. L., Raag, R., Wariishi, H., Gold, M. H., and Poulos, T. L. (1993) *Proceedings of the National Academy of Sciences of the United States of America* **90**, 750-754
45. Sundaramoorthy, M., Kishi, K., Gold, M. H., and Poulos, T. L. (1994) *Journal of Biological Chemistry* **269**, 32759-32767
46. Petersen, J. F. W., Tams, J. W., Vind, J., Svensson, A., Dalboge, H., Welinder, K. G., and Larsen, S. (1993) *Journal of Biological Chemistry* **232**, 989-991
47. Sievers, G. (1981) *FEBS Letters* **127**, 253-256
48. Gajhede, M., Schuller, D. J., Henriksen, A., Smith, A. T., and Poulos, T. L. (1997) *Nature Structural Biology* **4**, 1032-1038
49. Schuller, D. J., Ban, N., vanHuystee, R. B., McPherson, A., and Poulos, T. L. (1996) *Structure* **4**, 311-321
50. Henriksen, A., Schuller, D. J., Meno, K., Welinder, K. G., Smith, A. T., and Gajhede, M. (1998) *Biochemistry* **37**, 8054-8060
51. Lad, L. (2001) in *PhD Thesis in Chemistry*, University of Leicester, Leicester
52. Kunishima, N., Fukuyama, K., Matsubara, H., Hatanaka, H., Shibano, Y., and Amachi, T. (1994) *Journal of Molecular Biology* **235**, 331-344
53. Sundaramoorthy, M., Turner, J., and Poulos, T. L. (1995) *Structure* **3**, 1367-1377

54. Henriksen, A., Welinder, K. G., and Gajhede, M. (1998) *Journal of Biological Chemistry* **273**, 2241-2248
55. Henriksen, A., Mirza, O., Indiani, C., Teilum, K., Smulevich, G., Welinder, K. G., and Gajhede, M. (2001) *Protein Science* **10**, 108-115
56. Pelletier, H., and Kraut, J. (1992) *Science* **258**, 1748-1755
57. Ortiz de Montellano, P. R. (1995) *Cytochrome P450: Structure, Mechanism and Biochemistry*, Prentice Hall, London
58. Finzel, B. C., Poulos, T. L., and Kraut, J. (1984) *Journal of Biological Chemistry* **259**, 13027-13036
59. Welinder, K. G., Bjorholm, B., and Dunford, H. B. (1995) *Biochemical Society Transactions* **23**, 257-262
60. Smulevich, G. (1998) *Biospectroscopy* **4**, S3-S17
61. Otto, B. R., Verweij-van Vught, A. M., and MacLaren, D. M. (1992) *Critical Reviews in Microbiology* **18**, 217-233
62. Moss, T. H., Ehrenberg, A., and Bearden, A. J. (1969) *Biochemistry* **8**, 4159-4162
63. Schultz, C. E., Rutter, R., Sage, J. T., Debrunner, P. G., and Hager, L. P. (1984) *Biochemistry* **23**, 4743-4754
64. Lang, G., Spartalian, K., and Yonetani, T. (1976) *Biochimica Et Biophysica Acta* **451**, 250-258
65. Penner-Hahn, J. E., Eble, K. S., McMurry, T. J., Renner, M., and Balch, A. L. (1986) *Journal of American Chemical Society* **108**, 7819-7825
66. Browett, W. R., Gasyna, Z., and Stillman, M. J. (1988) *Journal of American Chemical Society* **110**, 3633-3640
67. Myers, D., and Palmer, G. (1985) *Journal of Biological Chemistry* **260**, 3887-3890

68. Roberts, J. E., Hoffman, B. M., Rutter, R., and Hager, L. P. (1981) *Journal of Biological Chemistry* **256**, 2118-2121
69. Iizuka, T., Kotani, M., and Yonetani, T. (1968) *Biochimica Et Biophysica Acta* **167**, 257-267
70. Hashimoto, S., Teraoka, J., Inubushi, T., Yonetani, T., and Kitagawa, T. (1986) *Journal of Biological Chemistry* **261**, 110-118
71. Hashimoto, S., Tatsuno, Y., and Kitagawa, T. (1986) *Proceedings of the National Academy of Sciences of the United States of America* **83**, 2417-2421
72. Oertling, W. A., and Babcock, G. T. (1985) *Journal of American Chemical Society* **107**, 6406-6407
73. Sitter, A. J., Reczek, C. M., and Turner, J. (1985) *Journal of Biological Chemistry* **260**, 7515-7522
74. Isaac, I. S., and Dawson, J. H. (1999) *Essays in Biochemistry* **34**, 51-69
75. Dunford, H. B., and Stillman, J. S. (1976) *Coordination Chemistry Reviews* **19**, 187-251
76. Dolphin, D., Forman, A., Borg, D. C., Fajer, J., and Felton, R. H. (1991) *Proceedings of the National Academy of Sciences of the United States of America* **68**, 614-618
77. Barrows, T. P., and Poulos, T. L. (2005) *Biochemistry* **44**, 14062-14068
78. Hanson, L. K., Chang, C. K., Davis, M. S., and Fajer, J. (1981) *Journal of American Chemical Society* **103**, 663-670
79. La Mar, G. N., de Ropp, J. S., Smith, K. M., and Langry, K. C. (1981) *Journal of Biological Chemistry* **256**, 237-243
80. Felton, R. H., Romans, A. Y., Yu, N. T., and Schonbaum, G. R. (1976) *Biochimica Et Biophysica Acta* **434**, 82-89
81. Loew, G., and Herman, Z. S. (1980) *Journal of American Chemical Society* **102**, 6173-6174

82. Erman, J. E., Vitello, L. B., Mauro, J. M., and Kraut, J. (1989) *Biochemistry* **28**, 7992-7995
83. Huyett, J. E., Doan, P. E., Gurbiel, R., Houseman, A. L. P., Sivaraja, M., Goodin, D. B., and Hoffman, B. M. (1995) *Journal of American Chemical Society* **117**, 9033-9041
84. Houseman, A. L. P., Doan, P. E., Goodin, D. B., and Hoffman, B. M. (1993) *Biochemistry* **32**, 4430-4443
85. Sivaraja, M., Goodin, D. B., Smith, M., and Hoffman, B. M. (1989) *Science* **245**, 738-746
86. Yonetani, T. (1976) *The Enzymes* (Boyer, B., Ed.), Academic Press, Orlando, Florida
87. Bonagura, C. A., Sundaramoorthy, M., Pappa, H. S., Patterson, W. R., and Poulos, T. L. (1996) *Biochemistry* **35**, 6107-6115
88. Sharp, K. H., Moody, P. C. E., and Raven, E. L. (2003) *Dalton Transactions*, 4208-4215
89. Raven, E. L. (2003) *Natural Product Reports* **20**, 367-381
90. Bosshard, H. R., Anni, H., and Yonetani, T. (1991) in *Peroxidases in Chemistry and Biology* (Everse, J., Everse, K. E., and Grisham, M. B., eds) Vol. 2, CRC Press, Boca Raton
91. Erman, J. E., and Vitello, L. B. (1998) *Journal of Biochemistry and Molecular Biology* **31**, 307-327
92. Veitch, N. C., and Smith, A. T. (2000) *Advances in Inorganic Chemistry* **51**, 107-162
93. Smith, A. T., and Veitch, N. C. (1998) *Current Opinion in Chemical Biology* **2**, 269-278
94. Erman, J. E., and Vitello, L. B. (2002) *Biochimica Et Biophysica Acta* **1597**, 193-220

95. Erman, J. E., Vitello, L. B., Miller, M. A., and Kraut, J. (1992) *Journal of American Chemical Society* **114**, 6592-6593
96. Erman, J. E., Vitello, L. B., Miller, M. A., Shaw, A., Browne, K. A., and Kraut, J. (1993) *Biochemistry* **32**, 9798-9806
97. Bateman, L., Leger, C., Goodin, D. B., and Armstrong, F. A. (2001) *Journal of American Chemical Society* **123**, 9260-9263
98. RodriguezLopez, J. N., Smith, A. T., and Thorneley, R. N. F. (1996) *Journal of Biological Inorganic Chemistry* **1**, 136-142
99. Newmyer, S., and Ortiz de Montellano, P. R. (1996) *Journal of Biological Chemistry* **271**, 14891-14896
100. Tanaka, M., Ishimori, K., and Morishima, I. (1996) *Biochemical and Biophysical Research Communications* **227**, 393-399
101. Tanaka, M., Ishimori, K., Mukai, M., Kitagawa, T., and Morishima, I. (1997) *Biochemistry* **36**, 9889-9898
102. Nagano, S., Tanaka, M., Watanabe, Y., and Morishima, I. (1995) *Biochemical and Biophysical Research Communications* **207**, 417-423
103. Nagano, S., Tanaka, M., Ishimori, K., Watanabe, Y., and Morishima, I. (1996) *Biochemistry* **35**, 14251-14258
104. Mukai, M., Nagano, S., Tanaka, M., Ishimori, K., Morishima, I., Ogura, T., Watanabe, Y., and Kitagawa, T. (1997) *Journal of the American Chemical Society* **119**, 1758-1766
105. Tanaka, M., Nagano, S., Ishimori, K., and Morishima, I. (1997) *Biochemistry* **36**, 9791-9798
106. Smith, A. T., Sanders, S. A., Sampson, C., Bray, R. C., Burke, J. F., and Thorneley, R. N. F. (1993) *Plant Peroxidases: Biochemistry and Physiology* (Welinder, K. G., Rasmussen, C. B., Penel, C., and Greppin, H., Eds.), University of Geneva, Geneva

107. Rodriguez-Lopez, J. N., Smith, A. T., and Thorneley, R. N. F. (1996) *Journal of Biological Chemistry* **271**, 4023-4030
108. Gazaryan, I. G., Doseeva, V. V., Galkin, A. G., and Tishkov, V. I. (1994) *FEBS Letters* **354**, 248-250
109. Ryan, B. J., Carolan, N., and O'Fagain, C. (2006) *Trends in Biotechnology* **24**, 355-363
110. Welinder, K. G., and Gajhede, M. (1993) *Plant Peroxidases: Biochemistry and Physiology* (Welinder, K. G., Rasmussen, C. B., Penel, C., and Greppin, H., Eds.), University of Geneva, Geneva
111. Johansson, A., Rasmussen, C. B., Harthill, S. K., and Welinder, K. G. (1992) *Plant Molecular Biology* **18**, 1151-1161
112. Fujiyama, K., Takemura, H., Shinmyo, A., Okada, H., and Takano, M. (1990) *Gene* **89**, 163-169
113. Goodin, D. B., and McRee, D. E. (1992) *Biochemistry* **32**, 3313-3324
114. Vitello, L. B., Erman, J. E., Miller, M. A., Mauro, J. M., and Kraut, J. (1992) *Biochemistry* **31**, 11524-11535
115. Howes, B. D., Heering, H. A., Roberts, T. O., Schneider-Belhadadd, F., Smith, A. T., and Smulevich, G. (2001) *Biopolymers* **62**, 261-267
116. Newmyer, S., Sun, J., Loehr, T. M., and Ortiz de Montellano, P. R. (1996) *Biochemistry* **35**, 12788-12795
117. Smulevich, G., Feis, A., and Howes, B. D. (2005) *Accounts of Chemical Research* **38**, 433-440
118. Vitello, L. B., Erman, J. E., Mauro, J. M., and Kraut, J. (1990) *Biochimica Et Biophysica Acta* **1038**, 90-97
119. Kelly, G. J., and Latzko, E. (1979) *Naturewissenschaften* **66**, 617-618
120. Groden, D., and Beck, E. (1979) *Biochimica Et Biophysica Acta* **546**, 426-435

121. Mittler, R., and Zilinskas, B. A. (1991) *Plant Physiology* **97**, 962-968
122. Bryan, D. M., Dell, S. D., Kumar, R., Clarke, M. J., Rodriguez-Lopez, J. N., Sherban, M., and Charkoudian, J. (1988) *Journal of American Chemical Society* **110**, 1498-1506
123. Borracciono, G., Dipierro, S., and Arrigoni, O. (1986) *Planta* **167**, 521-526
124. Chen, Z., Young, T. E., Ling, J., Chang, S. C., and R, G. D. (2003) *Proceedings of the National Academy of Sciences of the United States of America* **100**, 3525-3530
125. Sano, S., Miyake, C., Mikami, B., and Asada, K. (1995) *Journal of Biological Chemistry* **270**, 21354-21361
126. Murthy, S. S., and Zilinskas, B. A. (1994) *Journal of Biological Chemistry* **269**, 31129-31133
127. Shigeoka, S., Yasumoto, R., Onishi, T., Nakano, Y., and Kitaoka, S. (1987) *Journal of General Microbiology* **133**, 227-232
128. Hossain, M. A., Nakano, Y., and Asada, K. (1984) *Plant and Cell Physiology* **25**, 385-395
129. Dalton, D. A., Langeberg, L., and Robbins, M. (1992) *Archives of Biochemistry and Biophysics* **292**, 281-286
130. Ushimara, T., Maki, Y., Sano, S., Koshiba, K., Asada, K., and Tsuji, H. (1997) *Plant and Cell Physiology* **38**, 541-549
131. Kelley, P. M., Jalukar, V., and Njus, D. (1990) *Journal of Biological Chemistry* **265**, 19409-19413
132. Foyer, C. H., and Mullineaux, P. M. (1998) *FEBS Letters* **425**, 528-529
133. Creutz, C. (1981) *Inorganic Chemistry* **20**, 4449-4452
134. Lu, Y., Berry, S. M., and Pfister, T. D. (2001) *Chemistry Review* **101**, 3047-3080

135. Chen, G. X., and Asada, K. (1989) *Plant and Cell Physiology* **30**, 987-998
136. Tanaka, K., Takeuchi, E., Kubo, A., Sakaki, T., Haraguchi, K., and Kawamura, Y. (1991) *Archives of Biochemistry and Biophysics* **286**, 371-375
137. Yoshimura, K., Ishikawa, T., Nakamura, Y., Tamoi, M., Takeda, T., Tada, T., Nishimura, K., and Shigeoka, S. (1998) *Biochimica Et Biophysica Acta* **353**, 55-63
138. Nakano, Y., and Asada, K. (1987) *Plant and Cell Physiology* **28**, 131-140
139. Miyake, C., Cao, W. H., and Asada, K. (1993) *Plant and Cell Physiology* **34**, 881-889
140. Jablonski, P. P., and Anderson, J. W. (1982) *Plant Physiology* **69**, 1407-1413
141. Gillham, D. J., and Dodge, A. D. (1986) *Planta* **167**, 246-251
142. Meneguzzo, S., Sgherri, C. L. M., Navari-Izzo, F., and Izzo, R. (1998) *Physiologia Plantarum* **104**, 735-740
143. Heering, H. A., Jansen, M. A. K., Thorneley, R. N. F., and Smulevich, G. (2001) *Biochemistry* **40**, 10360-10370
144. Amako, K., Chen, G. X., and Asada, K. (1994) *Plant and Cell Physiology* **35**, 497-504
145. Chen, G. X., Sano, S., and Asada, K. (1992) *Plant and Cell Physiology* **33**, 109-116
146. Kvaratskhelia, M., Winkel, C., Naldrett, M. T., and Thorneley, R. N. F. (1999) *Journal of Plant Physiology* **154**, 273-282
147. Gerbling, K. P., Kelley, G. J., Fischer, K. H., and Latzko, E. (1984) *Journal of Plant Physiology* **115**, 59-67
148. Ohya, T., Morimura, Y., Saji, H., Mihara, T., and Ikawa, T. (1997) *Plant Science* **125**, 137-145

149. Dalton, D. A., Joe Hanus, F., Sterling, A., Evans, R., and Evans, H. J. (1987) *Plant Physiology* **83**, 789-794
150. De Gara, L., De Pinto, M. C., and Arrigoni, O. (1997) *Physiologia Plantarum* **100**, 894-898
151. De Gara, L., De Pinton, M. C., Paciolla, C., Cappetti, V., and Arrigoni, O. (1996) in *Plant peroxides: Biochemistry and Physiology* (Obinger, C., Burner, U., Ebermann, R., Penel, C., and Greppin, H., eds), University of Geneva, Geneva
152. Elia, M. R., Borracciono, G., and Dipierro, S. (1992) *Plant Science* **85**, 17-21
153. Koshiba, T. (1993) *Plant and Cell Physiology* **34**, 713-721
154. Ishikawa, T., Takeda, T., and Shigeoka, S. (1996) *Plant Science* **120**, 11-18
155. Kvaratskhelia, M., Winkel, C., and Thorneley, R. N. F. (1997) *Plant Physiology* **114**, 1237-1245
156. Battistuzzi, G., D'Onofrio, M., Loschi, L., and Sola, M. (2001) *Archives of Biochemistry and Biophysics* **388**, 100-112
157. Preger, V., Pesaresi, A., Pupillo, P., and Trost, P. (2001) *Protoplasma* **217**, 137-145
158. Bunkelmann, J. R., and Trelease, R. N. (1997) *Plant Science* **122**, 209-216
159. Yamaguchi, K., Hori, H., and Nishimura, M. (1995) *Plant and Cell Physiology* **36**, 1157-1162
160. Ishikawa, T., Sakai, K., Takeda, T., and Shigeoka, S. (1995) *FEBS Letters* **367**, 28-32
161. Ishikawa, T., Yoshimura, K., Sakai, K., Tamoi, M., Takeda, T., and Shigeoka, S. (1998) *Plant and Cell Physiology* **39**, 23-34
162. Corpas, F. J., and Trelease, R. N. (1998) *Journal of Plant Physiology* **153**, 332-338

163. Jimenez, A., Jimenez, J. A., Barcelo, A. R., Sandalio, L. M., del Rio, L. A., and Sevilla, F. (1998) *Physiologia Plantarum* **118**, 1327-1335
164. Jimenez, A., Hernandez, J. A., del Rio, L. A., and Sevilla, F. (1997) *Plant Physiology* **114**, 275-284
165. Sano, S., Ueda, M., Kurano, N., Miyachi, S., and Yokota, A. (1996) in *Plant Peroxidases: Biochemistry and Physiology* (Obinger, C., Burner, U., Ebermann, R., Penel, C., and Greppin, H., eds), 168-172 vols., University of Geneva, Geneva
166. Kitajima, S., Ueda, M., Sano, S., Miyake, C., Kohchi, T., Tomizawa, K., Shigeoka, S., and Yokota, A. (2002) *Bioscience Biotechnology and Biochemistry* **66**, 2367-2375
167. Sauser, K. R., Liu, J. K., and Wong, T. Y. (1997) *Biometals* **10**, 163-168
168. Takeda, T., Yoshimura, K., Ishikawa, T., and Shigeoka, S. (1998) *Biochimie* **80**, 295-301
169. Takeda, T., Yoshimura, K., Yoshii, M., Kanohoshi, H., Miyasaka, H., and Shigeoka, S. (2000) *Archives of Biochemistry and Biophysics* **376**, 82-90
170. Shigeoka, S., Nakano, Y., and Kitaoka, S. (1980) *Archives of Biochemistry and Biophysics* **201**, 121-127
171. Ishikawa, T., Takeda, T., Kohno, H., and Shigeoka, S. (1996) *Biochimica Et Biophysica Acta* **1290**, 69-75
172. Tel-Or, E., Huflejt, M. E., and Packer, L. (1986) *Archives of Biochemistry and Biophysics* **246**, 396-402
173. Miyake, C., Michihata, F., and Asada, K. (1991) *Plant and Cell Physiology* **32**, 33-43
174. Matthews, M. C., Summers, C. B., and Felton, G. W. (1997) *Archives in Insect Biochemistry and Physiology* **34**, 57-68

175. Leonardis, S. D., Dipierro, N., and Dipierro, S. (2000) *Plant Physiology and Biochemistry* **38**, 773-779
176. Wada, N., Kinoshita, S., Matsuo, M., Amako, C., Miyake, C., and Asada, K. (1998) *Biochemical and Biophysical Research Communications* **242**, 256-261
177. Caldwell, C. R., Turano, F. J., and MacMahon, M. B. (1998) *Planta* **204**, 120-121
178. Chatfield, M., and Dalton, D. A. (1993) *Plant Physiology* **103**, 661-662
179. Webb, R. P., and Allen, R. D. (1995) *Plant Physiology* **108**, 1325-1339
180. Kubo, A., Saji, H., Tanaka, K., and Kondo, N. (1992) *Plant Molecular Biology* **18**, 691-701
181. Genebank accession number 217398
182. Lopez, F., Vansuyt, G., Derancourt, J., Fourcroy, P., and Casse-Delbart, F. (1994) *Cellular and Molecular Biology* **40**, 85-90
183. Lopez, F., Vansuyt, G., Casse-Delbart, F., and Fourcroy, P. (1996) *Physiologia Plantarum* **97**, 13-20
184. van Breusegem, F., Villarroel, R., van Montagu, M., and Inze, D. (1995) *Plant Physiology* **107**, 649-650
185. Kawakami, S., Matsumoto, Y., Matsunaga, A., Mayama, S., and Mizuno, M. (2002) *Plant Science* **163**, 829-836
186. Orvar, B. L., and Ellis, B. E. (1995) *Plant Physiology* **108**, 839-840
187. Morita, S., Kaminaka, H., Yokoi, H., Masumara, T., and Tanaka, K. (1997) *Plant Physiology* **114**, 437-437
188. Morita, S., Kaminaka, H., Yokoi, H., Masumara, T., and Tanaka, K. (1997) *Plant Physiology* **114**, 102-110
189. Kim, I. J., and Chung, W. I. (1998) *Plant Science* **133**, 69-77

190. Gadea, J., Conejero, V., and Vera, P. (1999) *Molecular and General Genetics* **262**, 212-219
191. Schantz, M. L., Schreiber, H., Guillemaut, P., and Schantz, R. (1995) *FEBS Letters* **358**, 149-157
192. Yoo, T. H., Park, C. J., Lee, G. J., Shin, R., Yun, J. H., Kim, K. J., Rhee, K. H., and Paek, K. H. (2002) *Molecules and cells* **14**, 75-84
193. Sohn, S. I., Kim, J. C., Lee, K. W., Rhee, K. H., and Wang, M. H. (2002) *Journal of Plant Physiology* **159**, 1029-1035
194. Jespersen, H. M., Kjaersgard, I. V. H., Ostergaard, L., and Welinder, K. G. (1997) *European Journal of Biochemistry* **326**, 305-310
195. Newman, T., De Bruiji, F. J., Green, P., Keegstra, K., Kende, H., McIntish, L., Ohlrogge, J., Raikhel, N., Somerville, S., Thomashow, M., Retzel, E., and Somerville, C. (1996) *Plant Physiology* **106**, 1241-1255
196. Ishikawa, T., Sakai, K., Yoshimura, K., Takeda, T., and Shigeoka, S. (1996) *FEBS Letters* **384**, 289-293
197. Mano, S., Yamaguchi, K., Hayashi, M., and Nishimura, M. (1997) *FEBS Letters* **413**, 21-26
198. Yamaguchi, K., Hayashi, M., and Nishimura, M. (1996) *Plant and Cell Physiology* **37**, 405-409
199. Zhang, H., Wang, J., Nickel, U., Allen, R. D., and Goodman, H. M. (1997) *Plant Molecular Biology* **34**, 967-971
200. Nito, K., Yamaguchi, M., Kono, M., Hayashi, M., and Nishimura, M. (2001) *Plant and Cell Physiology* **42**, 20-27
201. Bunkelmann, J. R., and Trelease, R. N. (1996) *Plant Physiology* **110**, 589-598
202. Shi, W. M., Muramoto, Y., Ueda, A., and Takabe, T. (2001) *Gene* **273**, 23-27
203. Genbank accession number U43561

204. Rapulo, M., Ishikawa, T., Sawa, Y., Shigeoka, S., and Shibata, H. (2002) *Plant and Cell Physiology* **43**, S161-S161
205. Patterson, W. R., and Poulos, T. L. (1994) *Journal of Biological Chemistry* **269**, 17020-17024
206. Cheek, J., Mandelman, D., Poulos, T. L., and Dawson, J. H. (1999) *Journal of Biological Inorganic Chemistry* **4**, 64-72
207. Dalton, D. A., Diaz del Castillo, L., Kahn, M. L., Joyner, S. L., and Chatfield, J. M. (1996) *Archives of Biochemistry and Biophysics* **328**, 1-8
208. Nissum, M., Feis, A., and Smulevich, G. (1998) *Biospectroscopy* **4**, 355-364
209. Jones, D. K., Dalton, D. A., Rosell, F. I., and Raven, E. L. (1998) *Archives of Biochemistry and Biophysics* **360**, 173-178
210. Patterson, W. R., Poulos, T. L., and Goodin, D. B. (1995) *Biochemistry* **34**, 4342-4345
211. Lad, L., Mewies, M., and Raven, E. L. (2002) *Biochemistry* **41**, 13774-13781
212. Lad, L., Mewies, M., Basran, J. S., Scrutton, N. S., and Raven, E. L. (2002) *European Journal of Biochemistry* **269**, 3182-3192
213. Nishikawa, F., Kato, M., Wang, R., Hyodo, H., Ikoma, Y., Sugiura, M., and Yano, M. (2003) *Postharvest Biology and Technology* **27**, 147-156
214. Sharp, K. H., Moody, P. C. E., Brown, K. A., and Raven, E. L. (2004) *Biochemistry* **43**, 8644-8651
215. Marquez, L. A., Quitariano, M., Zlinskas, B. A., and Dunford, H. B. (1996) *FEBS Letters* **389**, 153-156
216. Mandelman, D., Jamal, J., and Poulos, T. L. (1998) *Biochemistry* **37**, 17610-17617
217. Pappa, H., Patterson, W. R., and Poulos, T. L. (1996) *Journal of Biological Inorganic Chemistry* **1**, 61-66

218. Bursley, E. H., and Poulos, T. L. (2000) *Biochemistry* **39**, 7374-7379
219. Ibers, J. A., and Holm, R. H. (1980) *Science* **209**, 223-230
220. Reid, L. S., Lim, A. R., and Mauk, A. G. (1986) *Journal of American Chemical Society* **108**, 8917-8201
221. Walker, F. A., Huynh, B. H., Scheidt, W. R., and Osvath, S. R. (1986) *Journal of American Chemical Society* **108**, 5288-5297
222. Veitch, N. C., and Smith, A. T. (2001) *Advances in Inorganic Chemistry* **51**, 107
223. Erman, J. E. (1998) *Journal of Biochemistry and Molecular Biology* **31**, 307-327
224. Ozaki, S. I., Inada, Y., and Watanabe, M. (1998) *Journal of American Chemical Society* **120**, 8020-8025
225. Baek, H. K., and Van Wart, H. E. (1989) *Biochemistry* **28**, 5714-5719
226. Baek, H. K., and Van Wart, H. E. (1992) *Journal of American Chemical Society* **114**, 718-725
227. Berglund, G. I., Carlsson, G. H., Smith, A. T., Szoke, H., Henriksen, A., and Hajdu, J. (2002) *Nature* **417**, 463-468
228. Rodriguez-Lopez, J. N., Lowe, D. J., Hernandez-Ruiz, J., Hiner, A. N. P., Garcia-Canovas, F., and Thorneley, R. N. F. (2001) *Journal of American Chemical Society* **123**, 11838-11847
229. Dunford, H. B. (1982) *Advances in Inorganic Biochemistry* **4**, 41-68
230. Hiner, A. N. P., Martinez, J. I., Arnao, M. B., Acosta, M., Turner, D. D., Raven, E. L., and Rodriguez-Lopez, J. N. (2001) *European Journal of Biochemistry* **268**, 3091-3098
231. Metcalfe, C. L., Ott, M., Patel, N., Singh, K., Mistry, S. C., Goff, H. M., and Raven, E. L. (2004) *Journal of the American Chemical Society* **126**, 16242-16248

232. Pipirou, Z., Bottrill, A. R., Metcalfe, C. M., Mistry, S. C., Badyal, S. K., Rawlings, B. J., and Raven, E. L. (2007) *Biochemistry* **46**, 2174-2180
233. Erman, J. E., and Yonetani, T. (1975) *Biochimica Et Biophysica Acta* **393**, 343-349
234. Mauro, J. M., Fishel, L. A., Hazzard, J. T., Meyer, T. E., Tollin, G., Cusanovich, M. A., and Kraut, J. (1988) *Biochemistry* **27**, 6243-6256
235. Bonagura, C. A., Sundaramoorthy, M., Bhaskar, B., and Poulos, T. L. (1999) *Biochemistry* **38**, 5538-5545
236. Bhaskar, B., Bonagura, C. A., Li, H. Y., and Poulos, T. L. (2002) *Biochemistry* **41**, 2684-2693
237. Barrows, T. P., Bhaskar, B., and Poulos, T. L. (2004) *Biochemistry* **43**, 8826-8834
238. Guallar, V., and Olsen, B. (2006) *Journal of Inorganic Biochemistry* **100**, 755-760
239. Jensen, G. M., Bunte, S. W., Warshel, A., and Goodin, D. B. (1998) *Journal of Physical Chemistry* **102**, 8221-8228
240. Harvey, J. N., Bathelt, C. M., and Mulholland, A. J. (2006) *Journal of Computational Chemistry* **27**, 1352-1362
241. Menyhard, D. K., and Naray-Szabo, G. (1999) *Journal of Physical Chemistry B* **103**, 227-233
242. NaraySzabo, G. (1997) *Journal of Biological Inorganic Chemistry* **2**, 135-138
243. Hill, A. P., Modi, S., Sutcliffe, M. J., Turner, D. D., Gilfoyle, D. J., Smith, A. T., Tam, B. M., and Lloyd, E. (1997) *European Journal of Biochemistry* **248**, 347-354
244. Mauk, M. R., Kishi, K., Gold, M. H., and Mauk, A. G. (1998) *Biochemistry* **37**, 6767-6771

245. DePillis, G. D., Sishta, B. P., Mauk, A. G., and Ortiz de Montellano, P. R. (1991) *Journal of Biological Chemistry* **266**, 19334-19341
246. Mandelman, D., Schwarz, F. P., Li, H., and Poulos, T. L. (1998) *Protein Science* **7**, 2089-2098
247. Meno, K., Jennings, S., Smith, A. T., Henriksen, A., and Gajhede, M. (2002) *Acta Crystallographica Section D-Biological Crystallography* **58**, 1803-1812
248. Henriksen, A., Smith, A. T., and Gajhede, M. (1999) *Journal of Biological Chemistry* **274**, 35005-35011
249. Fiedle, T. J., Davey, C. A., and Fenna, R. E. (2000) *Journal of Biological Chemistry* **275**, 11964-11971
250. Itakura, H., Oda, Y., and Fukuyama, K. (1997) *FEBS Letters* **412**, 107-110
251. Fukuyama, K., Sato, K., Itakura, H., Takahashi, S., and Hosoya, T. (1997) *Journal of Biological Chemistry* **272**, 5752-5756
252. Tsukamoto, K., Itakura, H., Sato, K., Fukuyama, K., Miura, S., Takahashi, S., Ikezawa, H., and Hosoya, T. (1999) *Biochemistry* **38**, 12558-12568
253. Macdonald, I. K., Badyal, S. K., Ghamsari, L., Moody, P. C. E., and Raven, E. L. (2006) *Biochemistry* **45**, 7808-7817
254. Raman, C. S., Li, H., Martasek, P., Kral, V., Masters, B. S., and Poulos, T. L. (1998) *Cell* **95**, 939-950
255. Crane, B. R., Arvai, A. S., Ghosh, D. K., Wu, C., Getzoff, E. D., Stuehr, D. J., and Tainer, J. A. (1998) *Science* **279**, 2121-2126
256. Fischmann, T. O., Hruza, A., Niu, X. D., Fossetta, J. D., Lunn, C. A., Dolphin, E., Prongay, A. J., Reichert, P., Lundell, D. J., Narula, S. K., and Patricia, C. W. (1999) *Nature Structural Biology* **6**, 233-242
257. Berghuis, A. M., and Brayer, G. D. (1992) *Journal of Molecular Biology* **223**, 959-976

258. Turano, P., and Lu, Y. (2001) (Bertini, I., and Sigel, A., eds), Marcel Decker, New York
259. Scott, R. A., and Mauk, A. G. (1996) *Cytochrome c. A multidisciplinary approach*, University Science Books, Sausalito, CA
260. Moore, G. R., and Pettigrew, G. W. (1990), Springer-Verlag, Berlin
261. Mauk, A. G. (1991) *Structure bonding* **75**, 131-157
262. Michel, L. V., Ye, T., Bowman, S. E. J., Levin, B. D., Hahn, M. A., Russel, B. A., Elliot, S. J., and Bren, K. L. (2007) *Biochemistry* **46**, 11753-11760
263. Valentine, J. S., Sheriden, R. P., Allen, L. C., and Kahn, P. C. (1979) *Proceedings of the National Academy of Sciences of the United States of America* **76**, 1009-1013
264. Walker, F. A., Rivera, J. E., Hanquet, B. J., and Buttlair, D. H. (1988) *Journal of American Chemical Society* **110**, 6234-6240
265. Garau, G., Geremia, S., and Randaccio, L. (2002) *FEBS Letters* **516**, 285-286
266. White, R. E., and Coon, M. J. (1980) *Annual Review of Biochemistry* **49**, 315-356
267. Loew, G. H., and Harris, D. L. (2002) *Chemical Reviews* **100**, 407-419
268. Dawson, J. H., and Eble, K. S. (1986) *Advances in Inorganic and Bioinorganic Mechanisms* **4**, 1-64
269. Poulos, T. L., Finzel, B. C., and Howard, A. J. (1987) *Journal of Molecular Biology* **195**, 687-700
270. Benhardt, R. (1995) *Reviews in Physiology, Biochemistry and Pharmacology* **127**, 137-221
271. Sligar, S. G. (1976) *Biochemistry* **15**, 5399-5406

272. Schlichting, I., Berendzen, J., Chu, K., Stock, A. M., Maves, S. A., Benson, D. E., Sweet, R. M., Ringe, D., Petsko, G. A., and Sligar, S. G. (2000) *Science* **287**, 1615-1622
273. Wilker, J. J., Dmochowski, I. J., Dawson, J. H., Winkler, J. R., and Gray, H. B. (1999) *Angewandte Chemie International Edition* **38**, 90-92
274. Poulos, T. L., Li, H., Raman, C. S., and Schuller, D. J. (2001) *Advances in Inorganic Chemistry* **51**, 243-293
275. Ortiz de Montellano, P. R. (1998) *Accounts of Chemical Research* **31**, 543-549
276. Ortiz de Montellano, P. R., and Wilks, A. (2001) *Advances in Inorganic Chemistry* **51**, 359-407
277. Dore, S., Takahashi, M., Ferris, C. D., Zakhary, R., Hester, L. D., Guastella, D., and Snyder, S. H. (1999) *Proceedings of the National Academy of Sciences of the United States of America* **96**, 2445-2450
278. Zhuo, M., Small, S. A., Kandel, E. R., and Hawkins, R. D. (1993) *Science* **260**, 1946-1950
279. Verma, A., Hirsch, D. L., Glatt, C. E., Ronnet, G. V., and Snyder, S. H. (1993) *Science* **259**, 381-384
280. Stevens, C. F., and Wang, Y. (1993) *Nature* **364**, 147-149
281. Schuller, D. J., Wilks, A., Ortiz de Montellano, P. R., and Poulos, T. L. (1999) *Nature Structural Biology* **6**, 860-867
282. Unno, M., Matsui, T., and Ikeda-Saito, M. (2007) *Natural Product Reports* **24**, 553-570
283. Friedman, J., Lad, L., Li, H., Wilks, A., and Poulos, T. L. (2004) *Biochemistry* **43**, 3793-3801
284. Lan, C., Lee, H. C., Tang, S., and Zhang, L. (2004) *Journal of Biological Chemistry* **279**, 27607-27612

285. Igarashi, I., Sato, A., Kitagawa, T., Sagami, I., and Shimizu, T. (2003) *Biochimica Et Biophysica Acta* **1650**, 99-104
286. Haruto, I., Bo-Geon, Y., Satoshi, T., Hiroshi, H., Roberts, M. F., Koichiro, I., and Isao, M. (2002) *Journal of American Chemical Society* **124**, 13696-13697
287. Igarashi, I., Sato, A., Kitagawa, T., Yoshimurama, T., Yamauchi, S., Sagami, I., and Shimizu, T. (2004) *Journal of Biological Chemistry* **279**, 15752-15762
288. Sasakura, Y., Yoshimura-Suzuki, T., Kurokawa, H., and Shimizu, T. (2006) *Accounts of Chemical Research* **39**, 37-43
289. <http://www.cchem.berkeley.edu/mmargrp/research/sgc/sgc.html>.
290. Lanzilotta, W. N., Schuller, D. J., Thorstensson, M. V., Kerby, R. L., Roberts, G. P., and Poulos, T. L. (2000) *Nature Structural Biology* **7**, 876-880
291. Gong, W., Hao, B., Mansy, S. S., Gonzalez, G., Gilles-Gonzalez, M. A., and Chan, M. K. (1998) *Proceedings of the National Academy of Sciences of the United States of America* **95**, 15177-15182
292. Roberts, G. P., Thorstensson, M. V., Kerby, K., Lanzilotta, W. N., and Poulos, T. L. (2001) *Progress in Nucleic Acid Research and Molecular Biology* **67**, 35-63
293. Taylor, B. L., and Zhulin, I. B. (1999) *Microbiology and Molecular Biology Reviews* **63**, 479-506
294. Kurokawa, H., Lee, D. S., Watanabe, M., Sagami, I., Mikami, B., Raman, C. S., and Shimizu, T. (2004) *Journal of Biological Chemistry* **279**, 20186-20193
295. Gilles-Gonzalez, M. A., and Gonzalez, G. (2005) *Journal of Inorganic Biochemistry* **99**, 1-22
296. Gilles-Gonzalez, M. A., Ditta, G. S., and Helinski, D. R. (1991) *Nature* **350**, 170-172

297. Nakamura, H., Kumita, H., Imai, K., Iizuka, T., and Shiro, Y. (2004) *Proceedings of the National Academy of Sciences of the United States of America* **101**, 2742-2746
298. Gilles-Gonzalez, M. A., and Gonzalez, G. (1993) *Journal of Biological Chemistry* **268**, 16293-16297
299. Gilles-Gonzalez, M. A., Gonzalez, G., and Perutz, M. F. (1995) *Biochemistry* **34**, 232-236
300. Lois, A. F., Weinstein, M., Ditta, G. S., and Helinski, D. R. (1993) *Journal of Biological Chemistry* **268**, 4370-4375
301. Delgado-Nixon, V. M., Gonzalez, G., and Gilles-Gonzalez, M. A. (2000) *Biochemistry* **39**, 2685-2691
302. Gilles-Gonzalez, M. A. (2001) *Life* **51**, 165-173
303. Dioum, E. M., Rutter, J., Tuckerman, J., R., Gonzalez, G., Gilles-Gonzalez, M. A., and McKnight, S. L. (2002) *Science* **298**, 2385-2387
304. Hou, S., Larsen, R. W., Boudko, D., Riley, C., W., Karatan, E., Zimmer, M., Ordal, G. W., and Alam, M. (2000) *Nature* **403**, 540-544
305. Hou, S., Freitas, T., Larsen, R. W., Piatibratov, M., Sivozhelezov, V., Yamamoto, A., Meleshkevitch, E. A., Zimmer, M., Ordal, G. W., and Alam, M. (2001) *Proceedings of the National Academy of Sciences of the United States of America* **98**, 9353-9358
306. Ohta, T., Yoshimura, H., Yoshioka, S., Aono, S., and Kitagawa, T. (2004) *Journal of American Chemical Society* **126**, 15000-15001

*CHAPTER TWO*

**CONFORMATIONAL MOBILITY IN THE ACTIVE SITE OF A  
HEME PEROXIDASE**

## CHAPTER TWO

# CONFORMATIONAL MOBILITY IN THE ACTIVE SITE OF A HEME PEROXIDASE

---

### 2.1 INTRODUCTION

The advent of site-directed mutagenesis (1) has revolutionized the way in which protein structure/function studies are conducted by allowing systematic perturbation of the protein architecture which, when combined with detailed spectroscopic and functional analysis, can provide very specific information on the role of individual residues in a protein. In the case of heme peroxidase enzymes, analysis of a wide variety of site-directed variants has aided the detailed investigation of the mechanism of peroxidase catalysis (2-7). Whilst there is a great deal of kinetic data available on active site variants for other peroxidases (notably CcP and HRP) (2,5,7); there is currently limited information for APX (8-11). In this chapter the role of the distal tryptophan (Trp-41) will be investigated by preparation of the W41A variant of rsAPX.

The architecture of the heme active site of rsAPX is shown in Figure [2.1], the catalytic histidine (His) and arginine (Arg) residues present in the distal cavity are highly conserved residues that play a concerted role in H<sub>2</sub>O<sub>2</sub> binding to the ferric-resting state and the two-electron oxidation of the enzyme to Compound I (7) (see Chapter 1, Section 1.5.3). The peroxidase heme architecture also harbors a conserved distal aromatic residue site; in the class I peroxidases this is a tryptophan

residue, whereas in class II and III peroxidases this site is occupied by a phenylalanine residue. Sequence alignments suggest that an aromatic residue is adjacent to the catalytic distal histidine in all plant and fungal peroxidases (12). As with the aromatic distal cavity residues in other peroxidases, Trp-41 in APX forms a hydrogen-bonding network with other residues present in this region of the protein and also forms a hydrogen bond to one of three water molecules present in the distal heme pocket that is displaced on H<sub>2</sub>O<sub>2</sub> binding (13,14). Despite the presence of these water molecules near the ligand binding site, the heme iron atom of the resting state of peroxidase enzymes remains predominantly five-coordinate and high-spin (12).

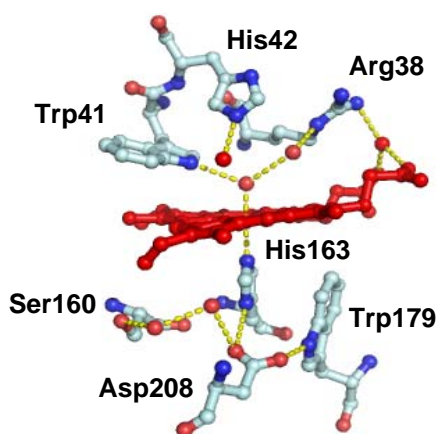


**Figure [2.1]:** The active site of rsAPX (PDB code: 1OAG) (15) showing the heme (red) and various active site residues. Water molecules are indicated by red spheres and hydrogen bonds by yellow dashed lines.

Structural information is available for a number of heme peroxidase enzymes and, in all cases; the heme iron is poised in a five-coordinate or weakly six-coordinate environment with the sixth ligand provided by a weakly coordinated water molecule. This differs from the heme coordination geometry in other, non-catalytic heme proteins that do not require binding of an exogenous ligand at the metal site: the classic example is the cytochromes which typically have a strong endogenous protein ligand at the sixth site (usually histidine or methionine) and no vacant coordination site for iron-catalysed chemistry to occur. The prevailing view that has emerged, therefore, is that the catalytic enzymes (which includes the heme peroxidases but also embraces other, more complex heme enzymes such as heme oxygenase, the cytochrome P450s and cytochrome c oxidase) usually contain five-

coordinate or weakly six-coordinate heme groups that allow facile reaction with substrate, whereas the electron transfer proteins, for example the cytochromes, have no vacant site at the metal ion for catalysis to occur. However the presence of a strongly bound ligand at the sixth coordination site of heme in catalytic proteins is being observed increasingly, where the distal aromatic residue has been mutated and is discussed below.

There are no known examples of a genuine heme peroxidases with bis-histidine ligation (where the fifth and sixth coordination sites are occupied by histidine residues) but there are a few examples in the literature of different heme peroxidases, or site-directed variants thereof, in which coordination of the distal histidine residue has been proposed on the basis of spectroscopic studies (16-25). These include: the W51A, D235N and R38L variants of CcP (19,22), the F41A variant of HRP (23), the various Phe-54 variants of CIP (24), the thermally inactivated manganese peroxidase (17) and manganese peroxidase at alkaline pH (21). Removal of the ligands coordinating to the bound potassium site in APX also leads to formation of a low-spin species (16). In none of these cases has unambiguous structural information been obtained, however structural evidence for coordination of distal histidine has been presented in the structure of the pH inactivated barley peroxidase (25).

In this Chapter, the first crystallographically-defined example of a functional peroxidase enzyme with bis-histidine ligation in the W41A variant of APX is presented. This variant duplicates the heme coordination geometry of the cytochromes *b* in the oxidised form but remains fully competent for formation of the catalytic Compound I and Compound II intermediates, as well as for substrate oxidation, by means of a reaction mechanism in which a conformationally mobile ligand (His-42) binds “on” and then “off” the iron during catalysis. This switch between the “on” and “off” forms is triggered by reaction with H<sub>2</sub>O<sub>2</sub> (or other anionic ligands) and, under catalytic conditions, is fully reversible, allowing essentially complete activity to be maintained. In this Chapter, crystallographic, spectroscopic and kinetic data indicate that coordination of the distal histidine to the heme iron does not automatically undermine peroxidase activity.

## 2.2 RESULTS

### 2.2.1 Expression and purification of W41A

Site-directed mutagenesis was performed according to the Quikchange™ protocol (Stratagene) using the rsAPX His-tag pQE-30 vector (Appendix B) and the appropriate purified mutagenic oligonucleotides (sequences shown in Table 6.1, Chapter 6, Section 6.2.1). The mutation (W41A) was confirmed by DNA sequencing, of the whole coding gene and was found to be free of any other mutations. The rsAPX and W41A variant were expressed with a six-histidine residue amino terminal tag (His-tag). Expression of W41A yielded red pellets (removal of the bulky tryptophan residue has probably created additional space in the distal cavity thus heme incorporation is more efficient in comparison to rsAPX) which were purified as described in Chapter 6, Section 6.3.

### 2.2.2 Analysis of the purity of W41A

#### 2.2.2.1 SDS-PAGE electrophoresis

The purity of the FPLC purified protein samples was assessed by gel electrophoresis on a 15 % polyacrylamide gel. The SDS-PAGE gel (Figure [2.2]), of the protein samples exhibited only one band of molecular weight ~30 kDa, therefore showing that all protein samples were homogeneous. The molecular weight of 30 kDa per monomer was consistent with that obtained for the native APX ( $M_r$  29.5 kDa per monomer determined from SDS-PAGE) (26) (APX exists as a dimer under non-reducing conditions).

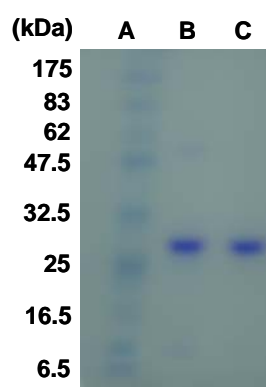


Figure [2.2]: Coomassie blue stained 15 % SDS-PAGE gel of purified rsAPX and W41A, Lane A: Bio-Rad molecular mass standards; Lane B: rsAPX and Lane C: W41A.

The purity of the protein samples (obtained in yields of ~30 mg/l) was also assessed by determining the Reinheitszahl ( $R_z$ ) value (the ratio of absorbance of the Soret peak (~400 nm) and that of the protein peak at 280 nm,  $A_{\text{Soret}}/A_{280}$ ), where a protein with an  $R_z$  value above 1.7 is deemed pure. A Reinheitszahl value of >3 was determined for W41A variant since there are two tryptophan residues in rsAPX and removal of one in the W41A variant results in an elevated  $R_z$  value.

### 2.2.2.2 Mass spectrometric analysis

The absence of post-translational modification of the expressed W41A variant was confirmed by mass spectrometric analysis. MALDI-TOF (Matrix-Assisted-Laser-Desorption-Time-of-Flight spectroscopy) analysis of W41A, (Figure [2.3]) gave an average mass of  $28,209.36 \pm 0.05$  Da (calculated mass 28,203.74 Da).

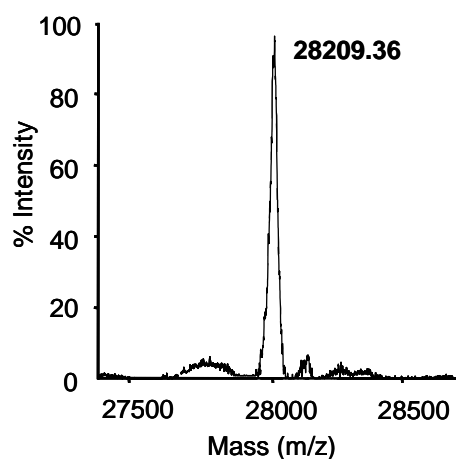


Figure [2.3]: MALDI-TOF mass spectrum of W41A.

## 2.2.3 Spectroscopic characterisation of W41A

### 2.2.3.1 Electronic absorption spectra

Analysis of the ferric W41A spectrum (Figure [2.4]), reveals wavelength maxima at ( $\lambda_{\text{max}}/\text{nm} = 405, 525, 564$  and  $630$ ), which differ from rsAPX ( $\lambda_{\text{max}}/\text{nm} = 407, 525$  and  $\sim 630$ ) (9). The ferric rsAPX spectrum (Figure [2.4]) revealed wavelength maxima which are consistent with a predominantly five-coordinate high-spin iron, with a broad Soret peak and a characteristic high-spin peak at 630 nm.

Although the high-spin peak at  $\sim 630$  nm in rsAPX is still apparent in W41A (Figure [2.4]), the peak at 564 nm in W41A is consistent with the presence low-spin heme (27). No evidence for the formation of (low-spin) hydroxide bound heme was observed at alkaline pH. The presence of six-coordinate heme species in heme peroxidases has been postulated to arise from ligation of the distal histidine (28,29). The six-coordinate/low-spin species in W41A was thus tentatively assigned as arising from coordination of an (internal) protein ligand, possibly histidine-42 (His-42).

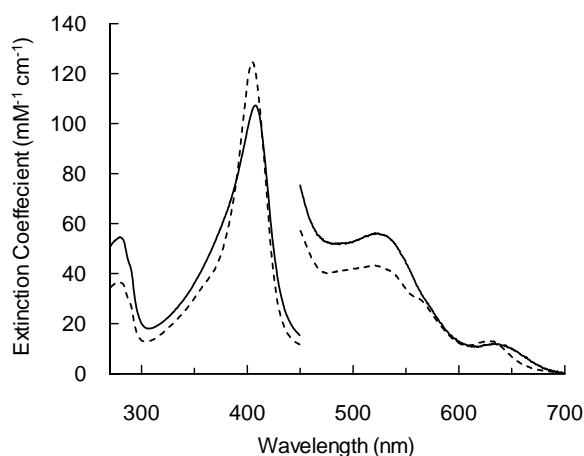


**Figure [2.4]:** Electronic spectra of ferric rsAPX (solid line) and ferric W41A (dashed line). The visible region has been multiplied by a factor of 5. Conditions: sodium phosphate, pH 7.0,  $\mu = 0.1$  M, 25.0 °C.

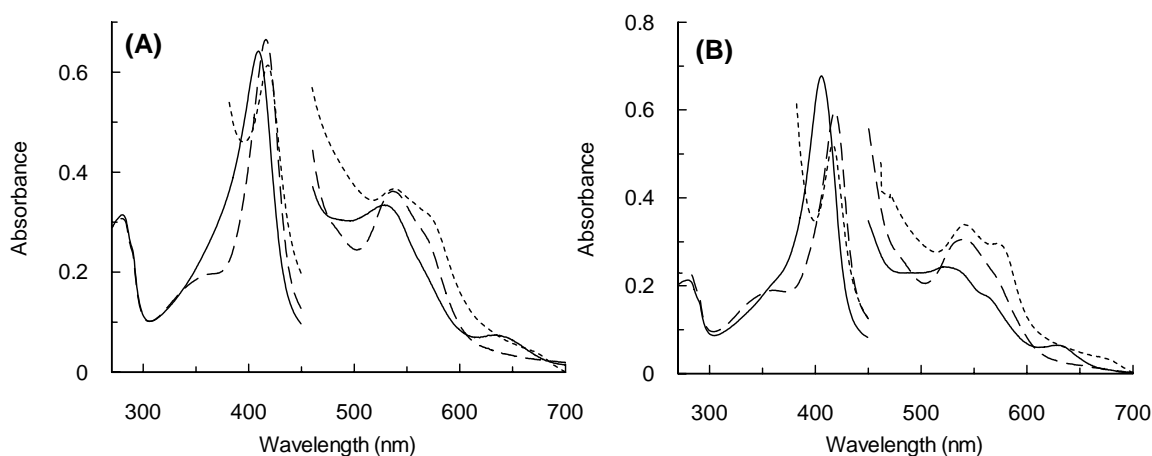
### 2.2.3.2 Pyridine hemochromogen assay

An absorption coefficient value of  $\epsilon_{405} = 125 \text{ mM}^{-1} \text{ cm}^{-1}$  was obtained for the W41A variant and has been used to calculate the concentration of the W41A variant reported throughout this thesis. Although the Soret maxima of W41A are similar to

rsAPX, in contrast the variant exhibits a large absorption coefficient value which is indicative of the presence of increased amounts of six-coordinate, possibly low-spin component heme.

### 2.2.3.3 Binding of non-catalytic ligands

To assess whether the proposed protein ligand is reversibly or irreversibly bound to the iron in the variant, ferric W41A was reacted with various non-catalytic ligands. Addition of cyanide to ferric W41A leads to a spectrum (Figure [2.5B]), in which complete formation of low-spin heme is attained, as observed for rsAPX (Figure [2.5A]) and this suggested that addition of a strong exogenous ligand leads to displacement of the existing (internal) ligand; absorption maxima are shown in Table [2.1]. Nitric oxide was found to cause similar changes in the heme pockets of both ferrous rsAPX and ferrous W41A (Figure [2.5] and Table [2.1]), thus the internal ligand was displaced on binding of non-catalytic ligands.



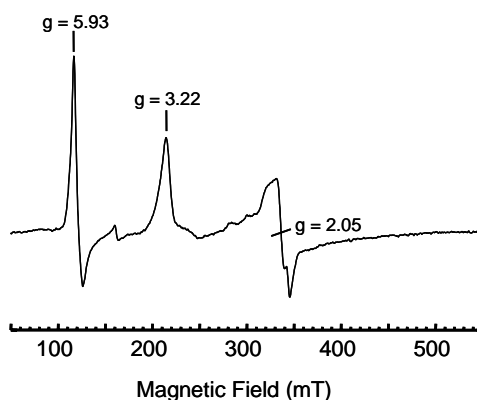
**Figure [2.5]: (A) Electronic spectrum of ferric rsAPX (solid line), rsAPX-cyanide (dashed line) and rsAPX-nitric oxide (dotted line). (B) Electronic spectrum of ferric W41A (solid line), W41A-cyanide (dashed line) and W41A-nitric oxide (dotted line). The visible region has been multiplied by a factor of 5. Conditions: sodium phosphate, pH 7.0,  $\mu = 0.1$  M, 25.0 °C.**

Table [2.1]: Wavelength maxima (nm) of cyanide (CN) and nitric oxide (NO) derivatives of rsAPX and W41A. Conditions: sodium phosphate buffer, pH 7.0,  $\mu = 0.1$  M at 25.0 °C. (<sup>sh</sup> denotes unresolved shoulder and \* denotes wavelength maxima less than 390 nm, obscured by the dithionite absorption).

Derivative	$\delta$	( $\gamma$ ) Soret	CT <sub>2</sub>	$\beta$	$\alpha$	CT <sub>1</sub>
<b>rsAPX</b>						
Fe <sup>III</sup>	-	407	525	-	-	~630
Fe <sup>III</sup> -CN	~360 <sup>sh</sup>	419	-	536	563 <sup>sh</sup>	-
Fe <sup>II</sup> -NO	*	418	-	537	570 <sup>sh</sup>	-
<b>W41A</b>						
Fe <sup>III</sup>	~380 <sup>sh</sup>	405	525	-	564	630
Fe <sup>III</sup> -CN	~365 <sup>sh</sup>	418	-	540	561 <sup>sh</sup>	-
Fe <sup>II</sup> -NO	*	417	-	541	574	-

### 2.2.3.4 Electronic paramagnetic resonance spectroscopy (EPR) of W41A

EPR spectroscopy of the W41A variant was conducted by Dr H. E. Seward (Department of Biochemistry, University of Leicester). The EPR spectrum of ferric W41A (Figure [2.6]) was dominated by a rhombic low-spin species with observed  $g$ -values of 3.22 and 2.05 (the third feature was too broad to be observed). A second, minor component with  $g$ -values of 5.67 and 1.99 is consistent with an axial, high-spin species. The low-spin species is the majority species at 10 K and is consistent with bis-histidine ligation; the  $g$ -values are consistent with an orientation in which the imidazole planes are not parallel to each other. Neither species resemble those observed in the EPR spectrum of rsAPX (30,31), which has a rhombic high-spin species ( $g = 6.04, 5.27, \text{ and } 1.98$ ) and a small amount of rhombic low-spin heme ( $g = 2.69, 2.21 \text{ and } 1.79$ ). A minor low-spin rhombic species ( $g_z = 2.95$ , as a shoulder on the  $g = 3.22$  feature) and the positive lobe of  $g_y$  feature ( $g_y = 2.30$ ) in W41A are likely to arise from a histidine/histidine ligated heme in which the imidazole planes are parallel to each other (however there is evidence for multiple conformations of the proximal histidine in the crystal structure of the cyanide bound form of W41A, see Section 2.2.4.4).



**Figure [2.6]: EPR spectrum of ferric W41A. Conditions: [W41A] = 300  $\mu$ M, sodium phosphate, pH 7.0,  $\mu = 0.1$  M and glycerol (50% v/v), microwave frequency = 9.67 GHz, microwave power = 2 milliwatts, temperature = 10.7 K, modulation amplitude = 10 G.**

## 2.2.4 Crystallography of W41A

Crystallisation of W41A was carried out as described in Chapter 6, Section 6.8. Highly ordered crystals of W41A were obtained after two weeks of incubation at 19.0 °C. These highly ordered crystals (Figure [2.7]), with flat surfaces and sharp edges, were about 150 µm long and 75 µm in cross-section. Data for rsAPX-cyanide and rsAPX-nitric oxide bound derivatives were obtained by Dr. K. H. Sharp (Department of Chemistry, University of Leicester).

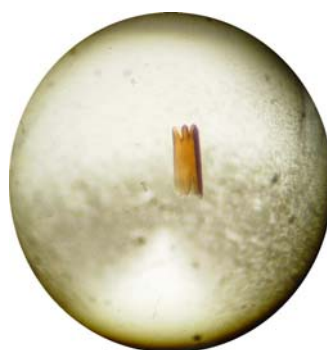


Figure [2.7]: Crystals of W41A. Sample conditions: 0.1 M HEPES pH 8.3, 2.25 M lithium sulphate and W41A (10 mg/ml) at 19.0 °C.

### 2.2.4.1 Interpretation and refinement of crystallographic data

The data for all the crystal structures discussed in this Chapter were interpreted by Dr M. G. Joyce with assistance from Dr P. C. E. Moody (Department of Biochemistry, University of Leicester). The structures were refined from a model derived from the 1.45 Å rsAPX-ascorbate complex (Protein Data Bank (PDB) code: 1OAF) by removal of the bound ligand and water molecules. Several cycles of refinement using REFMAC5 (32) from the CCP4 suite (33) and manual rebuilding of the protein model using COOT (34) followed by addition of water molecules were carried out until the  $R_{\text{free}}$  and  $R_{\text{factor}}$  values converged. The refinement statistics of all structures are presented in Table [2.2]. In total, six crystal structures and diffraction data were deposited in the Protein Data Bank with the following accession codes: 2GGN (ferric W41A), 2GHC (W41A-nitric oxide complex), 2GHD (W41A-cyanide complex) 2GHE (W41A-H<sub>2</sub>O<sub>2</sub> soak), 2GHH (rsAPX-nitric oxide complex) and 2GHK (rsAPX-cyanide complex). Data collection and processing statistics are shown in Table [2.2].

**Table [2.2]: Data collection and refinement statistics. Values for outer shells are given in parentheses. RMSD, root-mean-square deviation; PDB, Protein Data Bank.**

Statistics	W41A	W41A-CN	rsAPX-CN	W41A-NO	rsAPX-NO	W41A-H <sub>2</sub> O <sub>2</sub>
<b><i>Data collection</i></b>						
Resolution (Å)	28.88-1.35	36.81-1.4	58.00-2.00	45.88-1.25	18.86-2.01	28.99-1.75
Outer shell	(1.42-1.35)	(1.44-1.40)	(2.07-2.00)	(1.32-1.25)	(2.06-2.01)	(1.84-1.75)
Total observations	599,082	248,232	58,820	299,270	59,132	360,725
Unique reflections	56,193	52,940	15,798	69,773	16,455	26,381
$I/\sigma I$	17.8 (4.00)	13.3 (3.10)	15.9 (2.98)	12.8 (3.90)	15.8 (3.12)	30.6 (11.60)
$R_{\text{merge}}$	0.097	0.088	0.052	0.107	0.051	0.059
Completeness (%)	99.4 (99.9)	92.8 (96.9)	95.2 (95.7)	98.6 (99.9)	97.3 (95.9)	99.8 (100)
<b><i>Refinement</i></b>						
$R_{\text{factor}}$	0.190	0.206	0.187	0.189	0.183	0.179
$R_{\text{free}}$	0.205	0.229	0.235	0.207	0.258	0.220
RMSD from ideal						
Angles (°)	1.086	1.110	1.290	1.049	1.457	1.188
Bonds (Å)	0.007	0.008	0.012	0.006	0.015	0.011
PDB accession codes	2GGN	2GHD	2GHK	2GHC	2GHH	2GHE

#### 2.2.4.2 Overall crystal structure of W41A and ligand bound derivatives

Although rsAPX is a homodimer in solution, only one monomer is found in the crystallographic asymmetric unit (30). The overall structure of rsAPX-cyanide and nitric oxide bound complexes (Figure [2.8A]) were similar to the rsAPX structure (15). The W41A variant also had an overall structure (Figure [2.8B]) similar to rsAPX; the root-mean-square deviation between C $\alpha$  positions (residues 2-249) for this structure and ferric rsAPX is 0.26 Å (determined using LSQKAB) (35). The overall structure of W41A was not substantially affected on binding of H<sub>2</sub>O<sub>2</sub>, nitric oxide or cyanide (Figure [2.8B]).

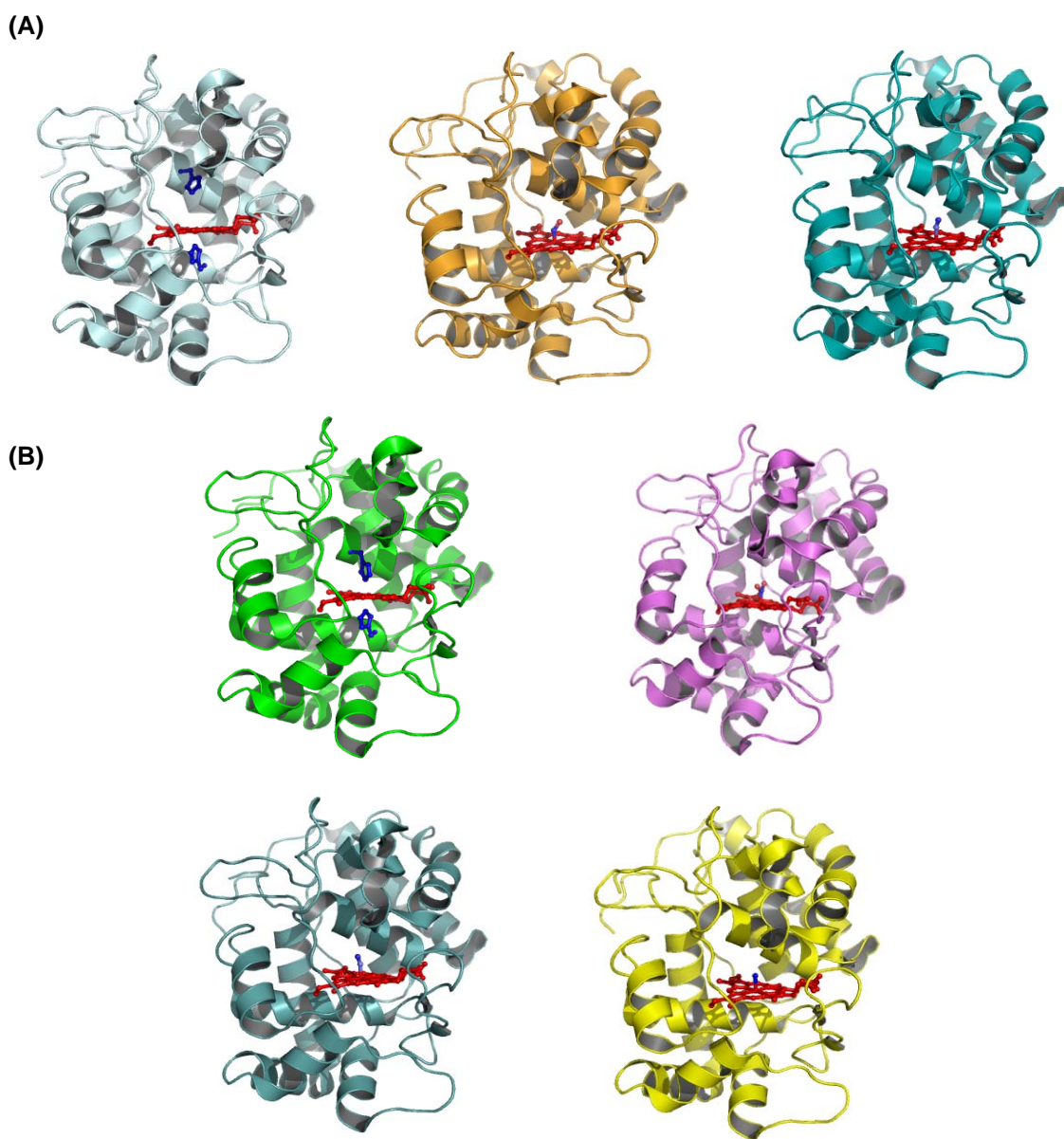


Figure [2.8]: (A) The overall structure of (*left*) rsAPX showing the heme, His-42 and His-163 (PDB code: 1OAG) (15), (*centre*) rsAPX-nitric oxide complex and (*right*) rsAPX-cyanide complex, showing the bound ligands, respectively. (B) The overall structure of (*top left*) W41A showing the heme, His-42 and His-163, (*top right*) W41A-nitric oxide complex, (*bottom left*) W41A-cyanide complex and (*bottom right*) W41A-H<sub>2</sub>O<sub>2</sub> complex, showing the bound ligands, respectively.

### 2.2.4.3 Active site of W41A

The active site structure of W41A (Figure [2.9]) revealed that the space previously occupied by the Trp-41 side chain in rsAPX is filled by two water molecules in the variant (labelled 1 and 2 in Figure [2.9A]). Although the overall structure and most of the active site structure is similar to rsAPX, there are local changes in protein conformation around His-42 (Figure [2.9B]). Hence, the main chain of His-42 moves toward the heme in W41A such that N<sup>ε</sup> of His-42 is now within bonding distance (2.3 Å, compared with 5.5 Å in rsAPX) of the iron. This form of the variant is termed the “on” form.

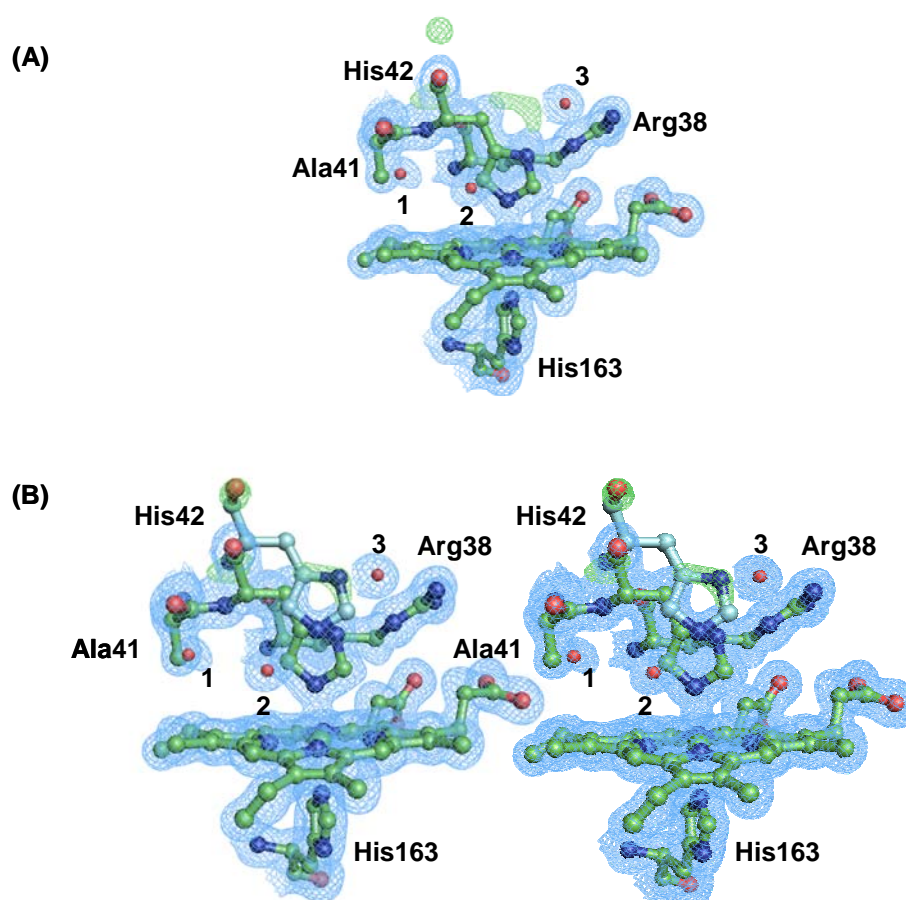


Figure [2.9]: (A) The active site of ferric W41A, showing the coordination of His-42 to the iron. SigmaA-weighted  $2F_o - F_c$  electron density at  $1 \sigma$  is shown in blue, and sigmaA-weighted  $F_o - F_c$  electron density at  $3 \sigma$  is shown in green. The positive  $F_o - F_c$  electron density (in green) overlays with the position of His-42 in the structure of rsAPX. Water molecules are shown as red spheres. (B) A stereo view of a structural alignment of the orientation of His-42 in rsAPX (in blue, PDB code: 1OAG) (15) with the active site in W41A (in green). Water molecules are shown as red spheres for W41A.

A further water molecule (labelled 3 in Figure [2.9A]) is located in the region that was previously occupied by His-42. The Fe-N<sup>ε</sup>(His-163) distance is essentially identical in both W41A and rsAPX (2.1 and 2.0 Å, respectively). This new histidine (His-42) ligand replaces a water molecule that is bonded to the iron in rsAPX (2.1 Å). This movement of the main chain of His-42 towards the heme in the “on” form and the subsequent alteration in the heme geometry are the consequences of the removal of the bulky Trp-41 side chain, which allows the His-42 side chain to ligate to the iron.

Examination of the electron density for W41A around His-42 indicates that there is positive  $F_o - F_c$  density above His-42 and also close to the main chain of His-42 (carbonyl oxygen, Figure [2.9]). This density overlays with the orientation of His-42 in rsAPX and is consistent with the presence of a minority (presumed high-spin) heme species in which His-42 is not ligated.

#### **2.2.4.4 Cyanide and nitric oxide derivatives of rsAPX and W41A**

In both the rsAPX-cyanide and rsAPX-nitric oxide structures, the ligand fills the sixth coordination site of the iron (Figure [2.10A,C]), with the cyanide or nitric oxide molecule replacing two of the water molecules from the rsAPX structure upon binding. In the rsAPX-cyanide structure (Figure [2.10A]), the nitrogen of the cyanide molecule is hydrogen bonded to His-42 (2.5 Å) and a water molecule (2.9 Å) which in turn is hydrogen bonded to Arg-38 (3.1 Å). In the rsAPX-nitric oxide structure (Figure [2.10C]), the nitrogen atom of the nitric oxide molecule is hydrogen bonded to Trp-41 (2.9 Å) and the oxygen atom is hydrogen bonded to His-42 (2.9 Å) and a water molecule (2.6 Å). This water molecule is in turn hydrogen bonded to Arg-38 (2.9 Å). The iron-nitrogen bond in the rsAPX-nitric oxide structure is 1.7 Å and the iron-carbon bond in the rsAPX-cyanide structure is 1.5 Å. In the rsAPX-nitric oxide structure the Fe-N-O angle is 130° and in the rsAPX-cyanide structure the Fe-C-N angle is 170°.

The crystal structure of the cyanide-bound derivative of W41A (Figure [2.10B]) confirms the observations made in solution. The structure closely maps onto that for the cyanide-bound form of rsAPX (Figure [2.10A]), the iron is ligated by the cyanide ligand in a tilted mode (Fe-CN distance: 2.0 Å, Fe-C-N angle: 163°) and the nitrogen of the bound ligand is hydrogen bonded (2.8 Å) to N<sup>ε</sup> of His-42 (2.5 Å in rsAPX). For

the W41A-cyanide complex, the electron density observed for the proximal His-163 residue is consistent with two orientations of this side chain (Figure [2.10B]). One orientation has His-163 hydrogen bonded to Asp-208 (3.3 Å) as for rsAPX (3.1 Å); the other orientation has His-163 hydrogen bonded (2.8 Å) to the backbone carbonyl of Ser-160 (3.8 Å). In the rsAPX-cyanide structure a single conformation of His-163 is observed however, the data are at lower resolution (2.0 Å compared with 1.4 Å), and a second orientation for the proximal histidine may not be observed because of the large effect of the electron density.

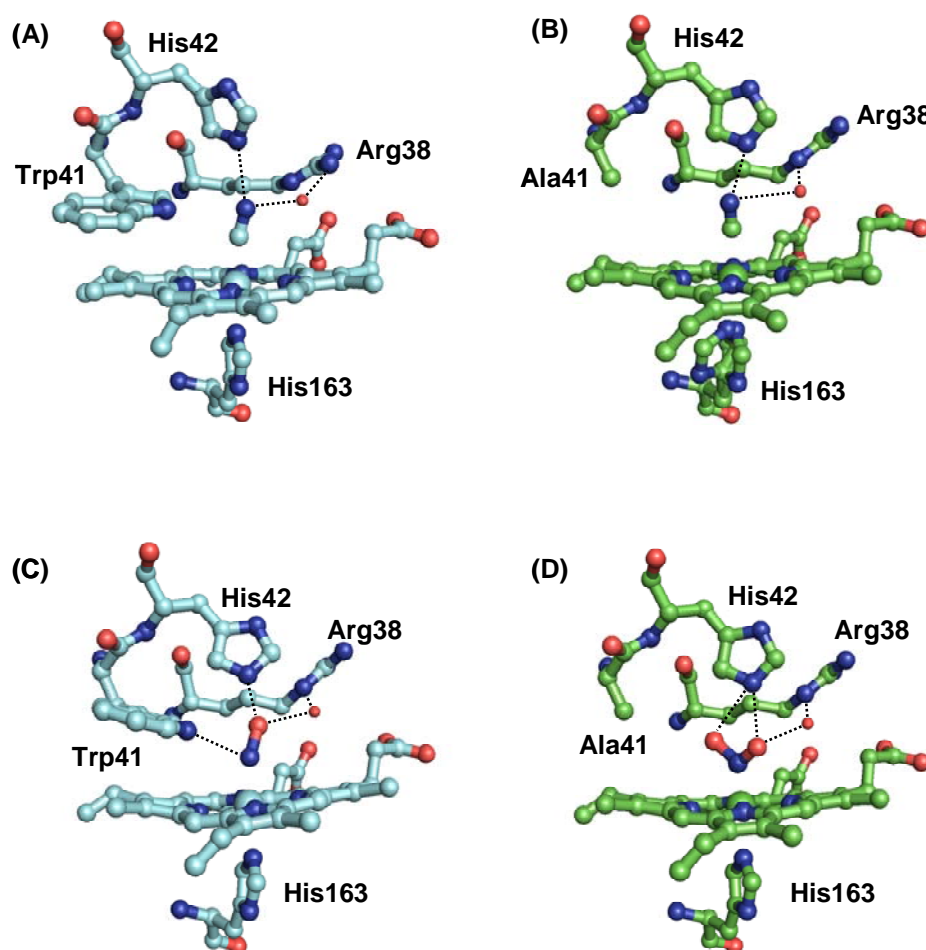


Figure [2.10]: (A) and (B) structures of the cyanide-bound complexes of rsAPX (A) and W41A (B) showing coordination of the diatomic ligand to the heme. For W41A, there are two orientations of His-163 observed. (C) and (D) structures of the nitric oxide-bound complexes of rsAPX (C) and W41A (D) in the region of the active site. The loss of the indole of Trp-41 in W41A allows the nitric oxide molecule to adopt two orientations. Hydrogen bonds are shown as black dotted lines and water molecules are shown as red spheres.

The crystal structure of the nitric oxide-bound derivative of W41A also confirms that His-42 is displaced (Figure [2.10D]). In this case, and in contrast to rsAPX-nitric oxide (Figure [2.10C]), removal of the hydrogen bond to Trp-41 means that the nitric oxide ligand now adopts two conformations (Fe-NO distance: 1.80 Å, Fe-N-O angle: 129°). In one conformation the oxygen of the nitric oxide ligand is hydrogen bonded to His-42 and in the other conformation the oxygen is hydrogen bonded to Arg-38 via a water molecule as well as His-42. Nitric oxide binds to the heme in rsAPX and W41A in a bent manner.

#### 2.2.4.5 Structural evidence for mobility of His-42 during catalysis in W41A

As the low-spin W41A protein was found to exhibit flexibility in its distal pocket, its ability to react with H<sub>2</sub>O<sub>2</sub> was tested. Crystals of rsAPX and W41A were soaked in H<sub>2</sub>O<sub>2</sub> (0.1 M H<sub>2</sub>O<sub>2</sub> in mother liquor) for five minutes. The overall structure of H<sub>2</sub>O<sub>2</sub>-soaked W41A crystal (Figure [2.8]), including most of the active site region, is very similar to both ferric W41A (root-mean-square deviation between C $\alpha$  positions is 0.179 Å) and to ferric rsAPX (0.10 Å), but in comparison with the ferric W41A structure there were local changes in conformation around His-42 (Figure [2.11]).

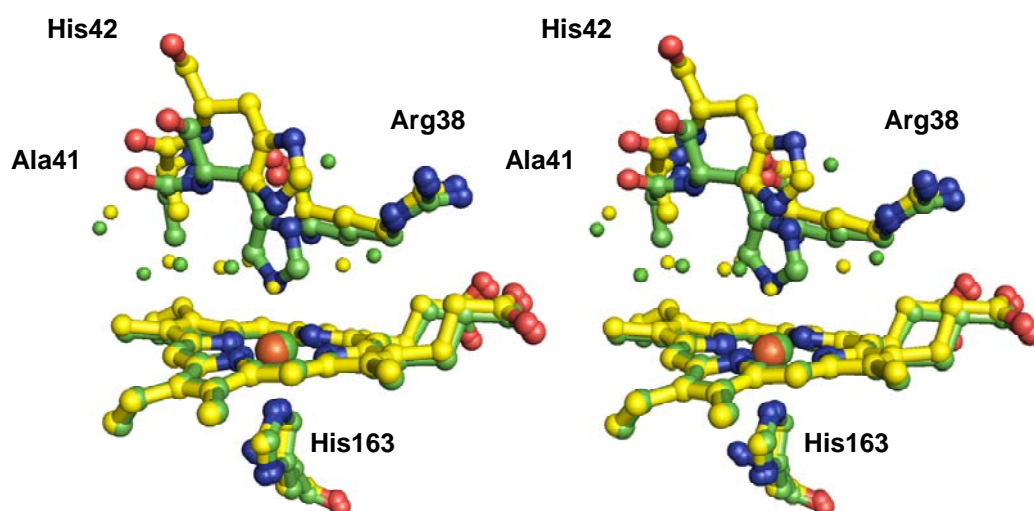
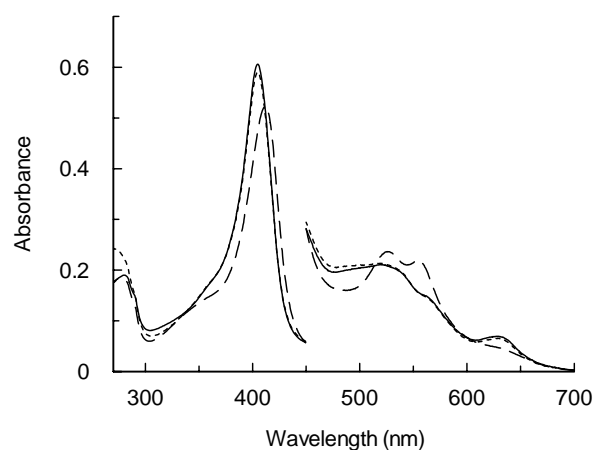


Figure [2.11]: A stereo view of the overlay of the structure of (light-green) ferric W41A and (yellow) ferric W41A after reaction with H<sub>2</sub>O<sub>2</sub>. Water molecules in the two structures are shown in light-green and yellow, respectively. The orientation of His-42 after reaction with H<sub>2</sub>O<sub>2</sub> (yellow) overlays with that of rsAPX (see Figure [2.9B]).

Hence, His-42 now swings off the iron to occupy a position that is identical to that observed in the ferric rsAPX structure. Clear electron density is observed directly above the iron in a region that for ferric rsAPX (15), as well as for other peroxidases, has been assigned as a water molecule (Figure [2.11]). The distance between the iron and this distal water molecule is very similar (2.2 Å) to that observed in ferric rsAPX (2.1 Å). The rsAPX-H<sub>2</sub>O<sub>2</sub> structure revealed no evidence of density relating to oxygen being bound at the distal cavity.

The heme geometry observed in the structure of H<sub>2</sub>O<sub>2</sub>-soaked W41A, in which His-42 swings off the heme, is different from the majority of low-spin species observed spectroscopically at both room temperature (electronic spectra) or cryogenic temperatures (EPR spectra and electronic spectra of the ferric W41A crystal during data collection, see Chapter 3, Section 3.2.3) or from that observed in the crystal structure of the ferric derivative. Thus, solution experiments were conducted, on a timescale identical to that of the crystallography experiments, to authenticate the nature of the heme species observed. Hence, ferric W41A was reacted with H<sub>2</sub>O<sub>2</sub> (varied from 1-100 equivalents), and the spectrum was collected immediately. This spectrum (Figure [2.12]) shows clear evidence for formation of a Compound II intermediate ( $\lambda_{\text{max}}/\text{nm} = 410, 534, 571^{\text{sh}}$  and 640).



**Figure [2.12]:** Electronic spectrum of ferric W41A (5  $\mu\text{M}$ ) prior to the addition of H<sub>2</sub>O<sub>2</sub> (solid line), ferric W41A immediately after reaction with 1 equivalent of H<sub>2</sub>O<sub>2</sub> (dashed line) and ferric W41A after reaction with 1 equivalent of H<sub>2</sub>O<sub>2</sub> followed by the addition of 1 equivalent of ascorbate (dotted line). The visible region has been multiplied by a factor of 5. Conditions: sodium phosphate, pH 7.0,  $\mu = 0.1 \text{ M}$ , 25.0 °C.

This Compound II species persisted for >15 minutes in W41A; subsequent reduction by ascorbate gave a spectrum that was essentially identical to the original ferric low-spin heme species (*i.e.* predominantly bis-histidine ligated). This is interpreted as evidence for reversibility between the “on” and “off” forms and is consistent with the kinetic data discussed in Sections 2.2.5 and 2.2.6. Similar changes were observed when these experiments were conducted under crystallographic conditions, 0.1 M HEPES pH 8.3, 2.25 M lithium sulphate.

In separate control experiments in the absence of ascorbate (Figure [2.13]), the spectrum of Compound II decayed over approximately 60 minutes to a species that resembles the original low-spin ferric form but had a slightly lower absorbance in the Soret region (probably due to partial heme degradation over long timescales).

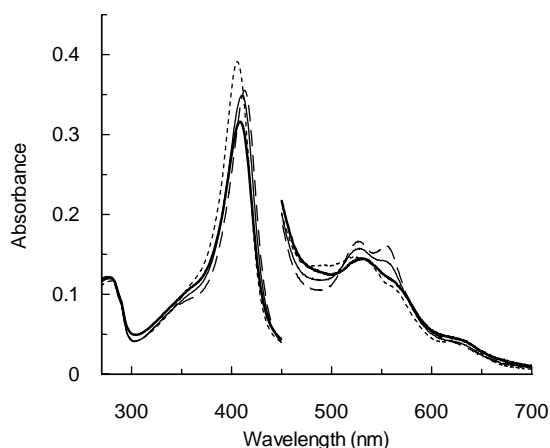


**Figure [2.13]:** Electronic spectrum of ferric W41A (3  $\mu\text{M}$ ) prior to the addition of  $\text{H}_2\text{O}_2$  (dotted line) and ferric W41A immediately after reaction with 2 equivalents of  $\text{H}_2\text{O}_2$  (dashed line) and after five and 60 minutes after reaction with 2 equivalents of  $\text{H}_2\text{O}_2$  (solid and heavy solid line, respectively). The visible region has been multiplied by a factor of 5. Conditions: sodium phosphate, pH 7.0,  $\mu = 0.1 \text{ M}$ , 25.0  $^\circ\text{C}$ .

## 2.2.5 Steady state kinetics of W41A

### 2.2.5.1 Ascorbate assays

Steady state oxidation of ascorbate by rsAPX exhibits sigmoidal kinetics (see Chapter 6, Section 6.5) whereas the reaction catalysed by W41A revealed hyperbolic kinetics and the data in this case were fitted to the Michaelis-Menten equation (Equation [2.1]), where  $v$  is the initial rate,  $V_{\max}$  is the maximum velocity;  $K_m$  is the substrate concentration at half the maximal rate and  $[S]$  is the substrate concentration.

$$v = \frac{V_{\max} [S]}{K_m + [S]} \quad (\text{Eq. [2.1]})$$

A least squares fit of the steady state data to the Michaelis-Menten equation is shown in Figure [2.14] for the W41A-ascorbate assay, and the following values were obtained:  $k_{\text{cat}} = 371 \pm 7.8 \text{ s}^{-1}$ ,  $K_m = 254 \pm 16 \text{ }\mu\text{M}$ ,  $k_{\text{cat}}/K_m = 1.46 \text{ }\mu\text{M}^{-1} \text{ s}^{-1}$ , which are comparable to the data obtained for rsAPX:  $k_{\text{cat}} = 272 \text{ s}^{-1}$ ,  $K_m = 389 \text{ }\mu\text{M}$ ,  $k_{\text{cat}}/K_m = 0.69 \text{ }\mu\text{M}^{-1} \text{ s}^{-1}$  (9). The hyperbolic dependence of ascorbate oxidation by W41A may arise from changes in cooperativity within the enzyme due to structural rearrangements in the variant.

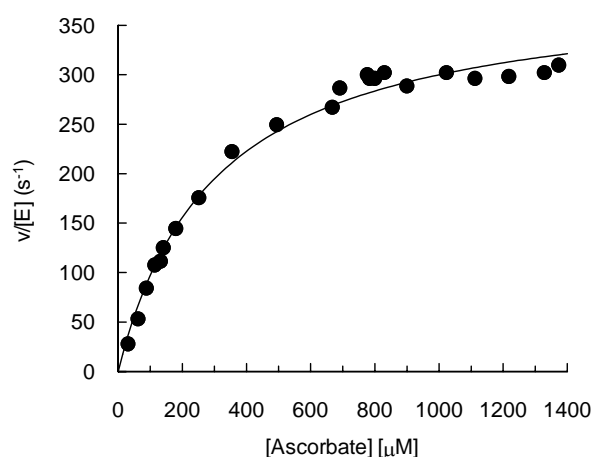


**Figure [2.14]:** Steady state oxidation of ascorbate by W41A. Solid line shows a fit of the data to the Michaelis-Menten equation (Equation [2.1]). Conditions: sodium phosphate buffer, pH 7.0,  $\mu = 0.10 \text{ M}$ ,  $25.0 \text{ }^\circ\text{C}$ .

### 2.2.5.2 Guaiacol assays

Steady state oxidation of guaiacol by rsAPX and W41A showed a hyperbolic dependence on guaiacol concentration and data were fitted to the Michaelis-Menten equation (Equation [2.1]). A least squares fit of the W41A-guaiacol steady state data to the Michaelis-Menten equation is shown in Figure [2.15] and gave the following steady state parameters:  $k_{\text{cat}} = 78 \pm 2 \text{ s}^{-1}$ ,  $K_{\text{m}} = 1.3 \pm 0.09 \text{ mM}$ ,  $k_{\text{cat}}/K_{\text{m}} = 61 \text{ mM}^{-1} \text{ s}^{-1}$ .

The W41A variant exhibited a ~10-fold increase in  $K_{\text{m}}$  for the aromatic substrate guaiacol ( $K_{\text{m}} = 1.3 \text{ mM}$  and  $12.9 \text{ mM}$  (9) for W41A and rsAPX, respectively) in comparison to rsAPX, but no change in  $k_{\text{cat}}$  was observed ( $k_{\text{cat}} = 78 \text{ s}^{-1}$  and  $68 \text{ s}^{-1}$  (9) for W41A and rsAPX, respectively). This almost certainly arises from the larger hydrophobic pocket that has been created in the W41A variant by removal of the bulky Trp-41 residue, which can accommodate the aromatic substrate guaiacol.

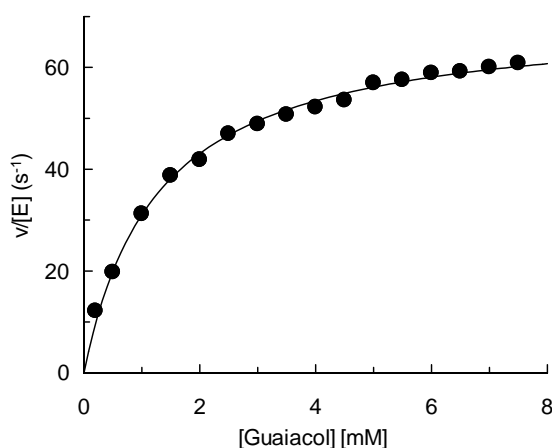


**Figure [2.15]:** Steady state oxidation of guaiacol by W41A. Solid line shows a fit of the data to the Michaelis-Menten equation (Equation [2.1]). Conditions: sodium phosphate buffer, pH 7.0,  $\mu = 0.10 \text{ M}$ ,  $25.0 \text{ }^\circ\text{C}$ .

## 2.2.6 Transient state kinetics

Catalysis in peroxidases occurs via the intermediates Compound I and Compound II, as shown in Equations [1.3]-[1.5] in Chapter 1, Section 1.5.3, and in the case of APX the reducing power of ascorbate is utilized as the substrate. The kinetic properties for the W41A variant discussed in this Chapter were measured as described in Chapter 6, Section 6.6.

### 2.2.6.1 Spectra of rsAPX and W41A oxidized intermediates Compound I and II

The reaction of W41A with  $\text{H}_2\text{O}_2$  was studied using the photodiode array detector (PDA) of the stopped-flow apparatus (Figure [2.16]). Data collected over a period of 500 ms were best fitted to a two step model ( $A \rightarrow B \rightarrow C$  as shown previously for rsAPX) (9), where  $A$  is ferric W41A,  $B$  is Compound I, and  $C$  is Compound II. Spectra for the Compound I and Compound II intermediates of W41A are in agreement with those observed for rsAPX and the wavelength maxima of the oxidised species for the W41A variant and rsAPX are listed in Table [2.3]. Formation of Compound I (*i.e.*  $A \rightarrow B$ ) for W41A occurs with an observed rate constant ( $k_{1,\text{obs}}$ ) of  $26 \pm 0.2 \text{ s}^{-1}$ , which is  $\sim 10$  fold slower than that observed for rsAPX ( $k_{1,\text{obs}} = 218 \pm 2.6 \text{ s}^{-1}$ ) (9).

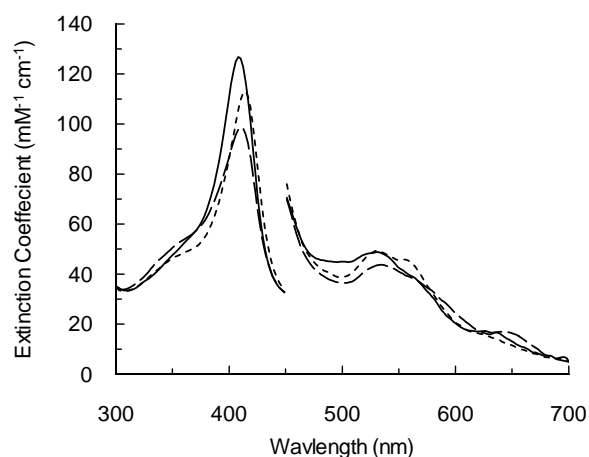


**Figure [2.16]: (A) Deconvoluted spectra for the reaction of W41A with  $\text{H}_2\text{O}_2$  showing ferric W41A (solid line) and oxidised intermediates Compound I (dashed line) and Compound II (dotted line). The data were fitted to a two-step model ( $A \rightarrow B \rightarrow C$ ) the visible region has been multiplied by a factor of 5. Conditions: sodium phosphate, pH 7.0,  $\mu = 0.10 \text{ M}$ ,  $5.0 \text{ }^\circ\text{C}$ .**

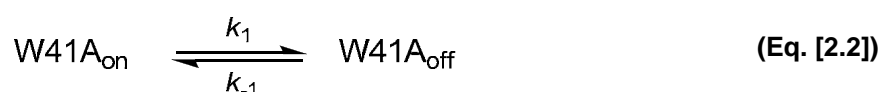
**Table [2.3]: Comparison of wavelength maxima (nm) of the catalytic intermediates Compound I and Compound II for rsAPX (9) and W41A. Conditions: sodium phosphate, pH 7.0,  $\mu = 0.10$  M, 5.0 °C. (<sup>sh</sup> denotes unresolved shoulder).**

	rsAPX	W41A
<b>Ferric</b>	407, 525, ~630	405, 525, 564, 630
<b>Compound I</b>	409, 530, 569 <sup>sh</sup> , 655	410, 530, 569 <sup>sh</sup> , 640
<b>Compound II</b>	417, 529, 560 <sup>sh</sup>	414, 530, 560 <sup>sh</sup>

Formation of Compound II (*i.e.*  $B \rightarrow C$ ) occurs with similar rate constants for both W41A and rsAPX ( $k_{2,obs} = 3.8 \pm 0.05$  and  $2.7 \pm 0.1$  s<sup>-1</sup> (9), respectively). These data clearly indicate that reaction of ferric W41A with H<sub>2</sub>O<sub>2</sub> leads to the formation of genuine Compound I and Compound II intermediates, as observed for rsAPX, and suggests that conformational rearrangement of the protein is involved during catalysis.

### 2.2.6.2 Formation of Compound I

The rate constant for Compound I formation  $k_{1,obs}$  in rsAPX is linearly dependent on H<sub>2</sub>O<sub>2</sub> concentration and is very fast ( $3.3 \pm 0.1 \times 10^7$  M<sup>-1</sup> s<sup>-1</sup>) (9). In contrast to rsAPX non-linear dependence of Compound I formation  $k_{1,obs}$  on the concentration of H<sub>2</sub>O<sub>2</sub> (Figure [2.17]) was apparent in W41A. This non-linear dependence is consistent with a mechanism that requires a conformational change of the protein, proposed to be conversion between the “on” and “off” forms, prior to reaction with H<sub>2</sub>O<sub>2</sub>, as shown in Equations [2.2] - [2.3].



In the presence of excess  $\text{H}_2\text{O}_2$ , the observed rate constant,  $k_{1,\text{obs}}$  can be expressed as follows (Equation [2.4]).

$$k_{1,\text{obs}} = \frac{k_1 k_1 [\text{H}_2\text{O}_2]}{k_{-1} + k_1 [\text{H}_2\text{O}_2]} \quad (\text{Eq. [2.4]})$$

A fit of these data for W41A to Equation [2.4] (Figure [2.17]), yields values for the limiting first-order-rate constant,  $k_1$ , of  $2370 \pm 229 \text{ s}^{-1}$  and the composite second-order-rate constant,  $k_1 k_1 / k_{-1}$ , of  $6.6 \times 10^6 \text{ M}^{-1} \text{ s}^{-1}$ .

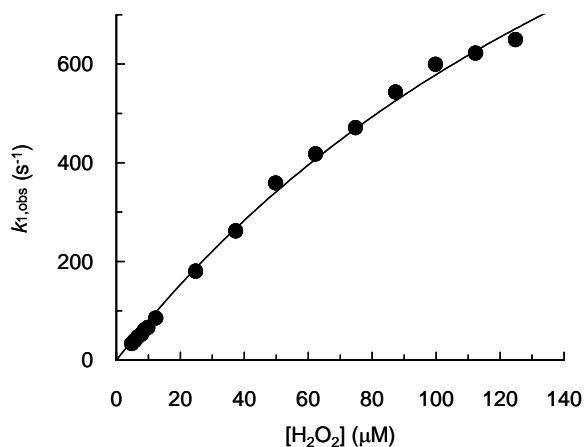


**Figure [2.17]:** Dependence of  $k_{1,\text{obs}}$ , the pseudo-first-order rate constant for W41A Compound I formation on  $\text{H}_2\text{O}_2$  concentration. Conditions: sodium phosphate, pH 7.0,  $\mu = 0.10 \text{ M}$ ,  $5.0 \text{ }^\circ\text{C}$ .

### 2.2.6.3 Reduction of Compound I

The second-order-rate constant for reduction of Compound I by ascorbate was determined as described in Chapter 6, Section 6.6.2. A linear dependence of  $k_{2,\text{obs}}$  on substrate concentration was observed for reduction of Compound I in W41A (as seen for rsAPX) (Figure [2.18]) and the second-order-rate constant  $k_2$  ( $2.6 \pm 0.15 \times 10^7 \text{ M}^{-1} \text{ s}^{-1}$ ), was obtained from the slope of this plot. This is comparable to the rate determined for Compound I reduction in rsAPX ( $5.2 \pm 0.3 \times 10^6 \text{ M}^{-1} \text{ s}^{-1}$ ) (9).

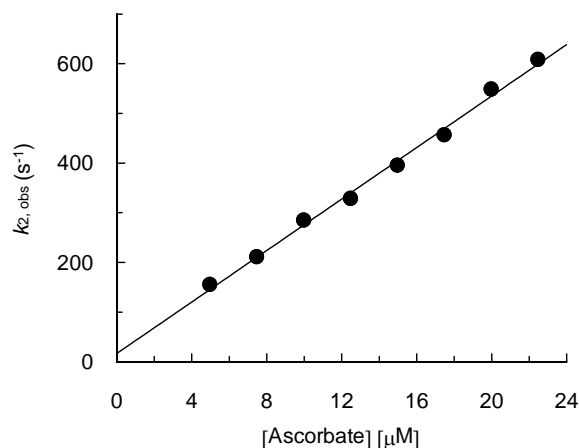


**Figure [2.18]:** Dependence of  $k_{2, \text{obs}}$ , the pseudo-first-order rate constant for reduction of Compound I in W41A on ascorbate concentration. Conditions: sodium phosphate, pH 7.0,  $\mu = 0.10 \text{ M}$ ,  $5.0 \text{ }^\circ\text{C}$ .

#### 2.2.6.4 Reduction of Compound II

Reduction of Compound II was measured as described in Chapter 6, Section 6.6.3. Plots of the pseudo-first-order rate constant,  $k_{3, \text{obs}}$  versus ascorbate concentration are non-linear (Figure [2.19]) and values for  $k_3$  and  $K_d$  were derived from a non-linear least squares fit of the data as described in Chapter 6, Section 6.6.3. The W41A variant was found to reduce Compound II at a faster rate than rsAPX, ( $k_3 = 1199 \pm 124 \text{ s}^{-1}$  and  $K_d = 544 \pm 92 \text{ } \mu\text{M}$  for W41A and  $k_3 = 67 \pm 11 \text{ s}^{-1}$  and  $K_d = 578 \pm 93 \text{ } \mu\text{M}$  for rsAPX) (9). However, both rsAPX and the variant exhibited the same affinity for substrate.

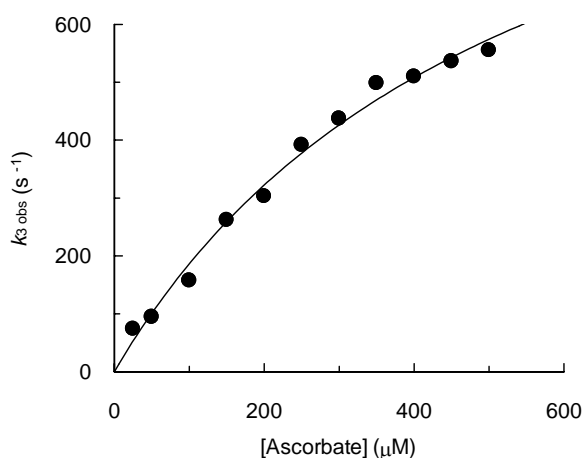


**Figure [2.19]:** Dependence of  $k_{3, \text{obs}}$ , the pseudo-first-order rate constant for reduction of Compound II in W41A on ascorbate concentration. Conditions: sodium phosphate, pH 7.0,  $\mu = 0.10 \text{ M}$ ,  $5.0 \text{ }^\circ\text{C}$ .

## 2.3 DISCUSSION

Conformational mobility of the distal histidine residue has been implicated for several different heme peroxidase enzymes (16-25), but unambiguous structural evidence is not available. In this chapter, mechanistic, spectroscopic, and structural evidence for H<sub>2</sub>O<sub>2</sub>- and ligand-induced conformational mobility of the distal histidine residue in the site-directed variant of APX (W41A) is described. In this variant, His-42 binds “on” to the heme in the oxidised form, duplicating the active site structure of the cytochromes *b* but, in contrast to the cytochromes *b*, is able to swing “off” the iron during catalysis. This conformational flexibility between the “on” and “off” forms is fully reversible and is used as a means to overcome the inherently unreactive nature of the “on” form toward H<sub>2</sub>O<sub>2</sub>, so that essentially complete catalytic activity is maintained. Contrary to the widely adopted view of heme enzyme catalysis, these data indicate that coordination of the distal histidine to the heme does not automatically undermine catalytic activity. The main findings in this Chapter are discussed below.

### 2.3.1 Heme electronic structure in W41A

The integrity of the W41A variant was authenticated using a variety of spectroscopic methods. Whilst the W41A DNA was sequenced without discovery of any spontaneous mutations, the integrity of the expressed variant was confirmed by MALDI-TOF spectrometry. The electronic absorption spectrum of W41A was found to differ in comparison to rsAPX (which is predominately five-coordinate high-spin) in that the W41A variant had a sharper Soret band at 405 nm and a transition at 564 nm which are both characteristic of low-spin heme. The calculated absorption coefficient from the heme content of W41A ( $\epsilon_{405} = 125 \text{ mM}^{-1} \text{ cm}^{-1}$ ) was greater than that of rsAPX ( $\epsilon_{407} = 107 \text{ mM}^{-1} \text{ cm}^{-1}$ ) (9). The sharp Soret peak at 405 nm, an extinction coefficient greater than  $100 \text{ mM}^{-1} \text{ cm}^{-1}$  and a characteristic low-spin transition at 564 nm are indicative of a six-coordinate/high-spin or six-coordinate/low-spin heme species (23). Similarly, low-spin signature peaks and high absorption coefficients were observed when the distal site aromatic residues, analogous to Trp-41 in APX, were mutated to an alanine residue in other heme peroxidases (CcP (W51A) and HRP (F41A)) (23,36). The W41A variant of rsAPX, W51A variant of CcP

and the F41A variant of HRP exhibit six-coordinate low-spin character. The nature of this low-spin character in the W41A variant of rsAPX and the W51A variant of CcP has been assessed using pH dependent studies. Spin state changes were observed in the W51A CcP variant upon variation of pH, where at low pH (pH 4) and high pH (pH 7) the variant was found to be predominantly low-spin, which was thought to arise from ligation of the distal histidine to the iron to form a bis-histidine heme species (20). Correspondingly, no evidence for formation of a hydroxide bound heme species was observed at alkaline pH in W41A of rsAPX; thus the low-spin species, as for W51A in CcP, was tentatively assigned as arising from coordination of an (internal) protein ligand, possibly His-42.

To assess whether the proposed protein ligand is reversibly or irreversibly bound to the iron in the variant, ferric W41A was reacted with various non-catalytic ligands. Low-spin heme was obtained on addition of cyanide to W41A as observed for rsAPX; also both W41A and rsAPX displayed similar spectral changes on addition of nitric oxide. Thus, the protein (internal) ligand was found to be displaced on addition of strong exogenous ligands. EPR spectroscopy further revealed that, in contrast to rsAPX, the EPR spectrum of W41A was dominated by low-spin heme species which was assigned to bis-histidine ligation of the heme. Similarly, low-spin heme signals also dominated the EPR spectrum of the W51A variant of CcP (36).

### **2.3.2 Crystallography: Evidence for displacement of His-42 by (a) exogenous ligands and (b) H<sub>2</sub>O<sub>2</sub>**

#### ***(a) Displacement of His-42 by exogenous ligands***

Diffraction of the highly ordered crystals of W41A revealed that the overall structure and most of the active site structure of the variant was similar to rsAPX, however local changes were observed around His-42. The main chain of His-42 was found to have moved closer to the heme such that His-42 was within bonding distance of the iron and this was termed the “on” form. Ligation of the distal histidine to the iron accounts for the low-spin species observed in the electronic spectrum of W41A. On further examination of the electron density around His-42 additional positive density was observed above and also close to the main chain of His-42. This density overlaid with the orientation of the distal histidine in rsAPX, consistent with

the presence of a minority high-spin species. A minority high-spin heme species was also observed in the electronic spectrum of W41A; hence the residual electron density arises from a mixed population of high- and low-spin iron in the crystal.

The ligated distal histidine was displaced on soaking crystals of W41A with cyanide or nitric oxide, thus the histidine is in the “off” form in the ligand bound structures. Cyanide was found to ligate to the iron in rsAPX and W41A in a tilted mode stabilised by hydrogen bonds from the distal site residues. A similar mode of cyanide binding was observed in the cyanide bound CcP, CPO, (37) HRP-CN-ferulic acid complex (38) and the cyanide complex of ARP (39).

The distal histidine was also displaced in W41A on addition of nitric oxide however, in contrast to rsAPX-nitric oxide; removal of the hydrogen bond to Trp-41 meant that the nitric oxide ligand was found to adopt two conformations. Similarly two conformations of binding nitric oxide were also observed in the nitric oxide bound CcP structure, these conformations were thought to arise from nitric oxide-Arg48 repulsion (40). Nitric oxide binds to the heme in rsAPX and W41A in a bent manner and this mode of binding is also observed in the nitric oxide complex of CcP, ARP and CPO (37,39,40).

### **(b) Displacement of His-42 by H<sub>2</sub>O<sub>2</sub>**

Despite the overall structure of the H<sub>2</sub>O<sub>2</sub>-soaked W41A crystal being similar to ferric W41A, local changes in conformation were observed around His-42. The distal histidine was displaced and was found to occupy the “off” position. Electron density was observed directly above the iron, which was initially assigned as a water molecule. To further examine the species formed on reaction of W41A crystal with H<sub>2</sub>O<sub>2</sub> solution studies were conducted. Reversibility between the “on” and “off” forms was observed during solution studies, where W41A was reacted with H<sub>2</sub>O<sub>2</sub> in the absence and presence of ascorbate. The initial Compound II species formed on reaction of W41A with H<sub>2</sub>O<sub>2</sub> was found to decay back over time (~60 minutes) to a species that resembled the original low-spin ferric form. A similar low-spin species was observed on addition of ascorbate to the oxidised Compound II species. However, no evidence for water bound/high-spin heme species was identified during solution studies conducted on a similar timescale as the crystallographic experiments. High-spin heme is easily identifiable because ferric (water bound)

rsAPX has a clear spectroscopic high-spin signature that is not observed for W41A, the crystallographic structure of W41A soaked in H<sub>2</sub>O<sub>2</sub> is therefore most sensibly rationalised as arising from a Compound II-derived structure. The iron-oxygen bond, at 2.2 Å, is longer than those previously reported for other Compound II intermediates (reported as 1.87 Å (41), 1.92 Å (42), 1.82 Å (43) and 1.8 Å (44)), which may reflect the fact that partial conversion back to the “on” form, as observed spectroscopically, has occurred.

### 2.3.3 Evidence for mobility of His-42 during catalysis

The data presented above is suggestive of a largely six-coordinate and low-spin heme species in ferric W41A (with two histidine ligands), in which His-42 is not irreversibly bound to the heme and is able to dissociate under certain conditions. To date there is no known example of a crystallographically defined bis-histidine-ligated peroxidase in the literature, thus it was of critical interest to establish whether axial ligation, analogous to that observed for example in the cytochromes *b*, would preclude reaction with substrate.

#### **(a) Steady state kinetics: oxidation of ascorbate and aromatic substrates**

The W41A variant catalysed the oxidation of ascorbate with similar efficiency as rsAPX; however, in contrast to rsAPX the variant displayed a hyperbolic dependence as opposed to sigmoidal dependence on ascorbate concentration. This difference could be because of structural rearrangement in the variant which may have affected the cooperativity within the enzyme.

The oxidation of guaiacol to tetraguaiacol by W41A and rsAPX occurred at a similar rate. However, the variant had a greater (~10-fold) affinity for the aromatic substrate, which is probably due to the presence of a larger hydrophobic pocket that has been created by removal of the bulky Trp-41 residue. Soaks of rsAPX and W41A crystals with guaiacol were attempted to obtain a structure of rsAPX/W41A-guaiacol complex, however this proved unsuccessful probably due to the limited solubility of guaiacol which affected the stability of the crystals (guaiacol needs to be dissolved in at least ~10 % ethanol to remain soluble). Soaks of W41A crystals with isoniazid (INH) revealed that this aromatic molecule binds in the hydrophobic cavity created upon removal of Trp-41 (45), further implicating that the  $\delta$ -heme edge is the site for

oxidation of aromatic substrates. The Trp-41 residue in APX has also been implicated in binding of the aromatic substrate analogue salicylhydroxamic acid close to the  $\delta$ -heme edge (46) (Chapter 1, Section 1.6.6).

It appears an increase in affinity for aromatic substrates is a general feature in peroxidases upon removal of the distal aromatic residue, because the W51A variant of CcP was found to bind various aromatic compounds (e.g. styrene and catechol) in the vicinity of the heme binding site with much greater affinity than wild type CcP (47). This significant increase in activity against aromatic substrates in Trp-51 CcP variants was rationalised by considering that the removal of the hydrogen bond between the Trp-51 and the ferryl oxygen atom will increase the affinity of the ferryl oxygen atom towards other hydrogen bond donors, either active site water molecules or phenol groups, thus making proton transfer from the aromatic substrate to the ferryl oxygen atom more efficient (48). Similarly, the F41A variant of HRP also exhibited an increased rate of oxidation of guaiacol in comparison to wild type HRP (12).

### **(b) Transient state kinetics**

Photodiode array experiments were conducted to observe the oxidised intermediates of W41A formed on reaction with  $\text{H}_2\text{O}_2$  and ascorbate. The spectrum of W41A Compound I, with a Soret maximum at 410 nm of reduced relative intensity, and additional wavelength maxima at 530, 560<sup>sh</sup> nm is similar to that of rsAPX. The W41A Compound I is reduced to form Compound II with wavelength maxima essentially identical to that reported previously for rsAPX.

Analysis of the second-order-rate constant,  $k_1$ , for formation of Compound I revealed that the W41A variant was competent for formation of Compound I as observed for rsAPX, albeit at a lower rate. The observed rate constants for this process,  $k_{1\text{obs}}$ , exhibited a clearly non-linear dependence on the concentration of  $\text{H}_2\text{O}_2$ . This is in contrast to the data for rsAPX, in which a linear dependence on  $\text{H}_2\text{O}_2$  was observed in the experimentally accessible concentration range. The non-linear dependence observed for W41A is consistent with a mechanism that requires a conformational change of the protein, proposed to be conversion between the “on” and “off” forms, prior to reaction with  $\text{H}_2\text{O}_2$ . A similar conformational mechanism of

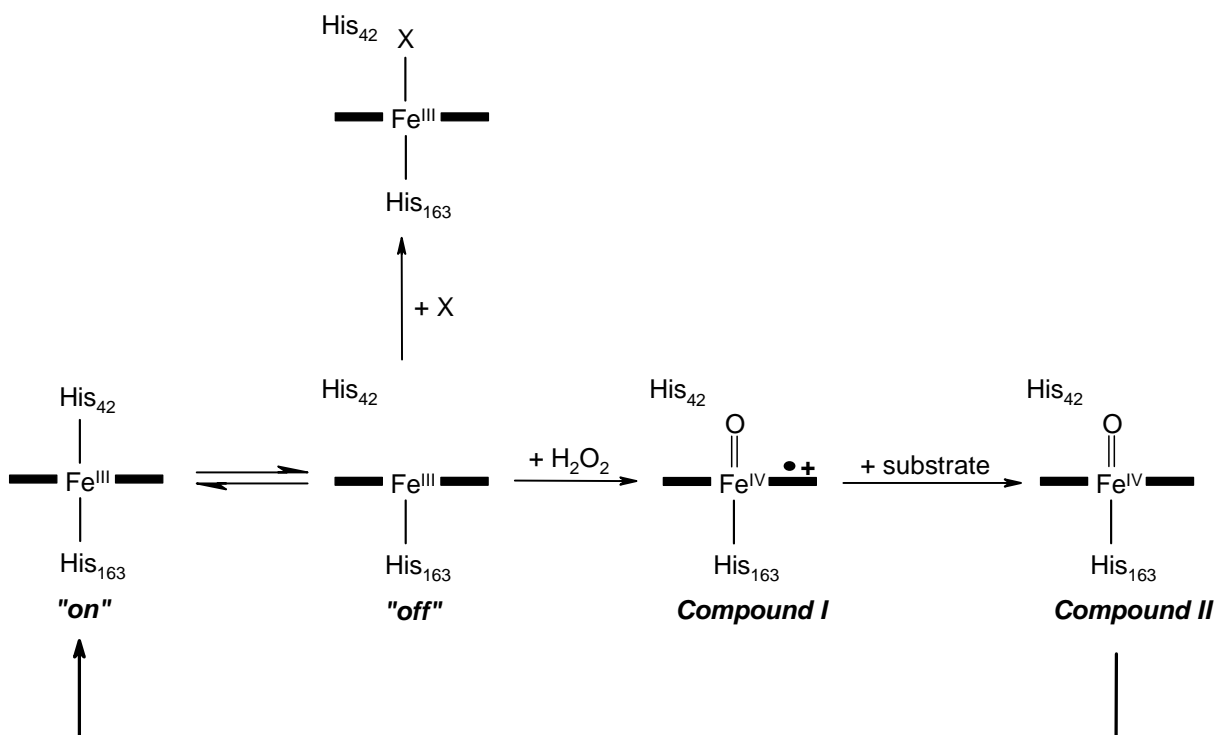
ligand exchange before reaction with  $\text{H}_2\text{O}_2$  was predicted to occur in the six-coordinate W51A variant of CcP (36).

Unlike the W41A variant, which reacted with  $\text{H}_2\text{O}_2$  at a slower rate in comparison to rsAPX, the F41A HRP (12) and W51A CcP (36) variants were able to catalyse the formation of Compound I at similar rates to the respective wild type enzymes. However, these experiments were performed at 25.0 °C, where some of the measured rates were close to the upper limit of the stopped-flow apparatus and some measurements were conducted under non-pseudo-first-order conditions.

Formation of Compound II in the W41A variant,  $k_2$ , was found to occur at a similar rate to that observed for rsAPX; however the mutant was found to undergo reduction of Compound II,  $k_3$ , at an elevated rate to that of rsAPX. This elevated rate may be due to changes in the heme environment in the oxidised state of W41A (electronic or structural) that have occurred upon removal of the distal tryptophan. The rate-limiting-step in peroxidase catalysis is known to be the reduction of Compound II,  $k_3$ , thus steady state turnover is a reflection of this rate constant. However, despite the rate for Compound II reduction in W41A being faster than rsAPX the steady state rates displayed by W41A are identical to that of rsAPX. This anomaly may be due to the “on” and “off” equilibrium in the variant, which is likely to be occurring at a slower rate than the rates ( $k_1$ ,  $k_2$ , and  $k_3$ ) measured on the stopped-flow (*i.e.* the conformational equilibrium is the rate-limiting-step during steady state catalysis).

## 2.4 SUMMARY

Collectively, the spectroscopic, mechanistic and crystallographic data presented here illustrate that removal of Trp-41 in APX leads to increased internal mobility of His-42 and clearly indicate that this residue can ligate to the heme in the oxidized derivative. The major findings are summarised in Scheme [2.1]. It appears that the role of the aromatic residue in APX as well as CcP (49) and HRP (23) is to maintain the heme iron coordination state and reactivity. Contrary to expectation, coordination of His-42 to the iron to form a bis-histidine-ligated heme does not preclude reaction with  $\text{H}_2\text{O}_2$  because His-42 is conformationally mobile and can reversibly interconvert between “on” and “off” forms to allow reaction with  $\text{H}_2\text{O}_2$  to occur normally. In this sense, W41A is able to act as a *bona fide* peroxidase because substrate binding at both the  $\gamma$ -heme edge (for ascorbate) and the  $\delta$ -heme edge (for aromatic substrates) is still possible.



**Scheme [2.1]:** Depicts the species observed in this work, showing His-42 in the “on” and “off” forms. X represents an exogenous ligand (e.g. cyanide). Conversion of Compound II back to the “on” form occurs either in the presence of substrate (*i.e.* during turnover) or, more slowly, in the absence of substrate.

These results therefore provide a new perspective on the widely-held view of heme enzyme catalysis in which strong axial ligation, as exemplified most famously in the cytochromes, is presumed to inhibit reaction with ligands at the heme iron. Reversible coordination of the distal histidine is also possible in some hemoglobins (50) and some heme-based sensors (51) (discussed in Chapter 1, Section 1.10), indicating that a similar mechanism for heme-catalysed biological activity might be used more widely in other, more complex heme enzymes.

## 2.5 REFERENCES

1. Zoller, M. J., and Smith, M. (1982) *Nucleic Acids Resonance* **10**, 6487-6493
2. Smith, A. T., and Veitch, N. C. (1998) *Current Opinion in Chemical Biology* **2**, 269-278
3. Erman, J. E., and Vitello, L. B. (1998) *Journal of Biochemistry and Molecular Biology* **31**, 307-327
4. English, A. M., and Tsaprailis, G. (1995) *Advances in Inorganic Chemistry* **43**, 79-125
5. Dunford, H. B. (1999) *Heme Peroxidases*, Wiley-VCH, New York, Chichester, Weinhein, Brisbane, Singapore, Toronto
6. Bosshard, H. R., Anni, H., and Yonetani, T. (1991) in *Peroxidases in Chemistry and Biology* (Everse, J., Everse, K. E., and Grisham, M. B., eds) Vol. 2, CRC Press, Boca Raton
7. Veitch, N. C., and Smith, A. T. (2000) *Advances in Inorganic Chemistry* **51**, 107-162
8. Lad, L. (2001) in *PhD Thesis in Chemistry*, University of Leicester, Leicester
9. Lad, L., Mewies, M., and Raven, E. L. (2002) *Biochemistry* **41**, 13774-13781
10. Lad, L., Mewies, M., Basran, J. S., Scrutton, N. S., and Raven, E. L. (2002) *European Journal of Biochemistry* **269**, 3182-3192
11. Macdonald, I. K., Badyal, S. K., Ghamsari, L., Moody, P. C. E., and Raven, E. L. (2006) *Biochemistry* **45**, 7808-7817
12. Newmyer, S. L., and Ortiz de Montellano, P. R. (1995) *Journal of Biological Chemistry* **270**, 19430-19438
13. Miller, M. A., Shaw, A., and Kraut, J. (1994) *Nature Structural Biology* **1**, 524-531

14. Finzel, B. C., Poulos, T. L., and Kraut, J. (1984) *Journal of Biological Chemistry* **259**, 13027-13036
15. Sharp, K. H., Mewies, M., Moody, P. C. E., and Raven, E. L. (2003) *Nature Structural Biology* **10**, 303-307
16. Cheek, J., Mandelman, D., Poulos, T. L., and Dawson, J. H. (1999) *Journal of Biological Inorganic Chemistry* **4**, 64-72
17. Sutherland, G. R. J., Zapanta, S., Tein, M., and Aust, S. D. (1997) *Biochemistry* **36**, 3654-3662
18. Smulevich, G., Miller, M. A., Kraut, J., and Spiro, T. G. (1991) *Biochemistry* **30**, 9546-9558
19. Vitello, L. B., Erman, J. E., Miller, M. A., Mauro, J. M., and Kraut, J. (1992) *Biochemistry* **31**, 11524-11535
20. Turano, P., Ferrer, J. C., Cheesman, M. R., Thomson, A. J., Banci, L., Bertini, I., and Mauk, A. G. (1995) *Biochemistry* **34**, 13895-13905
21. Youngs, H. L., Moenne-Loccoz, P., Loehr, T. M., and Gold, M. H. (2000) *Biochemistry* **39**, 9994-10000
22. Vitello, L. B., Erman, J. E., Miller, M. A., Wang, J., and Kraut, J. (1993) *Biochemistry* **32**, 9807-9818
23. Heering, H. A., Smith, A. T., and Smulevich, G. (2002) *Journal of Biochemistry* **363**, 571-579
24. Neri, F., Indiani, C., Baldi, B., Vind, J., Welinder, K. G., and Smulevich, G. (1999) *Biochemistry* **38**, 7819-7827
25. Henriksen, A., Welinder, K. G., and Gajhede, M. (1998) *Journal of Biological Chemistry* **273**, 2241-2248
26. Mittler, R., and Zilinskas, B. A. (1991) *Plant Physiology* **97**, 962-968

27. Smulevich, G. (1996) in *Plant Peroxidases: Biochemistry and Physiology* (Obinger, C., Burner, U., Ebermann, R., Penel, C., and Greppin, H., eds), Geneva
28. Smulevich, G., Mauro, J. M., Fishel, L. A., English, A. M., Kraut, J., and Spiro, T. G. (1988) *Biochemistry* **27**, 5477-5485
29. Smulevich, G., Paoli, M., Burke, J. F., Sanders, S. A., Thorneley, R. N. F., and Smith, A. T. (1994) *Biochemistry* **33**, 7398-7407
30. Jones, D. K., Dalton, D. A., Rosell, F. I., and Raven, E. L. (1998) *Archives of Biochemistry and Biophysics* **360**, 173-178
31. Gadsby, P. M., and Thomson, A. J. (1990) *Journal of American Chemical Society* **112**, 5003-5011
32. Murshudov, G. N., Vagin, A., A., and Dodson, E. J. (1997) *Acta Crystallographica Section D. Biological Crystallography* **53**, 240-255
33. Collaborative Computational Project, N. (1994) *Acta Crystallographica Section D-Biological Crystallography* **D50**, 760-763
34. Emsley, P., and Cowtan, K. (2004) *Acta Crystallographica Section D. Biological Crystallography* **60**, 2126-2132
35. Kabsch, W. (1976) *Acta Crystallographica Section A* **32**, 922-923
36. Goodin, D. B., Davidson, M. G., Roe, J. A., Mauk, A. G., and Smith, M. (1991) *Biochemistry* **30**, 4953-4961
37. Sundaramoorthy, M., Turner, J., and Poulos, T. L. (1998) *Chemistry & Biology* **5**, 461-473
38. Henriksen, A., Smith, A. T., and Gajhede, M. (1999) *Journal of Biological Chemistry* **274**, 35005-35011
39. Fukuyama, K., and Okada, K. (2007) *Acta Crystallographica Section D-Biological Crystallography* **D63**, 472-477

40. Edwards, S. L., and Poulos, T. L. (1990) *Journal of Biological Chemistry* **265**, 2588-2595
41. Bonagura, C. A., Bhaskar, B., Shimizu, H., Li, H., Sundaramoorthy, M., McRee, D. E., Goodin, D. B., and Poulos, T. L. (2003) *Biochemistry* **42**, 5600-5608
42. Hersleth, H. P., Dalhus, B., Gorbitz, C. H., and Andersson, K. K. (2002) *Journal of Biological Inorganic Chemistry* **7**, 299-304
43. Green, M. T., Dawson, J. H., and Gray, H. B. (2004) *Science* **304**, 1653-1656
44. Berglund, G. I., Carlsson, G. H., Smith, A. T., Szoke, H., Henriksen, A., and Hajdu, J. (2002) *Nature* **417**, 463-468
45. Metcalfe, C. L., Macdonald, I. K., Murphy, E. J., Brown, K. A., Raven, E. L., and Moody, P. C. E. (2007) *Journal of Biological Chemistry* **283**, 6193-6200
46. Sharp, K. H., Moody, P. C. E., Brown, K. A., and Raven, E. L. (2004) *Biochemistry* **43**, 8644-8651
47. Miller, V. P., Depillis, G. D., Ferrer, J. C., Mauk, A. G., and Ortiz de Montellano, P. R. (1992) *Journal of Biological Chemistry* **267**, 8936-8942
48. Wilming, M., Iffland, A., Tafelmeyer, P., Arrivoli, C., Saudan, C., and Johnsson, K. (2002) *ChemBiochem* **3**, 1097-1104
49. Smulevich, G. (1995) *Biochemical Society Transactions* **23**, 240-244
50. Trent, J. T., III, and Hargrove, M. S. (2002) *Trends in Plant Science* **8**, 387-393
51. Sasakura, Y., Yoshimura-Suzuki, T., Kurokawa, H., and Shimizu, T. (2006) *Accounts of Chemical Research* **39**, 37-43

***CHAPTER THREE***

**IRON OXIDATION STATE MODULATES ACTIVE SITE STRUCTURE  
IN A HEME PEROXIDASE**

## CHAPTER THREE

# IRON OXIDATION STATE MODULATES ACTIVE SITE STRUCTURE IN A HEME PEROXIDASE

---

### 3.1 INTRODUCTION

One of the most challenging questions in bio-inorganic chemistry has been to identify and understand the relationships that exist between different classes of heme proteins: that is, to rationalise the mechanisms by which the protein structure controls the specific chemical reactivity of the heme group (1,2). Traditionally, heme-containing proteins have been categorised into the oxygen transport proteins (the globins), the electron transfer proteins (the cytochromes) and the catalytic heme-containing enzymes (e.g. the cytochrome P450s, peroxidases *etc*). This categorisation conveniently differentiated the non-catalytic electron transfer proteins from the transport proteins and the catalytic enzymes, and it became clear that at least part of this differentiation arose from differences in heme coordination geometry. Hence, the electron transfer proteins contain six-coordinated heme groups, as a means of facilitating rapid electron transfer, whereas the transport proteins and the catalytic enzymes are most often found as five- or weakly six-coordinated heme structures to allow ligand binding or catalysis at the sixth site.

Over several years, a few examples have emerged in the literature of heme proteins that do not fit this categorisation. This was because these proteins actually switched their heme coordination geometry through conformational rearrangements

of the protein structure. Examples include cytochrome *c* (3), *Chlamydomonas* hemoglobin (4), cytochrome *cd*<sub>1</sub> (5), the di-heme cytochrome *c* peroxidase (6), the heme chaperone protein CcmE (7) and leghemoglobin (8). The trigger for these conformational rearrangements appeared to be, variously, pH, oxidation state of the iron, and the binding of ligands, substrate or other (non-catalytic) metal ions. Although these documented examples were significant in their own right, their collective significance was not immediately apparent. This was partly because a functional basis for the ligand switch could not be identified in all cases. Later on, further examples were published of conformational rearrangements in other regulatory heme proteins linked to, for example, gas-sensing processes, signalling and gene transcription (see Chapter 1, Section 1.10 and (9) for a recent review). It was only then that it started to become clear that conformational rearrangements associated with the heme group, its ligands/substrates and its oxidation state might actually be used more widely as a means of regulation and/or sensing in biology.

Currently, therefore, it appears that at least some heme protein architectures are intrinsically mobile, that this mobility can be triggered by redox changes or ligand/substrate binding, and that this trigger is used, in certain cases, as a link to more complex downstream biological processes. What is not yet clear is whether conformational mobility is a more general characteristic of other heme protein structures and whether these triggering mechanisms are more generally accessible in other protein structures.

In this context, work carried out in the previous Chapter (Chapter 2) reported an example of a six-coordinate heme peroxidase, the W41A variant of APX, which had bis-histidine coordination, like a cytochrome, but was catalytically active because the distal histidine was able to reversibly dissociate to form a five-coordinate heme in response to binding of H<sub>2</sub>O<sub>2</sub>. In an extension to this, work conducted in this Chapter shows this conformational movement can also be triggered by a change in oxidation state. Hence, crystallographic, spectroscopic and ligand binding data provide support for dissociation of His-42 from the iron in the ferrous form of W41A and structural evidence is also provided that is indicative of heme reduction occurring through formation of a reduced, bis-histidine-ligated species that subsequently decays by dissociation of His-42 from the heme. Collectively, the data provide clear evidence that conformational movement within the same heme active site can be controlled by both ligand binding (see Chapter 2) and metal oxidation state. These observations

are consistent with emerging data on other, more complex regulatory and gas sensing heme proteins in which heme plays a “passive” role.

## 3.2 RESULTS

### 3.2.1 Electronic absorption spectra of ferric and ferrous W41A

The electronic spectrum of the ferric and ferrous derivatives of rsAPX and W41A are shown in Figure [3.1]. The spectrum of the ferric derivative of W41A ( $\lambda_{\text{max}}/\text{nm}$  ( $\epsilon/\text{mM}^{-1} \text{cm}^{-1}$ ) = 405 (125), 525, 564 and 630) shows a peak in the visible region (564 nm) that is consistent with the presence of low-spin heme, Figure [3.1.B]. This distinguishes it from the spectrum of ferric rsAPX Figure [3.1.A], in which no low-spin peaks are observed ( $\lambda_{\text{max}}/\text{nm}$  ( $\epsilon/\text{mM}^{-1} \text{cm}^{-1}$ ) = 407 (107), 525 and  $\sim$ 630) (10). The low-spin component in W41A has been shown, crystallographically, to derive from coordination of the distal histidine (His-42) to the ferric heme (see Chapter 2).

In contrast, the spectra of the ferrous derivatives of rsAPX and W41A (Figure [3.1A,B]) are similar to each other ( $\lambda_{\text{max}}/\text{nm}$  = 430, 555 and 583<sup>sh</sup> for rsAPX;  $\lambda_{\text{max}}/\text{nm}$  = 428, 556 and 581<sup>sh</sup> for W41A), with both spectra being consistent with a reduced heme species. As reduced rsAPX is five coordinate, this suggests that in the dithionite-reduced form of W41A the His-42 ligand dissociates from the iron. The wavelength maxima for ferrous rsAPX in this study are identical to those obtained previously for native (11) and recombinant soybean APX (12).

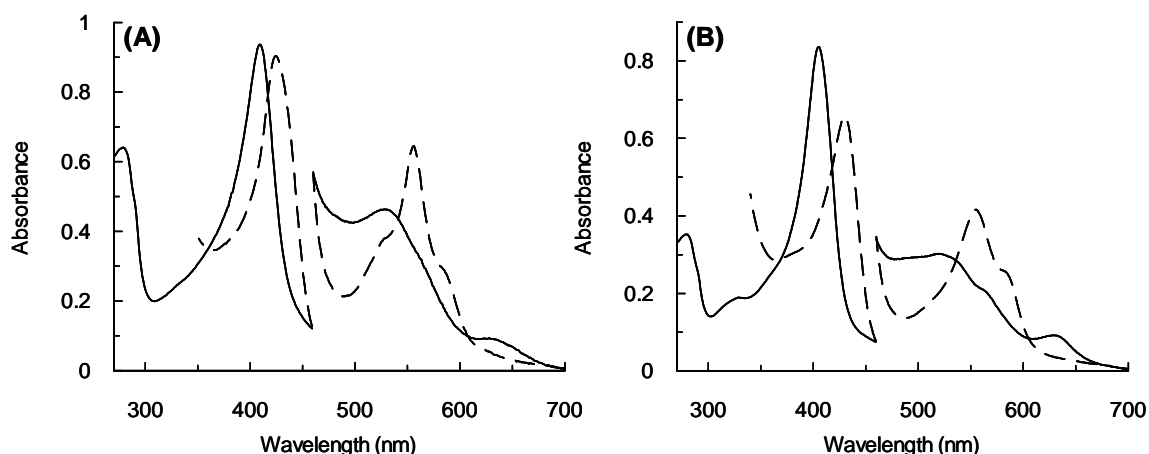


Figure [3.1]: Electronic spectra of (A) rsAPX and (B) W41A, showing the ferric (solid line) and ferrous (dashed line) species. The visible region has been multiplied by a factor of five. Conditions: sodium phosphate buffer, pH 7.0,  $\mu = 0.10 \text{ M}$ , 25.0 °C.

### 3.2.2 Ligand binding studies on W41A

Ligand binding studies were performed on rsAPX and W41A in the ferric and ferrous forms to evaluate the difference in affinity for ligands in the different redox states and provide further evidence for mobility of His-42 in W41A.

#### 3.2.2.1 Ligand binding in the ferric form of W41A

The electronic spectra of ferric rsAPX and W41A were altered in the presence of cyanide, indicative of the formation of a low-spin heme species with an apparent red-shift of the Soret band and disappearance of the charge transfer (CT<sub>1</sub>) band in the visible region (Figure [3.2]).

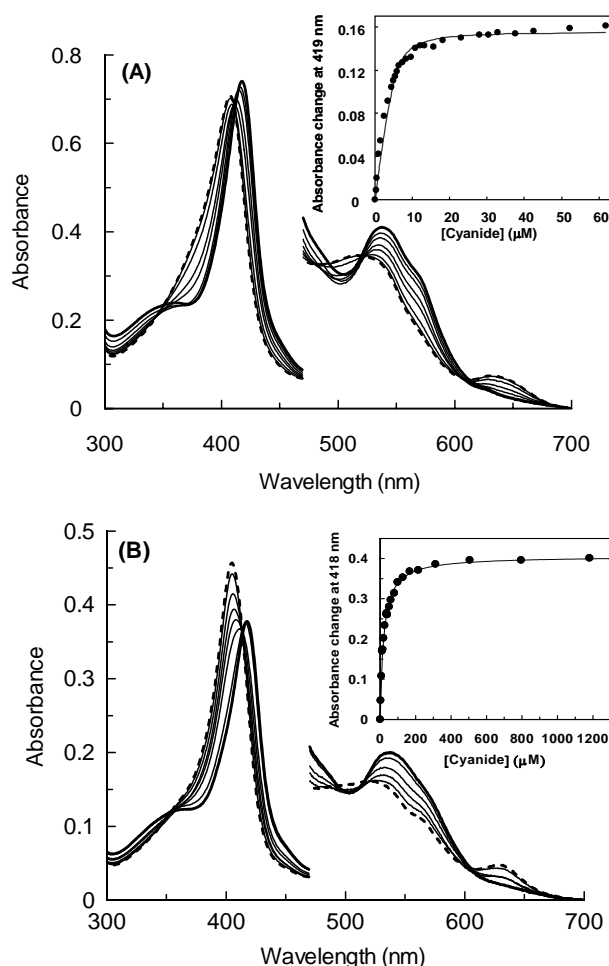


**Figure [3.2]:** Selected spectra collected during titration of ferric (A) rsAPX and (B) W41A with cyanide. Selected intermediate spectra between the initial spectrum (dashed line) and the final saturated spectrum (solid line) are shown as lines. The visible region has been expanded by a factor of five. Conditions: sodium phosphate buffer, pH 7.0,  $\mu = 0.10$  M, 25.0 °C. *Inset:* Shows the calculated fit of the experimental data to Equations [6.5, 6.6] (Chapter 6, Section 6.4.6) for determination of  $K_d$  values for rsAPX and W41A, respectively.

This is consistent with binding of cyanide at the sixth coordination site, as confirmed crystallographically in both cases (see Chapter 2). Absorption maxima for the ferric-cyanide derivatives of rsAPX and W41A are reported in Table [3.1]. Figure [3.2] shows a family of spectra collected during the titration of rsAPX and W41A with cyanide. Both enzymes were consistent with a 1:1 stoichiometric binding process, and showed well-defined isobestic points, indicating the presence of only two absorbing species (ferric enzyme and ferric-cyanide complex).

The absorbance changes at 418 nm for W41A were fitted to Equation [6.6] (Chapter 6, Section 6.4.6) and the equilibrium dissociation constant,  $K_d$ , calculated from the fit of these data are reported in Table [3.1]. Cyanide binding occurs with higher affinity in rsAPX than W41A in the ferric form, thus the absorbance changes at 419 nm for rsAPX were fitted to a quadratic equation (Equation [6.5], Chapter 6, Section 6.4.6).

**Table [3.1]: Wavelength maxima (nm) and equilibrium binding constants ( $K_d$ ) for formation of the ferric-cyanide (CN), ferrous-cyanide and ferric-azide ( $N_3$ ) complexes of rsAPX and W41A. Conditions: sodium phosphate buffer, pH 7.0,  $\mu = 0.10$  M, 25.0 °C. (<sup>sh</sup> denotes shoulder and \* denotes wavelength maxima less than 390 nm obscured by the dithionite absorption).**

	$\delta$	( $\gamma$ ) Soret	CT <sub>2</sub>	$\beta$	$\alpha$	CT <sub>1</sub>	$K_d$
<b>rsAPX</b>							
<b>Fe<sup>III</sup> - CN</b>	~360 <sup>sh</sup>	419	–	536	563 <sup>sh</sup>	–	0.73 ± 0.075 $\mu$ M
<b>Fe<sup>III</sup> - N<sub>3</sub></b>	~360 <sup>sh</sup>	412	528 <sup>sh</sup>		562 <sup>sh</sup>	630	0.40 ± 0.019 mM
<b>Fe<sup>II</sup> - CN</b>	*	426	–	529	560	–	0.31 ± 0.025 mM
<b>W41A</b>							
<b>Fe<sup>III</sup> - CN</b>	~365 <sup>sh</sup>	418	–	540	561 <sup>sh</sup>	–	20 ± 0.75 $\mu$ M
<b>Fe<sup>III</sup> - N<sub>3</sub></b>	~365 <sup>sh</sup>	415	538 <sup>sh</sup>		562 <sup>sh</sup>	630	3.80 ± 0.09 mM
<b>Fe<sup>II</sup> - CN</b>	*	426	–	530	560	–	1.50 ± 0.17 mM

A low-spin heme species was observed on addition of azide to rsAPX and W41A, Figure [3.3], absorption maxima for the ferric-azide derivatives are reported in

Table [3.1]. Both enzymes were consistent with a 1:1 stoichiometric binding process, and show well-defined isobestic points, indicating the presence of only two absorbing species (ferric enzyme and ferric-azide complex). The corresponding changes at 411.5 nm for rsAPX and 405 nm for W41A are consistent with Equation [6.6] (Chapter 6, Section 6.4.6), and the equilibrium dissociation constant,  $K_d$ , calculated from the fit of these data are reported in Table [3.1]. As above for cyanide binding, azide binding occurs with greater affinity in rsAPX than W41A in the ferric form. This reflects the coordination of His-42 to the heme in W41A.

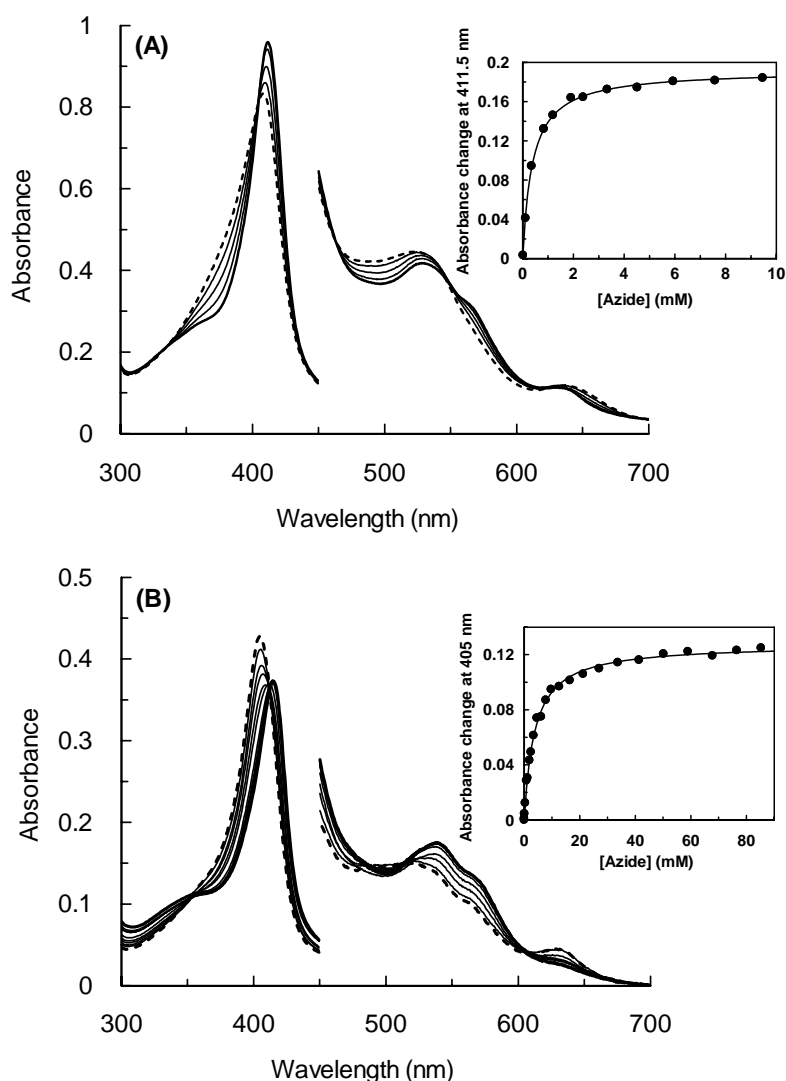


**Figure [3.3]:** Selected spectra collected during titration of ferric (A) rsAPX and (B) W41A with azide. Selected intermediate spectra between the initial spectrum (dashed line) and the final saturated spectrum (solid line) are shown as lines. The visible region has been expanded by a factor of five. Conditions: sodium phosphate buffer, pH 7.0,  $\mu = 0.10$  M, 25.0 °C. *Inset:* Shows the calculated fit of the experimental data to Equation [6.6] (Chapter 6, Section 6.4.6) for determination of  $K_d$  values.

### 3.2.2.2 Ligand binding in the ferrous form of W41A

Addition of cyanide to ferrous rsAPX and W41A led to formation of a six-coordinate ferrous heme species. The wavelength maxima of the low-spin ferrous cyanide species for rsAPX and W41A are reported in Table [3.1]. Figure [3.4] shows a family of spectra collected during the titration of ferrous rsAPX and ferrous W41A with cyanide.

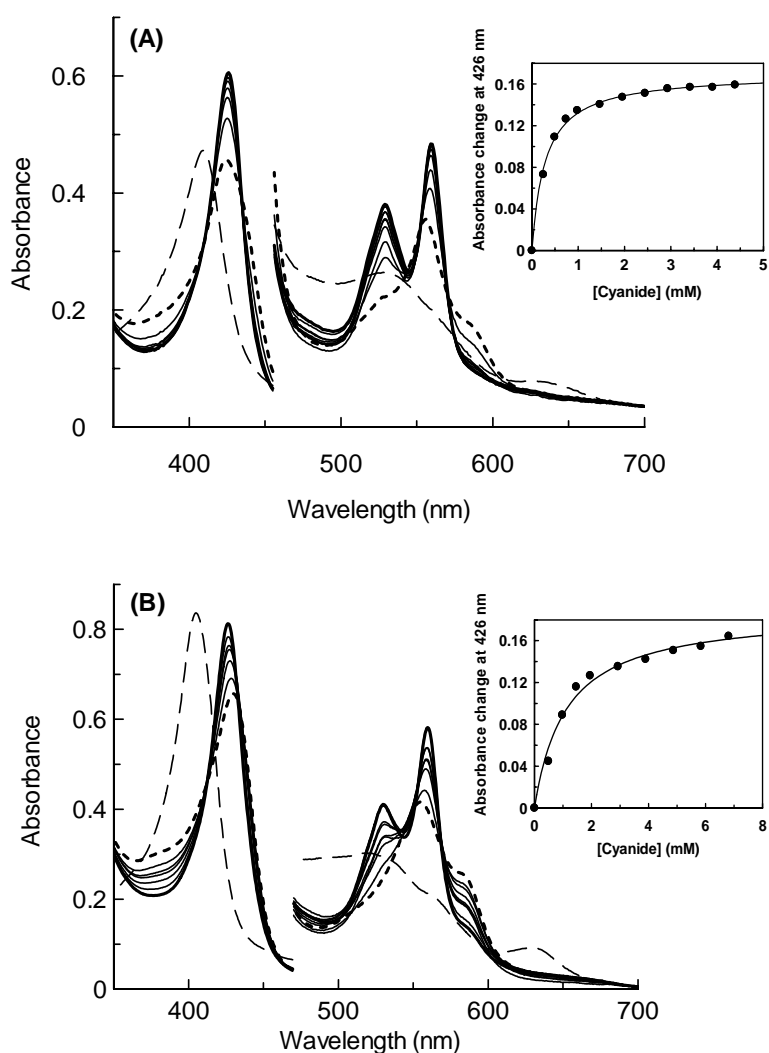


Figure [3.4]: Selected spectra collected during titration of ferrous (A) rsAPX and (B) W41A with cyanide. Intermediate spectra between the initial spectrum (solid dashed line) and the final saturated spectrum (solid line) are shown as lines. The ferric spectra of rsAPX and W41A are also shown (dashed line). The visible region has been expanded by a factor of five. Conditions: sodium phosphate buffer, pH 7.0,  $\mu = 0.10$  M, 25.0 °C. *Inset:* Shows the calculated fit of the experimental data to Equation [6.6] (Chapter 6, Section 6.4.6) for determination of  $K_d$  values.

Both enzymes were consistent with a 1:1 stoichiometric binding process, and show well-defined isobestic points, indicating the presence of only two absorbing species (ferrous enzyme and ferrous-cyanide complex). The corresponding changes at 426 nm are consistent with Equation [6.6] (Chapter 6, Section 6.4.6), and the equilibrium dissociation constant,  $K_d$ , calculated from the fit of these data are reported in Table [3.1]. In contrast to the ferric-ligand binding data above, cyanide binding to ferrous rsAPX and ferrous W41A occurs with similar affinity indicating that the coordination geometry in the reduced forms of rsAPX and W41A are the same (*i.e.* five-coordinate). The wavelength maxima for cyanide and azide binding for rsAPX in this study are essentially identical to those obtained previously for recombinant soybean APX (12).

### 3.2.3 Crystallography

Crystallisation of W41A was carried out as described in Chapter 6, Section 6.8. The crystal structure of ferric W41A (Figure [3.5A]), was found to differ from that of rsAPX (13) in that His-42 was found to be within bonding distance (2.3 Å, compared to 5.5 Å in rsAPX) of the iron, to give a six-coordinate heme structure. We referred to this as the “on” form (see Chapter 2).

Spectroscopic studies on the reduced form of W41A indicate that the reduced heme environment is similar to that of ferrous rsAPX (Section 3.2.1). To further probe the structural changes that occur on reduction with dithionite, crystal structure of dithionite-soaked W41A was determined.

#### 3.2.3.1 Interpretation and refinement of crystallographic data

The data collection and refinement for the crystal structures discussed in this chapter were conducted with assistance from Dr P. C. E. Moody (Department of Biochemistry, University of Leicester) and Dr C. L. Metcalfe (Department of Chemistry, University of Leicester). The structures in this chapter were refined from the 1.35 Å ferric W41A structure (PDB code: 2GGN). Several cycles of refinement using RefMAC5 (14) from the CCP4 suite (15) and manual rebuilding of the protein model using COOT (16) followed by addition of water molecules were carried out until the  $R_{\text{free}}$  and  $R_{\text{factor}}$  values converged. The data collection, processing and refinement statistics are presented in Table [3.2].

**Table [3.2]: Data collection and refinement statistics. Values for outer shells are given in parentheses. RMSD, root-mean-square deviation; PDB, Protein Data Bank.**

Statistics	Ferrous	Low-dose	High-dose
<b>Data collection</b>			
Resolution (Å)	45.83-1.30	46.03-2.00	37.80-1.60
Outer shell	(1.39-1.30)	(2.11-2.00)	(1.69-1.60)
Total observations	649696 (94551)	63697 (9264)	352976 (49343)
Unique reflections	63112 (9091)	17935 (2570)	34661 (4988)
$I/\sigma$	21.6 (4.3)	6.2 (0.9)	19.5 (3.1)
$R_{\text{merge}}$	0.09 (0.45)	0.026 (0.138)	0.086 (0.66)
Completeness (%)	99.9 (100)	99.7 (100)	100 (100)
<b>Refinement</b>			
$R_{\text{factor}}$	0.182	0.174	0.175
$R_{\text{free}}$	0.199	0.236	0.209
RMSD from ideal			
Angles (°)	1.117	1.507	1.152
Bonds (Å)	0.006	0.016	0.010
PDB code	2VNZ	2VO2	2VNX

### 3.2.3.2 Structure of ferrous W41A

Although the overall structure and most of the active site of dithionite-reduced W41A is similar to that of ferric W41A, there are local changes in protein conformation centred around His-42. The crystal structure of the dithionite-reduced form of W41A (Figure [3.5B], Table 3.2) reveals that His-42 is no longer bound to the iron and shows a water molecule in the active site (Fe-O bond distance of 2.12 Å). Hence the main chain of His-42 in ferrous W41A has moved away from the heme to a position analogous to that of His-42 in the structure of ferric rsAPX. We have referred to this conformation of His-42 as the “off” form. For the dithionite-reduced form of W41A, there is no additional density directly above the iron that correlates to

the histidine being ligated to the iron (*i.e.* in the “on” form); the only density is for the water molecule as described above.

Single-crystal microspectrophotometry was also used to monitor the dithionite-reduced crystal during exposure to the X-ray beam. The spectrum of the ferrous W41A crystal (Figure [3.6]) before data collection was found to be essentially identical to that observed in solution studies (see Figure [3.1B]). During data collection the dithionite-reduced crystal was unaffected by the X-ray beam and the spectrum of ferrous W41A on completion remained unaltered. Similarly, the spectrum of the dithionite-reduced crystal of HRP has been reported to be unaltered on exposure to X-ray beam (17).

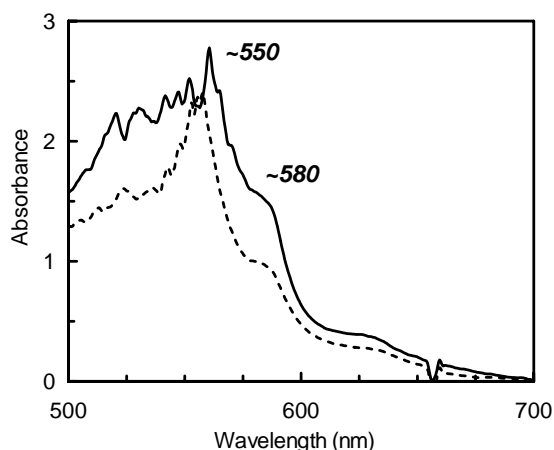


**Figure [3.6]:** The absorption spectrum (100 K) of a crystal of sodium dithionite-soaked (ferrous) W41A before (solid line) and after (dotted line) exposure to the X-ray beam.

### 3.2.3.3 Reduction of ferric W41A crystals during X-ray data collection

The crystal structures determined after exposure of ferric W41A to an attenuated low intensity X-ray source (low-dose) and the full intensity unattenuated X-ray source (high-dose) are shown in Figures 3.5C and D, respectively. The structure for the low-dose sample (Figure 3.5C) is similar to that of ferric W41A (Figure [3.5A]), in which His-42 is in the “on” position and within bonding distance (2.3 Å) of the iron and there is no additional density above the heme corresponding to the “off” position for His-42. In contrast, for the high-dose structure there is positive  $F_o - F_c$  density above His-42, near the main chain of His-42 and close to the “off” position (Figure [3.5D]). This second conformation (which is not observed at low X-ray doses Figure [3.5C]) was refined placing His-42 in an orientation identical to that

of His-42 in the dithionite-reduced ferrous structure of W41A (Figure [3.5B]). The occupancies of the two conformations were estimated to be 0.3 for the “off” form and 0.7 for the “on” form and included in the final stages of refinement; the resulting electron density is shown in Figure [3.5D]. Thus, on exposure to the high-dose beam the ferric W41A crystal is reduced and His-42 is observed to partially move away from the iron on reduction.

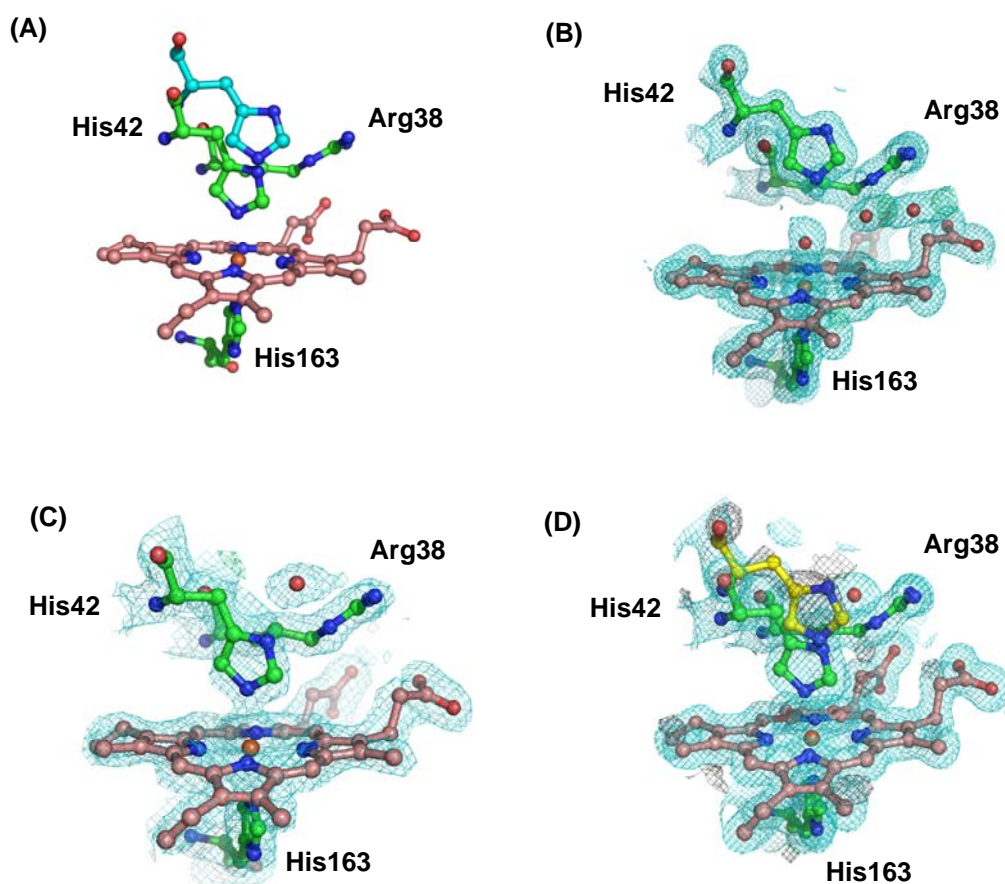
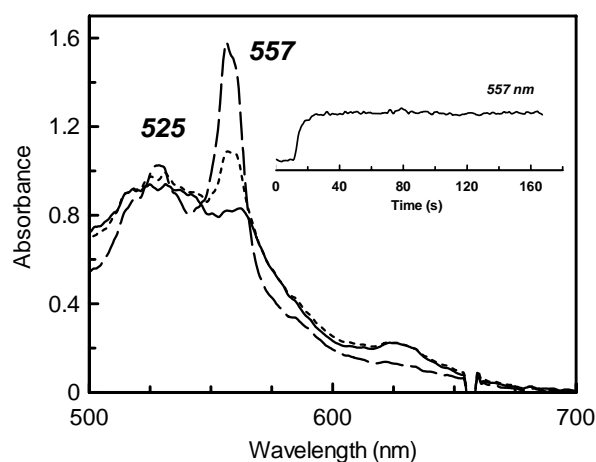


Figure [3.5]: (A) Structural alignment of the active sites of rsAPX (in blue, PDB code: 1OAG) (13) and W41A (in green), showing the orientation of His-42 in the “off” and “on” positions, respectively. (B) Structure of W41A after reduction by dithionite, showing His-42 in the “off” position. (C) Structure of W41A after exposure to low-intensity irradiation. (D) Structure of W41A after exposure to high-intensity irradiation showing the dual occupancy of His-42. The SigmaA-weighted  $2F_o - F_c$  electron density at  $1\sigma$  is shown in blue. The “off” position of His-42 is coloured yellow (modelled with an occupancy of 0.3), and the “on” position of His-42 is coloured green (modelled with an occupancy of 0.7). The positive SigmaA-weighted  $F_o - F_c$  electron density at  $3\sigma$  is shown in grey. Water molecules are shown as red spheres in all cases.

In parallel experiments, single-crystal microspectrophotometry was used to observe changes in the electronic spectrum of the ferric W41A crystal that correspond to the structures presented in Figure [3.5C,D]. The initial spectrum of the ferric W41A crystal at 100 K (Figure [3.7]) before exposure to the beam is the same as that observed in solution at room temperature (Figure [3.1B]), indicating that the species in solution and in the crystal are similar, thus providing evidence that the ligation of the distal histidine to the heme in W41A is not a crystallographic artefact

When the ferric W41A crystal was exposed to a low-intensity beam, an increase in absorbance at 525 and 557 nm (close to the absorption maximum for the ferrous derivative, Figure [3.1B]) was observed (Figure [3.7]). Note, however, that no additional density was observed for His-42 in the “off” position in the corresponding structure of this species (Figure 3.5C), indicating that under these conditions His-42 is not yet dissociated from the iron even though a significant population of the heme groups have been reduced by the X-ray beam, as evidenced by the change in absorbance at 557 nm.



**Figure [3.7]:** Changes in the absorption spectrum of a crystal of ferric W41A (solid line) on exposure to low (dotted line) and high (dashed line) X-ray doses. *Inset:* A plot showing the time-dependent changes in absorbance at 557 nm on exposure of the crystal to high-intensity X-ray beam.

On further exposure of the ferric W41A crystal to a high-intensity X-ray beam, much larger increases in absorbance at 557 nm were observed over time (Figure [3.7] and *inset*), so that the final spectrum of the ferric W41A crystal after data collection resembled the spectrum of a ferrous bis-histidine (low-spin) heme protein,

such as cytochrome  $b_5$  (18). The structure that corresponds to this reduced spectrum (Figure [3.5D]) clearly shows that His-42 is still within bonding distance of the iron but there is additional density above His-42 which is consistent with a percentage of the bound histidine in the “off” position. Reduction of the ferric crystal was complete within ~40 s at 100 K (Figure [3.7] *inset*).

### 3.2.3.4 Transient state kinetics for detection of bis-histidine intermediate observed during X-ray reduction

To ascertain whether a reduced, bis-histidine species (analogous to that observed in Figure [3.7]) could be detected as a transient intermediate in solution, photodiode array stopped-flow experiments were carried out at 5 °C in which the reaction of W41A with dithionite was studied (Figure [3.8A]). After spectral deconvolution, only two species were observed in these experiments: the ferric and ferrous forms. Analogous to data for rsAPX (Figure [3.8B]) no evidence for a reduced, bis-histidine species was obtained.

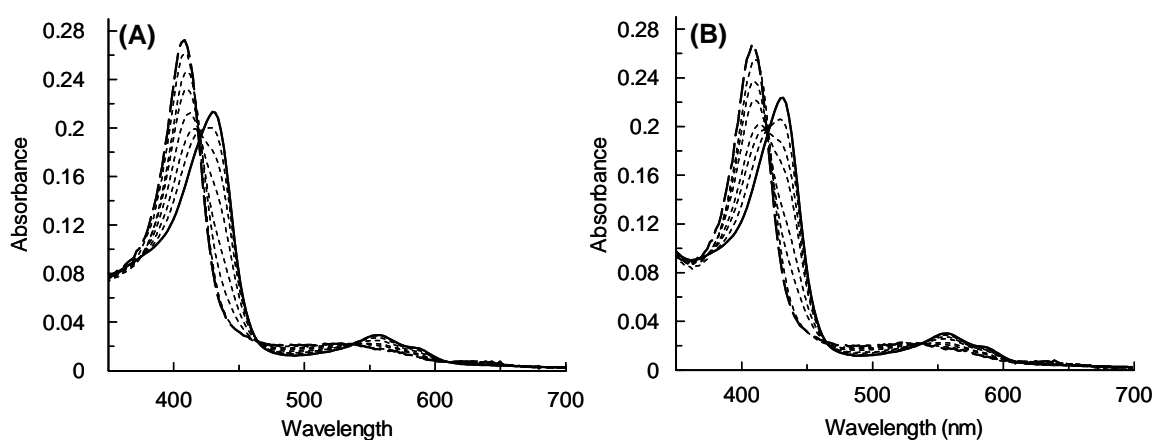


**Figure [3.8]:** Spectral changes observed during PDA analysis of reaction of (A) W41A and (B) rsAPX with dithionite over 200 ms. Selected intermediate spectra between the initial ferric spectrum (dashed line) and final ferrous spectrum (solid line) are shown as dotted lines. Conditions: sodium phosphate buffer, pH 7.0,  $\mu = 0.10$  M, 5.0 °C

**NOTE:** All solution experiments discussed in this Chapter were repeated in crystal screen buffers (0.1 M HEPES, pH 8.3, 2.25 M lithium sulphate) and were found to exhibit analogous results to those observed when using sodium phosphate buffer, pH 7.0,  $\mu = 0.10$  M.

### 3.2.4 Electrochemistry

#### 3.2.4.1 Xanthine/xanthine oxidase assay for determination of the ferric/ferrous reduction potential

The ferric/ferrous reduction potentials for rsAPX and W41A were determined using the xanthine/xanthine oxidase assay with simultaneous reduction of a dye of known potential and were conducted with the assistance of Dr I. Efimov (Department of Chemistry, University of Leicester). This method has the advantage over the optically transparent thin layer electrode (OTTLE) method in that it allows better equilibria to be obtained because electron exchange occurs in the bulk solution; this means that the method is quicker than the OTTLE method and does not require the correct choice of mediators. The assay comprises of xanthine, xanthine oxidase, ferric enzyme (rsAPX or W41A) and a dye of a known potential.

Xanthine oxidase catalyses the oxidation of xanthine to uric acid (Figure [3.9]), with simultaneous reduction of the dye (phenosafranine,  $E^{\circ} = -252$  mV, (19), Figure [3.10]) and ferric enzyme (20). The glucose/glucose oxidase/catalase system (Figure [3.11]), was used to keep the system oxygen free.

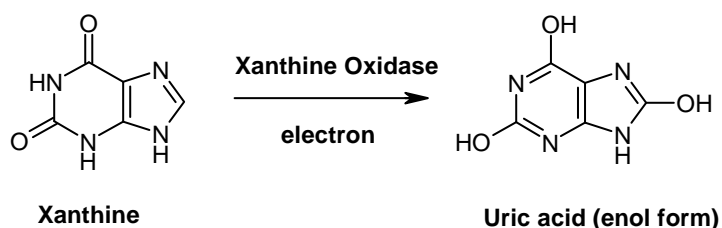


Figure [3.9]: The oxidation of xanthine to uric acid by xanthine oxidase (21).

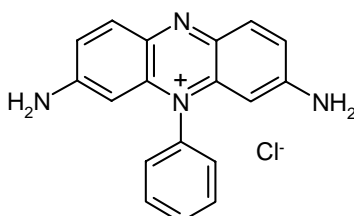
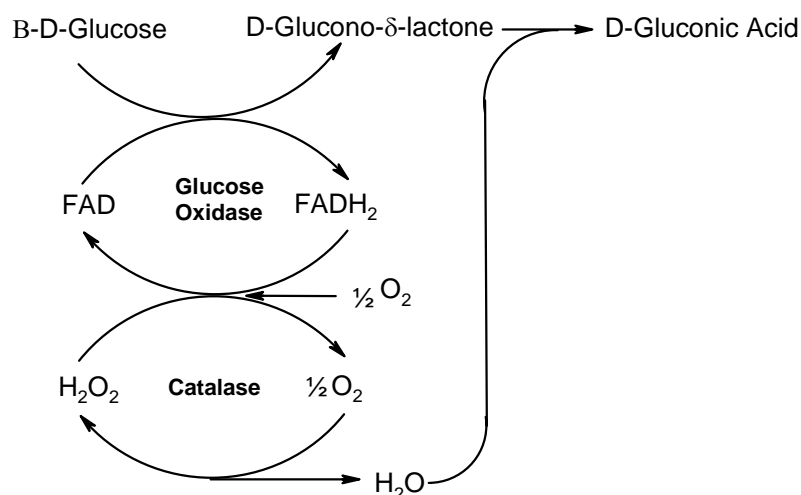


Figure [3.10]: Structure of phenosafranine, the dye used in the xanthine/xanthine oxidase assays in this study (19).



**Figure [3.11]: Scheme to show how the glucose/glucose oxidase/catalase system maintains an anaerobic environment (22).**

Figure [3.12] shows spectra collected during rsAPX and W41A redox assays. In these experiments, some formation of peroxide (as an oxidation product of glucose) leads to initial oxidation of the ferric enzyme to Compound II (spectra not shown). However, since Compound II has a very high reduction potential compared to that for phenosafranine and the ferric/ferrous couple, it was quickly reduced back to ferric form by the xanthine/xanthine oxidase system without reduction of the dye.

The ferric/ferrous reduction potentials for rsAPX and W41A were determined by fitting the data collected from the xanthine/xanthine oxidase assay to the Nernst equation (Equation [6.16], Chapter 6, Section 6.7). The ferric/ferrous reduction potentials for rsAPX and W41A were -206 mV and -227 mV, respectively. The value for rsAPX is according to the literature (20); the value determined for W41A has been published separately (20).

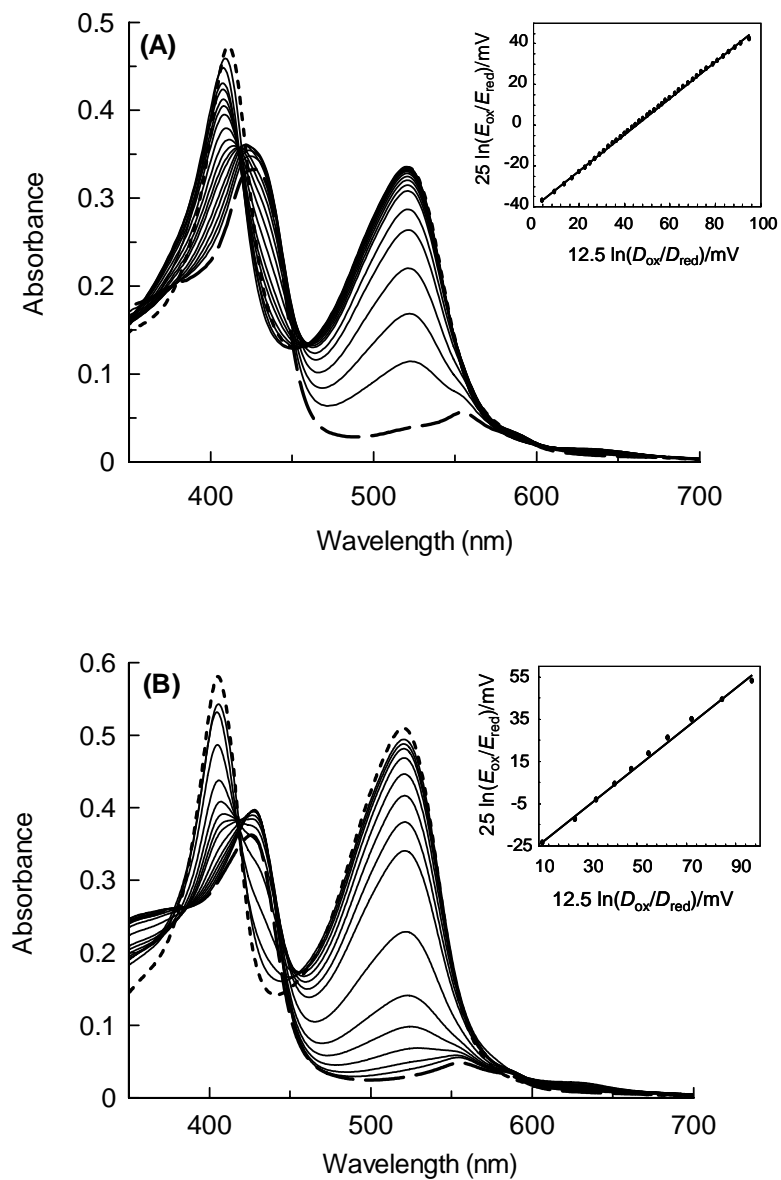


Figure [3.12]: Representative families of spectra collected during determination of ferric/ferrous reduction potential in (A) rsAPX and (B) W41A. Selected intermediate spectra between the initial ferric spectrum of rsAPX/W41A (dotted line) and final ferrous spectrum (dashed line) are shown as lines. Conditions: 50 mM potassium phosphate, pH 7.0, 25.0 °C. *Inset*: The corresponding linear Nernst plot.

### 3.2.4.2 Reduction potential of the ferric-cyanide/ferrous-cyanide couple

Attempts to measure the ferric-cyanide/ferrous-cyanide redox couple for rsAPX and W41A proved difficult due to the low potential of the ferric-cyanide/ferrous-cyanide redox couple. However, because the previously measured ferric/ferrous reduction potential and the equilibrium binding constants for cyanide in the two redox states are related, as shown in Figure [3.13], it was possible to calculate the reduction potential in the presence of cyanide using a derivation of the Nernst equation (Equation [3.1]), where  $E_2^\circ$  is the ferric/ferrous reduction potential measured using the xanthine/xanthine oxidase assay,  $K_{d\text{-ferrous}}$  is the equilibrium binding constant for cyanide in the ferrous form of rsAPX/W41A and  $K_{d\text{-ferric}}$  is the equilibrium binding constant for cyanide in the ferric form of rsAPX/W41A. The calculated ferric-cyanide/ferrous-cyanide redox couples for rsAPX and W41A were determined as -357 mV and -334 mV, respectively.

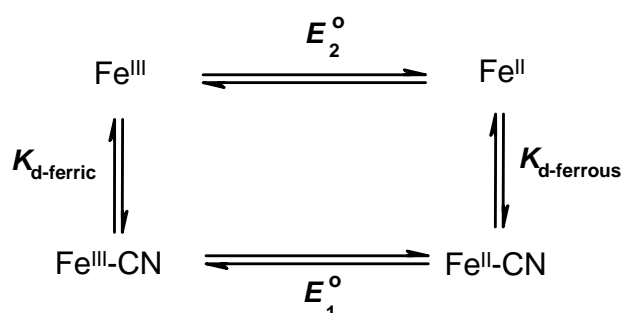


Figure [3.13]: Thermodynamic cycle which expresses a relationship between ferric/ferrous reduction potential and equilibrium binding constant in the presence and absence of cyanide.

$$E_{1(\text{Fe}^{\text{III}}\text{-CN}/\text{Fe}^{\text{II}}\text{-CN})}^{\circ} = E_{2(\text{Fe}^{\text{III}}/\text{Fe}^{\text{II}})}^{\circ} - \ln \left[ \frac{K_{d\text{-ferrous}}}{K_{d\text{-ferric}}} \right] \quad (\text{Eq.}[3.1])$$

### 3.3 DISCUSSION

There are relatively few examples of crystallographically-defined conformational changes in heme proteins. In previous work (described in Chapter 2), the distal histidine (His-42) in the W41A variant of APX was found to be mobile. The coordination geometry in this enzyme was variable, such that His-42 binds “on” to the heme in the oxidized form but addition of H<sub>2</sub>O<sub>2</sub> triggered a conformational change that led to displacement of His-42, so that essentially complete catalytic activity was maintained. This was in contrast to the widely adopted views of heme enzyme catalysis because (1) it showed that W41A could switch its heme coordination geometry and (2) it showed that strong coordination of His-42 to the heme does not, automatically, undermine catalytic activity.

This chapter describes how conformational movement within a heme peroxidase can also be triggered by a change in oxidation state of the iron. With the use of spectroscopic and crystallographic techniques, a mechanism for reduction that involves initial formation of a reduced, bis-histidine-ligated species that subsequently decays by dissociation of His-42 from the heme is presented.

#### 3.3.1 Heme electronic structure and ligand binding

The ferric form of W41A was shown to have greater low-spin character in comparison to ferric rsAPX (described in Chapter 2) due to ligation of distal histidine to the iron in the variant. In the reduced form, wavelength maxima for W41A ( $\lambda_{\text{max}}/\text{nm} = 428, 556 \text{ and } 581^{\text{sh}}$ ) were similar to those of rsAPX ( $\lambda_{\text{max}}/\text{nm} = 430, 555 \text{ and } 583^{\text{sh}}$ ) and were indicative of formation of five-coordinate ferrous heme as observed in other heme peroxidases (23) (Table [3.3]). The five-coordinate geometry in ferrous W41A was indicative of loss of the histidine ligand to the iron upon reduction.

The binding of exogenous ligands to heme proteins has been extensively studied as a method for monitoring heme accessibility, electronic structure and general heme protein conformation (24). Ligand binding studies were performed to assess how the mobility of the distal histidine in W41A affected access of anionic ligands to the heme iron in comparison to rsAPX. Addition of cyanide to ferric W41A and rsAPX leads to formation of a characteristic low-spin heme species. Crystallographic studies described in Chapter 2 have shown that cyanide binds in a

similar manner in both enzymes, where the diatomic cyanide ligand is stabilised by hydrogen bonds to the distal histidine (His-42) and arginine (Arg-38) residues. Despite this similarity in the mode of binding cyanide shown by both enzymes, the binding affinity of W41A for cyanide was found to be ~30 fold lower than that of rsAPX. The ligand binding affinity of W41A for azide (which also leads to formation of a low-spin heme species) was also found to be lower (~10-fold) in comparison to rsAPX. This can be rationalised by the different coordination geometries in the two proteins; rsAPX contains a weakly bound water molecule at the sixth coordination position, whereas in W41A, the distal histidine binds to the heme at the sixth site (*i.e.*, the anionic ligands have restricted access to the iron in W41A due to ligation of His-42 to the heme).

Formation of low-spin hexa-coordinate ferrous heme was observed on addition of cyanide to dithionite-reduced rsAPX and W41A, which is consistent with previous literature (Table [3.3]) (12,25-27). The binding affinities for cyanide to the ferrous form were found to be closely matched for both rsAPX and W41A, suggesting the heme environment in reduced W41A is similar to that observed for rsAPX; *i.e.* His-42 is in the “off” position.

**Table [3.3]: Wavelength maxima (nm) of ferric and ferrous derivatives for rsAPX, W41A, CcP (26), HRP (26) and the F41A HRP-C variant (27).**

	rsAPX	W41A	CcP	HRP F41A
<b>Fe<sup>III</sup></b>	407, 525, 630	405, 525, 564, 630	408, 505, 535, 645	403, 498, 640 403, 501, 543, 635
<b>Fe<sup>III</sup>-CN</b>	419, 536, 563	418, 540, 561	424, 540, 570	422, 439, 580
<b>Fe<sup>III</sup>-N<sub>3</sub></b>	412, 528, 562, 630,	415, 538, 562, 630	535, 570, 635	416, 534, 565, 635
<b>Fe<sup>II</sup></b>	430, 555, 583	428, 556, 581	438, 530, 561, 625	440, 510, 557, 580 435, 557, 587
<b>Fe<sup>II</sup>-CN</b>	426, 529, 560	426, 530, 560	–	432, 536, 566

The wavelength maxima for a number of ferric and ferrous ligand bound derivatives for rsAPX and W41A are comparable with the data reported for other peroxidases, as shown in Table [3.3]. In a related heme peroxidase, HRP-C, mutation of the distal site aromatic residue (Phe-41, F41) to alanine (F41A) also resulted in an increase in the proportion of six-coordinate high-spin heme as observed for the W41A variant. As for ferrous W41A, a five-coordinate ferrous heme species was observed upon reduction of the F41A variant (28). However, unlike W41A the F41A variant in HRP-C was found to have similar cyanide binding affinity as the wild type enzyme in the ferric form (27). The distal phenylalanine in HRP-C, unlike the distal tryptophan in APX (see Chapter 2), is incapable of providing a stabilising interaction to the bound cyanide ligand thus the presence or absence of this aromatic residue appears to have no effect on cyanide binding affinity. The absence of this stabilising interaction in HRP-C is also confirmed by analysis of the crystal structure of the HRP-C-cyanide-ferulic acid complex (29).

It is also instructive to compare these ligand binding data with those of related proteins which have bis-histidine ligation. Hence, as for the W41A variant, the association of diatomic ligands to *Drosophila melanogaster* hemoglobin is a slow process in comparison with the penta-coordinate hemoglobins, in that the bis-histidine hexa-coordinate hemoglobins require extensive conformational re-adjustment of the distal site structure as well as removal of the distal histidine from the iron for ligand binding (30). Similarly the plant hemoglobins, which are also hexa-coordinate with the distal histidine weakly bound, exhibit greater bis-histidine character on mutation of a distal site phenylalanine. The enhanced coordination of the distal histidine to the heme in the phenylalanine variants resulted in a substantially reduced affinity for azide compared to the wild type plant hemoglobins (31). These results are similar to the data presented in this work. Thus it appears that some distal site residues not involved directly in catalysis/or the chemistry that occurs at the active site have an indirect role in that these residues are essential for maintaining the heme environment in its most optimum state.

### 3.3.2 Electrochemistry

In heme peroxidases, the ferric/ferrous reduction potentials are generally low, ranging from -180 to -300 mV (32,33). This is due to the “push effect” of the proximal anionic ligand, which guarantees a stable ferric form of the enzyme under

physiological conditions (34). The reduction potential of the ferric/ferrous couple for the W41A variant ( $E^\circ = -227$  mV) was comparable to rsAPX ( $E^\circ = -206$  mV) despite ligation of His-42 to the heme as a result of the Trp41Ala mutation. The presence of negative charge near the heme is generally known to lead to a decrease in the reduction potential (34). Similarly, when the aromatic distal site tryptophan in CcP was mutated to a histidine, the W51H variant was found to have a similar potential ( $E^\circ = -200$  mV) to that of the wild type enzyme ( $E^\circ = -189$  mV). This small difference in reduction potential was attributed to the increased low-spin character in the variant in both the ferric and ferrous forms (35).

The ferric/ferrous reduction potential for heme peroxidases becomes substantially more negative in the presence of cyanide and thus this potential is not measurable using the xanthine/xanthine oxidase method because dyes with such low reduction potentials are not available (but the reduction potential in the presence of cyanide can be measured using the OTTLE cell method). Therefore, the ferric/ferrous redox potential in the presence of cyanide was calculated using Equation [3.1]. The calculated redox potentials in the presence of cyanide for both rsAPX and W41A (-357 mV and -334 mV, respectively) are in good agreement with the redox potential of ARP (-390 mV) (36) and HRP (-430 mV) (37) measured in the presence of cyanide.

### **3.3.3 Crystallographic evidence for mobility of His-42 on reduction of heme in W41A**

The phenomenon of radiation damage in protein crystals has been demonstrated in several cases where diffraction data were collected with synchrotron radiation (38). The ability of X-rays to reduce protein crystals is particularly important in the case of redox enzymes (39). Reduction of the heme is also possible during data collection (see for example (17,40-42)) and this was used to obtain further structural evidence for movement of His-42 between the “on” and “off” positions. Single-crystal microspectrophotometry was used to monitor changes in the electronic spectrum of a ferric and ferrous W41A crystal during X-ray data collection.

Difficulties can arise in interpreting electronic spectra of crystals because the spectra can differ depending on the orientation of the crystal with respect to the direction of the incident light (41). Due to this anisotropic nature of crystals, the spectra for crystalline and solution samples can exhibit different features. The

sensitive microspectrophotometer is easily saturated by strongly absorbing proteins, especially in the crystalline state, which is highly concentrated (42-44). Measurements are therefore possible only on relatively thin crystals, and the highly absorbing Soret peaks are not determined accurately (42).

The single-crystal absorption spectrum of the dithionite-reduced W41A crystal was similar to that obtained for ferrous W41A in solution, with the data in both states (crystalline and solution) indicating a five-coordinate ferrous heme species. This spectroscopic data is in agreement with the crystal structure of the dithionite-reduced form of W41A (Figure [3.5B]), which reveals that His-42 is no longer bound to the iron and instead shows a water molecule at the same location in the active site. Therefore a change in the redox state of W41A has triggered a conformational change in the distal histidine of the variant. The heme environment of ferrous W41A is similar to that observed in the structure of ferrous HRP (17) and heme oxygenase (17,45,46).

Single-crystal microspectrophotometry was also used to monitor changes in the electronic spectrum of a ferric W41A crystal during X-ray data collection. The single-crystal microspectrophotometry spectrum of the ferric W41A crystal (at 100 K) before data collection was identical to that observed in solution studies (at room temperature). Initially the electronic spectrum of W41A at room temperature (Figure 3.1) was puzzling due to the prominent high-spin charge transition at 630 nm, despite the low-spin peak at 564 nm. Thus the possibility of the conformational mobility in ferric W41A (discussed in Chapter 2) being induced by freezing or crystallisation was not dismissed; however observation of a similar spectrum in the crystal of ferric W41A (Figure [3.7]) at 100 K in this work, demonstrates that this movement is not a freezing or crystallisation effect. In fact, the iron-histidine bond in W41A (2.3 Å) was found to be longer than usual, which probably accounts for the 630 nm (high-spin) band in the visible region at both room temperature and 100 K and suggests that His-42 is quite weakly coordinated.

During exposure to the X-ray beam the absorbance peaks at 564 and 630 nm of ferric W41A disappeared, while new peaks in the spectrum were formed at 525 and 557 nm; this is symptomatic of reduction of the heme. No movement of the distal histidine was observed in the W41A crystal exposed to a low-attenuated X-ray beam; however within ~40 s of exposure to the full intensity X-ray beam an increase in the intensity of peaks at 525 and 557 nm was observed. The spectrum of the X-ray reduced W41A crystal was found to be characteristic of ferrous bis-histidine (low-spin) heme as observed in cytochrome *b*<sub>5</sub> (18), thus indicating that reduction of the

iron has occurred without movement of the distal histidine. The structure of the W41A crystal exposed to this high-intensity beam (Figure [3.5D]) was in agreement with the single-crystal spectroscopy, in that the distal histidine was found to be within bonding distance of the iron. However additional density was observed above His-42 which was suggestive of partial movement of His-42 away from the heme close to the “off” position. This movement was confirmed because the additional density was found to overlay with the orientation of His-42, which is in the “off” position, in the dithionite-reduced ferrous derivative of W41A.

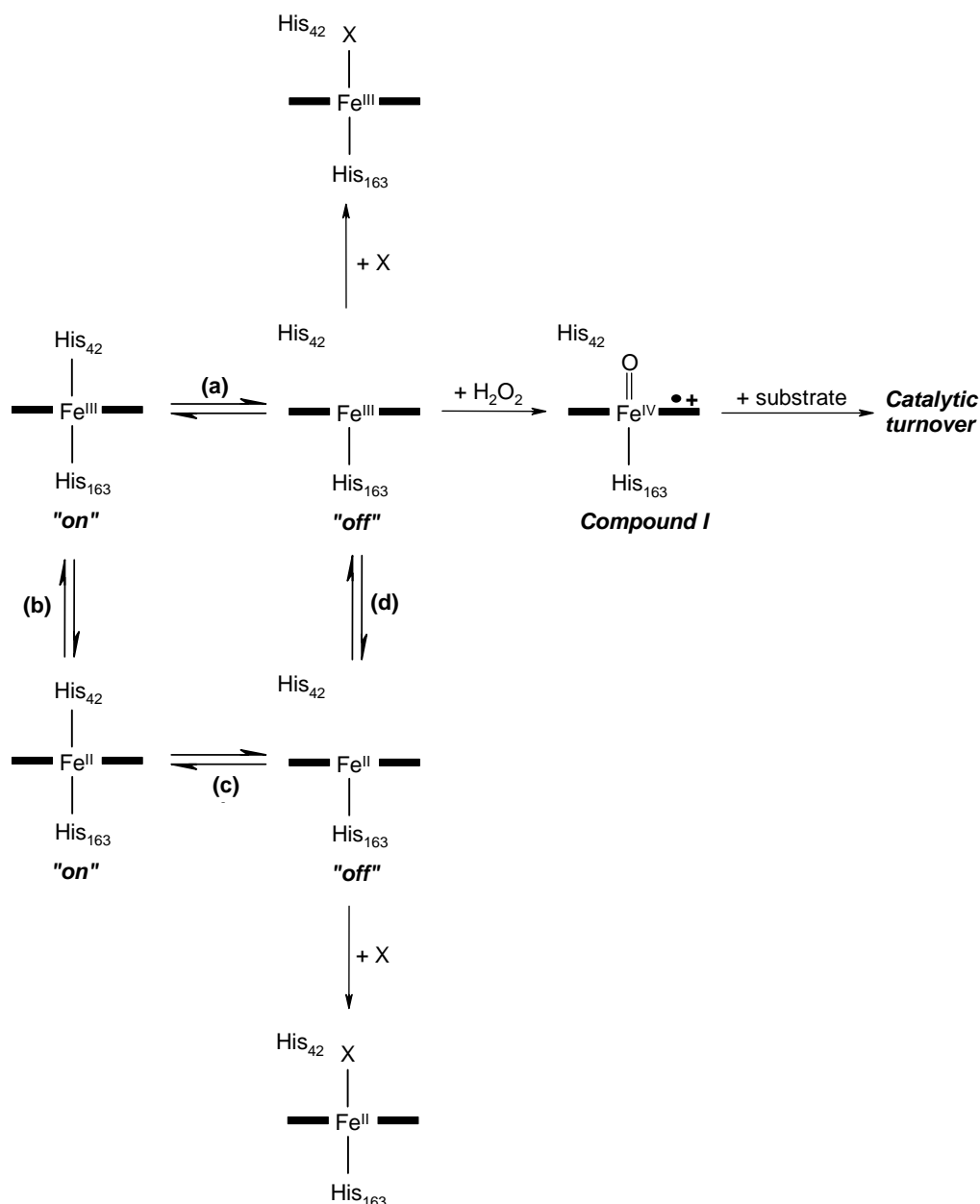
Significantly, the single-crystal electronic spectrum of the W41A crystal after 40 s of X-ray exposure (Figure [3.7]) was found to differ to that obtained when W41A was chemically reduced by dithionite in solution or in the crystalline form, (Figures [3.1B] and [3.6]). This can be interpreted as evidence that reduction of W41A in the beam at 100 K leads to an initial reduced, bis-histidine species which presumably then subsequently decays back to a final species that is the same as that observed when W41A is reduced with dithionite in solution. Also no evidence for the presence of a bis-histidine ligated ferrous heme protein was observed in photodiode array stopped-flow experiments performed at 5 °C. It can be assumed that at this temperature the conformational rearrangements occur more rapidly so that the reduced, bis-histidine species decays too quickly for detection by the stopped-flow technique. However under the cryo-conditions used for X-ray data collection, reduction of the heme occurs efficiently with the subsequent active site rearrangement occurring more slowly.

Identical peaks at 525 and 555 nm were also observed in the single-crystal electronic spectrum of the X-ray reduced form of myoglobin; however the low-spin signal was attributed to iron-ligated water/hydroxide molecule which, due to low temperatures used, was not able to move away from the iron to generate the normal ferrous deoxy state (42).

### 3.4 SUMMARY

To conclude it is clear that the data in this chapter show that conformational mobility can be induced within the *same* protein structure either by ligand (anionic ligands or H<sub>2</sub>O<sub>2</sub>) binding (see Chapter 2) or by a change in the redox state of the heme. The major findings are summarised in Scheme [3.1]. On the basis of the data presented, a mechanism for reduction that involves initial formation of a reduced, bis-histidine-ligated species that subsequently decays by dissociation of His-42 from the heme is proposed. As noted earlier, other examples of conformationally-mobile heme protein structures have appeared sporadically (for example (3-8)). Collectively, this data can be interpreted as evidence that these protein structures are intrinsically mobile and allows speculation that conformational mobility may be a more general feature of other heme protein structures.

These observations coincide with the developing views on the wider “passive” role of heme in biological systems (discussed in Chapter 1, Section 1.10), because it is now becoming clear that the role of heme is not restricted to its involvement as a prosthetic group in specific proteins and enzymes, but that it is also involved in various regulatory processes, including gas sensing, control of gene transcription and modulation of ion channels. The limited information that is currently available seems to suggest that the trigger for these regulatory processes is similarly controlled either by ligand binding or by the oxidation state of the iron, and that either of these events are used to initiate downstream conformational rearrangements of the protein architecture either at the active site or beyond. Heme-linked protein conformational changes have been found to play a role in many regulatory heme-proteins (47), examples include ligand binding to the heme-regulated inhibitor kinase (48) and the heme sensor HemAT (49), and reduction of the iron in the heme-regulated phosphodiesterase from *E. coli* (50) and in CooA (51,52). Similar mechanisms may also apply to the gas-responsive transcription factor NPAS2 (53), the heme-binding transcription factor Hap1 (54) and the heme-based sensor FixL (55). Collectively, the data reported here and in the previous chapter provides clear evidence that conformational movement within the same heme active site can be controlled by both ligand binding and metal oxidation state.



Scheme [3.1]: Scheme summarising the species observed in this and previous work (Chapter 2), showing the mobility of His-42 during catalysis and reduction. Step (a) shows the equilibrium between the "on" and "off" forms of the ferric protein. This form has been previously shown (Chapter 2) to bind both exogenous ligands (represented by an X) and to be catalytically active (reaction with H<sub>2</sub>O<sub>2</sub>), as shown in the Scheme. Step (b) represents the reduction of ferric W41A to an initial low-spin ferrous form, which is the likely route in the X-ray beam. Step (c) represents loss of His-42 from this initial low-spin ferrous intermediate; this form can also bind exogenous ligands. Step (d) shows the re-oxidation of the ferrous "off" form to ferric form. On reaction with dithionite in solution, step (b) followed by (c) is possible, but an alternative mechanism in which reduction of the ferrous form with dithionite involves prior dissociation of His-42 from the heme before reduction, step (a) followed by (d), is also possible.

### 3.5 REFERENCES

1. Dawson, J. H. (1988) *Science* **240**, 433-439
2. Ortiz de Montellano, P. R. (1987) *Accounts of Chemical Research* **20**, 289-294
3. Rosell, F. I., Ferrer, J. C., and Mauk, A. G. (1998) *Journal of the American Chemical Society* **120**, 11234-11245
4. Das, K. T., Couture, M., Lee, H. C., Peisach, J., Rousseau, D. L., Wittenberg, B. A., Wittenberg, J. B., and Guertin, H. (1999) *Biochemistry* **38**, 15360-15368
5. Williams, P. A., Fulop, V., Garman, E. F., Saunders, N. F. W., Ferguson, S. J., and Hajdu, J. (1997) *Nature* **389**, 406-412
6. Dias, J. M., Alves, T., Bonoifacio, C., Pereira, A. S., Trincao, J., Bougeois, D., Moura, I., and Romano, M. (2004) *Structure* **12**, 961-973
7. Uchida, T., Stevens, J. M., Daltrop, O., Harvat, E. M., Hong, L., Ferguson, S. J., and Kitagawa, T. (2004) *Journal of Biological Chemistry* **279**, 51981-51988
8. Patel, N., Seward, H. E., Svensson, A., Gurman, S. J., Thomson, A. J., and Raven, E. L. (2003) *Archives of Biochemistry and Biophysics* **418**, 197-204
9. Poulos, T. L. (2007) *Natural Product Reports* **24**, 504-510
10. Lad, L., Mewies, M., and Raven, E. L. (2002) *Biochemistry* **41**, 13774-13781
11. Dalton, D. A., Joe Hanus, F., Sterling, A., Evans, R., and Evans, H. J. (1987) *Plant Physiology* **83**, 789-794
12. Dalton, D. A., Diaz del Castillo, L., Kahn, M. L., Joyner, S. L., and Chatfield, J. M. (1996) *Archives of Biochemistry and Biophysics* **328**, 1-8
13. Sharp, K. H., Mewies, M., Moody, P. C. E., and Raven, E. L. (2003) *Nature Structural Biology* **10**, 303-307
14. Murshudov, G. N., Vagin, A., A., and Dodson, E. J. (1997) *Acta Crystallographica Section D. Biological Crystallography* **53**, 240-255

15. Collaborative Computational Project, N. (1994) *Acta Crystallography* **D50**, 760-763
16. Emsley, P., and Cowtan, K. (2004) *Acta Crystallographica Section D. Biological Crystallography* **60**, 2126-2132
17. Berglund, G. I., Carlsson, G. H., Smith, A. T., Szoke, H., Henriksen, A., and Hajdu, J. (2002) *Nature* **417**, 463-468
18. Ozols, J., and Strittmatter, P. (1964) *Journal of Biological Chemistry* **239**, 1018-1023
19. Clark, W. M. (1972) *Oxidation-reduction Potentials of Organic Systems*, Robert E. Kreiger Publishing Co., Huntington, New York
20. Efimov, I., Papadopoulou, N. D., McLean, K. J., Badyal, S. K., Macdonald, I. K., Munro, A. W., Moody, P. C. E., and Raven, E. L. (2007) *Biochemistry* **46**, 8017-8023
21. Li, L. (ed) (2001) *Xanthine Oxidase*, Iowa
22. <http://www.csu.edu/research/rpcgwr/research/gglucoxi.gif>.
23. Smulevich, G. (1996) in *Plant Peroxidases: Biochemistry and Physiology* (Obinger, C., Burner, U., Ebermann, R., Penel, C., and Greppin, H., eds), Geneva
24. Saleem, M. M. M., and Wilsson, M. T. (1988) *Inorganic Chemica Acta* **153**, 93-98
25. Cheek, J., Mandelman, D., Poulos, T. L., and Dawson, J. H. (1999) *Journal of Biological Inorganic Chemistry* **4**, 64-72
26. Dunford, H. B., and Stillman, J. S. (1976) *Coordination Chemistry Reviews* **19**, 187-251
27. Meunier, B., Rodriguez-Lopez, J. N., Smith, A. T., Thorneley, R. N. F., and Rich, P. R. (1998) *Journal of Biochemistry* **330**, 303-309

28. Heering, H. A., Smith, A. T., and Smulevich, G. (2002) *Journal of Biochemistry* **363**, 571-579
29. Henriksen, A., Smith, A. T., and Gajhede, M. (1999) *Journal of Biological Chemistry* **274**, 35005-35011
30. de Sanctis, D., Dewilde, S., Vonrhein, C., Pesce, A., Moens, L., Ascenzi, P., Hankeln, T., Burmester, T., Ponassi, M., Nardini, M., and Bolognesi, M. (2005) *Journal of Biological Chemistry* **280**, 27222-27229
31. Smagghe, B. J., Kundu, S., Hoy, A. J., Halder, P., Weiland, T. R., Savage, A., Venugopal, A., Goodman, M., Premer, S., and Hargrove, M. S. (2006) *Biochemistry* **45**, 9735-9745
32. Williams, R. J. P. (1974) in *Iron in Biochemistry and Medicine* (Jacobs, E. A., and Worwood, M., eds), pp. 183, Academic Press, New York
33. Gunsalus, I. C., Meek, J. R., Lipscomb, P., Munk, D., and Munk, E. (1974) *Molecular mechanisms of Oxygen Activation*, Academic Press, New York
34. Battistuzzi, G., Bellei, M., Zederbauer, M., Furtmuller, P. G., Sola, M., and Obinger, C. (2006) *Biochemistry* **45**, 12750-12755
35. DiCarlo, C. M., Vitello, L. B., and Erman, J. E. (2007) *Journal of Inorganic Biochemistry* **101**, 603-613
36. Battistuzzi, G., Bellei, M., De Rienzo, F., and Sola, M. (2006) *Journal of Biological Inorganic Chemistry* **11**, 586-592
37. Battistuzzi, G., Borsari, M., Ranieri, A., and Sola, M. (2002) *Journal of the American Chemical Society* **124**, 26-27
38. Weik, M., Raimond, B. G. R., Kryger, G., McSweeney, S., Raves, M. L., Harel, M., Gros, P., Silman, I., Kroon, J., and Sussman, J. L. (2000) *Proceedings of the National Academy of Sciences of the United States of America* **97**, 623-628
39. Karlsson, A., Parales, J. V., Parales, R. E., Gibson, D. T., Eklund, H., and Ramaswamy, S. J. (2000) *Journal of Inorganic Biochemistry* **78**, 83-87

40. Schlichting, I., Berendzen, J., Chu, K., Stock, A. M., Maves, S. A., Benson, D. E., Sweet, R. M., Ringe, D., Petsko, G. A., and Sligar, S. G. (2000) *Science* **287**, 1615-1622
41. Kuhnel, K., Derat, E., Turner, J., Shaik, S., and Schlichting, I. (2002) *Proceedings of the National Academy of Sciences of the United States of America* **104**, 99-104
42. Hersleth, H. P., Uchida, T., Rohr, A. K., Teschner, T., Schunemann, V., Kitagawa, T., Trautwein, A. X., Gorbitz, C. H., and Andersson, K. K. (2007) *Journal of Biological Chemistry* **282**, 23372-23386
43. Srajer, V., Ren, Z., Teng, T. Y., Schmidt, M., Ursby, T., Bourgeois, D., Pradervand, C., Schildkamp, W., Wulff, M., and Moffat, K. (2001) *Biochemistry* **40**, 13802-13815
44. Wilmot, C. M., Sjogren, T., Carlsson, G. H., Berglund, G. I., and Hajdu, J. (2002) *Methods Enzymology* **353**, 301-318
45. Lad, L., de Montellano, P. R. O., and Poulos, T. L. (2004) *Journal of Inorganic Biochemistry* **98**, 1686-1695
46. Lad, L., Wang, J. L., and Li, H. Y. (2003) *Journal of Molecular Biology* **330**, 527-538
47. Paoli, M., Marles-Wright, J., and Smith, A. (2002) *DNA and Cell Biology* **21**, 271-280
48. Igarashi, N., Sato, T., Kitagawa, T., Yoshimura, T., Yamauchi, S., Sagami, I., and Shimizu, T. (2004) *Journal of Biological Chemistry* **279**, 15752-15762
49. Pinakoulaki, E., Yoshimura, H., Daskalalis, V., Yoshioka, S., Aono, S., and Varatsis, C. (2006) *Proceedings of the National Academy of Sciences of the United States of America* **103**, 14796-14801
50. Kurokawa, H., Lee, D. S., Watanabe, M., Sagami, I., Mikami, B., Raman, C. S., and Shimizu, T. (2004) *Journal of Biological Chemistry* **279**, 20186-20193

51. Lanzilotta, W. N., Schuller, D. J., Thorstensson, M. V., Kerby, R. L., Roberts, G. P., and Poulos, T. L. (2000) *Nature Structural Biology* **7**, 876-880
52. Nakajima, H., Honma, Y., Tawara, T., Kato, T., Park, S. Y., Miyatake, H., Shiro, Y., and Aono, S. (2001) *Journal of Biological Chemistry* **276**, 7055-7061
53. Dioum, E. M., Rutter, J., Tuckerman, J., R., Gonzalez, G., Gilles-Gonzalez, M. A., and McKnight, S. L. (2002) *Science* **298**, 2385-2387
54. Lan, C., Lee, H. C., Tang, S., and Zhang, L. (2004) *Journal of Biological Chemistry* **279**, 27607-27612
55. Gilles-Gonzalez, M. A., and Gonzalez, G. (2005) *Journal of Inorganic Biochemistry* **99**, 1-22

***CHAPTER FOUR***

**HEME OXYGENASE ACTIVITY IN ASCORBATE PEROXIDASE**

## CHAPTER FOUR

### HEME OXYGENASE ACTIVITY IN ASCORBATE PEROXIDASE

---

#### 4.1 INTRODUCTION

Oxidative degradation of heme is an important catabolic step in biology which is catalysed by heme oxygenase (discussed briefly in Chapter One). Heme oxygenase (HO) is a membrane-bound enzyme found in mammals, cyanobacteria, algae and higher plants (1-3), that catalyses the oxygen-dependent degradation of heme to biliverdin, carbon monoxide (CO), and free iron in the presence of reducing equivalents (4-6) (Figure [4.1]). All the products of heme oxygenase catalysis play important biological functions, where the ferrous iron released by HO is normally recycled and forms part of the daily iron requirement. Biliverdin is reduced by biliverdin reductase to bilirubin which is subsequently conjugated with glucuronic acid and excreted (7). The carbon monoxide released during HO catalysis has been reported to act as a messenger molecule, participating in neuronal transmission and vascular regulation through the activation of soluble guanylate cyclase (see Chapter One, Section 1.10 and (8-10)).

Crystallisation and structure determination of human- and rat-HO enzymes complexed with heme and the degradation product, biliverdin (11-14) provided significant insights into both the mechanism and regiospecificity of the HO reaction. The HO reaction proceeds via a multi-step mechanism (Figure [4.1]) that depends on reduction equivalents provided by NADPH and NADPH-dependent-cytochrome P450

reductase. The first electron provided by the P450 reductase reduces the ferric heme iron to the ferrous state, and a molecule of oxygen binds to form a meta-stable oxygen-bound complex which is reduced by a second electron to generate a hydroperoxo intermediate in HO ( $\text{Fe}^{\text{III}}\text{-OOH}$ ) (15) also known as Compound 0. The hydroperoxo intermediate regioselectively oxidises the  $\alpha$ -*meso*-carbon to form  $\alpha$ -*meso*-hydroxyheme, which is then converted to ferrous verdoheme with the concomitant formation of carbon monoxide from the hydroxylated  $\alpha$ -*meso*-carbon by molecular oxygen and an electron from the P450 reductase. The ferrous verdoheme is cleaved in an NADPH- and oxygen-dependent manner to give ferric biliverdin. Finally, biliverdin and ferrous iron are released from the enzyme upon the reduction of the ferric iron of ferric biliverdin.

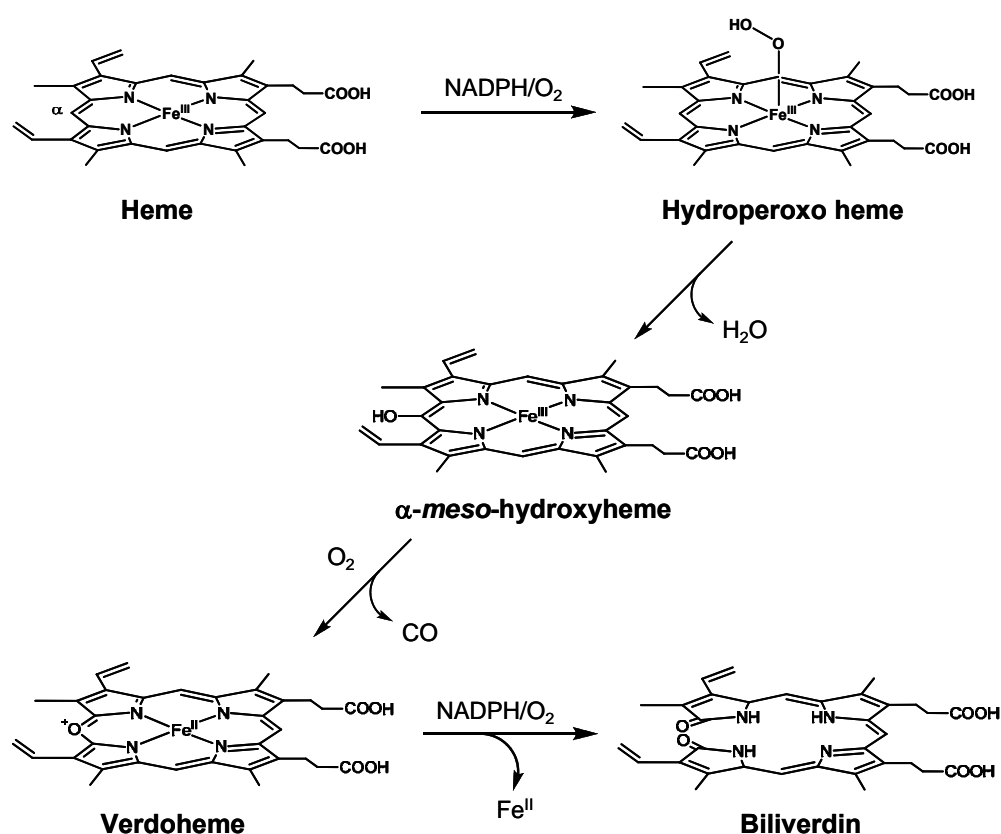
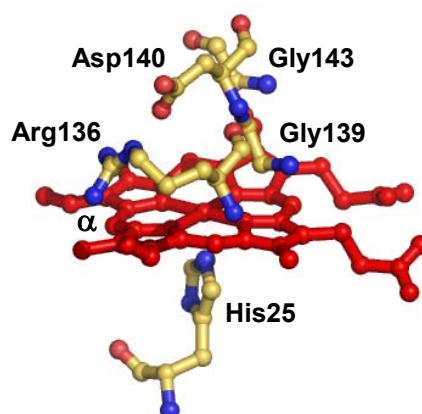


Figure [4.1]: A scheme showing the overall reaction catalysed by HO, which results in the oxidation of heme and release of  $\alpha$ -*meso*-carbon atom as carbon monoxide. Adapted from (13).

The catalytic mechanism of HO includes several interesting aspects. First, HO utilises heme as both a substrate and a cofactor. Second, the carbon monoxide produced by HO does not appear to severely interfere with heme degradation, although carbon monoxide generally binds to ferrous heme with a higher affinity than oxygen does (7). Third, the heme cleavage by HO displays regioselectivity such that only the  $\alpha$ -*meso*-carbon is oxygenated. Fourth, the hydroperoxo species ( $\text{Fe}^{\text{III}}\text{-OOH}$ ) self-hydroxylates the  $\alpha$ -*meso*-carbon of the porphyrin ring to generate  $\alpha$ -*meso*-hydroxyheme in HO. This is different from the cytochrome P450 and peroxidase heme proteins, where the oxygen bond of the hydroperoxo species is heterolytically cleaved to generate an actively hydroxylating Compound I, a ferryl species coupled with a porphyrin  $\pi$ -cation radical (see Chapter one, Figure [1.24]) (16). Similar to the peroxidases, HO harbours a proximal histidine residue in its active site (Figure [4.2]); however the HO proximal histidine hydrogen bonding interaction is considered to be much weaker than that in the peroxidase enzymes, where the strong iron histidine interaction results in the iron being displaced from the porphyrin plane. It is this strong interaction in peroxidases that has been postulated to facilitate oxygen bond cleavage to generate the ferryl Compound I intermediate (17). The neutral imidazole axial ligand in HO helps to prevent hydroperoxo oxygen bond cleavage prior to hydroxylation of the porphyrin *meso*-carbon. In the distal pocket (Figure [4.2]), HO (unlike peroxidases) lacks a distal histidine or any other polar side chain that could assist stabilisation of the oxy form and the catalytic process.



**Figure [4.2]:** The active structure of human HO (PDB code: 1N45) (11,14), showing the heme (red) and various active site residues. The  $\alpha$ -*meso* heme carbon is also indicated.

The possibility that H<sub>2</sub>O<sub>2</sub> might substitute in HO catalysis for oxygen and two reducing equivalents *in vitro*, and possibly *in vivo* under severe oxidative stress conditions, has been studied extensively (18-24). Degradation of heme to dipyrrolic compounds (propentdyopents) by H<sub>2</sub>O<sub>2</sub> was first reported by Fisher and Muller in 1937 (25). Later reports revealed that H<sub>2</sub>O<sub>2</sub> degrades the ferric heme to produce verdoheme (21,26) which upon addition of cytochrome P450 reductase and NADPH is converted to biliverdin and carbon monoxide in much the same way as HO (21,27). However, recent studies conducted by Matsui *et al* (28,29) have shown that HO can utilise H<sub>2</sub>O<sub>2</sub> and its analogue, methyl hydroperoxide, for verdoheme degradation to biliverdin. Similarly, the reaction of HO with *m*-chloroperoxybenzoic acid (*m*-CPBA) and alkyl peroxides (cumene hydroperoxide, *tert*-butyl hydroperoxide and ethyl hydroperoxide, Figure [4.3]) have also been examined (21,30). Reaction with the cumene hydroperoxide, *tert*-butyl hydroperoxide and *m*-cpba results in formation of a ferryl species which reverts back to the ferric state when reduced with ascorbate, guaiacol or phenol (21). There is no evidence for formation of verdoheme in these reactions; however the reaction with the alkyl peroxides, cumene hydroperoxide and *tert*-butyl hydroperoxide, is accompanied by some degradation of the heme to non-biliverdin products (19). The reaction with ethyl hydroperoxide also gives rise to a ferryl species which upon reduction with ascorbate (addition of ascorbate prevents oxidative degradation of the prosthetic group) followed by extensive HPLC isolation-purification and spectroscopic characterisation studies revealed that the heme was partially converted to iron  $\alpha$ -*meso*-ethoxyheme (Figure [4.4]) (30).

The work carried out in this Chapter demonstrates that on replacement of the distal tryptophan-41 (with alanine), new heme oxygenase activity is introduced into rsAPX. The resulting variant, W41A, is capable of formation of a *tert*-butyl-derivative of biliverdin on exposure to the bulky peroxide, *tert*-butyl hydroperoxide (<sup>t</sup>BuO<sub>2</sub>H, Figure [4.3]). A mechanism for the reaction is proposed, based on the intermediates and products identified during the heme degradation process. To our knowledge, this work reports for the first time a peroxidase that is capable of exhibiting heme oxygenase activity on reaction with peroxide.

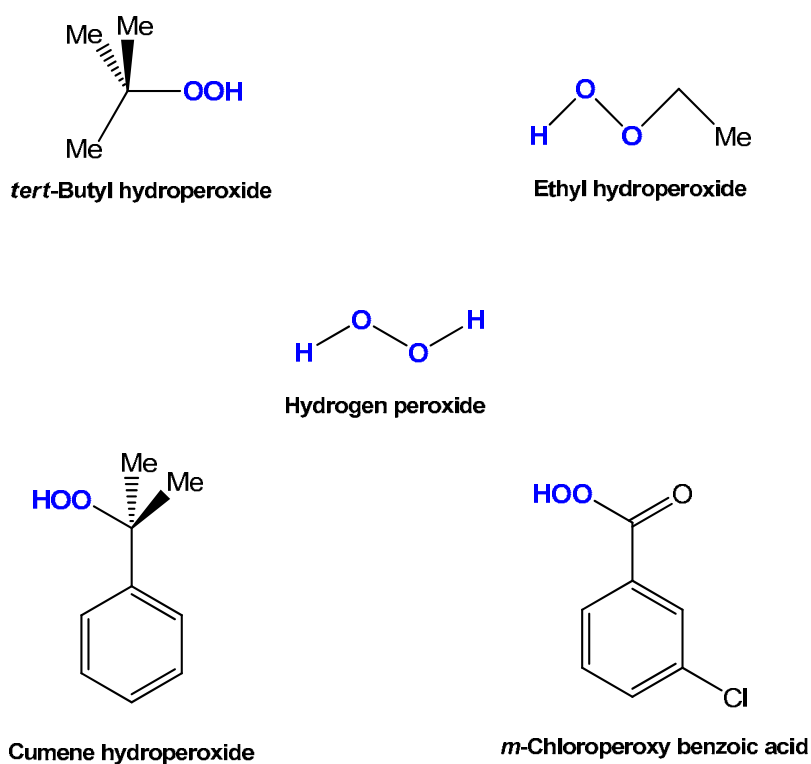


Figure [4.3]: The structures of the organic peroxides discussed in the Chapter.

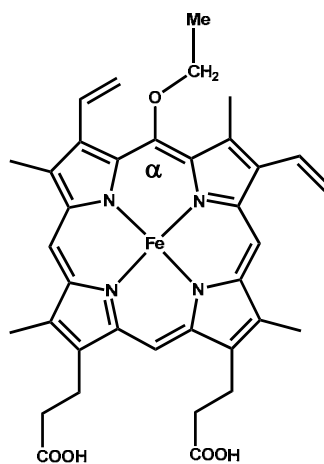


Figure [4.4]: The structure of  $\alpha$ -meso-ethoxyheme, formed on reaction of HO with ethyl hydroperoxide (30).

## 4.2 RESULTS

### 4.2.1 Reaction of W41A and rsAPX with *tert*-butyl hydroperoxide: spectroscopic analysis

The reaction of the W41A variant with  ${}^t\text{BuO}_2\text{H}$  was monitored spectrophotometrically over 15 minutes (Figure [4.5A]). A rapid decrease of the absorbance at the Soret maxima and absorbance of  $\alpha$  and  $\beta$  bands was observed. No evidence of formation of a ferryl species was detected. Similar spectral changes are observed when HO is exposed to  $\text{H}_2\text{O}_2$  (18,21-24); however in HO an increase in absorbance at  $\sim 700$  nm, indicative of verdoheme formation, is also prevalent. The W41A variant has previously been established (Chapter 2 and (31)) as a fully active peroxidase which catalyses the oxidation of ascorbate in a similar manner to rsAPX, with formation of the authentic catalytic intermediates, Compound I and Compound II. Initially the reaction of W41A with  $\text{H}_2\text{O}_2$  (Figure [4.5B]) leads to formation of a mixture of Compound I and Compound II species, as evidenced by the presence of the Compound I peak at  $\sim 650$  nm, which then leads to the sole formation of a Compound II species ( $\lambda_{\text{max}}/\text{nm} = 412, 530$  and  $554^{\text{sh}}$ ), which over the course of 15 minutes decayed to a ferric-like spectrum with decreased absorbance.

Similarly, the reaction of rsAPX with  $\text{H}_2\text{O}_2$  (Figure [4.5D]), which also proceeds through a mixture of a Compound I and Compound II species (detection of a peak at  $\sim 650$  nm), results in formation of a characteristic Compound II species ( $\lambda_{\text{max}}/\text{nm} = 412, 529$  and  $558^{\text{sh}}$ ). Correspondingly, formation of a Compound II-like species ( $\lambda_{\text{max}}/\text{nm} = 414, 527$  and  $560^{\text{sh}}$ ) is also observed on reaction of rsAPX with  ${}^t\text{BuO}_2\text{H}$  (Figure [4.5C]); however, this reaction proceeds slowly over the course of 15 minutes and possible evidence of a Compound I species may be evident.

No colour change was observed in rsAPX upon reaction with either peroxide (Figure [4.6A]) and similarly no significant colour change was observed in the W41A variant upon reaction with  $\text{H}_2\text{O}_2$  (Figure [4.6B]). However a change in colour from red to green, suggesting degradation of heme to a bilin pigment (32), was observed on reaction of the W41A variant with  ${}^t\text{BuO}_2\text{H}$  (Figure [4.6B]). When left over longer time periods ( $\sim 8$  hours) after addition of  ${}^t\text{BuO}_2\text{H}$ , the decrease in the Soret absorbance continued in both the W41A variant and rsAPX (data not shown) and the visible region was also found to lose character. On the other hand, on reaction with  $\text{H}_2\text{O}_2$ ,

over longer time periods (~8 hours), the spectra remained similar to those observed after 15 minutes of addition of H<sub>2</sub>O<sub>2</sub> (Figure [4.5B,D]) but a slight reduction in the Soret absorbance in both W41A and rsAPX was observed (data not shown).

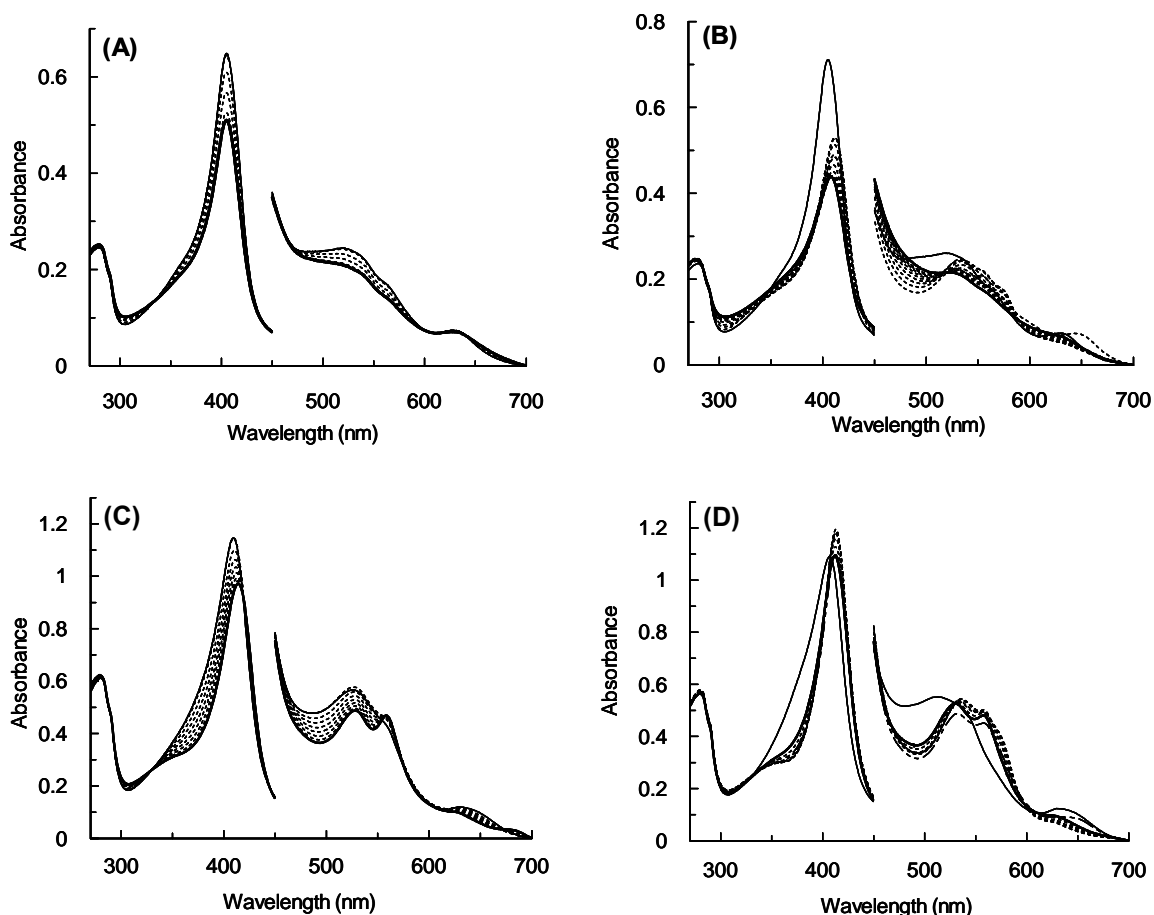


**Figure [4.5]:** Selected electronic spectra collected during the reaction of ferric W41A (A and B) and rsAPX (C and D) with 14.5 equivalents of <sup>t</sup>BuO<sub>2</sub>H (A and C) and H<sub>2</sub>O<sub>2</sub> (B and D). The intermediate spectra between ferric W41A/rsAPX (line) and final spectra of reaction (solid line) are shown as dotted lines. The total reaction time was 15 minutes. The visible region has been multiplied by a factor of 5. Conditions: sodium phosphate, pH 8.3,  $\mu = 0.1$  M, 25.0 °C.

**Note:** All experiments discussed in this Chapter were repeated using sodium phosphate buffer (pH 7.0,  $\mu = 0.1$  M) or crystal screen buffers (0.1 M HEPES pH 8.3, 2.25 M lithium sulphate). Identical spectroscopic changes to those observed using sodium phosphate buffer (pH 8.3,  $\mu = 0.1$  M) were detected; however, precipitation did occur on use of crystal screen buffers. pH-dependent studies conducted on the reaction of HRP with <sup>t</sup>BuO<sub>2</sub>H (33) revealed that a maximal yield of modified heme was obtained at pH 8.0. Thus taking into consideration these findings and to ensure consistency with crystallographic data, experiments were conducted using sodium phosphate buffer (pH 8.3,  $\mu = 0.1$  M).

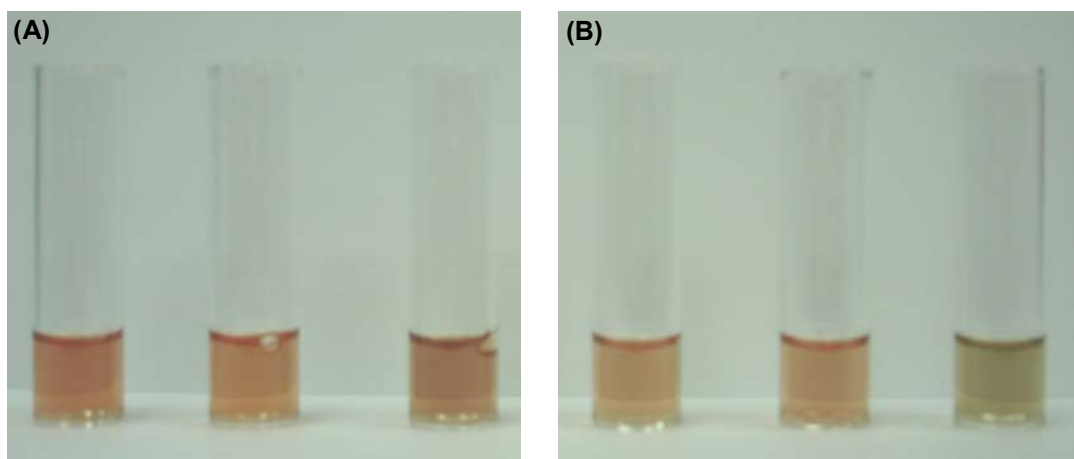
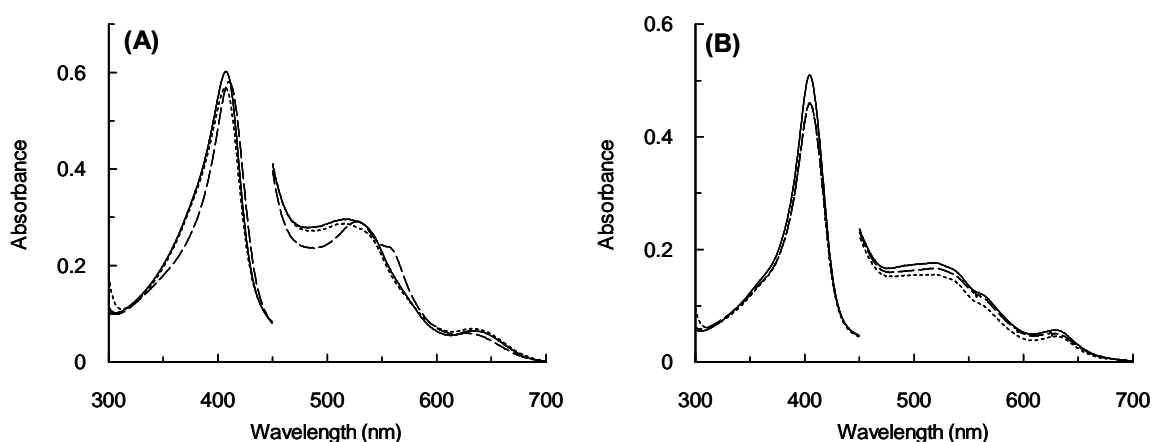


Figure [4.6]: (A) Ferric rsAPX before (centre) and after treatment with 14.5 equivalents  $\text{H}_2\text{O}_2$  (left) and  ${}^t\text{BuO}_2\text{H}$  (right). (B) Ferric W41A before (centre) and after treatment with 14.5 equivalents  $\text{H}_2\text{O}_2$  (left) and  ${}^t\text{BuO}_2\text{H}$  (right). The total reaction time was 15 minutes. Conditions: sodium phosphate, pH 8.3,  $\mu = 0.1 \text{ M}$ ,  $25.0 \text{ }^\circ\text{C}$ .

#### 4.2.1.1 Absence of a ferryl intermediate in W41A on reaction with tert-butyl hydroperoxide: addition of ascorbate

The reaction of HO with *m*-CPBA and  ${}^t\text{BuO}_2\text{H}$  triggers a decrease in the intensity of the Soret band with a slight (1-3 nm) red shift in its position and the resulting species resembles the ferryl-Compound II species of the peroxidases (21,30). Support for a ferryl intermediate is provided by the observation that addition of substrate (ascorbate, guaiacol or phenol) regenerates the spectrum of ferric HO (21,23). Note, no ferryl species is observed on addition of ascorbate to  $\text{H}_2\text{O}_2$ -treated HO (21,23,24). Similarly, as expected, addition of ascorbate to W41A and rsAPX after reaction with  $\text{H}_2\text{O}_2$  results in formation of a ferric-like species (see Chapter 2, Section 2.2.4, Figure [2.12]). Equally recovery of a ferric-like species was observed in  ${}^t\text{BuO}_2\text{H}$ -treated rsAPX, which shows spectral evidence for formation of a ferryl species, on addition of ascorbate (Figure [4.7A]). The reaction of the W41A variant with  ${}^t\text{BuO}_2\text{H}$  however, shows no spectral evidence for formation of a ferryl species, which is further confirmed by the minimal spectral change observed upon addition of ascorbate (Figure [4.7B]).



**Figure [4.7]:** Electronic spectra of ferric rsAPX (A) and W41A (B) prior to addition of  $t\text{BuO}_2\text{H}$  (solid line) and immediately after addition of 14.5 equivalents of  $t\text{BuO}_2\text{H}$  (dashed line). The spectra obtained immediately after addition of 14.5 equivalents of ascorbate to  $t\text{BuO}_2\text{H}$ -treated rsAPX and W41A are shown as dotted lines. The visible region has been multiplied by a factor of 5. Conditions: sodium phosphate, pH 8.3,  $\mu = 0.1 \text{ M}$ ,  $25.0 \text{ }^\circ\text{C}$ .

#### 4.2.1.2 Absence of a ferryl intermediate in W41A on reaction with *tert*-butyl hydroperoxide: stopped-flow analysis

To ascertain whether a ferryl intermediate could be detected as a transient intermediate in the reaction of W41A with  $t\text{BuO}_2\text{H}$ , photodiode array (PDA) stopped-flow experiments were conducted at  $5.0 \text{ }^\circ\text{C}$  as described in Chapter 6, Section 6.6.5. The ferryl transient intermediates Compound I and Compound II were detected in control experiments, where the reaction of rsAPX with  $t\text{BuO}_2\text{H}$  was studied using the PDA detector of the stopped-flow apparatus (Figure [4.8]). Data collected over a period of 500 ms were best fitted to a two step model ( $A \rightarrow B \rightarrow C$  as shown previously for rsAPX) (34), where  $A$  is ferric rsAPX,  $B$  is Compound I, and  $C$  is Compound II. Spectra for the Compound I ( $\lambda_{\text{max}}/\text{nm} = 410, 530, 570^{\text{sh}}$  and 650) and Compound II ( $\lambda_{\text{max}}/\text{nm} = 416, 530$  and  $562^{\text{sh}}$ ) intermediates of rsAPX formed on reaction with  $t\text{BuO}_2\text{H}$  are in agreement with those observed on reaction of rsAPX with  $\text{H}_2\text{O}_2$  (Chapter 2, Section 2.2.6, Table [2.3]). Formation of Compound I (*i.e.*  $A \rightarrow B$ ) in rsAPX on reaction with  $t\text{BuO}_2\text{H}$  occurs with an observed rate constant ( $k_{1,\text{obs}}$ ) of  $120 \pm 1.2 \text{ s}^{-1}$ , which is  $\sim 2$  fold slower than that observed on reaction of rsAPX with  $\text{H}_2\text{O}_2$  ( $k_{1,\text{obs}} = 218 \pm 2.6 \text{ s}^{-1}$ ) (34). Formation of Compound II (*i.e.*  $B \rightarrow C$ ) occurs with similar rate constants for reaction of rsAPX with both  $t\text{BuO}_2\text{H}$  and  $\text{H}_2\text{O}_2$  ( $k_{2,\text{obs}} = 2.1 \pm 0.1$  and  $2.7$

$\pm 0.1 \text{ s}^{-1}$  (34), respectively). The rate constant for Compound I formation,  $k_1$ , in rsAPX was found to be linearly dependent on  ${}^t\text{BuO}_2\text{H}$  concentration (Figure [4.9]), with a second-order rate constant of  $k_1 = 9.7 \pm 0.5 \times 10^4 \text{ M}^{-1} \text{ s}^{-1}$  compared to  $k_1 = 3.3 \pm 0.1 \times 10^7 \text{ M}^{-1} \text{ s}^{-1}$  (34) for reaction with  $\text{H}_2\text{O}_2$ .

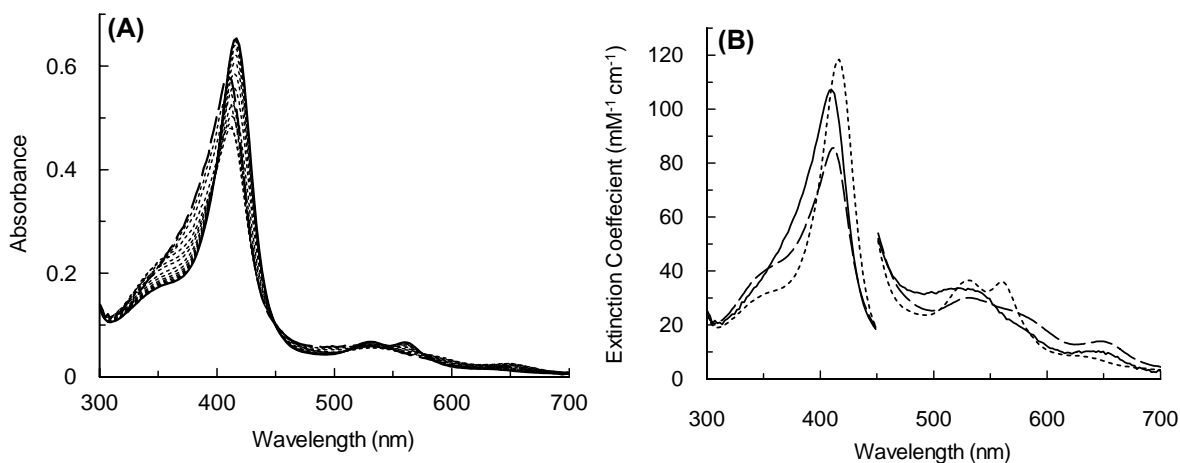


**Figure [4.8]: (A) Spectral changes observed upon reaction of rsAPX with  ${}^t\text{BuO}_2\text{H}$  monitored by stopped-flow diode array spectroscopy over 500 ms. Intermediate spectra between initial ferric rsAPX spectrum (solid dashed line) and final oxidised spectrum (solid line) are shown as dotted lines. For clarity only selected spectra are shown. (B) Deconvoluted spectra for the reaction of rsAPX with  ${}^t\text{BuO}_2\text{H}$ , shown in (A), showing ferric rsAPX (solid line) and oxidised intermediates Compound I (dashed line) and Compound II (dotted line). The data were fitted to a two-step model ( $A \rightarrow B \rightarrow C$ ). The visible region has been multiplied by a factor of 5. Conditions: sodium phosphate, pH 8.3,  $\mu = 0.10 \text{ M}$ ,  $5.0 \text{ }^\circ\text{C}$ .**

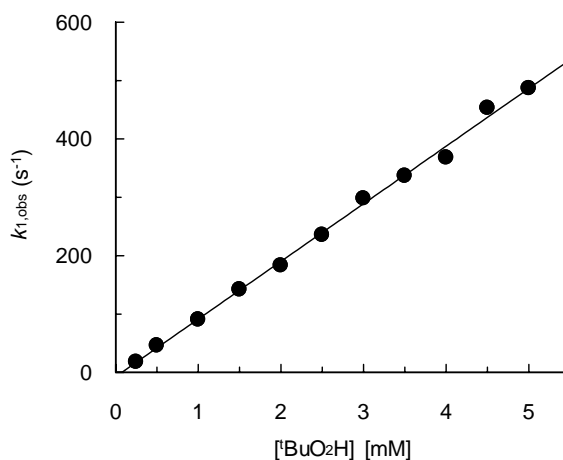


**Figure [4.9]: Dependence of  $k_{1,\text{obs}}$ , the pseudo-first-order rate constant for rsAPX Compound I formation, on  ${}^t\text{BuO}_2\text{H}$  concentration. Conditions: sodium phosphate, pH 8.3,  $\mu = 0.10 \text{ M}$ ,  $5.0 \text{ }^\circ\text{C}$ .**

However, no evidence for formation of ferryl species was observed, between 1.28 - 500 ms, on reaction of W41A with  $t\text{BuO}_2\text{H}$  (Figure [4.10]). Instead, similar spectral changes (decay of the Soret peak) to those detected when using a conventional UV-visible spectrophotometer were observed (Figure [4.5]). Due to the intensity of the lamp, the degradation process appeared to occur at an accelerated rate.

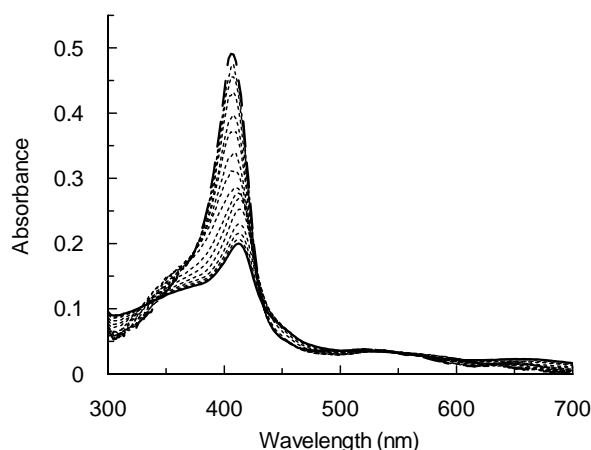


**Figure [4.10]: Spectral changes observed upon reaction of W41A with  $t\text{BuO}_2\text{H}$  monitored by stopped-flow diode array spectroscopy over 500 ms. Intermediate spectra between initial ferric W41A spectrum (solid dashed line) and final  $t\text{BuO}_2\text{H}$ -W41A spectrum (solid line) are shown as dotted lines. For clarity only selected spectra are shown. Conditions: sodium phosphate, pH 8.3,  $\mu = 0.10\text{ M}$ ,  $5.0\text{ }^\circ\text{C}$ .**

#### **4.2.2 Identification of the species formed on reaction of W41A with *tert*-butyl hydroperoxide: Mass spectrometry and HPLC analysis**

The products formed on reaction of rsAPX and W41A variant with  $t\text{BuO}_2\text{H}$  and  $\text{H}_2\text{O}_2$  were examined using HPLC analysis, MALDI-TOF and ESI mass spectrometry. Collection of the mass spectrometric data was conducted with assistance from Drs S. C. Mistry and A. R. Bottrill (Protein Nucleic Acid Chemistry Laboratory, University of Leicester) and Dr G. Eaton (Department of Chemistry, University of Leicester).

HPLC analysis of rsAPX and W41A (Figure [4.11A,D]) before treatment with peroxide showed a single peak with a retention time of 33 min, identical to that of authentic heme obtained under identical conditions (Figure [4.11G]) and mass spectral analysis of the peaks revealed a mass at 616 Da (Figure [4.12C]) further confirming assignment as heme. Iron-containing heme species can be assigned with

ease due to the specific isotope pattern of iron (Figure [4.12A]). The HPLC elution profiles of rsAPX after treatment with  $\text{H}_2\text{O}_2$  and  $^t\text{BuO}_2\text{H}$  (Figure 4.11B,C) were essentially identical to those obtained for untreated rsAPX, showing mainly the presence of unmodified heme (33 min); however a peak with a retention time of 31 min was also present, which had a corresponding mass of 611 Da when analysed using MALDI-TOF mass spectrometry. This species, due to the presence of a distinct iron isotope pattern, may be a cleaved/bleached form of heme.

Similarly, peaks corresponding to unmodified (33 min) and cleaved/bleached heme (31 min) were the species detected upon treatment of W41A variant with  $\text{H}_2\text{O}_2$  (Figure [4.11E]). The presence of cleaved/bleached heme was a major species observed upon treatment of W41A with  $^t\text{BuO}_2\text{H}$  (Figure [4.11F]) and MALDI-TOF analysis of this peak again revealed a mass of 611 Da (Figure [4.12C]). The HPLC elution profile of  $^t\text{BuO}_2\text{H}$ -treated W41A also exhibited presence of unmodified heme (33 min) as well as other heme species with retention times of 17, 23, 42 and 46 min. MALDI-TOF analysis was conducted on these heme species (pooled together from several HPLC purification runs) obtained from treatment of W41A with  $^t\text{BuO}_2\text{H}$  to identify the products.

MALDI-TOF analysis of the peak with retention time of 17 min was dominated by a species with mass of 664 Da (Figure [4.12E]). A similar mass was obtained from the products formed on incubation of HRP with  $^t\text{BuO}_2\text{H}$  (33), thus the species was assigned as a  $^t\text{BuO}_2\text{H}$ -modified heme porphyrin (Figure [4.12E] *inset*, see iron isotope pattern of peak at 664 Da and also see peak at 608 Da which is consistent with loss of iron (664 - Fe (56)) formed by a radical mechanism (see (33)). Also a peak with a mass of 583 Da was also detected in the MADLI-TOF spectrum of the heme species with retention time of 17 min. This mass is consistent with the presence of biliverdin (Figure [4.12B]) (biliverdin (582) + H (1)) and from examination of HPLC elution profile of authentic biliverdin (Figure [4.11H]) it appears both the heme species from  $^t\text{BuO}_2\text{H}$ -treated W41A and biliverdin elute at similar retention times (17 and 20 min, respectively). The presence of the major heme species with a mass 664 Da in the heme fragment with retention time of 17 min and the use of DMSO to initially get biliverdin into solution (see Chapter 6, Section 6.9) may be the cause of the slight discrepancy in retention times observed between biliverdin from the purified heme fragment and authentic biliverdin.

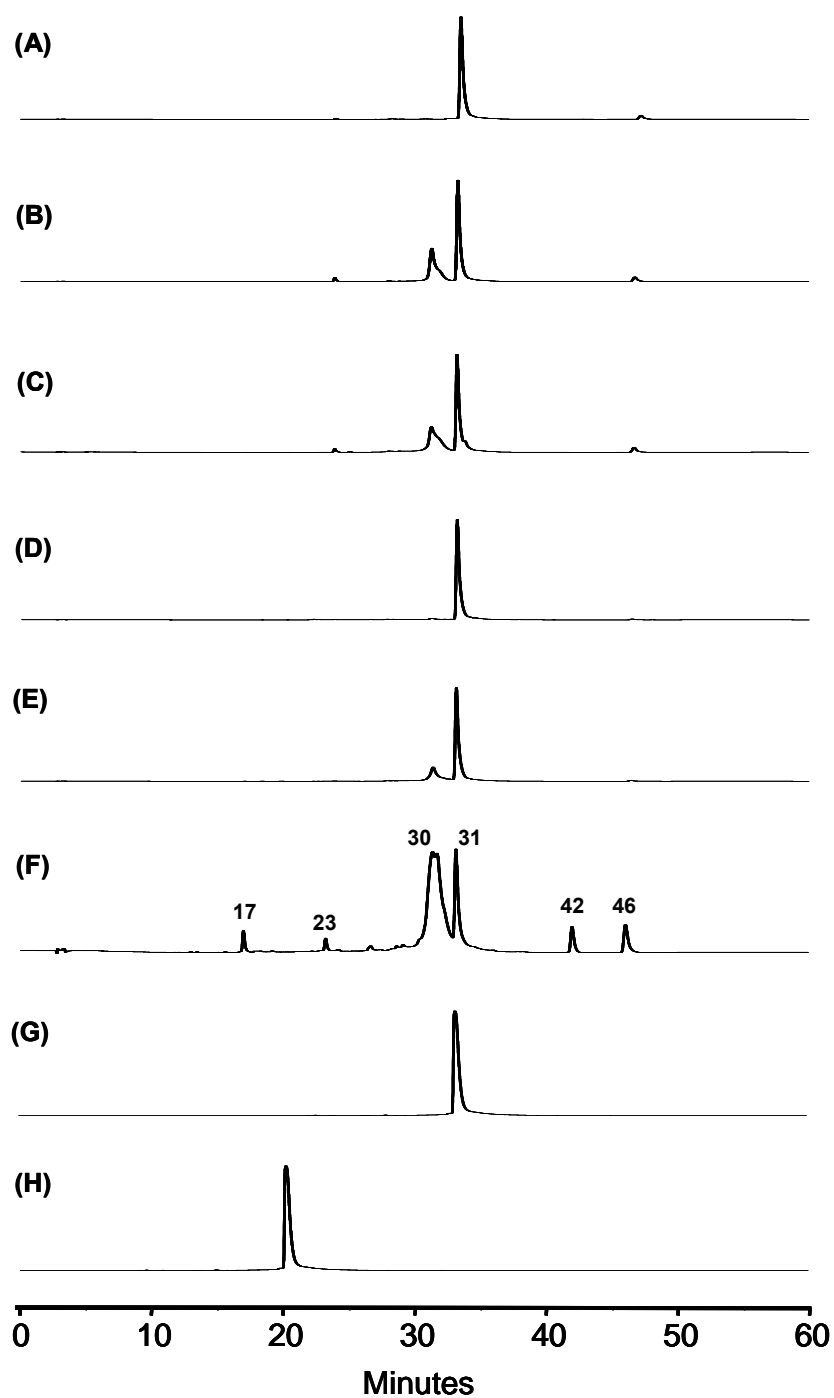


Figure [4.11]: HPLC analyses of rsAPX and W41A before and after treatment with  $t\text{BuO}_2\text{H}$  and  $\text{H}_2\text{O}_2$  monitored at 398 nm. HPLC elution profiles of rsAPX before (A) and after treatment with  $\text{H}_2\text{O}_2$  (B) and  $t\text{BuO}_2\text{H}$  (C). HPLC elution profiles of W41A before (D) and after treatment with  $\text{H}_2\text{O}_2$  (E) and  $t\text{BuO}_2\text{H}$  (F). HPLC elution profiles of authentic hemin (G) and authentic biliverdin (H).

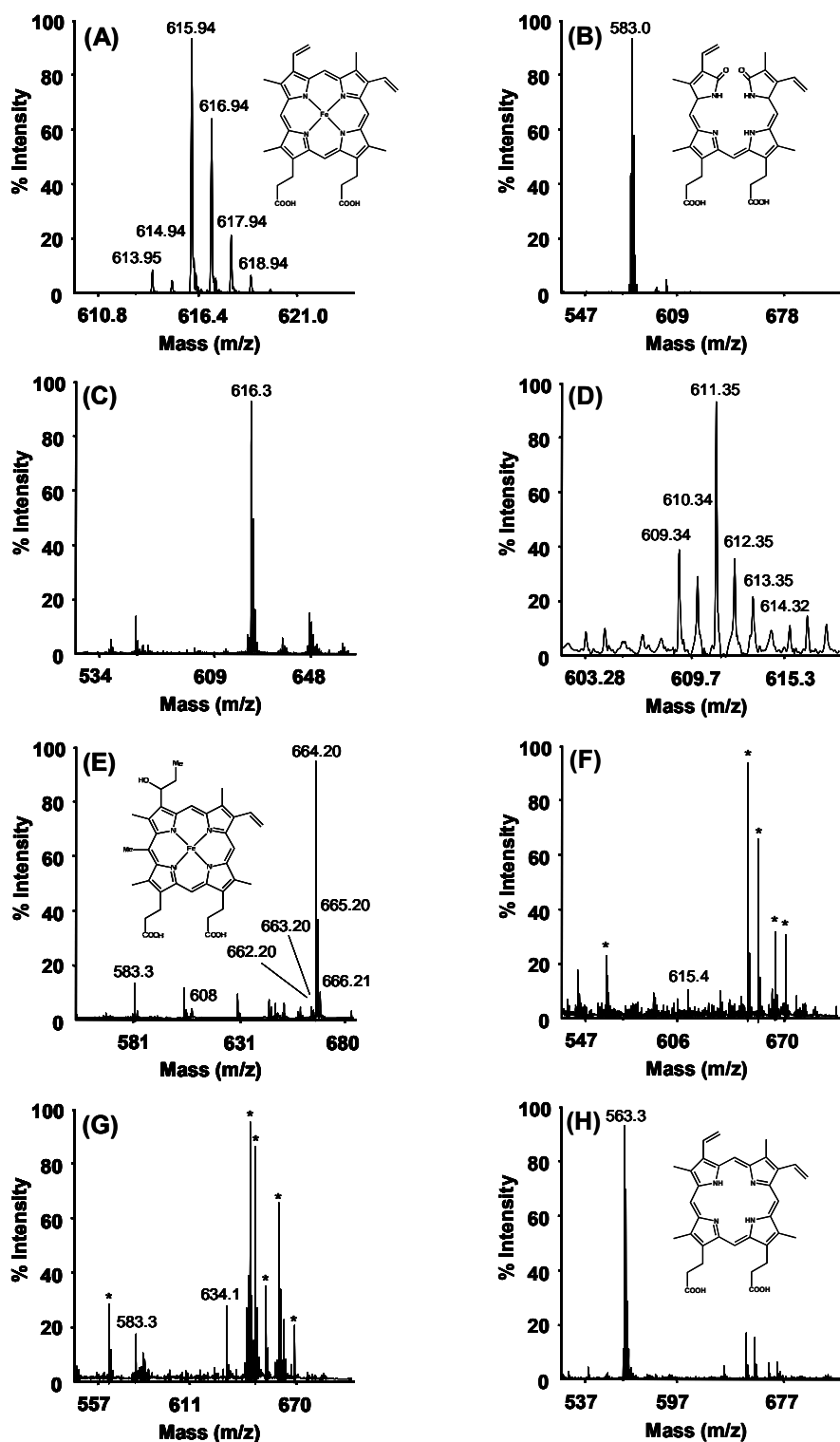


Figure [4.12]: MALDI-TOF mass spectra of authentic heme (A showing the iron isotope pattern), authentic biliverdin (B) and heme fragments obtained from the HPLC purification of  $^t\text{BuO}_2\text{H}$ -treated W41A (Figure [4.11F] eluting at 30 min (C); 31 min (D); 17 min (E); 23 min (F); 42 min (G) and 46 min (H). \* denotes matrix peaks.

MALDI-TOF analysis of the heme species with retention time of 23 min (Figure [4.12F]), proved difficult (presence of matrix peaks) which may be due to complications in ionisation of the species; however a mass of 615 Da (Figure [4.12F]) was routinely observed in the MALDI-TOF analysis of this heme species. It is noteworthy that traces of a heme species with retention time of 23 min was also observed in the HPLC elution profiles of untreated and peroxide-treated rsAPX. Taking these details into consideration the heme species was assigned as heme after loss of a proton (heme (616) – H (1)).

The heme species with retention time of 42 min was only observed in the HPLC elution profile of <sup>t</sup>BuO<sub>2</sub>H-treated W41A and although MALDI-TOF analysis proved complicated a species with a mass of 634 and 583 Da was clearly present (Figure [4.12G]). Again this data is consistent with the presence of biliverdin; which is probably formed from fragmentation of the species with mass of 634 Da. Coincidentally, the presence of this heme species with retention time of 42 min gradually disappeared in HPLC elution profiles of samples of <sup>t</sup>BuO<sub>2</sub>H-treated W41A conducted after several hours (~6 hours) of treatment, despite the fact the reaction mixtures were kept frozen until analysis. Assignment of a possible structure of the modified-biliverdin species is discussed later.

Finally, analysis of the heme species with retention time of 46 min, revealed a mass of 563 Da (Figure [4.12H]). Traces of this heme species were also observed in the HPLC elution profiles of untreated and peroxide-treated rsAPX. MALDI-TOF analysis of this heme species is consistent with the mass of iron-free porphyrin (heme (616) - Fe (56) + 3H (3), the pyrrole nitrogens are also protonated on loss of the iron, as observed in structures of biliverdin, Figure [4.12H] *inset*).

Although MALDI-TOF analysis proved extremely helpful, due to the low mass range of the heme species being analysed the interference of matrix mass peaks ( $\alpha$ -cyano-4-hydroxycinnamic acid, molecular weight of 188.16 Da, Figure [4.13]) in the MALDI-TOF mass spectra of the heme species made analysis of data difficult at times. Thus ESI mass spectrometry was employed to analyse the heme degradation products obtained from the HPLC purification procedure; however non productive results were obtained in these experiments, which may be due to the lengthy time required to initially prepare the samples (degradation of the heme species may have occurred over the long periods it takes to HPLC purify and concentrate the samples). Hence, ESI analysis was conducted on samples immediately after treatment with

peroxide, without HPLC purification, to gain further information of the modified heme species. ESI analysis of untreated and peroxide-treated rsAPX revealed the presence of mainly unmodified heme (616 Da, Figure [4.14]). Similarly, unmodified heme was also detected in untreated and H<sub>2</sub>O<sub>2</sub>-treated W41A. As well as unmodified heme, biliverdin (583 Da), identical to authentic biliverdin (583 Da, Figure [4.14B]), was also detected in <sup>t</sup>BuO<sub>2</sub>H-treated W41A (Figure [4.14H]). The ESI mass spectrum of <sup>t</sup>BuO<sub>2</sub>H-treated W41A (Figure [4.14H]) also revealed many peaks also found in authentic heme and untreated W41A (Figure [4.14A and F]). The ESI mass spectrum of authentic biliverdin gave an amplified signal when the ESI mass spectrometer was in the negative ion mode (Figure [4.15A]). The influence of ionisation mode on the fragmentation pattern of biliverdin has been reported previously (35). Thus all samples were re-examined in the negative ion mode and the signal of the biliverdin species present in <sup>t</sup>BuO<sub>2</sub>H-treated W41A was found to be amplified (Figure [4.15B]), however the signal of the remaining control samples was poor when collected in the negative ion mode.

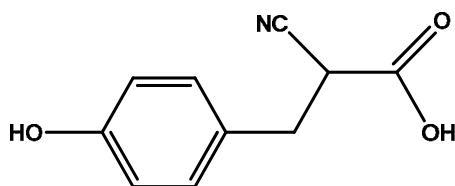


**Figure [4.13]:** The structure of  $\alpha$ -cyano-4-hydroxycinnamic acid, the matrix used in MADLI-TOF analysis.

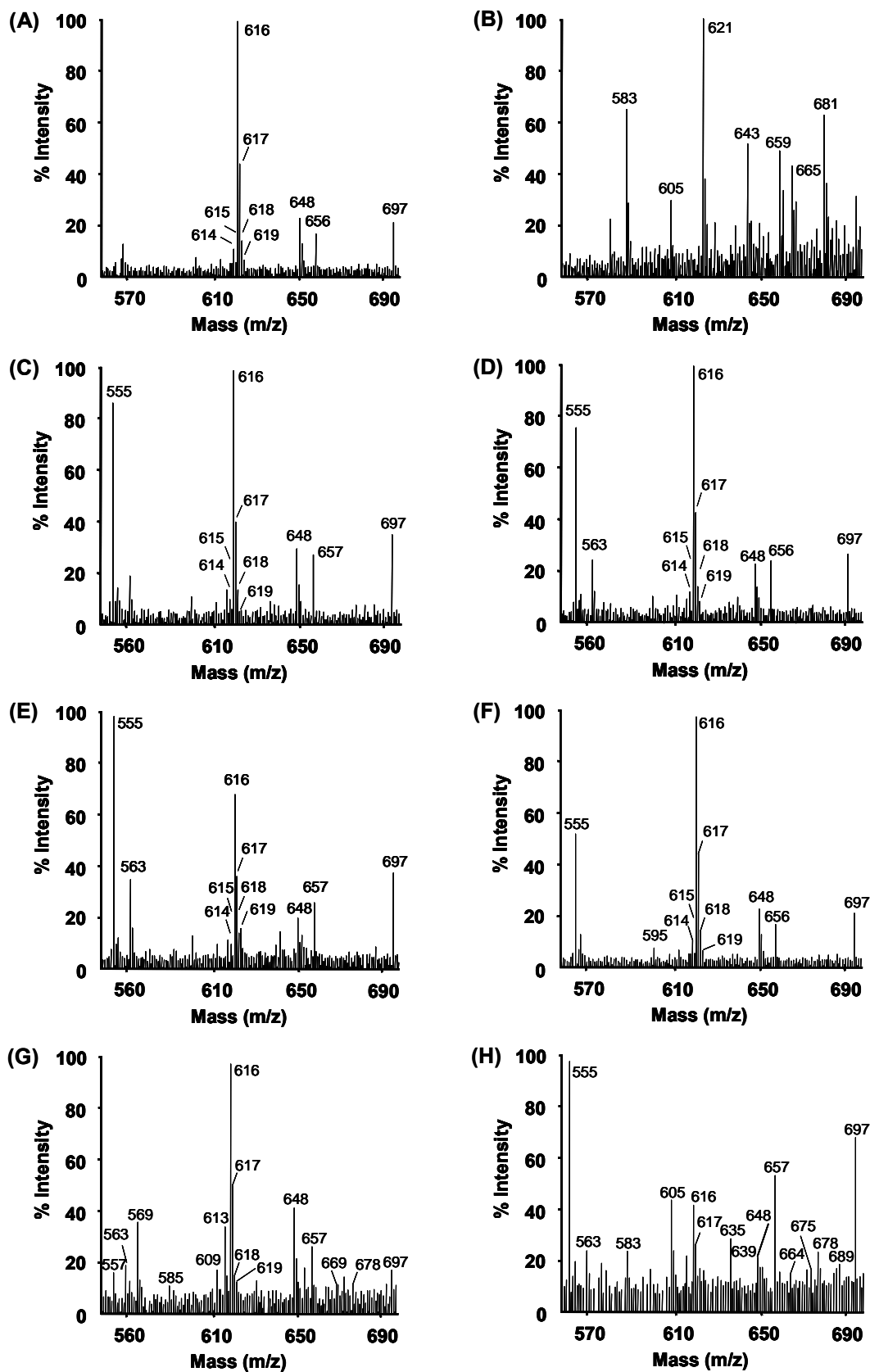


Figure [4.14]: ESI mass spectra of authentic heme (A), authentic biliverdin (B), rsAPX before (C) and after treatment with H<sub>2</sub>O<sub>2</sub> (D) and <sup>t</sup>BuO<sub>2</sub>H (E) and W41A before (F) and after treatment with H<sub>2</sub>O<sub>2</sub> (G) and <sup>t</sup>BuO<sub>2</sub>H (H).

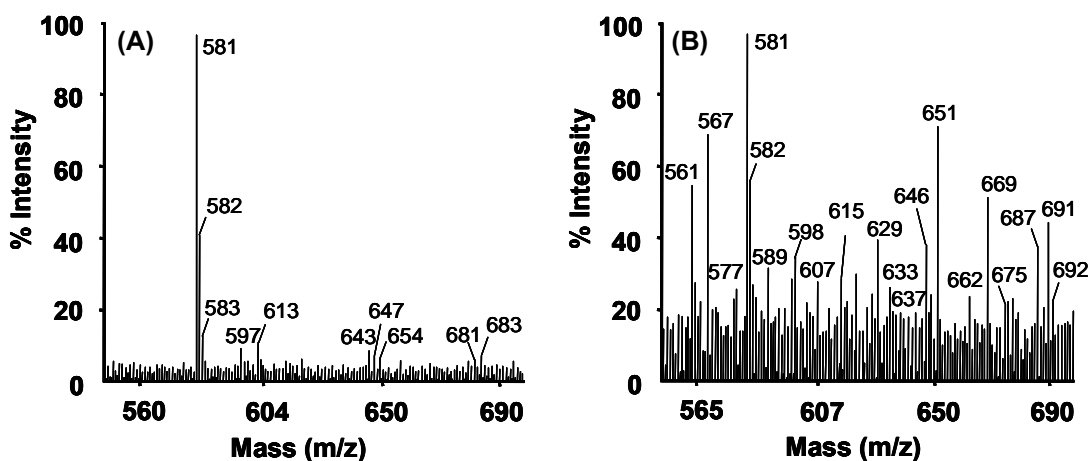


Figure [4.15]: ESI mass spectra (collected in negative mode) of authentic biliverdin (A) and W41A after treatment with <sup>t</sup>BuO<sub>2</sub>H (B).

Previously, reaction of HO with alkoxy peroxides has been found to result in modification of the heme porphyrin (29,30); thus with definitive mass spectral evidence for presence of a modified biliverdin in <sup>t</sup>BuO<sub>2</sub>H-treated W41A it was proposed the simplest modification to biliverdin would be addition of a *tert*-butyl group (<sup>t</sup>Bu), which would give a <sup>t</sup>Bu-modified biliverdin (<sup>t</sup>Bu-biliverdin) species (Figure [4.16A]) with a mass of 638 Da (583 - H (1) + <sup>t</sup>Bu (57)). The mass spectral data collected for the <sup>t</sup>BuO<sub>2</sub>H-treated W41A samples in both positive (Figure [4.14H]) and negative (Figure [4.15B]) ion mode were consistent with the presence of the <sup>t</sup>Bu-biliverdin species proposed in Figure [4.16A] (639 and 637 Da, respectively). A mass of 691 Da was observed in the ESI spectrum of <sup>t</sup>BuO<sub>2</sub>H-treated W41A (Figure 4.15B), which is consistent with the presence of a <sup>t</sup>Bu-biliverdin-iron chelate (calculated mass 692 Da (636 + Fe (56))); however no iron isotope was observed for this mass peak, this may be because the iron is not fully coordinated by the four pyrrole nitrogen's. On observation of the low mass region of the <sup>t</sup>BuO<sub>2</sub>H-treated W41A ESI data, evidence for a pyrrole ring harbouring the *tert*-butyl group was evident (Figure [4.16B]), which further confirmed the <sup>t</sup>Bu-modified structure to be consistent with that proposed in Figure [4.16A]. (Note: a peak with mass of 634 Da was also observed in MALDI-TOF analysis of the fragment with retention time 42 min collected during HPLC purification of <sup>t</sup>BuO<sub>2</sub>H-treated W41A, Figure [4.12G]).

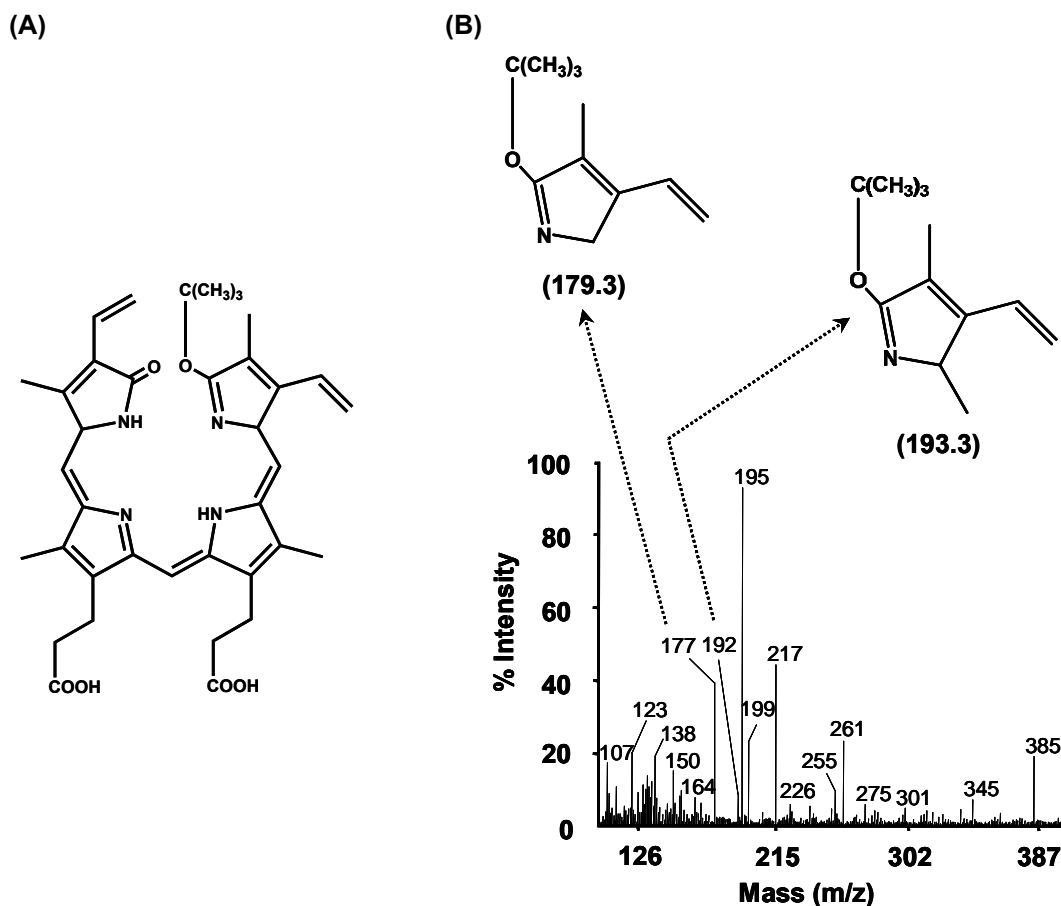


Figure [4.16]: (A) Proposed structure of <sup>1</sup>Bu-biliverdin species (638 Da) observed in ESI mass spectra of <sup>1</sup>BuO<sub>2</sub>H-treated W41A. (B) Low mass range ESI spectrum of <sup>1</sup>BuO<sub>2</sub>H-treated W41A, collected in the negative ion mode, showing evidence for a <sup>1</sup>Bu-modified pyrrole ring. *Inset*: shows assignment of the fragments with mass of 177 and 192 Da, which are consistent with the presence of <sup>1</sup>Bu-modified pyrrole ring. Values shown in parenthesis are the calculated mass (Da) of the corresponding fragment.

### 4.2.3 Detection of a modified-heme species in W41A on reaction with *tert*-butyl hydroperoxide: Crystallographic analysis

To gain a further insight into the reactivity of W41A towards <sup>t</sup>BuO<sub>2</sub>H, the crystal structure of <sup>t</sup>BuO<sub>2</sub>H-soaked W41A was determined. Crystallisation of W41A was performed as described in Chapter 6, Section 6.8.

#### 4.2.3.1 Data interpretation and refinement

Data collection and refinement of the <sup>t</sup>BuO<sub>2</sub>H-soaked W41A crystal structure was conducted with assistance from Dr P. C. E. Moody (Department of Biochemistry, University of Leicester). The <sup>t</sup>BuO<sub>2</sub>H-soaked W41A structure was refined from the 1.35 Å ferric W41A structure (PDB code: 2GGN). The modified heme porphyrin in <sup>t</sup>BuO<sub>2</sub>H-soaked W41A was refined from the 2.19 Å iron-free biliverdin structure from human-HO (PDB code: 1S8C) (13). Several cycles of refinement using RefMAC5 (36) from the CCP4 suite (37) and manual rebuilding of the protein model using COOT (38) followed by addition of water molecules were carried out until the  $R_{\text{free}}$  and  $R_{\text{factor}}$  values converged. The data collection, processing and refinement statistics are presented in Table [4.1].

#### 4.2.3.2. Structure of the *tert*-butyl-modified heme species in W41A

The overall structure (Figure [4.17A]) and most of the active site of <sup>t</sup>BuO<sub>2</sub>H-soaked W41A was found to be similar to that of ferric W41A, although local changes in protein conformation centred around His-42 were detected. The crystal structure of <sup>t</sup>BuO<sub>2</sub>H-soaked W41A (Figure [4.17], Table [4.1]) is similar to the H<sub>2</sub>O<sub>2</sub>-soaked crystal structure of W41A (Chapter 2, Section 2.2.4, Figure [2.11]) in that His-42 is no longer bound to the iron and shows a water molecule in the active site (Fe-O bond distance of 1.9 Å). Hence, the main chain of His-42 in <sup>t</sup>BuO<sub>2</sub>H-soaked W41A has moved away from the heme to a position analogous to that of His-42 in the structure of ferric rsAPX, *i.e.* His-42 is in the “off” position (see Chapter 2).

**Table [4.1]: Data collection and refinement statistics. Values for outer shells are given in parentheses. RMSD, root-mean-square deviation.**

Statistics	<sup>t</sup> BuO <sub>2</sub> H-W41A
<b>Data collection</b>	
Resolution (Å)	82.20-1.40
Outer shell	(1.48-1.40)
Total observations	386646 (51240)
Unique reflections	51023 (7330)
<i>I</i> / $\sigma$	16.5 (3.7)
<i>R</i> <sub>merge</sub>	0.06 (0.57)
Completeness (%)	100 (100)
<b>Refinement</b>	
<i>R</i> <sub>factor</sub>	0.189
<i>R</i> <sub>free</sub>	0.217
RMSD from ideal	
Angles (°)	1.618
Bonds (Å)	0.008

On further examination of the electron density around the heme porphyrin in the <sup>t</sup>BuO<sub>2</sub>H-soaked W41A crystal structure, evidence for cleavage, modification and puckering of the heme porphyrin was observed (Figure [4.17B]). The  $2F_o - F_c$  map was clearly assignable to the electron density of biliverdin, consistent with the fact that heme cleavage occurs at the  $\alpha$ -*meso*-carbon. It is important to note that the  $\alpha$ -*meso*-carbon of heme lies directly below the Ala-41 distal residue in the W41A variant of rsAPX. The additional density observed directly above the site of heme cleavage ( $\alpha$ -*meso*-carbon) in the <sup>t</sup>BuO<sub>2</sub>H-soaked W41A crystal structure was assigned as a *tert*-butyl group, and the resulting <sup>t</sup>Bu-biliverdin species (Figure [4.17B]) was consistent with structure proposed from ESI and MALDI-TOF mass spectrometry analysis (Figure [4.16A]); however, there was unambiguous electron density for the presence of an iron atom in the <sup>t</sup>Bu-modified biliverdin species. In contrast to the iron atom of the biliverdin-iron chelate in rat-HO (Figure [4.17B]) (12),

the iron atom in the <sup>t</sup>Bu-biliverdin-iron chelate was found to be in close proximity to an active site water molecule (Fe-O bond distance of 1.9 Å).

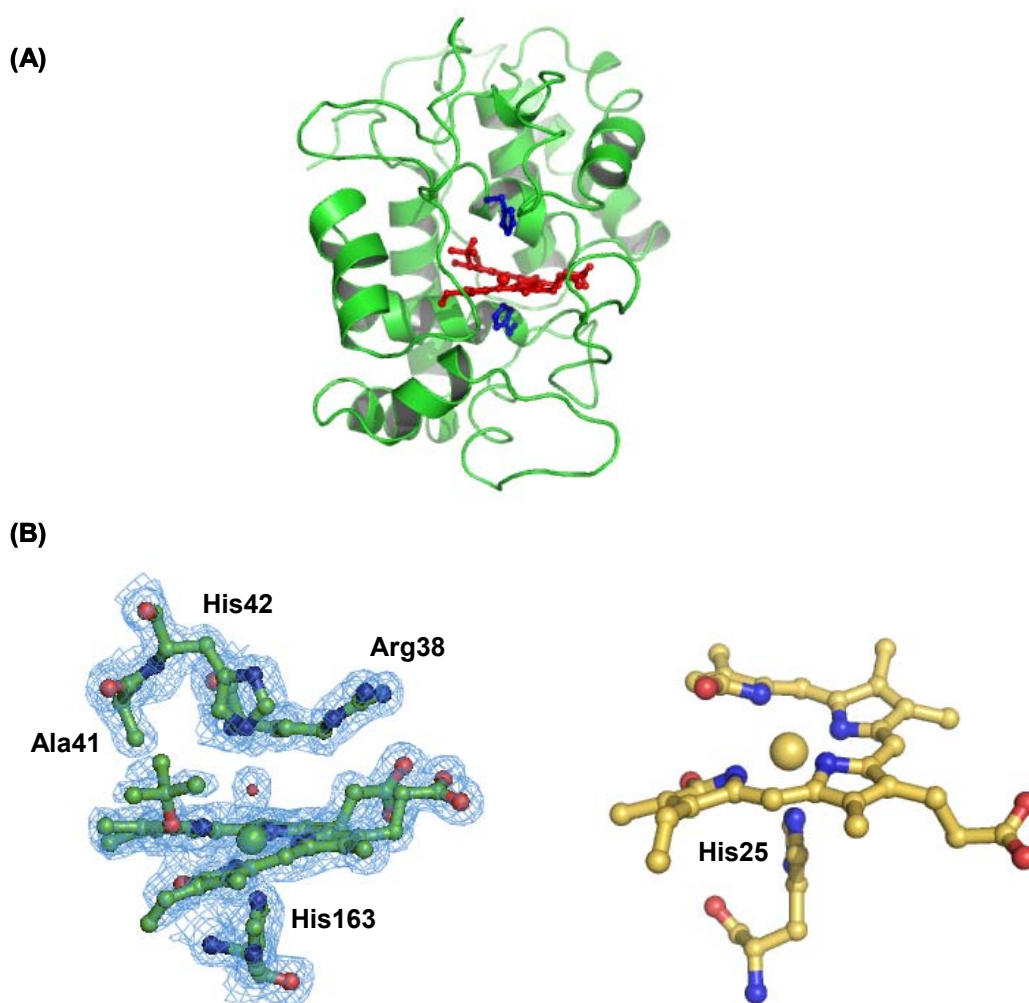
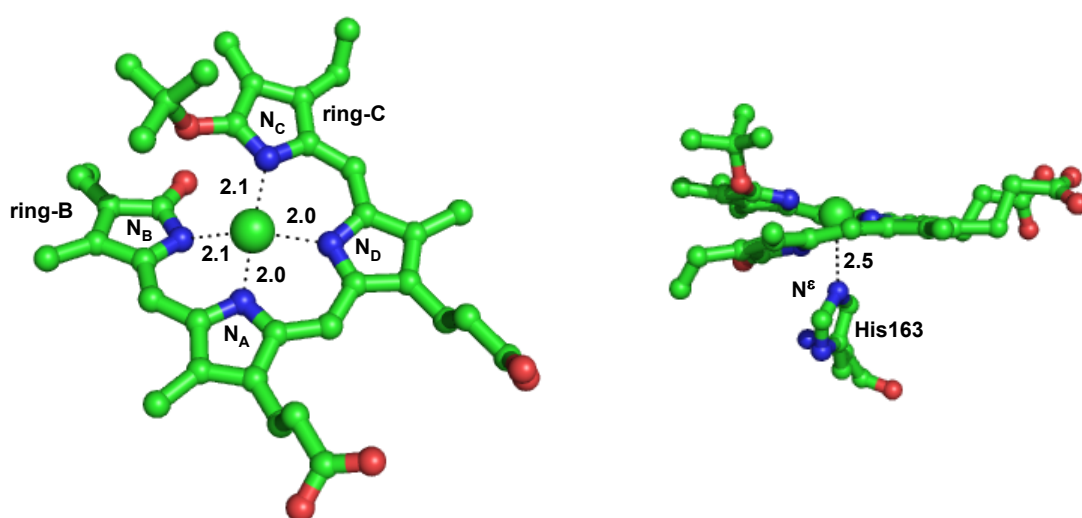


Figure [4.17]: (A) The overall structure of <sup>t</sup>BuO<sub>2</sub>H-treated W41A, showing the <sup>t</sup>Bu-biliverdin-iron chelate (red) and active site (distal and proximal) histidine residues (blue). (B) The active site of <sup>t</sup>BuO<sub>2</sub>H-treated W41A (*left*), showing the <sup>t</sup>Bu-biliverdin-iron chelate. SigmaA-weighted 2F<sub>o</sub> - F<sub>c</sub> electron density at 1 σ is shown in blue and the active site water molecule is shown as a red sphere. The active site of rat-HO (*right*) showing the biliverdin-iron chelate (PDB code: 1J2C, this structure was obtained at 2.4 Å and one propionate group was found to be disordered) (12).

Figure [4.18] shows the coordination geometry to the iron atom in the <sup>t</sup>Bu-biliverdin-iron chelate. The distances between the iron atom and the nitrogen atoms of the four pyrrole rings were found to be similar, ranging from 2.0 to 2.1 Å. A variation was observed in the coordination angles of the four nitrogen atoms about the Fe-N<sup>ε</sup>(His-163) axis (N<sub>A</sub>-Fe-N<sup>ε</sup> = 85.6°; N<sub>B</sub>-Fe-N<sup>ε</sup> = 72.2°; N<sub>C</sub>-Fe-N<sup>ε</sup> = 103.9°; and

$N_D-Fe-N^{\epsilon} = 84.2^{\circ}$ ). Similarly, variation in coordination geometry was also observed in the biliverdin-iron chelate of rat-HO (12), however the corresponding  $N_C-Fe-N^{\epsilon}$  angle in the biliverdin-iron chelate was larger,  $130.9^{\circ}$ , than that observed for the  ${}^t\text{Bu}$ -biliverdin-iron chelate. This difference is likely to be due to the attachment of the bulky *tert*-butyl group to ring C in the  ${}^t\text{Bu}$ -biliverdin-iron chelate, which occupies a lot of space in the distal cavity and thus the  $N_C-Fe-N^{\epsilon}$  angle is restricted. Also recent crystallographic studies have provided evidence for a large internal cavity in HO to accommodate biliverdin, which in the iron-free form prefers to adopt the more energetically favourable linear conformation (13).



**Figure [4.18]:** The coordination geometry of the iron atom in the  ${}^t\text{Bu}$ -biliverdin-iron chelate of W41A. Coordinate bonds to the iron are indicated by black dashed lines and the distances between atoms are shown in Angstroms (Å).

The  ${}^t\text{Bu}$ -biliverdin-iron chelate similar to the biliverdin-iron chelate in rat-HO (12) also has a helical conformation with the lactam oxygen atoms of ring C and ring B pointing upward and downward, respectively (Figure [4.17B]). By nature, biliverdin assumes a helical structure to avoid collision with the lactam oxygen atoms (12). The helical pitch of the biliverdin in the  ${}^t\text{Bu}$ -biliverdin-iron chelate, defined as the distance between the two oxygen atoms, was  $2.5 \text{ \AA}$  which is shorter than that observed for the biliverdin-iron chelate in rat-HO ( $3.4 \text{ \AA}$ ) (12). The helical pitch in  ${}^t\text{Bu}$ -biliverdin-iron chelate is probably restricted due to the presence of the bulky *tert*-butyl group. Similarly, shorter helical pitches have been reported in biliverdin crystallised with apomyoglobin,  $2.9 - 3.0 \text{ \AA}$  (39) and for biliverdin IX $\beta$  reductase,  $2.8 \text{ \AA}$  (40). The Fe-

$N^{\epsilon}$ (His-163) distance was found to be longer in <sup>t</sup>Bu-biliverdin-iron chelate (2.5 Å) of W41A than that reported for heme in the W41A variant (2.1 Å) (31).

In parallel experiments, single-crystal microspectrophotometry was also used to monitor the <sup>t</sup>BuO<sub>2</sub>H-soaked W41A crystal during exposure to the X-ray beam. Surprisingly, the spectrum of the <sup>t</sup>BuO<sub>2</sub>H-soaked W41A crystal (Figure [4.19]) before data collection was found to be characteristically different to that in solution (see Figure [4.5 and 4.10]). The wavelength maxima ( $\lambda_{\text{max}}$ /nm = 532 and 559) of <sup>t</sup>BuO<sub>2</sub>H-soaked W41A crystal before data collection was identical to that observed for the hydroperoxo HO intermediate ( $\lambda_{\text{max}}$ /nm = 421, 530 and 557) (41) determined using cryogenic UV-visible spectroscopy and was also in good agreement with the spectrum of hydroperoxo intermediate detected in HRP (42) and the H64Q variant of myoglobin (42-44). During data collection the <sup>t</sup>BuO<sub>2</sub>H-soaked W41A crystal was affected by the X-ray beam (the phenomenon of X-ray reduction is discussed in Chapter 3) and the spectrum of <sup>t</sup>BuO<sub>2</sub>H-soaked W41A (Figure [4.19]) on completion of data collection was altered ( $\lambda_{\text{max}}$ /nm = 532, 563 and 630) and was indicative of ferric W41A.

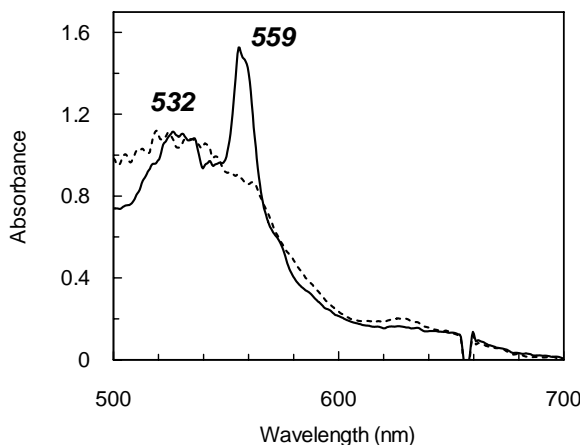


**Figure [4.19]:** Changes in the absorption spectrum (100 K) of a crystal of <sup>t</sup>BuO<sub>2</sub>H-soaked W41A crystal before (solid line) and after (dotted line) exposure to the X-ray beam.

**Note:** The X-ray data collected in conjunction with single-crystal microspectrophotometry yielded a structure with resolution of 1.90 Å, thus another data set was collected at higher resolution (1.40 Å) for which single-crystal microspectrophotometry analysis was not possible. The structures presented above are from the 1.40 Å crystal structure. However, both data sets showed clear evidence for cleavage and modification of the heme porphyrin.

### 4.3 DISCUSSION

It has been known for many years that some heme proteins, such as myoglobin (45-48) and variants of cytochrome  $b_5$  (49,50) and cytochrome  $b_{562}$  (51), undergo a series of reactions in the presence of ascorbate and oxygen (coupled oxidation) that resemble the catalytic cycle of HO. However, only HO is known to catalyse the analogous process of heme degradation in the presence of peroxides ( $H_2O_2$  and methyl hydroperoxide) (28,29). This Chapter describes how the W41A variant of rsAPX, like HO, catalyses the cleavage of the  $\alpha$ -meso-carbon of the heme porphyrin on exposure to the bulky peroxide,  $^tBuO_2H$ . With the use of spectroscopic, crystallographic and analytical techniques, a mechanism for regiospecific cleavage of the  $\alpha$ -meso-carbon of the heme porphyrin that involves formation of a hydroperoxo type intermediate is presented.

#### 4.3.1 Spectroscopic analysis of the reaction of W41A with *tert*-butyl hydroperoxide

Reaction of W41A with  $H_2O_2$  yields the peroxidase cycle catalytic (ferryl) intermediates, however on exposure to the bulky peroxide,  $^tBuO_2H$  no spectral changes indicative of the peroxidase cycle catalytic intermediates were detected. Instead, a rapid decrease of the absorbance at the Soret maxima and visible region, similar to that observed on reaction of HO with  $H_2O_2$  (18-24), was detected. Similar spectral changes were observed when the reaction of W41A with  $^tBuO_2H$  was examined using stopped-flow apparatus, *i.e.* no evidence of a ferryl species. In contrast, spectral changes indicative of the peroxidase catalytic intermediates observed on reaction of rsAPX with  $H_2O_2$  were also detected on reaction with  $^tBuO_2H$ . Stopped-flow analysis of the reaction of rsAPX with  $^tBuO_2H$  further confirmed the results obtained using the conventional UV-visible spectrophotometer and the rate constant for Compound I formation on reaction of rsAPX with  $^tBuO_2H$  ( $k_1 = 9.7 \pm 0.5 \times 10^4 \text{ M}^{-1} \text{ s}^{-1}$ ) was found to be slower in comparison to reaction with  $H_2O_2$  ( $k_1 = 3.3 \pm 0.1 \times 10^7 \text{ M}^{-1} \text{ s}^{-1}$ ) (34).

A ferric-like rsAPX species was observed when ascorbate was added to  $^tBuO_2H/H_2O_2$ -treated rsAPX. Similarly, a ferric-like species was revealed on addition of ascorbate to  $H_2O_2$ -treated W41A. However, no spectral changes were observed

when ascorbate was added to <sup>t</sup>BuO<sub>2</sub>H-treated W41A, thus providing further evidence for absence of a ferryl species on reaction of W41A with <sup>t</sup>BuO<sub>2</sub>H. Also the reaction of W41A with <sup>t</sup>BuO<sub>2</sub>H proceeded with a change of the W41A protein from a red to a green colour, which is indicative of heme degradation to bilin pigments (32).

Collectively the above spectroscopic data provide evidence for the absence of a ferryl species in reaction of the W41A with the bulky peroxide <sup>t</sup>BuO<sub>2</sub>H and these data further support the idea of the non-involvement of a ferryl (Compound I/II) species in heme oxygenase catalysis (7).

#### 4.3.2 Mass spectrometry and HPLC analysis of the reaction of W41A with *tert*-butyl hydroperoxide

Unmodified and cleaved/bleached forms of heme were the major heme species observed in the HPLC elution profiles of H<sub>2</sub>O<sub>2</sub>-treated W41A and H<sub>2</sub>O<sub>2</sub>/<sup>t</sup>BuO<sub>2</sub>H-treated rsAPX. In addition to unmodified and cleaved/bleached heme, a further four peaks (retention times of 17, 23, 42 and 46 min) were detected in the HPLC elution profile of <sup>t</sup>BuO<sub>2</sub>H-treated W41A. Using MALDI-TOF analysis the heme species with retention time of 23 and 46 min were assigned as heme minus a proton and heme without the iron atom, respectively. Traces of the heme species with retention time of 23 and 46 min were also detected in HPLC elution profiles of rsAPX and H<sub>2</sub>O<sub>2</sub>/<sup>t</sup>BuO<sub>2</sub>H-treated rsAPX. The heme species with retention times of 17 and 42 min were solely detected in the elution profile of <sup>t</sup>BuO<sub>2</sub>H-treated W41A and MALDI-TOF analysis of these fragments revealed presence of modified heme species. MALDI-TOF analysis of the heme species from <sup>t</sup>BuO<sub>2</sub>H-treated W41A with retention time of 17 min revealed a mass of 583 Da, which is indicative of biliverdin (authentic biliverdin was found to elute with a retention time of 20 min), as well as a major species with a mass of 664 Da. This major species was identified as <sup>t</sup>BuO<sub>2</sub>H-modified heme porphyrin (Figure [4.12E] *inset*) formed by a radical mechanism as proposed by Wojciechowski and Ortiz de Montellano (33) on studies of the phenylalanine variant (F152M) of HRP with <sup>t</sup>BuO<sub>2</sub>H. Cleavage of the  $\alpha$ -meso-carbon was not evident in studies of the HRP variant (F152M) with <sup>t</sup>BuO<sub>2</sub>H, this may be because the bulky distal phenylalanine residue blocks correct orientation of <sup>t</sup>BuO<sub>2</sub>H (discussed later) in the heme cavity thus the reaction proceeds via a radical mechanism. The heme species that eluted with a retention time of 42 min was only

observed in the HPLC elution profile of <sup>t</sup>BuO<sub>2</sub>H-treated W41A and MALDI-TOF analysis of this heme species revealed peaks with mass of 634 Da and 583 Da. The presence of biliverdin (583 Da) in the heme species eluting with retention time of 42 min was thought to arise from fragmentation of a <sup>t</sup>Bu-modified form of biliverdin (634 Da), and not due to the sole formation of biliverdin (because of the significant difference in retention time of this heme species in comparison to authentic biliverdin, 42 and 17 min, respectively). Similarly biliverdin (583 Da) and <sup>t</sup>Bu-modified biliverdin (638 Da) were also detected in ESI mass spectrometry experiments conducted on <sup>t</sup>BuO<sub>2</sub>H-treated W41A. Based on the fragmentation patterns observed in the mass spectra of <sup>t</sup>BuO<sub>2</sub>H-treated W41A, a structure was assigned to the <sup>t</sup>Bu-biliverdin species (638 Da, Figure [4.16A]).

### **4.3.3 Evidence for formation of a hydroperoxo species in reaction of W41A with *tert*-butyl hydroperoxide: crystallographic analysis**

#### ***4.3.3.1 The tert-butyl hydroperoxide-soaked W41A crystal structure***

The overall structure <sup>t</sup>Bu-treated W41A was similar to that observed for ferric W41A, however His-42 was displaced and was found to move a way from the iron occupying the “off” position (see Chapter 2). Analysis of the electron density revealed evidence for cleavage and modification of the heme moiety of the <sup>t</sup>BuO<sub>2</sub>H-treated W41A variant. The structure of the <sup>t</sup>Bu-biliverdin-iron chelate observed in the <sup>t</sup>BuO<sub>2</sub>H-soaked W41A crystal was identical to the structure proposed from analysis of the ESI and MALDI-TOF data (Figure [4.16A]). The <sup>t</sup>Bu-biliverdin-iron chelate was found to adopt a helical conformation as observed for biliverdin-iron chelate of rat-HO (12).

#### ***4.3.3.2 Evidence for formation of a hydroperoxo species***

The hydroperoxo intermediate, or “Compound 0”, is a common intermediate in heme enzyme catalysis (52). It appears as a distinct transient species on the path to the higher valent ferryl-oxo states in enzymatic cycles of the cytochromes P450, nitric oxide synthases, and heme oxygenases, all of which reduce dioxygen, as well as in heme peroxidases and catalases in their reactions with H<sub>2</sub>O<sub>2</sub>. Compound 0 is intrinsically unstable and is found to decompose faster than it forms, and hence is extremely difficult to observe and characterise (53,54). However, many methods to

detect and characterise this transient intermediate, Compound 0, have been employed including cryogenic radiolytic reduction of the one-electron precursor oxyferrous complex in frozen solution or crystals (55-57), EPR (42,58-66), optical absorption (41,42,67,68), and Raman spectroscopy (68,69) in various heme proteins.

In this study the single-crystal microspectrophotometry spectrum of  $^t\text{BuO}_2\text{H}$ -soaked W41A crystal before data collection was found to be similar to the ferric hydroperoxo HO species detected using cryogenic UV-visible spectroscopy (41). Detection of the transient hydroperoxo intermediate would require formation of a stable  $^t\text{BuO}_2\text{H}$ -W41A complex and thus it is likely that the species detected for the  $^t\text{BuO}_2\text{H}$ -soaked W41A crystal is a *tert*-butyl substituted form of a hydroperoxo species (Figure [4.20]). This *tert*-butyl-hydroperoxo intermediate, as illustrated in Figure [4.20], is likely to orientate the bulky *tert*-butyl group in the space above the  $\alpha$ -*meso*-carbon of the heme porphyrin in the W41A active site, which is occupied by the tryptophan residue in rsAPX (shown in faint blue in Figure [4.20]). This proposal is further confirmed from the crystal structure of  $^t\text{BuO}_2\text{H}$ -treated W41A where the *tert*-butyl group attaches to the porphyrin ring directly beneath the residue at position 41. The active site of peroxidases are quite constricted thus alternative conformation of the bulky  $^t\text{BuO}_2\text{H}$  would be unlikely. The binding orientation of  $^t\text{BuO}_2\text{H}$  depicted in Figure [4.20], differs from that proposed for  $\text{H}_2\text{O}_2$  by Finzel *et al.* (70) in which the peroxide bond is directed towards the propionate groups (Figure [4.20]), so that the conserved distal histidine (His-42) and arginine (Arg-38) can polarise the peroxide bond thus favouring heterolytic cleavage.

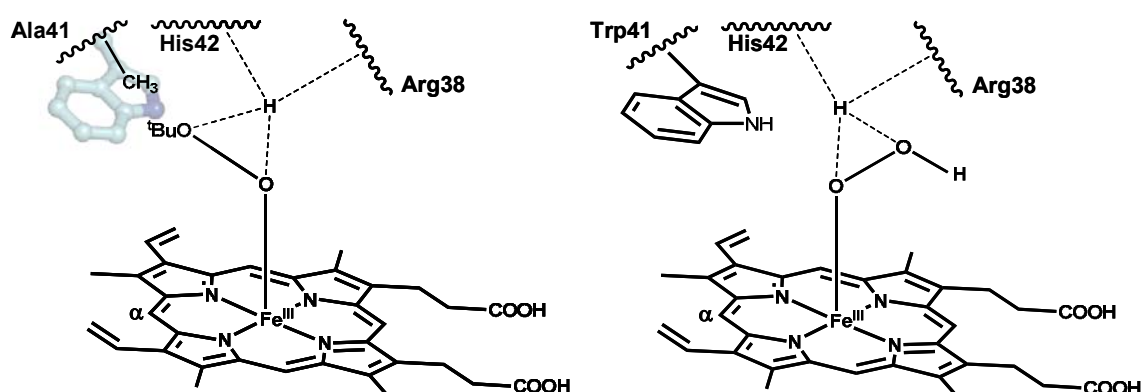
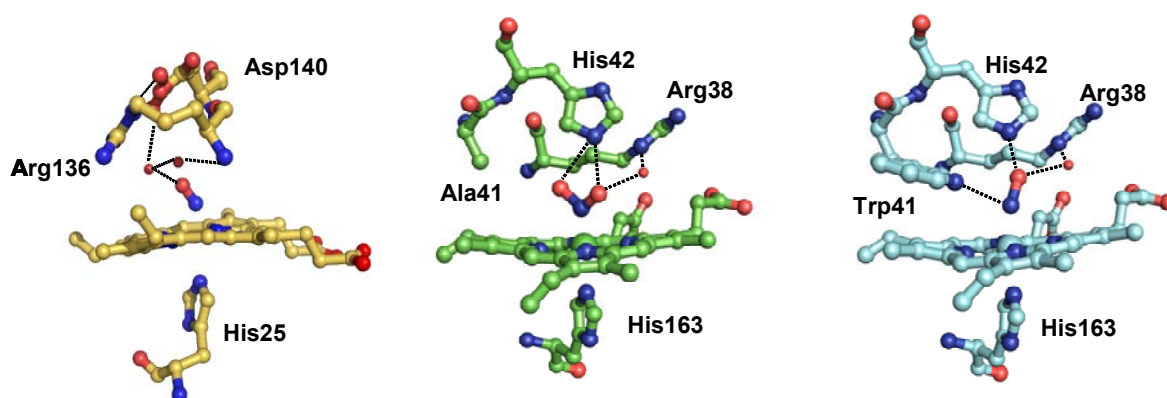


Figure [4.20]: (A) Proposed binding orientation of  $^t\text{BuO}_2\text{H}$  in W41A (position of Trp-41 (faint blue) of rsAPX is also shown). (B) Proposed binding orientation of  $\text{H}_2\text{O}_2$  in peroxidases. Adapted from (70). The  $\alpha$ -carbon is indicated in both cases. Hydrogen bonds are indicated by dashed lines.

Diatomic ligands, such as cyanide, nitric oxide and carbon monoxide are used in crystallographic studies as mimics of the hydroperoxo intermediate and thus it is instructive here to compare the crystal structures for the nitric oxide complexes of HO (71), W41A (31) and rsAPX (31). The nitric oxide ligand in the W41A-nitric oxide complex (Chapter 2, Section 2.2.4) was found to adopt two conformations due to loss of a hydrogen bond from the distal tryptophan (Trp-41). In one conformation the nitric oxide ligand in W41A (Figure [4.21]) is directed towards the  $\alpha$ -*meso*-carbon as observed in the crystal structure of the HO-nitric oxide complex (Figure [4.21]). In the other conformation, as observed in the rsAPX-nitric oxide complex (Figure [4.21]), the nitric oxide ligand in W41A is directed towards the propionates. A similar *tert*-butyl-hydroperoxo intermediate was reported during Electron Spin Resonance (ESR) studies on <sup>t</sup>BuO<sub>2</sub>H-treated cytochrome P450 (72).



**Figure [4.21]:** Structures of the nitric oxide-bound complexes of HO (*left*) (71), W41A (*centre*) (31) and rsAPX (*right*) (31). PDB code: 1OZW, 2GHC and 2GHH, respectively. The loss of the indole of Trp-41 in W41A allows the nitric oxide molecule to adopt two conformations. Hydrogen bonds are shown as black dotted lines. Water molecules are shown as red spheres.

The single-crystal microspectrophotometry spectrum of the <sup>t</sup>BuO<sub>2</sub>H-soaked W41A crystal before data collection revealed absorbance peaks at 532 and 559 nm which disappeared during data collection to yield a ferric-like spectrum. Interestingly the single-crystal microspectrophotometry spectrum of the <sup>t</sup>BuO<sub>2</sub>H-soaked W41A crystal before data collection was significantly different to that observed in solution studies. This may be due to the cryogenic conditions employed during crystallographic studies that slow down the reaction between <sup>t</sup>BuO<sub>2</sub>H and W41A allowing detection of a transient hydroperoxo intermediate which is not observed

during spectroscopic and transient kinetic studies, which are conducted at 5.0 °C, because of rapid addition of the <sup>t</sup>BuO-group to the  $\alpha$ -*meso*-carbon of the heme porphyrin.

#### 4.3.3.3 Mechanism for formation of *tert*-butyl-biliverdin

A possible mechanism for formation of <sup>t</sup>Bu-biliverdin that embodies all the available data collected for reaction of W41A with <sup>t</sup>BuO<sub>2</sub>H is presented in Figure [4.22]. The mechanism has been proposed to involve the following steps:

- (a) reaction of heme with <sup>t</sup>BuO<sub>2</sub>H to form a *tert*-butyl-hydroperoxo intermediate [1].
- (b) Electrophilic attack on the distal oxygen by the porphyrin ring to yield a *tert*-butyl variant of  $\alpha$ -*meso*-hydroxyheme termed  $\alpha$ -*meso-tert*-butyl-oxyheme [2].
- (c) The mechanism for conversion of  $\alpha$ -*meso*-hydroxyheme to verdoheme is speculative thus a hypothetical mechanism based on the mechanism proposed by Ortiz de Montellano (73) is discussed with respect to conversion of  $\alpha$ -*meso-tert*-butyl-oxyheme to verdoheme. The electronic structure of ferric  $\alpha$ -*meso*-hydroxyheme can be presented by three resonance structures [3]: a ferric keto anion, a ferric phenolate ion and a ferrous neutral radical. The ferrous neutral radical form is generated by an intramolecular electron transfer between the iron and the porphyrin ring (26).
- (d) Binding of oxygen to the porphyrin free radical, (e) followed by binding of the terminal oxygen to the iron, produces a bridged peroxo species;
- (f) homolytic cleavage of the dioxygen bond is followed (g-h) by extrusion of carbon monoxide.
- (i) Electron transfer from the resulting vinyl cation, and
- (j) trapping of the cation by the carbonyl group, produces verdoheme [4]. The oxygen bound to the iron in the sequence is lost in the final step as a water molecule.

Verdoheme then has two fates it can react, as usual, with oxygen to form biliverdin or can react with <sup>t</sup>BuO<sub>2</sub>H to form <sup>t</sup>Bu-biliverdin or biliverdin. Again a

speculative mechanism for conversion of verdoheme to biliverdin upon reaction with oxygen has been proposed by Ortiz de Montellano (73). The mechanism involves:

- (k) binding of oxygen to the porphyrin (can also get binding of oxygen to iron).
- (l) One-electron reduction of the bound oxygen then produces a hydroperoxide that bridges the iron and porphyrin.
- (m-n) Heterolytic cleavage of the peroxo bridge species cleaves the verdoheme ring; and
- (o) subsequent reduction and loss of the bound oxygen as a water molecule yields ferric biliverdin [5].

The reaction of verdoheme [4] with  ${}^t\text{BuO}_2\text{H}$  (based on the mechanism proposed for reaction of verdoheme with  $\text{H}_2\text{O}_2$  and methyl hydroperoxide) (28,29) proceeds in a less complicated manner than that observed for the reaction with oxygen (steps k-o). The mechanism has been proposed to involve the following steps:

- (p, r) due to the resonance structures of verdoheme,  ${}^t\text{BuO}_2\text{H}$  can bind at either the  $\alpha$ -pyrrole carbon cation of verdoheme [6] or the verdoheme iron [7].
- (q) The peroxide bond of [6] may be cleaved ionically to form (formally) a ferryl-biliverdin complex which undergoes a one-electron reduction to yield ferric biliverdin [5] (28).
- (s) The  ${}^t\text{Bu}$ -bound verdoheme [7] can be a resonance form of ferric and ferrous hydroperoxo species with varied oxidation states of the porphyrin. The partial radical character on the  $\alpha$ -pyrrole carbon of [7] promotes peroxide bond homolysis leading to addition of a *tert*-butyl-oxy radical to the  $\alpha$ -pyrrole radical to yield [8].
- (t) The ring opening and subsequent reduction of [8], followed by a loss of a water molecule yields  ${}^t\text{Bu}$ -biliverdin [9].

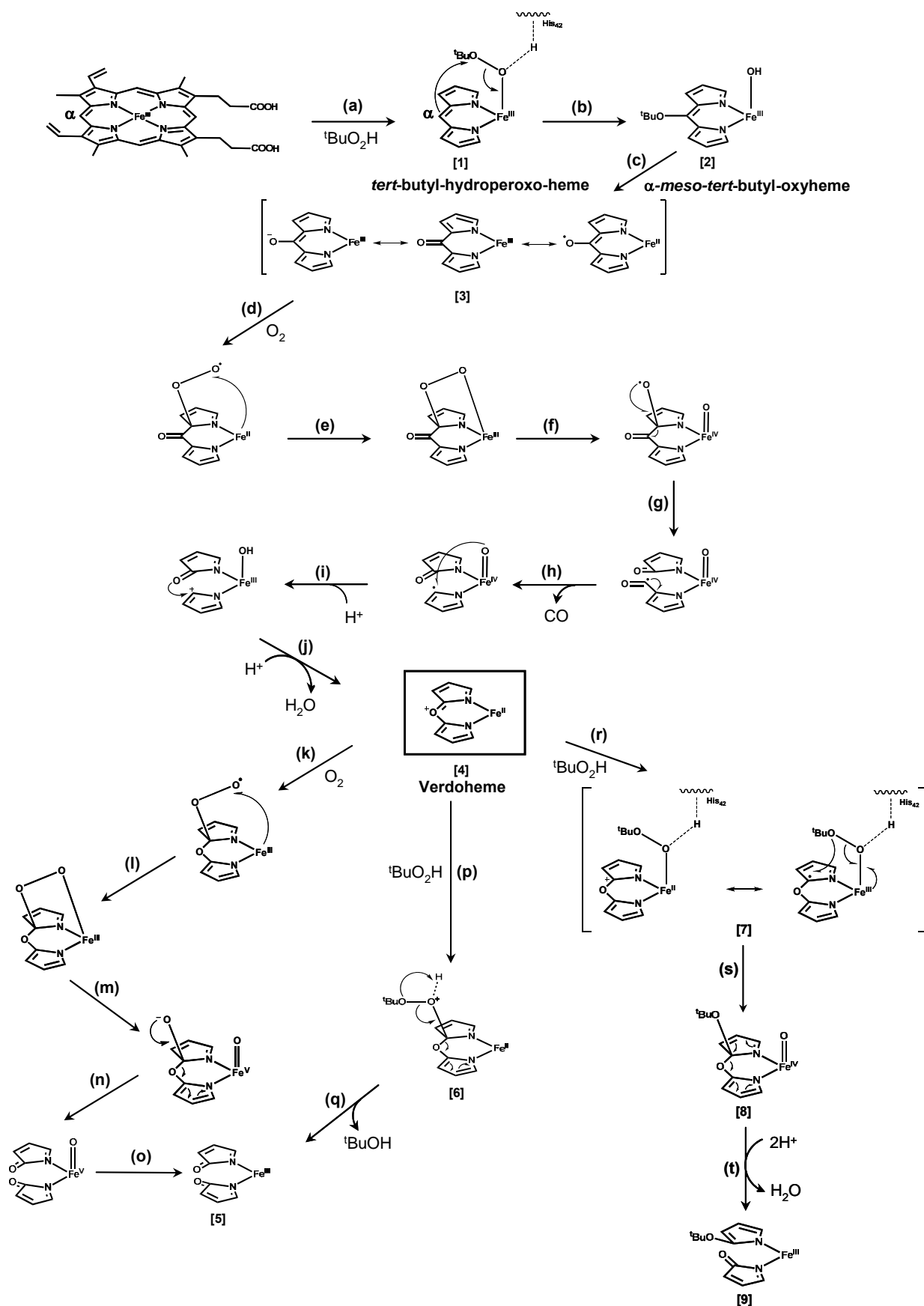


Figure [4.22]: Proposed mechanism for formation of biliverdin and <sup>t</sup>Bu-biliverdin on reaction of W41A with <sup>t</sup>BuO<sub>2</sub>H. Peripheral substituents and the right side of the porphyrin are omitted for clarity. Steps (a) – (t) are described in the text.

#### 4.4 SUMMARY

In summary, the present studies show that it is possible to introduce new reactivity into APX, by replacement of the distal tryptophan 41 residue (with alanine). The W41A variant formed a modified heme species, similar to that observed during HO catalysis, on reaction with  ${}^t\text{BuO}_2\text{H}$ . Spectroscopic studies revealed that the W41A variant, unlike rsAPX, did not form a ferryl species on reaction with  ${}^t\text{BuO}_2\text{H}$ . Analysis of the HPLC and mass spectrometry (MALDI-TOF and ESI) data for  ${}^t\text{BuO}_2\text{H}$ -treated W41A provided clear evidence for presence of the heme degradation product biliverdin and a modified ( ${}^t\text{Bu}$ -biliverdin) heme species. The structure of the modified heme species was confirmed from analysis of the  ${}^t\text{BuO}_2\text{H}$ -treated W41A crystal structure and a mechanism for this reaction is proposed in Figure [4.22]. The reaction proceeds in a similar manner to that proposed for HO, with formation of hydroperoxo,  $\alpha$ -meso-hydroxyheme and verdoheme type intermediates. Single-crystal microspectrophotometry data were consistent with the presence of a hydroperoxo-like intermediate in the  ${}^t\text{BuO}_2\text{H}$ -soaked W41A crystal. Interestingly, the hydroperoxo intermediate is common to the catalytic cycles of many heme proteins, *i.e.*, catalases, cytochrome P450 monooxygenases, nitric oxide synthases and peroxidases. The hydroperoxo intermediate in these heme proteins forms a ferryl species (Figure [4.23]); whereas in HO catalysis, the hydroperoxo species hydroxylates the heme porphyrin (Figure [4.23]). The question that arises is what governs the fate of this common intermediate; the hypothesis to date is that the hydroperoxo intermediate must decay to the ferryl species fast enough to avoid self-oxidation of the heme group (19). The speed of reactivity, which governs the fate of the hydroperoxo intermediate, appears to be dependent on the heme protein environment and the nature of the oxidising agent (29). For example, in this study the reaction of rsAPX with  $\text{H}_2\text{O}_2$ / ${}^t\text{BuO}_2\text{H}$  proceeds down the peroxidase route as does the reaction of W41A with  $\text{H}_2\text{O}_2$ . However, the reaction of W41A with a bulky analogue of  $\text{H}_2\text{O}_2$ ,  ${}^t\text{BuO}_2\text{H}$ , diverts the peroxidase to follow the heme oxygenase mechanism. In the case of W41A the nature of the peroxide defines whether a peroxidase or heme oxygenase mechanism is utilised.

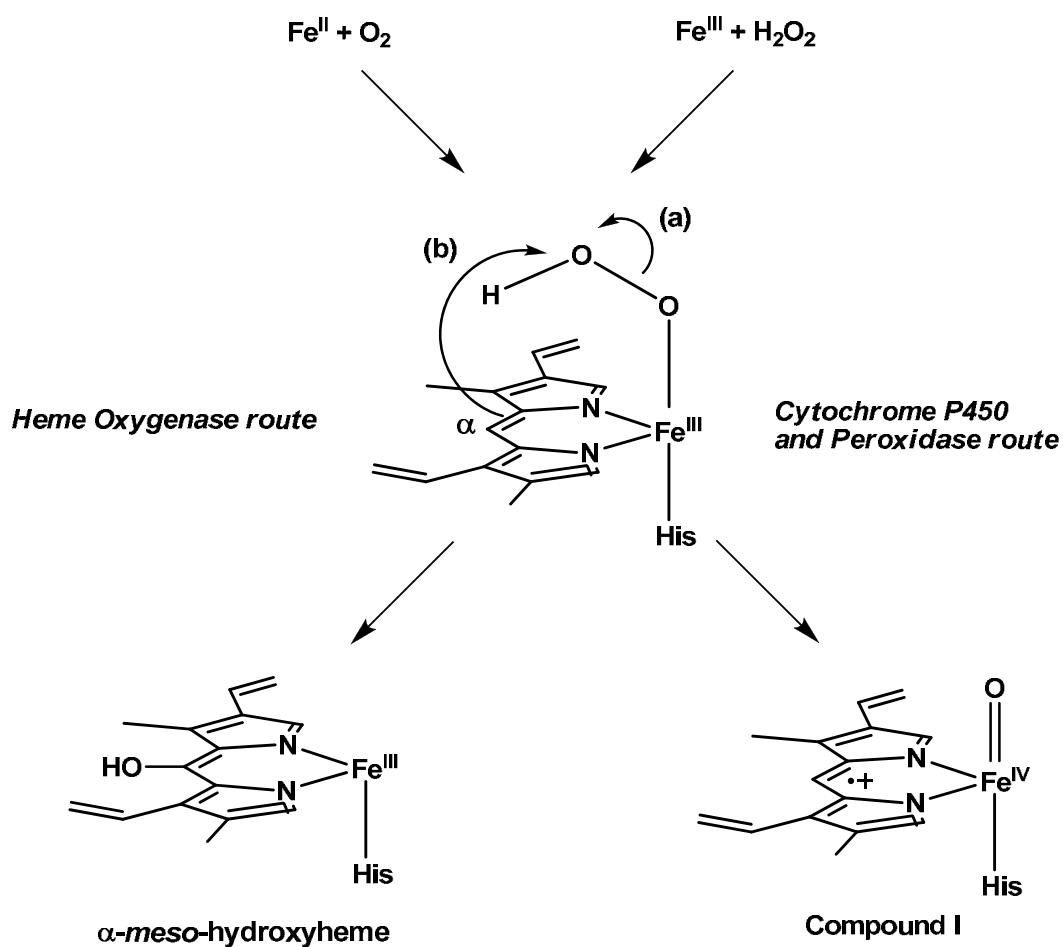


Figure [4.23]: Comparison of the fate of the common catalytic hydroperoxo intermediate in cytochrome P450, peroxidases and heme oxygenases. One-electron reduction and protonation of the ferrous-oxygen complex in heme oxygenase or in the case of heme peroxidases and cytochrome P450 reaction with hydrogen peroxide yields a ferric hydroperoxo species ( $\text{Fe}^{\text{III}}\text{-OOH}$ ). In cytochrome P450 and the peroxidases (a) the O-O bond of  $\text{Fe}^{\text{III}}\text{-OOH}$  is heterolytically cleaved to afford a reactive oxo-ferryl species (Compound I); Whereas in heme oxygenase (b) the terminal oxygen of  $\text{Fe}^{\text{III}}\text{-OOH}$  is attacked by the porphyrin  $\alpha$ -meso-carbon to form  $\alpha$ -meso-hydroxyheme. Adapted from (7).

**4.5 REFERNECES**

1. Beale, S. I., and Cornejo, J. (1984) *Archives of Biochemistry and Biophysics* **235**, 371-384
2. Cornejo, J., Willows, R. D., and Beale, S. I. (1998) *Plant Journal* **15**, 99-107
3. Davis, S. J., Kurepa, J., and Vierstra, R. D. (1999) *Proceedings of the National Academy of Sciences of the United States of America* **96**, 6541-6546
4. Tenhunen, R., Marver, H. S., and Schmid, R. J. (1969) *Journal of Biological Chemistry* **244**, 6388-6394
5. Yoshida, T., and Kikuchi, G. J. (1978) *Journal of Biological Chemistry* **253**, 4224-4229
6. Yoshida, T., and Kikuchi, G. J. (1979) *Journal of Biological Chemistry* **254**, 4487-4491
7. Unno, M., Matsui, T., and Ikeda-Saito, M. (2007) *Natural Product Reports* **24**, 553-570
8. Verma, A., Hirsch, D. L., Glatt, C. E., Ronnet, G. V., and Snyder, S. H. (1993) *Science* **259**, 381-384
9. Nathanson, J. A., Scavone, C., Scanlon, C., and McKee, M. (1995) *Neuron* **14**, 781-794
10. Zakhary, R., Gaine, S. P., Dinerman, J. L., Ruat, M., Flavahan, N. A., and Snyder, S. H. (1996) *Proceedings of the National Academy of Sciences of the United States of America* **93**, 795-798
11. Schuller, D. J., Wilks, A., Ortiz de Montellano, P. R., and Poulos, T. L. (1999) *Nature Structural Biology* **6**, 860-867
12. Sugishima, M., Sakamoto, H., Higashimoto, Y., Noguchi, M., and Fukuyama, K. (2003) *Journal of Biological Chemistry* **278**, 32352-32358

13. Lad, L., Friedman, J., Li, H., Bhaskar, B., Ortiz de Montellano, P. R., and Poulos, T. L. (2004) *Biochemistry* **43**, 3793-3801
14. Lad, L., Schuller, D. J., Shimizu, H., Friedman, J., Li, H. Y., Ortiz de Montellano, P. R., and Poulos, T. L. (2003) *Journal of Biological Chemistry* **278**, 7834-7843
15. Yoshida, T., Noguchi, M., and Kikuchi, G. J. (1980) *Journal of Biological Chemistry* **255**, 4418-4420
16. Ortiz de Montellano, P. R., and Wilks, A. (2001) *Advances in Inorganic Chemistry* **51**, 359-407
17. Sono, M., Roach, M. P., Coulter, E. D., and Dawson, J. H. (1996) *Chemical Reviews* **96**, 2841-2887
18. Fujii, H., Zhang, X., Tomita, T., Ikeda-Saito, M., and Yoshida, T. (2001) *Journal of American Chemical Society* **123**, 6475-6484
19. Ortiz de Montellano, P. R. (1998) *Accounts of Chemical Research* **31**, 543-549
20. Avila, L., Hong, H., Damaso, C., Shen, L., Moenne-Loccoz, P., and Rivera, M. (2003) *Journal of American Chemical Society* **125**, 4103-4110
21. Wilks, A., and Ortiz de Montellano, P. R. (1993) *Journal of Biological Chemistry* **268**, 22357-22362
22. Chu, C. G., Katakura, K., Zhang, X., Yoshida, T., and Ikeda-Saito, M. (1999) *Journal of Biological Chemistry* **274**, 21319-21325
23. Ishikawa, K., Takauechi, N., Takahashi, S., Matera, K. M., Sato, M., Shibahara, S., Rousseau, D. L., Ikeda-Saito, M., and Yoshida, T. (1995) *Journal of Biological Chemistry* **270**, 6345-6350
24. Liu, Y., Moenne-Loccoz, P., Loehr, T. M., and Ortiz de Montellano, P. R. (1997) *Journal of Biological Chemistry* **272**, 6909-6917
25. Fisher, H., and Muller, A. (1937) *Hoppe-Seyler's Z Physiological Chemistry* **246**, 43-58

26. Matera, K. M., Takahashi, S., Fujii, H., Zhou, H., Ishikawa, K., Yoshimura, T., Rousseau, D. L., Yoshida, T., and Ikeda-Saito, M. (1996) *Journal of Biological Chemistry* **271**, 6618-6624
27. Nagababu, E., and Rifkind, J. M. (2004) *Antioxidants & Redox Signalling* **6**, 967-978
28. Matsui, T., Nakajima, A., Fujii, H., Matera, K. M., Migita, C. T., Yoshida, T., and Ikeda-Saito, M. (2005) *Journal of Biological Chemistry* **280**, 36833-36840
29. Matsui, T., Omori, K., Jin, H., and Ikeda-Saito, M. (2008) *Journal of American Chemical Society*, ja710495z
30. Wilks, A., Torpey, J., and Ortiz de Montellano, P. R. (1994) *Journal of Biological Chemistry* **269**, 29553-29556
31. Badyal, S. K., Joyce, M. G., Sharp, K. H., Seward, H. E., Mewies, M., Basran, J., Macdonald, I. K., Moody, P. C. E., and Raven, E. L. (2006) *Journal of Biological Chemistry* **281**, 24512-24520
32. Pereira, L. O. R., Oliveira, P. L., Almeida, I. C., and Paiva-Silva, G. O. (2007) *Biochemistry* **46**, 6822-6829
33. Wojciechowski, G., and Ortiz de Montellano, P. R. (2007) *Journal of American Chemical Society* **129**, 1663-1672
34. Lad, L., Mewies, M., and Raven, E. L. (2002) *Biochemistry* **41**, 13774-13781
35. De Matteis, F., Lord, G. A., Kee Lim, C., and Pons, N. (2006) *Rapid Communications in Mass Spectrometry* **20**, 1209-1217
36. Murshudov, G. N., Vagin, A., A., and Dodson, E. J. (1997) *Acta Crystallographica Section D. Biological Crystallography* **53**, 240-255
37. Collaborative Computational Project, N. (1994) *Acta Crystallographica Section D-Biological Crystallography* **D50**, 760-763
38. Emsley, P., and Cowtan, K. (2004) *Acta Crystallographica Section D. Biological Crystallography* **60**, 2126-2132

39. Wagner, U. G., Muller, N., Schmitzberger, W., Falk, H., and Kratky, C. (1995) *Journal of Molecular Biology* **247**, 326-337
40. Pereira, P. J., Macedo-Ribeiro, S., Parraga, A., Perez-Luque, R., Cunningham, O., Darcy, K., Mantle, T. J., and Coll, M. (2001) *Nature Structural Biology* **8**, 215-220
41. Denisov, I. G., Ikeda-Saito, M., Yoshida, T., and Sligar, S. G. (2002) *FEBS Letters* **532**, 203-206
42. Denisov, I. G., Makris, T. M., and Sligar, S. G. (2002) *Journal of Biological Chemistry* **277**, 42706-42710
43. Silaghi-Dumitrescu, R. (2004) *Archives of Biochemistry and Biophysics* **424**, 137-140
44. Veeger, C. (2002) *Journal of Inorganic Biochemistry* **91**, 35-45
45. Murakami, T., Morishima, I., Matsui, T., Ozaki, S., Hara, I., Yang, H., and Watanabe, M. (1999) *Journal of American Chemical Society* **121**, 2007-2011
46. Murakami, T., Morishima, I., Matsui, T., Ozaki, S., and Watanabe, M. (1998) *Chemical Communications* **7**, 773-775
47. Hildebrand, D. P., Tang, H.-L., Luo, Y., Hunter, C. L., Smith, M., Brayer, G. D., and Mauk, A. G. (1996) *Journal of American Chemical Society* **118**, 12909-12915
48. Sano, S., Sano, T., Morishima, I., Shiro, Y., and Maeda, Y. (1986) *Proceedings of the National Academy of Sciences of the United States of America* **83**, 531-535
49. Avila, L., Huang, H., Rodriguez-Lopez, J. C., Moenne-Loccoz, P., and Rivera, M. (2000) *Journal of American Chemical Society* **122**, 7618-7620
50. Rodriguez-Lopez, J. C., and Rivera, M. (1998) *Biochemistry* **37**, 13082-11390
51. Rice, J. K., Fearnley, I. M., and Barker, P. D. (1999) *Biochemistry* **38**, 16847-16856

52. Sligar, S. G., Makris, T. M., and Denisov, I. G. (2005) *Biochemical and Biophysical Research Communications* **338**, 346-354
53. Egawa, T., Yoshioka, S., Takahashi, S., Hori, H., Nagano, S., Shimada, H., Ishimori, K., Morishima, I., Suematsu, M., and Ishimura, Y. (2003) *Journal of Biological Chemistry* **278**, 41597-41606
54. Shintaku, M., Matsuura, K., Yoshioka, S., Takahashi, S., Ishimori, K., and Morishima, I. (2005) *Journal of Biological Chemistry* **280**, 40934-40938
55. Makris, T. M., Davydov, R., Denisov, I. G., Hoffman, B. M., and Sligar, S. G. (2002) *Drug Metabolism Reviews* **34**, 691-708
56. Kuhnel, K., Derat, E., Terner, J., Shaik, S., and Schlichting, I. (2007) *Proceedings of the National Academy of Sciences of the United States of America* **104**, 99-104
57. Denisov, I. G., Dawson, J. H., Hager, L. P., and Sligar, S. G. (2007) *Biochemical and Biophysical Research Communications* **363**, 954-958
58. Symons, M. C. R., and Petersen, R. L. (1978) *Biochimica Et Biophysica Acta* **535**, 241-247
59. Kappl, R., Hoehn-Berlage, M., Huettermann, J., Bartlett, N., and Symons, M. C. R. (1985) *Biochimica Et Biophysica Acta* **827**, 327-343
60. Davydov, R. M. (1980) *Biofizika* **25**, 203-207
61. Davydov, R. M., and Ledenev, A. N. (1981) *Biofizika* **26**, 1096-1099
62. Davydov, R., Kappl, R., Huettermann, J., and Peterson, J. A. (1991) *FEBS Letters* **295**, 113-115
63. Davydov, R., Makris, T. M., Kofman, V., Werst, D. E., Sligar, S. G., and Hoffman, B. M. (2001) *Journal of American Chemical Society* **123**, 1403-1415
64. Davydov, R., Kofman, V., Fujii, H., Yoshida, T., Ikeda-Saito, M., and Hoffman, B. M. (2002) *Journal of American Chemical Society* **124**, 1798-1808

65. Davydov, R., Kofman, V., Nocek, J. M., Noble, R. W., Hui, H., and Hoffman, B. M. (2004) *Biochemistry* **43**, 6330-6338
66. Davydov, R., Chemerisov, S., Werst, D. E., Rajh, T., Matsui, T., Ikeda-Saito, M., and Hoffman, B. M. (2004) *Journal of American Chemical Society* **126**, 15960-15961
67. Denisov, I. G., Makris, T. M., and Sligar, S. G. (2001) *Journal of Biological Chemistry* **276**, 11648-11652
68. Ibrahim, M., Denisov, I. G., Makris, T. M., Kincaid, J. R., and Sligar, S. G. (2003) *Journal of American Chemical Society* **125**, 13714-13718
69. Mak, P. J., Denisov, I. G., Victoria, D., Makris, T. M., Deng, T., and Sligar, S. G. (2007) *Journal of American Chemical Society* **129**, 6382-6383
70. Finzel, B. C., Poulos, T. L., and Kraut, J. (1984) *Journal of Biological Chemistry* **259**, 13027-13036
71. Lad, L., Wang, J. L., and Li, H. Y. (2003) *Journal of Molecular Biology* **330**, 527-538
72. Tajima, K., Edo, T., Ishizu, K., Imaoka, S., Funae, Y., Oka, S., and Sakurai, H. (1993) *Biochemical and Biophysical Research Communications* **191**, 157-164
73. Ortiz de Montellano, P. R. (2000) *Current Opinion in Chemical Biology* **4**, 221-227

***CHAPTER FIVE***

**THE CONSERVED DISTAL HISTIDINE-ASPARAGINE BOND IN  
ASCORBATE PEROXIDASE**

## CHAPTER FIVE

# THE CONSERVED DISTAL HISTIDINE-ASPARAGINE BOND IN ASCORBATE PEROXIDASE

---

### 5.1 INTRODUCTION

Conformational mobility of the distal histidine residue (His-42) in the W41A variant of APX, triggered upon addition of H<sub>2</sub>O<sub>2</sub>, anionic ligands or a change in oxidation state, has been discussed in previous chapters. The distal tryptophan (Trp-41) has been found to play a structural role in the peroxidase heme architecture preventing ligation of the distal histidine to the heme. Further examination of the distal cavity in APX (Figure [5.1]), reveals that His-42 is hydrogen bonded (2.77 Å) to asparagine-71 (Asn-71), an amino acid further removed from the immediate vicinity of the active site. This hydrogen bond is known to be conserved among many plant and fungal peroxidases (see Chapter 1) (1-9) suggesting that it is one of the key determinants for peroxidase activity. The role of this hydrogen bond in catalysis has been studied in CcP (10), HRP (11-14) and Kat-G (15) and is discussed later (Section 5.3.4). The main findings from these previous studies suggest that the asparagine residue is involved in controlling the basicity of the distal histidine.

In this study the hydrogen bond between the distal histidine and asparagine has been probed to observe how Asn-71 affects mobility of His-42. The hypothesis is that any alteration in peroxidase structure that alters mobility of His-42, either through

removal of the hydrogen bonding interaction between His-42 and Asn-71 or by introduction of bulk at position 71 (e.g. by replacement of Asn-71 with a more bulky residue) should encourage conversion to a bis-histidine, cytochrome *b*-type geometry. Thus, the following variants of APX were prepared to study their effects on His-42 mobility: N71A, W41A/N71A, W41A/N71L and W41A/N71W.

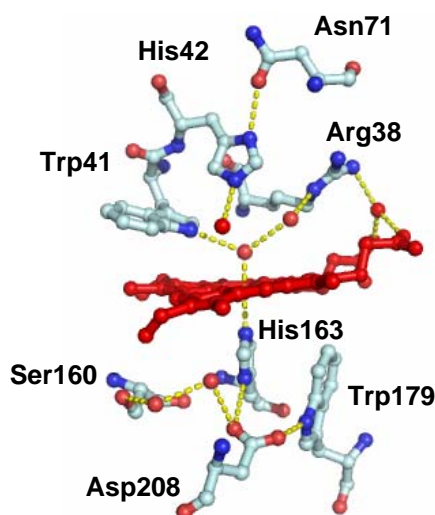


Figure [5.1]: The heme (red) and active site residues in the crystal structure of rsAPX (PDB code: 1OAG) (16). Water molecules are indicated by red spheres and hydrogen bonds are represented by yellow dashed lines.

The single alanine variant (N71A), although structurally quite a drastic substitution, was constructed to abolish the interaction with His-42. The double alanine mutant, W41A/N71A, was created in order to try to clarify some of the results obtained on the single W41A and N71A mutants and in hope of forming a variant in which the mobility of the distal histidine was not so restrained. A bulky residue was introduced at position 71, in the W41A/N71W variant, in order to have a “push” effect on His-42 towards the iron. The W41A/N71L mutation is a more “conservative” substitution relative to the other three variants, in that a leucine residue would eliminate the capacity for a hydrogen bonding interaction but at the same time have minimum effect on the structure of the protein.

## 5.2 RESULTS

### 5.2.1 Expression and purification of the Asn-71 variants

Preparation of the Asn-71 variants of rsAPX, N71A, W41A/N71A, W41A/N71L and W41A/N71W, using site-directed mutagenesis was conducted according to the Quikchange™ protocol (Stratagene), using the rsAPX encoded gene and the appropriate Asn-71 mutagenic oligonucleotides (sequences shown in Table [6.1] Chapter 6, Section 6.2.2). Individual mutations were confirmed by sequencing across the entire rsAPX-coding gene to ensure that it was free of any other mutations. The Asn-71 variants were expressed, isolated and purified according to published procedures (17,18) (Chapter 6, Section 6.3). All four variants were isolated as mainly the holo-protein form (~25 mg/l) and these were then further reconstituted by addition of hemin. Excess hemin was removed as described in Chapter 6, Section 6.3.2. Purified proteins were obtained with  $R_z$  values >2.5 and purity of the isolated Asn-71 variants was confirmed using SDS-PAGE analysis. The preparations were judged to be homogenous by the migration of a single band (molecular weight of ~30 kDa) on a Coomassie Blue-stained reducing SDS-PAGE gel (Figure [5.2]).

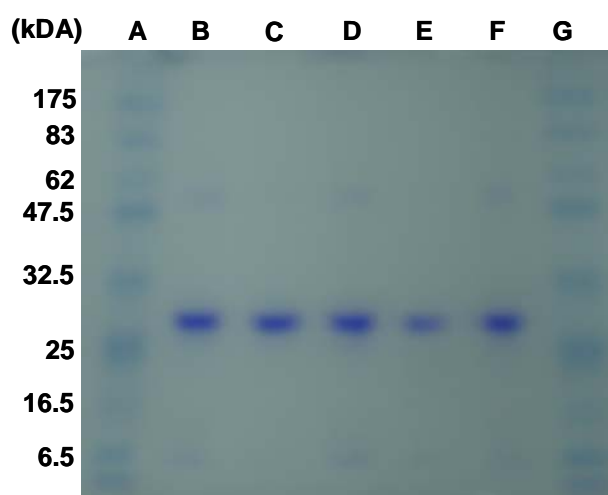


Figure [5.2]: Coomassie Blue-stained 15 % SDS-PAGE gel of purified rsAPX and Asn-71 variants, Lane A and G: Bio-Rad molecular mass standard, Lane B: rsAPX, Lane C: N71A, Lane D: W41A/N71A, Lane E: W41A/N71L and Lane F: W41A/N71W.

### 5.2.2 Mass spectrometric analysis of the Asn-71 variants

Although the genes encoding the Asn-71 variants were sequenced without the discovery of any additional undesirable mutations, the absence of post-translational modification in the expressed enzymes was confirmed by mass spectrometry. MALDI-TOF analysis was conducted in order to further confirm and evaluate the integrity of the variants. The values obtained from mass spectral analysis of the Asn-71 variants are listed in Table [5.1] and Figure [5.3] shows the MALDI-TOF mass spectrum of W41A/N71W.

**Table [5.1] Average mass of the Asn-71 mutants determined using MALDI-TOF mass spectrometry (average error of  $\pm 0.05$  % Da).**

	<b>MW<sub>obs</sub></b>	<b>MW<sub>calc</sub></b>
<b>N71A</b>	28, 269.43	28, 275.85
<b>W41A/N71A</b>	28, 155.07	28, 160.71
<b>W41A/N71L</b>	28, 207.50	28, 202.80
<b>W41A/N71W</b>	28, 274.72	28, 275.85

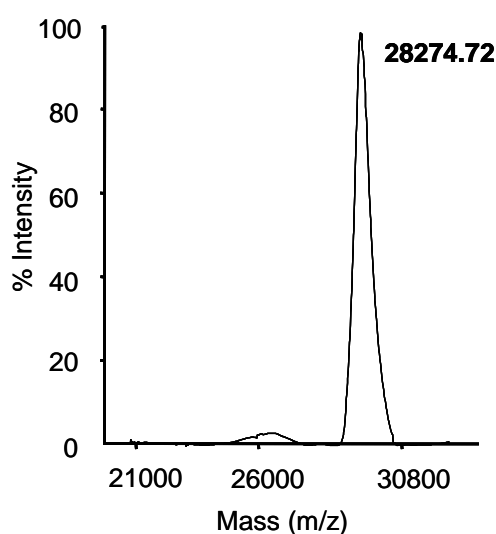


**Figure [5.3]: MALDI-TOF mass spectrum of W41A/N71W.**

### 5.2.3 Spectroscopic characterisation of the Asn-71 variants

#### 5.2.3.1 Electronic absorption spectra

Analysis of the ferric Asn-71 variant electronic absorption spectra (Figure [5.4]) revealed maxima (Table [5.2]) that differ from rsAPX. The red-shift in the Soret absorption and the lack of the high-spin peak at ~630 nm in the Asn-71 variants in comparison to rsAPX revealed that these variants were predominately low-spin. The sharp Soret and the relative intensities of the low-spin transitions ([530 nm]  $\beta > \alpha$  [560 nm]) of the variants are also indicative of low-spin heme. This low-spin nature of heme in the Asn-71 variants probably arises from ligation of the distal histidine (His-42) to the heme.

The ferrous spectrum of the Asn-71 variants (Figure [5.4]), revealed the presence of predominantly five-coordinate heme similar to that observed for rsAPX and W41A (Figure [5.4A,B] and Chapter 3), thus the bound ligand (His-42) in the distal pocket is displaced on reduction; however the reduced spectrum of N71A (Figure [5.4C]), revealed the presence of low-spin ferrous heme (six-coordinate heme). The ferrous spectrum of N71A, with peaks at 528 and 557 nm that are indicative of low-spin ferrous heme, is analogous to the spectrum of ferrous bis-histidine cytochrome  $b_5$  (19). The mobility of His-42 in the distal pocket of the N71A variant is likely to be more restricted due to the presence of the bulky distal tryptophan, which is absent in the other Asn-71 variants, thus a low-spin species is observed in ferrous N71A. The absorption coefficient values for the Asn-71 variants were determined and are reported in Table [5.2]. The absorption coefficient values of all four variants were larger than that of rsAPX ( $\epsilon_{407} = 107 \text{ mM}^{-1} \text{ cm}^{-1}$ ) (18) as expected for low-spin proteins.

#### 5.2.3.2 Equilibrium binding experiments

The electronic spectra of the ferric Asn-71 variants were altered in the presence of cyanide, indicative of the formation of a low-spin heme species. Absorption maxima for the ferric-cyanide derivatives of the Asn-71 variants (Table [5.3]) are similar to those for rsAPX. The spectra of all four Asn-71 variants were, on the other hand, unaffected by the addition of either azide or fluoride, suggesting that these (weak field) ligands do not bind to the heme under these conditions.

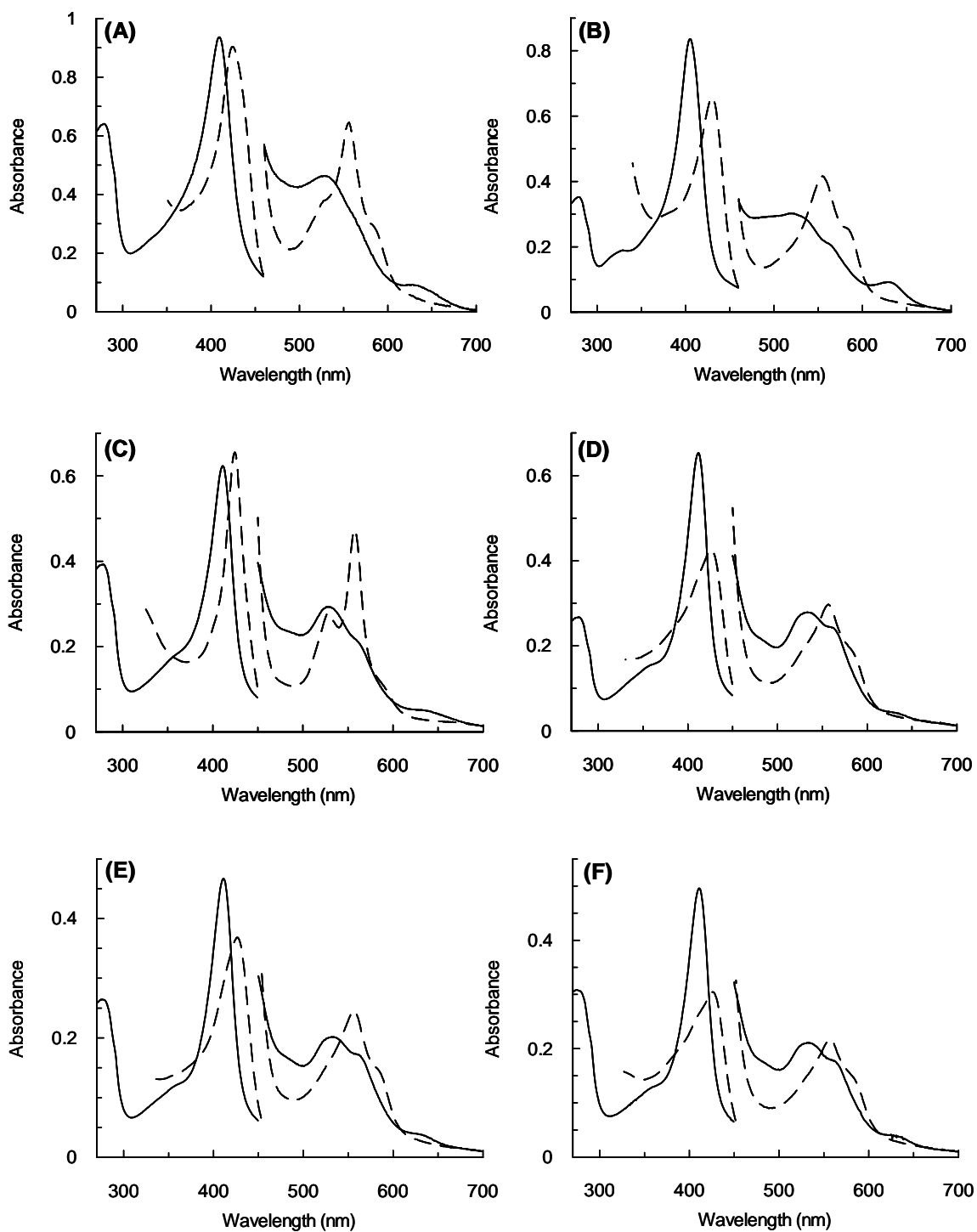


**Figure [5.4]:** Electronic spectra showing the ferric (solid line) and ferrous (dashed line) species of (A) rsAPX, (B) W41A, (C) N71A, (D) W41A/N71A, (E) W41A/N71L and (F) W41A/N71W. The visible region has been multiplied by a factor of five. Conditions: sodium phosphate buffer, pH 7.0,  $\mu = 0.10$  M, 25.0 °C.

Table [5.2]: Wavelength maxima (nm) and in parentheses absorption coefficients ( $\text{mM}^{-1} \text{cm}^{-1}$ ) of ferric and ferrous rsAPX (18), W41A (Chapters 2 and 3) and Asn71 variants. Conditions: sodium phosphate, pH 7.0,  $\mu = 0.10 \text{ M}$ ,  $25.0 \text{ }^\circ\text{C}$ . (<sup>sh</sup> denotes shoulder and \* denotes wavelength maxima, less than 390 nm obscured by the dithionite absorption).

	$\delta$	( $\gamma$ ) Soret	CT <sub>2</sub>	$\beta$	$\alpha$	CT <sub>1</sub>
<b>rsAPX</b>						
Fe <sup>III</sup>	-	407 (107)	525	-	-	~630
Fe <sup>II</sup>	*	430	-	555	583 <sup>sh</sup>	-
<b>W41A</b>						
Fe <sup>III</sup>	~380 <sup>sh</sup>	405 (125)	525		564	630
Fe <sup>II</sup>	*	428	-	556	581 <sup>sh</sup>	-
<b>N71A</b>						
Fe <sup>III</sup>	~357 <sup>sh</sup>	411 (117)	-	529	560 <sup>sh</sup>	635
Fe <sup>II</sup>	*	424	-	528	557	-
<b>W41A/N71A</b>						
Fe <sup>III</sup>	~360 <sup>sh</sup>	412 (123)	-	533	560 <sup>sh</sup>	630 <sup>sh</sup>
Fe <sup>II</sup>	*	426	-	557	583 <sup>sh</sup>	-
<b>W41A/N71L</b>						
Fe <sup>III</sup>	~355 <sup>sh</sup>	411 (116)	-	532	560 <sup>sh</sup>	630 <sup>sh</sup>
Fe <sup>II</sup>	*	426	-	556	583 <sup>sh</sup>	-
<b>W41A/N71W</b>						
Fe <sup>III</sup>	~356 <sup>sh</sup>	411 (118)	-	533	560 <sup>sh</sup>	627
Fe <sup>II</sup>	*	426	-	556	583 <sup>sh</sup>	-

The effect of the mutations at Trp-41 and Asn-71 on the ability of the enzyme to bind exogenous ligands was determined by equilibrium binding measurements. Figure [5.5] shows a family of spectra collected during the titration of W41A/N71W with cyanide, the other Asn-71 variants showed similar absorption changes during the cyanide titrations (data not shown). All four variants were consistent with a 1:1 stoichiometric binding process, and show well-defined isobestic points, indicating the presence of only two absorbing species (ferric enzyme and ferric-cyanide complex). The corresponding changes at 419 nm are consistent with Equation [6.8] (Chapter 6, Section 6.4.6), and the equilibrium dissociation constant,  $K_d$ , calculated from the fit of these data are reported in Table [5.3]. The Asn-71 variants were found to bind cyanide weakly in comparison to rsAPX ( $K_d = 0.73 \pm 0.075 \mu\text{M}$ ). This reflects the coordination of His-42 to the heme in the Asn-71 variants.

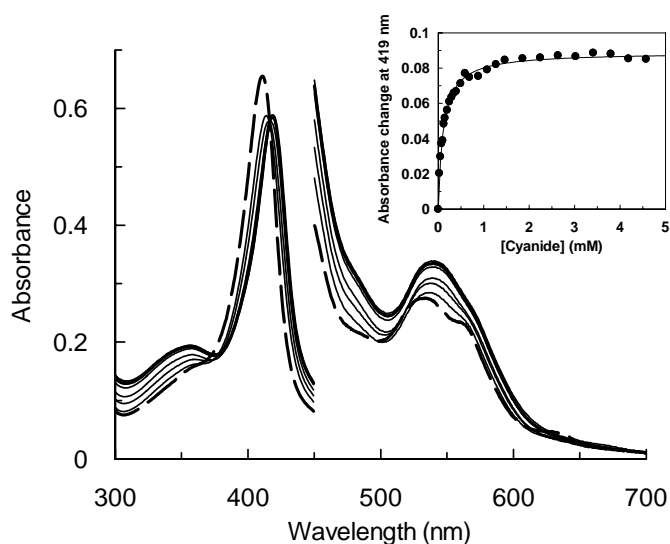


**Figure [5.5]:** Selected spectra collected during titration of ferric W41A/N71W with cyanide. Intermediate spectra between the initial spectrum (dashed line) and the final saturated spectrum (solid line) are shown as lines. The visible region has been multiplied by a factor of five. Conditions: sodium phosphate buffer, pH 7.0,  $\mu = 0.10 \text{ M}$ ,  $25.0 \text{ }^\circ\text{C}$ . *Inset:* Shows the calculated fit of the experimental data to Equation [6.8] (Chapter 6, Section 6.4.6) for determination of the  $K_d$  value.

**Table [5.3]: Wavelength maxima (nm) and equilibrium binding constants ( $K_d$ ) of ferric-cyanide (CN)-bound complexes of rsAPX, W41A and Asn-71 variants. Conditions: sodium phosphate, pH 7.0,  $\mu = 0.10$  M, 25.0 °C. (<sup>sh</sup> denotes shoulder).**

	$\delta$	( $\gamma$ ) Soret	$\beta$	$\alpha$	$K_d$ ( $\mu$ M)
<b>rsAPX-CN</b>	~360 <sup>sh</sup>	419	536	563 <sup>sh</sup>	0.73 $\pm$ 0.075
<b>W41A-CN</b>	~365 <sup>sh</sup>	418	540	561 <sup>sh</sup>	20 $\pm$ 1
<b>N71A-CN</b>	~357 <sup>sh</sup>	419	539	568 <sup>sh</sup>	16 $\pm$ 2
<b>W41A/N71A-CN</b>	~358 <sup>sh</sup>	419	539	568 <sup>sh</sup>	51 $\pm$ 3
<b>W41A/N71L-CN</b>	~360 <sup>sh</sup>	419	539	567 <sup>sh</sup>	93 $\pm$ 12
<b>W41A/N71W-CN</b>	~356 <sup>sh</sup>	419	540	567 <sup>sh</sup>	104 $\pm$ 6

#### 5.2.4 Crystal screen trials of the Asn-71 variants

Crystal screens of the Asn-71 variants based around the conditions used to crystallise rsAPX (16) and W41A (Chapter 6, Section 6.8) were unsuccessful (10 mg/ml protein and 0.1 M Hepes, pH 8.3, 2.25 M lithium sulphate). Variation in protein concentration (10-50 mg/ml), pH of Hepes buffer (pH 7-9.5, increments of 0.5 pH units) and temperature (4 or 19 °C) also proved unsuccessful. No sign of crystallisation was observed when commercial screens (Wizard I, II and Cryo I, II sparse matrix crystallisation screens, Emerald BioStructures) of the Asn-71 variants were attempted.

#### 5.2.5 Electrochemistry of the Asn-71 variants

The xanthine/xanthine oxidase assay (described in Chapter 3, Section 3.2.4 and Chapter 6, Section 6.7, were performed with the assistance of Dr I. Efimov, Department of Chemistry, University of Leicester) was employed to determine the ferric/ferrous reduction potentials for the Asn-71 variants (Table [5.4]). The data collected during the redox assay was fitted to the Nernst equation (Equation [6.16], Chapter 6, Section 6.7). The Asn-71 variants were found to exhibit a somewhat

negative reduction potential in comparison to rsAPX. Figure [5.6] shows a family of spectra collected during the redox measurement of (A) N71A and (B) W41A/N71L. Again, the low-spin ferrous heme was observed for the N71A variant where as the other Asn-71 variants yielded formation of a five-coordinate ferrous heme on reduction by the xanthine/xanthine oxidase assay. Similar families of spectra were obtained for the other Asn-71 variants.

**Table [5.4]: Reduction potentials (mV vs NHE) for the ferric/ferrous redox couples in rsAPX (20), W41A (20) and the Asn-71 variants, determined using the phenosafranine/xanthine/xanthine oxidase method. Conditions: 50 mM potassium phosphate, pH 7.0, 25.0 °C.**

	rsAPX	W41A	N71A	W41A/N71A	W41A/N71L	W41A/N71W
<b><math>E^\circ</math> (mV)</b>	-206	-227	-215	-225	-228	-223

### 5.2.6 Kinetic analysis of the Asn-71 variants

Steady state studies for oxidation of ascorbate by the Asn-71 variants were carried out to evaluate the effect of mutation at residues Trp-41 and Asn-71 on the catalytic properties of APX. Unlike rsAPX, oxidation of ascorbate by the Asn-71 variants obeyed Michaelis-Menten kinetics (Figure [5.7]) and steady state parameters,  $k_{\text{cat}}$ ,  $K_m$  and the arithmetically calculated selectivity coefficient ( $k_{\text{cat}}/K_m$ ) are reported in Table [5.5]. The Asn-71 variants catalysed the oxidation of ascorbate at a slower rate in comparison to rsAPX ( $k_{\text{cat}} = 272 \text{ s}^{-1}$ ,  $K_m = 389 \text{ }\mu\text{M}$ ,  $k_{\text{cat}}/K_m = 0.69 \text{ }\mu\text{M}^{-1} \text{ s}^{-1}$ ) (18). All the Asn-71 variants, apart from W41A/N71L had a similar  $K_m$  to rsAPX. Despite the large  $K_m$ , the W41A/N71L variant catalysed ascorbate turnover at an elevated rate in comparison to the other Asn-71 variants.

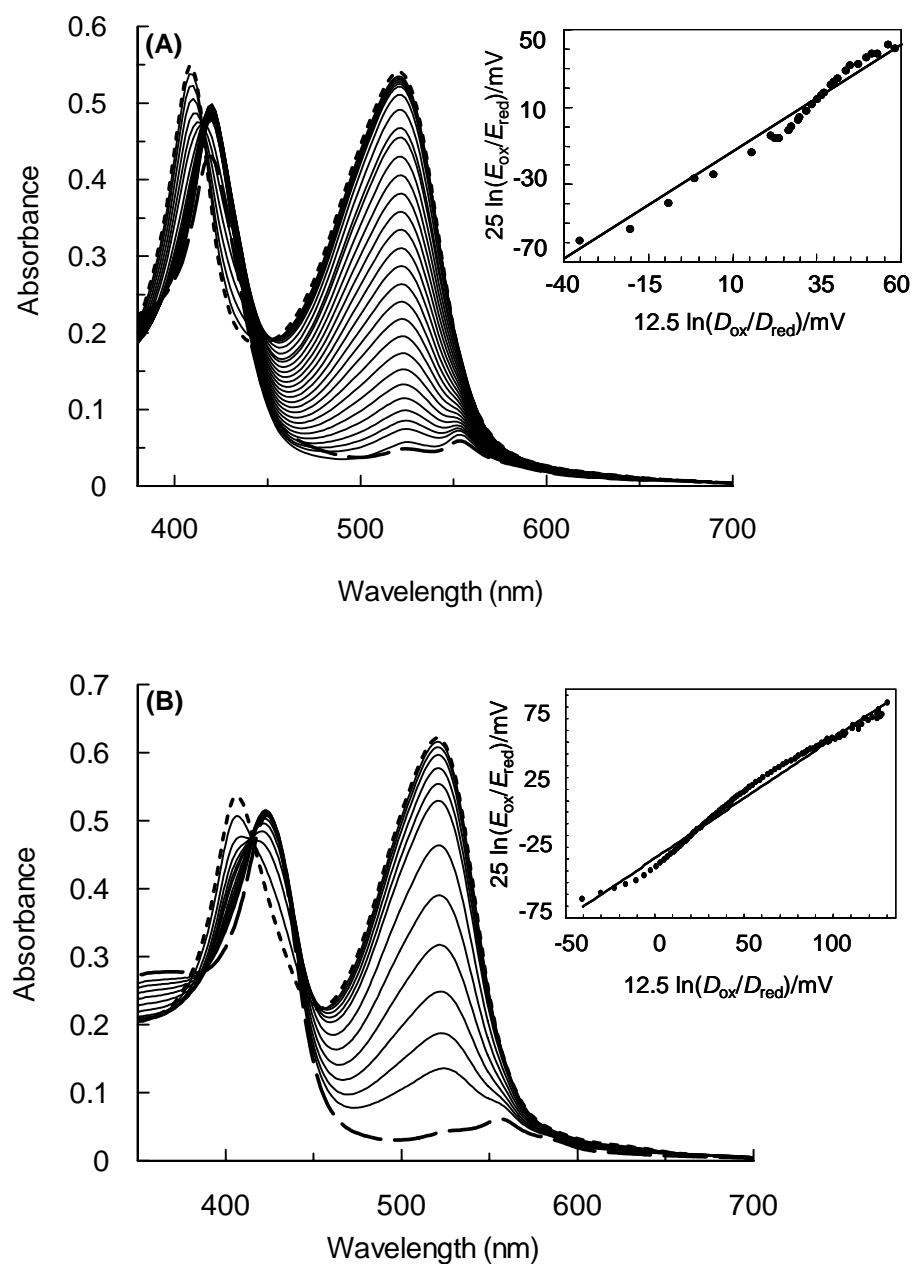


Figure [5.6]: Representative family of spectra collected during determination of ferric/ferrous reduction potential in (A) N71A and (B) W41A/N71L. Selected intermediate spectra between initial ferric spectrum of N71A and W41A/N71L (dotted line) and the final ferrous spectrum (dashed line) are shown as lines. Conditions: 50 mM potassium phosphate, pH 7.0, 25.0 °C. *Inset*: The corresponding linear Nerst plot.

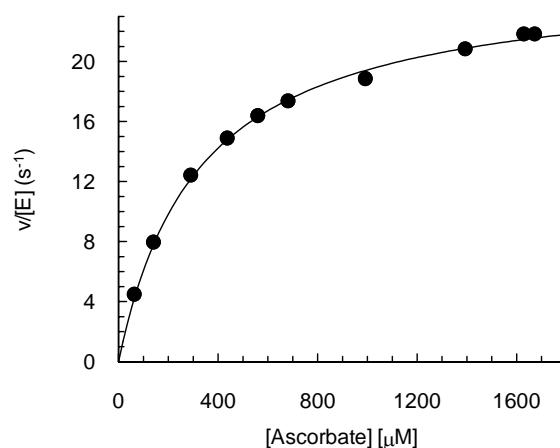


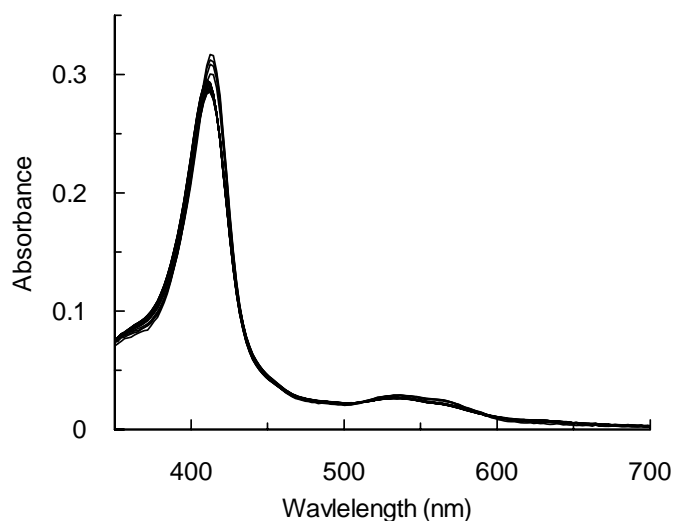
Figure [5.7]: Steady state oxidation of ascorbate by N71A. Solid line shows a fit of the data to the Michaelis-Menten Equation (Equation [2.1], Chapter 2, Section 2.2.5). Conditions: sodium phosphate buffer, pH 7.0,  $\mu = 0.10$  M, 25.0 °C.

Table [5.5]: Steady state kinetic parameters and selectivity coefficients for the oxidation of ascorbate by rsAPX (18), W41A (Chapter 2) and Asn-71. All data were fitted using the Michaelis-Menten equation (Equation [2.1], Chapter 2, Section 2.2.5), except (a) where data were fitted to the Hill Equation (Equation [6.7], Chapter 6, Section 6.5.1). Errors quoted are standard deviations. Conditions: sodium phosphate buffer, pH 7.0,  $\mu = 0.10$  M, 25.0 °C.

	$k_{\text{cat}}$ (s <sup>-1</sup> )	$K_m$ (μM)	$k_{\text{cat}}/K_m$ (μM <sup>-1</sup> s <sup>-1</sup> )
rsAPX <sup>a</sup>	272 ± 32	389 ± 64	0.69
W41A	371 ± 7.8	254 ± 16	1.46
N71A	27 ± 0.54	288 ± 18	0.094
W41A/N71A	17 ± 0.42	199 ± 19	0.085
W41A/N71L	104 ± 3.1	701 ± 49	0.15
W41A/N71W	7 ± 0.11	281 ± 2	0.025

Attempts to measure Compound I formation in the Asn-71 variants (Chapter 6, Section 6.6.5) proved unsuccessful because significant spectral changes were only observed on long time scales (1000 s) even when a large excess (>100-fold) of H<sub>2</sub>O<sub>2</sub> was added. In addition, spectral changes (heme bleaching) were observed in the

Asn-71 variants in buffer alone over such long time scales (Figure [5.8]). The intensity of the xenon lamp was thought to be the cause of heme bleaching in the Asn-71 variants. Due to time constraints, further progress on kinetic analysis of the Asn-71 variants proved difficult.



**Figure [5.8]: Spectral changes occurring upon incubation of W41A/N71W with buffer monitored by stopped-flow photodiode array spectroscopy (1000 secs). Conditions: sodium phosphate buffer, pH 7.0,  $\mu = 0.10$  M, 5.0 °C.**

## 5.3 DISCUSSION

In previous work (described in Chapters 2 and 3), the distal histidine (His-42) in the W41A variant of APX was found to be mobile. This conformational mobility was found to be triggered by addition of substrate, anionic ligands or a change in oxidation state. On further examination of the active site of APX a hydrogen bond between His-42 and Asn-71, a conserved interaction in heme peroxidases, was identified as a possible factor controlling the mobility of the distal histidine. To investigate the role of this conserved interaction in APX, four site-directed variants were prepared: N71A, W41A/N71A, W41A/N71L, and W41A/N71W. This chapter reports on the spectroscopic and kinetic data of these distal variants and their impact upon the mobility of His-42.

### 5.3.1 Heme electronic structure of the Asn-71 variants and ligand binding studies

The integrity of the Asn-71 variants was authenticated using a variety of spectroscopic methods. Whilst the DNA of Asn-71 variants were sequenced without discovery of any spontaneous mutations, the integrity of the expressed variants was confirmed by MALDI-TOF spectrometry. The electronic absorption spectra of the Asn-71 variants, like W41A, were found to differ in comparison to rsAPX (which is predominantly five-coordinate high-spin) in that the Asn-71 variants had a sharper Soret band at ~411 nm and a transition at ~560 nm, which are characteristic of low-spin heme. In contrast to W41A, the Asn-71 variants showed no peak at ~630 nm which is indicative of high-spin heme but exhibited a transition at ~530 nm. The relative intensities of the transitions at ~530 and ~560 nm ( $\beta > \alpha$ ) in the Asn-71 variants are indicative of low-spin heme, which is probably due to ligation of His-42 to the heme. Hence, the Asn-71 variants were found to have relatively more low-spin character in comparison to the W41A variant due to the strong interaction (pull) of the iron for His-42. However, in the W41A variant the strong interaction (pull) of the iron for His-42 is counteracted by the conserved hydrogen bonding interaction in the distal cavity between His-42 and Asn-71, resulting in a long iron-histidine bond (2.3 Å) and greater high-spin character of the W41A variant in comparison to the Asn-71 variants. Like W41A, the calculated absorption coefficients for the Asn-71 variants,

were also greater than that of rsAPX ( $\epsilon_{407} = 107 \text{ mM}^{-1} \text{ cm}^{-1}$ ) (18). The sharp Soret peak at  $\sim 411 \text{ nm}$ , an extinction coefficient greater than  $100 \text{ mM}^{-1} \text{ cm}^{-1}$  and a characteristic low-spin transitions at  $\sim 530$  and  $\sim 560 \text{ nm}$  are collectively indicative of a six-coordinate/low-spin heme species (21).

All the Asn-71 variants apart from the N71A variant had ferrous spectra similar to ferrous rsAPX and W41A, *i.e.* indicative of five-coordinate heme, meaning that the distal histidine was displaced on reduction of the heme as observed for W41A (see Chapter 3). In contrast, the spectrum of ferrous N71A resembled the spectrum of a ferrous bis-histidine (low-spin) heme protein, such as cytochrome  $b_5$  (19). Unlike the other Asn-71 variants, the flexibility of His-42 in the distal pocket of the N71A is likely to be controlled/restricted by the bulky tryptophan residue; however, detailed analysis is difficult without structural data (crystal screens of all four Asn-71 variants were unsuccessful).

Ligand binding studies were performed to assess how the mobility of the distal histidine in the Asn-71 variants affected access of cyanide to the heme iron in comparison to rsAPX and W41A. Formation of a characteristic low-spin heme species was observed on addition of cyanide to all the Asn-71 variants. The wavelength maxima of the cyanide bound Asn-71 variants were essentially identical to those observed for rsAPX and W41A, however all four Asn-71 variants were unable to coordinate to the weak field ligand azide. The Asn-71 variants were found to bind cyanide substantially more weakly in comparison to rsAPX and W41A. This weaker binding of cyanide to the Asn-71 variants, may be influenced by the fact the distal histidine may not be able to hydrogen bond stabilise binding of the ligand which is thought to be an important interaction in ligand binding affinity in other heme proteins (13). The N71A variant was found to have similar cyanide binding affinity as W41A. The W41A/N71A variant, unlike the other two double variants, had a  $\sim 2$ -fold lower affinity for cyanide in comparison to W41A and N71A, this likely to be because the distal histidine is no longer restrained by interaction from either Trp-41 or Asn-71 and is able to orient itself without regulation. The N71A and W41A/N71A variants were found to have greater binding affinity for cyanide in contrast to W41A/N71L and W41A/N71W variants. The hydrogen bond interaction between the distal asparagine and histidine is abolished in the N71A, W41A/N71A and W41A/N71L mutants; however, the alanine variants still have relatively high binding affinity for cyanide in comparison to the leucine variant. This difference may have to do with the fact that

His-42 has greater space in the distal cavity on replacement of the large asparagine with a small alanine residue, whereas in the leucine variant the hydrogen bond is lost but the distal cavity remains occupied by the leucine side chain. The affinity of W41A/N71W for cyanide, as expected due to the presence of the bulky tryptophan, was low (~5-fold lower than W41A) in comparison to the other variants.

### 5.3.2 Electrochemistry and steady state kinetics of the Asn-71 variants

The presence of negative charge near the heme is generally known to lead to a decrease in the reduction potential. Despite the characteristic low-spin features of the Asn-71 variants the ferric/ferrous reduction potentials, albeit lowered to small extent, were similar to rsAPX ( $E^\circ = -206$  mV) (20).

All four Asn-71 variants catalysed the oxidation of ascorbate with a decreased rate in comparison to rsAPX and W41A; however similar to W41A the variants displayed hyperbolic dependence as opposed to sigmoidal dependence on ascorbate concentration. Again this difference could be because of structural rearrangement in the variants which may have affected the cooperativity within the enzyme. The N71A, W41A/N71A and W41A/N71W variants had similar  $K_m$  for ascorbate as rsAPX, however the W41A/N71L variant, although turned over ascorbate at an elevated rate in comparison to the other three Asn-71 variants had very high  $K_m$  for ascorbate. As expected, the W41A/N71W variant had a low turnover rate in comparison to the other Asn-71 variants due to the presence of a bulky residue at position 71, which probably restricts access of  $H_2O_2$  to the heme. Measurement of Compound I formation,  $k_1$ , was not possible for these variants due to extensive heme bleaching during data collection in single wavelength and PDA mode.

### 5.3.3 Conclusions

A series of mutations at position 71 in APX were performed to assess how removal of the conserved hydrogen bond between Asn-71 and His-42 would affect mobility of the latter. In the N71L variant, this conserved bond was abolished by replacement of Asn-71 with a leucine, a residue similar in structure to the asparagine residue but lacking hydrogen bonding capacity. In the N71A and W41A/N71A variants, the asparagine residue was replaced by a smaller side chain alanine

residue, which probably created additional space for His-42 in the distal cavity. Evidence for this additional distal space comes from the observation that the alanine variants displayed greater binding affinity for cyanide, in comparison to the leucine variant. This difference in ligand affinity is probably due to the fact that His-42 is able to reorient itself from the heme into this additional space in the alanine mutants where as this movement is restricted in the leucine variant. However, the additional free space appears to affect the catalytic ability of the alanine variants, which were found to catalyse the oxidation of ascorbate at a decreased rate in comparison to W41A/N71L, because the His-42 is able to move to a position in the additional space of the distal cavity that is distant from the heme centre. Where as in the leucine variant due to the restriction in orientation and location, the distal histidine is ideally positioned for catalysis. As expected the ligand binding and steady state data reveal that His-42 has restricted mobility in the W41A/N71W variant, due to the presence of the bulky tryptophan, which acquires a lot space in the active site.

It appears, from the data reported in this and previous chapters (see Chapters 2 and 3), that the precise location and mobility of His-42 is controlled by the bulky distal tryptophan (Trp-41) and the conserved hydrogen bond to Asn-71, however discussion of structure-function relationships is difficult in the case of the Asn-71 variants due to the lack of crystallographic data.

#### **5.3.4 Disruption of the conserved histidine-asparagine (His-Asn) hydrogen bond in HRP, CcP and KatG**

The crystal structures and sequence alignments of all peroxidases determined so far show many common features at the heme active site. In addition to the conserved amino acids, as reported in Chapter 1, a common characteristic appears to be a hydrogen bond network (Figure [5.9]) extending from the distal functional residues (His, Arg, Asn) to the functional residues (His, Asp) of the proximal side of the heme through various water molecules. No information is available for mutation of the conserved distal asparagine in APX however information of mutations on the conserved distal asparagine have been previously reported for HRP, CcP and KatG and are summarised here.

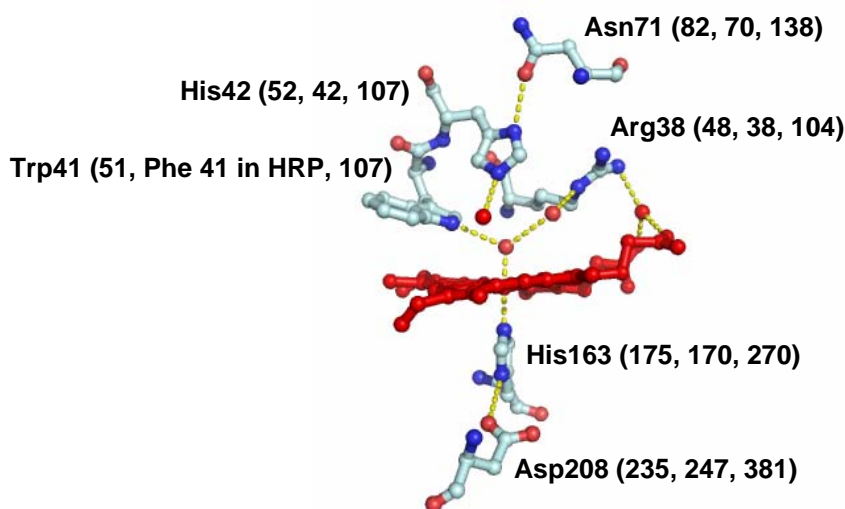


Figure [5.9]: The heme (red) and active site residues in the crystal structure of rsAPX (PDB code: 1OAG) (16). Water molecules are indicated by red spheres and hydrogen bonds are represented by yellow dashed lines. The amino acid numbering is for APX, but the numbers in parentheses denote the numbering in CcP, HRP and KatG, respectively.

#### 5.3.4.1 Mutation of the conserved His-Asn bond in HRP

The catalytic role of the conserved hydrogen bond in HRP was investigated by replacement of Asn-70 with valine (N70V) or aspartate (N70D) (12,22). The HRP variants, as with the Asn-71 variants of APX, were also found to exist as six-coordinate low-spin heme species (11). The distal histidine in peroxidases has been shown to participate in the reaction with  $\text{H}_2\text{O}_2$  (see Chapter 1, Section 1.5.4) by serving as a base, accepting a proton from  $\text{H}_2\text{O}_2$  (23). However, disruption of the conserved His-Asn bond was found to reduce the basicity of the distal histidine (12). The partial occupation of the sixth coordination site of the heme, as well the decrease of the basicity of the distal histidine, was thought to account for the low reactivity with  $\text{H}_2\text{O}_2$ , since the six-coordinated heme would have to undergo ligand exchange (like that observed for W41A in APX) before reacting with  $\text{H}_2\text{O}_2$ . The N70D variant, like the Asn-71 APX variants, was found to bind cyanide with less affinity in comparison to wild type HRP (13) and with the use of NMR and IR (Infra-red) spectroscopy together with kinetic data on the N70D variant it was demonstrated that the subtle reorientation of the distal histidine depressed the catalytic activity of the variant. Thus, the role of His-Asn hydrogen bond in the HRP distal site was accredited to improving the function of the distal histidine as a general acid-base catalyst by

adjusting the precise location of the distal histidine (13). The data for the Asn-71 variants of APX are also consistent with this proposed role of the conserved His-Asn bond in HRP.

#### **5.3.4.2 Mutation of the conserved His-Asn bond in CcP**

The corresponding His-Asn conserved bond in CcP has also been studied by mutation of the asparagine at position 82 with an aspartate (N82D) (10). The N82D-cyanide bound form has been studied extensively using NMR spectroscopy and it was found that three hyperfine-shifted resonances disappear from the NMR spectrum of the N82D-cyanide complex compared to the wild type CcP-cyanide complex. This disappearance can be ascribed to elimination of the His-Asn hydrogen bond; the disruption of the hydrogen bond renders the distal histidine able to reorient in a different direction, thus shifting the three resonances in to the unresolvable region of the NMR spectrum (10). Again, the phenomenon of reorientation of the distal histidine on disruption of the conserved His-Asn bond observed for HRP and APX is also present in the N82D CcP variant.

#### **5.3.4.3 Mutation of the conserved His-Asn bond in KatG**

KatG, on the basis of sequence alignments with CcP and APX, has been shown to be a member of the class I division of the plant, fungal and bacterial heme peroxidase superfamily. KatGs have predominant catalase activity but differ from mono-functional catalases in also exhibiting substantial peroxidatic activity with broad specificity but differ dramatically in reactivity from CcP and APX. However, from structure and sequence alignments of the crystal structures of CcP, APX and KatG (3,8,15,16,24) it appears that all class I peroxidases have conserved amino acid triads in the distal (His, Arg and Trp) and proximal (His, Asp and Trp) pockets. The conserved His-Asn hydrogen bond is also present in the active site of KatGs. The catalytic role of this conserved hydrogen bond on the bi-functional activity of KatGs was investigated by mutation of Asn-153 in *Synechocystis* KatG to an alanine or an aspartate residue (15). Both variants exhibited overall peroxidase activity similar to wild type KatG however the catalase activity of the variants was substantially reduced (15). This decrease in activity was assigned to the reduced basicity of the

distal histidine in the KatG variants a common feature also observed in the heme peroxidases described above. Also it appears the integrity of the KatG hydrogen bond network seems to be essential to provide optimal conditions for binding and oxidation of the second H<sub>2</sub>O<sub>2</sub> molecule necessary in the catalase reaction.

## 5.4 SUMMARY

In summary, in previous work (described in Chapters 2 and 3) the distal histidine (His-42) in the W41A variant of APX was found to be mobile. This conformational mobility was found to be triggered by addition of substrate, anionic ligands or change in oxidation state. On further examination of the active site of APX a hydrogen bond between His-42 and Asn-71, a conserved interaction in heme peroxidases, was identified as a possible factor controlling the mobility of the distal histidine. To investigate the role of this conserved interaction on mobility of the distal histidine, four site-directed variants were prepared: N71A, W41A/N71A, W41A/N71L, and W41A/N71W.

All four variants were expressed as holo-proteins and no post-translational modification was identified on investigation with MALDI-TOF spectrometry. The electronic absorption spectra of the Asn-71 variants were found to differ from that of rsAPX, in that the Asn-71 variants exhibited characteristic features of low-spin heme: sharp Soret band at around ~411 nm, low-spin transitions at ~530 and ~560 nm and large extinction coefficient values. The low-spin nature of the Asn-71 variants was postulated, due to the absence of structural evidence, to arise from ligation of His-42 to the heme. Despite clear low-spin character in the ferric form, the ferrous derivatives of the Asn-71 variants were indicative of five-coordinate heme, thus the distal histidine is probably displaced in the variants on reduction as observed previously for W41A variant (see Chapter 3). The exception is the ferrous form of the N71A variant, which exhibited a spectrum suggestive of low-spin ferrous heme similar to that seen for cytochrome  $b_5$ . The spectral changes observed in the Asn-71 variants on addition of cyanide were consistent with those observed for rsAPX; however, the variants were found to bind cyanide with lower affinity in comparison to rsAPX. The ferric/ferrous reduction potentials of the Asn-71 variants were comparable to rsAPX. The Asn-71 variants were able to turnover ascorbate albeit at a lower rate in comparison to rsAPX.

Collectively, the data reported here and present in the literature provides clear evidence that the conserved His-Asn hydrogen bond in the distal site of heme peroxidases is essential for controlling the precise location and thus mobility of the distal histidine. However, discussion of structure-function relationships is difficult for the Asn-71 variants due to the lack of crystallographic data.

## 5.5 REFERENCES

1. Sundaramoorthy, M., Kishi, K., Gold, M. H., and Poulos, T. L. (1994) *Journal of Biological Chemistry* **269**, 32759-32767
2. Smulevich, G. (1998) *Biospectroscopy* **4**, S3-S17
3. Finzel, B. C., Poulos, T. L., and Kraut, J. (1984) *Journal of Biological Chemistry* **259**, 13027-13036
4. Edwards, S. L., Raag, R., Wariishi, H., Gold, M. H., and Poulos, T. L. (1993) *Proceedings of the National Academy of Sciences of the United States of America* **90**, 750-754
5. Kunishima, N., Fukuyama, K., Matsubara, H., Hatanaka, H., Shibano, Y., and Amachi, T. (1994) *Journal of Molecular Biology* **235**, 331-344
6. Poulos, T. L., Edwards, S. L., Wariishi, H., and Gold, M. H. (1993) *Journal of Biological Chemistry* **268**, 4429-4440
7. Petersen, J., F. W, Kadziola, A., and Larsen, E. (1994) *FEBS Letters* **339**, 291-296
8. Patterson, W. R., and Poulos, T. L. (1995) *Biochemistry* **34**, 4331-4341
9. Schuller, D. J., Ban, N., vanHuystee, R. B., McPherson, A., and Poulos, T. L. (1996) *Structure* **4**, 311-321
10. Satterlee, J. D., Alam, S. L., Mauro, J. M., Erman, J. E., and Poulos, T. L. (1994) *European Journal of Biochemistry* **224**, 81-87
11. Mukai, M., Nagano, S., Tanaka, M., Ishimori, K., Morishima, I., Ogura, T., Watanabe, Y., and Kitagawa, T. (1997) *Journal of the American Chemical Society* **119**, 1758-1766
12. Nagano, S., Tanaka, M., Ishimori, K., Watanabe, Y., and Morishima, I. (1996) *Biochemistry* **35**, 14251-14258

13. Tanaka, M., Nagano, S., Ishimori, K., and Morishima, I. (1997) *Biochemistry* **36**, 9791-9798
14. Savenkova, M. L., and de Montellano, P. R. O. (1998) *Archives of Biochemistry and Biophysics* **351**, 286-293
15. Jakopitsch, C., Auer, M., Regelsberger, G., Jantschko, W., Furtmuller, P. G., Ruker, F., and Obinger, C. (2003) *European Journal of Biochemistry* **270**, 1006-1013
16. Sharp, K. H., Mewies, M., Moody, P. C. E., and Raven, E. L. (2003) *Nature Structural Biology* **10**, 303-307
17. Metcalfe, C. L., Ott, M., Patel, N., Singh, K., Mistry, S. C., Goff, H. M., and Raven, E. L. (2004) *Journal of the American Chemical Society* **126**, 16242-16248
18. Lad, L., Mewies, M., and Raven, E. L. (2002) *Biochemistry* **41**, 13774-13781
19. Ozols, J., and Strittmatter, P. (1964) *Journal of Biological Chemistry* **239**, 1018-1023
20. Efimov, I., Papadopoulou, N. D., McLean, K. J., Badyal, S. K., Macdonald, I. K., Munro, A. W., Moody, P. C. E., and Raven, E. L. (2007) *Biochemistry* **46**, 8017-8023
21. Heering, H. A., Smith, A. T., and Smulevich, G. (2002) *Journal of Biochemistry* **363**, 571-579
22. Nagano, S., Tanaka, M., Watanabe, Y., and Morishima, I. (1995) *Biochemical and Biophysical Research Communications* **207**, 417-423
23. Poulos, T. L., and Kraut, J. (1980) *Journal of Biological Chemistry* **255**, 8199-8205
24. Yamada, Y., Fujiwara, T., Sato, T., Igarashi, N., and Tanaka, N. (2002) *Nature Structural Biology* **9**, 691-695

***CHAPTER SIX***

**MATERIALS AND METHODS**

## CHAPTER SIX

### MATERIALS AND METHODS

---

#### 6.1 MATERIALS

##### 6.1.1 Chemicals and reagents

All chemicals used were of the highest analytical grade (>99 %), the exception being bacteriological media and acetic acid used in polyacrylamide gel electrophoresis (PAGE) gel staining, which were of laboratory grade. Chemicals used to make buffer solutions were purchased from Fisher Chemicals. All other chemicals and reagents were obtained from commercial sources and used without further purification unless otherwise stated. Sodium dodecyl sulphate (SDS) was from BDH Chemicals. Hydrogen peroxide (H<sub>2</sub>O<sub>2</sub>) solutions were freshly prepared by dilution of a 30 % (v/v) solution (BDH Chemicals): exact concentration were measured spectrophotometrically ( $\epsilon_{240} = 39.4 \text{ M}^{-1} \text{ cm}^{-1}$ ) (1). Water was of high quality, doubly deionised and was drawn from an Elga PureLab Option (DV35) water purifier, which itself was fed with deionised water. All molecular biology kits and enzymes were used according to manufacturer's protocols.

## 6.2 RECOMBINANT DNA TECHNIQUES

rsAPX DNA was obtained from Dr I. K. Macdonald (Department of Chemistry, University of Leicester) and was the starting point for mutagenesis and protein isolation of the APX variants.

### 6.2.1 Oligonucleotides

Complementary oligonucleotides (29 - 35 bases in length) were designed to have ~15 bases either side of the residue to be mutated and end in the base G or C. The complementary pairs of oligonucleotides, synthesised and desalted by Invitrogen, containing the appropriate mismatch bases (indicated in red) are depicted in Table [6.1]. The melting temperatures ( $T_m$ ) of primers were calculated according to Equation [6.1]:

$$T_m = 81.5 + 16.6 (\log_{10}[J^+] + 0.41(\% \text{ GC}) - (600/L) \quad (\text{Eq.}[6.1])$$

where  $J^+$  is the concentration of the monovalent cations present in the buffers (entered in as M, usually 0.1 M), % GC is the percentage of the bases G and C in the designed oligonucleotide and L is the length of the oligonucleotide in base pairs.

The W41A/N71A mutant ( $T_m = 85 \text{ }^\circ\text{C}$ ) was made using the W41A oligonucleotide and N71A DNA. The double mutants W41A/N71W and W41A/N71L were made using W41A DNA as template.

### 6.2.2 Site-directed mutagenesis

Site-directed mutagenesis, using the appropriate pair of oligonucleotides, was carried out using the Quikchange™ mutagenesis kit (Stratagene) for the W41A variant whereas the Asn-71 variants were made using KOD Hot Start DNA polymerase kit (Novogen). Reactions were prepared in thin-walled PCR tubes on ice as described in the protocol (reactions performed with *pfu Ultra* polymerase were set up using half the suggested volume) and in the order listed in Tables [6.2 - 6.3]. The 10x buffer and dNTP mix were supplied with the *pfu Ultra* polymerase (Stratagene) or KOD Hot Start DNA polymerase (Novogen).

**Table [6.1]: The forward and reverse oligonucleotides used to generate variants of rsAPX. The mismatch codons are highlighted in red.**

Variant
<b>W41A</b> $T_m = 80\text{ }^\circ\text{C}$ Forward: 5' G CTC CGT TTG GCA <b>GCG</b> CAC TCT GCT GGA ACC 3' Reverse: 3' C GAG GCA AAC CGT <b>CGC</b> GTG AGA CGA CCT TGG 5'
<b>N71A</b> $T_m = 72\text{ }^\circ\text{C}$ Forward: 5' G GCT CAC AGC GCT <b>GCT</b> AAC GGT CTT GAC ATC GC 3' Reverse: 3' C CGA GTG TCG CGA <b>CGA</b> TTG CCA GAA CTG TAG CG 5'
<b>W41A/N71W</b> $T_m = 72\text{ }^\circ\text{C}$ Forward: 5' G GCT CAC AGC GCT <b>TGG</b> AAC GGT CTT GAC ATC GC 3' Reverse: 3' C CGA GTG TCG CGA <b>ACC</b> TTG CCA GAA CTG TAG CG 5'
<b>W41A/N71L</b> $T_m = 72\text{ }^\circ\text{C}$ Forward: 5' G GCT CAC AGC GCT <b>CTG</b> AAC GGT CTT GAC ATC GC 3' Reverse: 3' C CGA GTG TCG CGA <b>GAC</b> TTG CCA GAA CTG TAG CG 5'

**Table [6.2]: Reaction volumes ( $\mu\text{l}$ ) used in successful site-directed mutagenesis of W41A.**

Reaction	1	2
Sterile water	16.5	15
Glycerol	2.5	2.5
10x buffer	2.5	2.5
MgCl <sub>2</sub>	1	2.5
Template	0.5	1
Forward primer	0.5	2
Reverse primer	0.5	0.5
dNTPs	0.5	0.5
<i>pfu Ultra</i>	0.5	0.5

**Table [6.3]: Reaction volumes ( $\mu\text{l}$ ) used in site-directed mutagenesis of Asn-71 variants that exhibited positive results on agarose gels.**

Reaction	N71A	W41A/N71A	W41A/N71L/W
<b>Sterile water</b>	27.5	27	27.5
<b>10x buffer</b>	5	5	5
<b>MgSO<sub>4</sub></b>	2	2	1
<b>Template</b>	2	2	2
<b>Forward primer</b>	4	4	4
<b>Reverse primer</b>	4	4	4
<b>dNTPs</b>	2.5	2.5	2.5
<b>DMSO</b>	2	2.5	3
<b>KOD polymerase</b>	1	1	1

Magnesium sulphate (25 mM, MgSO<sub>4</sub>) and DMSO were provided with the KOD Hot Start DNA polymerase (Novogen) kit whereas with the *pfu Ultra* magnesium chloride (100 mM) was used, which was filter sterilised using a 0.2  $\mu\text{m}$  syringe-top filter (Acrodisc) prior to use. The pQE-30 vector (Appendix B) containing the rsAPX or W41A gene (12.5 ng/ $\mu\text{l}$  of DNA) was the template in the PCR reactions. Oligonucleotide stocks (made up in TE (100 mM Tris-HCl, pH 8, 1 mM EDTA) buffer) with an OD at A<sub>260</sub> of 1 were used in the mutagenesis.

The PCR reaction mixtures were centrifuged (13,000 rpm, for 1 minute) and the temperature cycling programs for the PCR reaction were entered into the PCR block (Perkin Elmer, 480 DNA Thermocycler) as described in Tables [6.4 - 6.6]. The annealing temperature was calculated using Equation [6.2].

$$\text{Primer annealing temperature } (^{\circ}\text{C}) = \text{Primer } T_m - 5 \quad (\text{Eq.}[6.2])$$

*pfu Ultra* or KOD Hot Start polymerase and a drop of mineral oil (Sigma, added to surface to prevent evaporation) were added to the reaction mixtures, which were then placed in the PCR block when the temperature had reached 95  $^{\circ}\text{C}$ , when using *pfu Ultra* polymerase or 94  $^{\circ}\text{C}$  when using KOD Hot Start polymerase (placing reactions in before the denaturing temperature is reached can lead to premature annealing of template and primers).

Table [6.4]: Temperature cycler program for W41A site-directed mutagenesis.

Number of Cycles	Temperature (°C)	Time (s)
1	95	30
16	95	30
	80	60
	72	300
1	72	600

Table [6.5]: Temperature cycler program for W41A/N71W/L and N71A site-directed mutagenesis.

Number of Cycles	Temperature (°C)	Time (s)
1	94	120
18 for W41A/N71L and W41A/N71W	94	30
30 for N71A	67	60
	68	480
1	68	600

Table [6.6]: Temperature cycler program for W41A/N71A site-directed mutagenesis.

Number of Cycles	Temperature (°C)	Time (s)
1	94	30
16	94	30
	80	60
	68	420

When the reaction was complete an agarose gel was run to assess the productivity of the reaction before proceeding onto parental DNA digestion and transformation. Reactions which exhibited a band at 5 kb on the agarose gel (Figure

[6.1]) were subjected to digestion of the methylated and hemimethylated parental DNA by addition of *DpnI* (1  $\mu$ l, Stratagene). The mixtures were centrifuged (13,000 rpm, 1 minute) and immediately incubated at 37 °C for 1 hour.

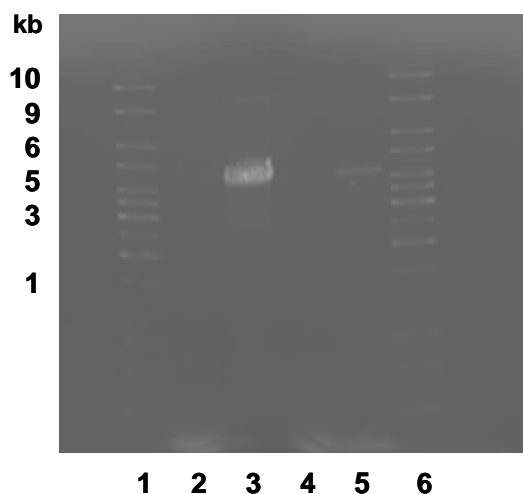


Figure [6.1]: Agarose gel showing results of site-directed mutagenesis of W41A. Lane 1: DNA ladder; Lane 2: PCR reaction 1; Lane 3: PCR reaction 2; Lane 4: PCR reaction 3; Lane 5: PCR reactions 4; Lane 6: DNA ladder.

### 6.2.3 Transformation into X11-Blue super-competent cells

The reaction product (1-5  $\mu$ l) was transformed into super-competent *Epicurian Coli* XL1-Blue cells (50  $\mu$ l, Stratagene) in prechilled Falcon® 2059 Propylene tubes (15 ml). The reactions were swirled to mix and stored on ice for 30 minutes. The cells were heat-pulsed at 42 °C for 45 seconds, returned to ice for 2 minutes and incubated with shaking for 1 hour at 37 °C, 225 rpm with 0.5 ml pre-heated LB media (42 °C, Appendix A) containing 70  $\mu$ l of 1 M MgCl<sub>2</sub> and 1 M MgSO<sub>4</sub> each. The cells were harvested using a bench centrifuge (1,500 rpm for 5 minutes at 5 °C) and 200  $\mu$ l of the supernatant discarded. The cell pellet was resuspended in the remaining supernatant before being plated (equal aliquots) onto LB agar plates (Appendix A) containing ampicillin (100  $\mu$ g/ml) and incubated inverted at 37 °C overnight. To confirm the identity of the transformants, a single colony from the overnight plates was selected and incubated into 10 ml LB media containing ampicillin (100  $\mu$ g/ml) overnight at 37 °C with shaking at 250 rpm. Variant DNA was isolated from the overnight cultures using the QIAprep® Spin Miniprep kit (Qiagen), as described in

Section 6.2.4, was analysed using agarose electrophoresis and the DNA was sequenced to confirm the mutation.

#### 6.2.4 Isolation of DNA

The variant DNA was prepared using stationary phase culture and the extraction procedure was performed using a QIAprep® Spin Miniprep kit (Qiagen catalogue number 27104) for microcentrifuges. The protocol from the kit was followed, except the eluting step was performed with sterile water and not eluting buffer (EB buffer). A 10 ml overnight culture (described above) was harvested using the bench centrifuge (1,500 rpm for 5 minutes at 5 °C). The supernatant was discarded and the tubes were inverted and placed on a paper towel to drain the excess solution. The cell pellet was resuspended in pre-lysis buffer (Buffer P1, 250 µl, Appendix A) and transferred to a sterile eppendorf. Alkaline lysis buffer (Buffer P2, 250 µl, Appendix A) was added and the tube inverted gently 5 times. Neutralisation solution (Buffer N3, 350 µl, Appendix A) was added to the cell suspension and the tube was inverted immediately but gently 5 times before centrifuging at 13,000 rpm for 10 minutes using a microcentrifuge. The supernatant was added to a QIAprep® spin column and centrifuged for 1 minute at 13,000 rpm. The solution collected in the spin column vial holder was discarded. Wash solution (PB buffer, 500 µl, Appendix A) was applied to the spin filter before centrifuging for 1 minute at 13,000 rpm. Again the solution collected in the bottom vial was discarded before the column was washed again with PE buffer (750 µl, Appendix A) and centrifuged for 1 minute at 13,000 rpm. The flow-through was discarded of and the column was further centrifuged at 13,000 rpm for 1 minute to remove residual buffer (ethanol). The column was transferred to a new sterile eppendorf and sterile water (50 µl) was added carefully to the centre of the spin column. The column was left to stand for 1 minute before centrifuging at 13,000 rpm for 1 minute to elute the DNA. The DNA sample obtained was stored at -20 °C. DNA concentration was determined using Equation [6.3] by measuring the absorbance at  $\lambda = 260$  nm ( $A_{260}$ ). DNA purity was assessed by calculating the  $A_{260}/A_{280}$  ratio; DNA with a ratio of 1.8 was deemed pure.

$$\text{Concentration of double stranded DNA} = A_{260} \times 50 \mu\text{g/ml} \quad (\text{Eq.}[6.3])$$

### 6.2.5 DNA sequencing

After mutagenesis sequencing of the entire APX variant gene was performed to ensure that no spurious mutations had arisen during the mutagenic reactions. Automated fluorescent sequencing was performed by the Protein and Nucleic Acid Chemistry Laboratory, University of Leicester, on an Applied Biosystems 3730 DNA analyzer and sequence data were analysed using the program SeqED (Applied Biosystems). The plasmid DNA sequencing was achieved using PQEF and PQER sequencing primers (designed and obtained from Qiagen, Appendix B).

### 6.2.6 Agarose gel electrophoresis

Agarose (0.7 % w/v) was dissolved in TAE buffer (200 ml, Appendix A) by heating in microwave. Ethidium bromide solution (20  $\mu$ l of 10 mg/ml in water) was added to the gel mixture and the gel was set in a horizontal bed. Electrophoresis was performed in TAE buffer at 120 V. Samples (10  $\mu$ l) were mixed with sample loading buffer (2  $\mu$ l, Fermentas) prior to being loaded on to the gel. DNA ladder (2  $\mu$ l, Generuler™, 1kb DNA ladder, Fermentas, catalogue number SM03111) was also loaded onto the gel to aid location of the desired bands. Nucleic acids were visualised by exposing the gel to long wavelength UV radiation on a transilluminator.

### 6.2.7 Transformation of the recombinant DNA into competent *E.Coli* cells

The sequenced variant DNA from the XL1-Blue cell transformation (1  $\mu$ l) was added to pre-chilled Falcon™ 2059 Propylene tubes (15 ml) containing *Escherichia coli* SG13009 cells (50  $\mu$ l) (Qiagen, containing pREP4 vector). The reaction mixtures were swirled to mix and placed on ice for 30 minutes. The cells were heat-pulsed at 42 °C for 45 seconds, returned to ice for 2 minutes and incubated with shaking for 1 hour at 37 °C, 225 rpm with 0.5 ml pre-heated LB media (42 °C, Appendix A) containing 70  $\mu$ l of 1 M MgCl<sub>2</sub> and 1 M MgSO<sub>4</sub> each. The cells were harvested using a bench centrifuge (1,500 rpm for 5 minutes at 5 °C) and 200  $\mu$ l of the supernatant discarded. The cell pellet was resuspended in the remaining supernatant before being plated (equal aliquots) onto LB agar plates (Appendix A) containing ampicillin (100  $\mu$ g/ml) and kanamycin (30  $\mu$ g/ml) and were incubated inverted at 37 °C overnight. To confirm the identity of the transformants, a single colony from the

overnight plates was selected and incubated into 10 ml LB media containing ampicillin (100 µg/ml) and kanamycin (30 µg/ml) overnight at 37 °C with shaking at 250 rpm. Variant DNA was isolated from the overnight cultures using the QIAprep® Spin Miniprep kit (Qiagen) using a microcentrifuge as described in Section 6.2.4 and the DNA was re-sequenced to confirm the mutation. Overnight cultures were also used to make glycerol stocks (500 µl of overnight culture and 500 µl of sterile glycerol, stored at -80 °C) as an inoculum for expression and isolation of the variant proteins.

## **6.3 PREPARATION OF RECOMBINANT SOYBEAN APX AND VARIANTS**

### **6.3.1 Protein expression**

*E. coli* SG13009 cells (Qiagen, containing pREP4 vector) incorporating pQE-30 expression plasmid (Qiagen, Appendix B) (2) taken from a frozen (-80 °C) glycerol stock, were streaked onto LB agar plates (Appendix A) containing ampicillin (100 µg/ml) and kanamycin (30 µg/ml). The plates were inverted and incubated at 37 °C overnight. Single colonies were used to inoculate LB media (400 ml) containing ampicillin (100 µg/ml) and kanamycin (30 µg/ml), and the flask was incubated overnight at 37 °C with shaking (225 rpm). An aliquot of this overnight culture (500 µl) was added to sterile glycerol (500 µl) to form a new glycerol stock, which was frozen on dry ice before storage at -80 °C. The overnight culture (50 ml) was used to seed LB media (1 l) containing ampicillin (100 µg/ml) and kanamycin (30 µg/ml) in a 2 l flask, and was further incubated at 37 °C with shaking (225 rpm), to an absorbance at 600 nm of 1. The temperature was adjusted to 27 °C before protein expression was induced with isopropyl-β-D-thiogalactopyranoside (IPTG, final concentration of 0.1 mM (1 ml of 1 M stock) Melford). The flasks were incubated overnight at 27 °C with shaking (225 rpm). Cells were harvested at 4 °C by centrifugation at 6,000 rpm for 10 minutes and the cell pellets were then frozen at -80 °C until required.

### **6.3.2 Protein expression and purification of soybean APX and variants**

All purification steps were performed at 4 °C. The cell pellets were thawed in sonication buffer (200 ml, Appendix A) with stirring and phenylmethylsulfonyl fluoride

(PMSF, 50 mg in 2 ml isopropanol) was added to the cell suspension. Cell lysis was accomplished enzymatically by stirring with hen egg white lysozyme (~5 mg) for 20 minutes until the suspension became viscous. DNase (50  $\mu$ l of 1 mg/ml) was added and the suspension stirred for 5 minutes. The mixture was then sonicated at maximum power for 1 minute, followed by a cooling period of 1 minute until the suspension became fluid. The mass of cells was centrifuged (20,000 rpm for 40 minutes) and the supernatant collected.

A nickel ( $\text{Ni}^{2+}$ ) - nitrilotracetic acid ( $\text{Ni}^{2+}$ - NTA) super flow agarose column (Qiagen) was used to isolate the hexa-histidine tagged proteins from the supernatant. A column of 5 ml  $\text{Ni}^{2+}$ - NTA super flow resin was packed and flushed through with water (100 ml). The resin was equilibrated with sonication buffer (100 ml, Appendix A), and the supernatant loaded on at a steady rate of 1ml/min. The column was flushed with sonication buffer (~500 ml) until the eluant gave an absorbance of 0.01 at 280 nm. The column was further washed with wash buffer (500 ml, Appendix A) and then the bound protein was eluted with elution buffer (100 - 200 ml, Appendix A). The pH of the eluted protein was adjusted to 6.0 by drop wise addition of 1 M dipotassium hydrogen phosphate buffer with stirring.

The next step involved reconstitution of the protein with hemin chloride. A solution of heme was prepared from hemin chloride (5 mg, Fluka) dissolved in 0.1 M potassium hydroxide (1 ml). Heme was added in 20  $\mu$ l aliquots (and monitored by electronic absorption spectroscopy to check for incorporation of heme) to the stirred solution of the protein with 5 minute intervals until a small excess had been added. The protein was loaded into pre-treated dialysis membranes (Medicell International Ltd) and dialysed against FFQ buffer (5 l, Appendix A) with gentle stirring overnight.

Excess heme was removed from the protein solution using Q Sepharose fast flow resin (FFQ, Amersham). After removal from the dialysis membranes the protein-heme solution was centrifuged (5,000 rpm for 5 minutes) and the protein solution decanted off the precipitate. A 2.5 x 10 cm column of FFQ-sepharose resin was prepared and flushed with water (300 ml) before equilibrating with at least 5 column volumes of FFQ buffer (Appendix A). The centrifuged protein solution was loaded onto the column at a flow rate of 1 ml/min. A dark band was observed as the protein bound at the top of the resin. The column was washed with FFQ buffer (100 ml) before eluting the bound protein with FFQ elution buffer (100 ml, Appendix A).

The purified protein was concentrated using a stirred cell fitted with an Amicon 10,000 MW cut off membrane (Millipore) to minimum volume (~10 ml) before exhaustively exchanging into water. The protein solution was then concentrated to a minimum volume (1 ml) using a Centriprep (YM10 membrane, Millipore) before FPLC purification.

### **6.3.3 Fast Performance Liquid Chromatography (FPLC) of protein samples**

Further purification using gel filtration chromatography (FPLC) was performed on the concentrated protein samples where a 1 ml sample of protein was injected on to a pre-equilibrated (with 0.15 M potassium phosphate, pH 7.0 buffer) gel filtration column (Superdex column 75 HR) on the ÄKTA FPLC (Amersham Pharmacia Biotech) that was linked to a Pentium 4 computer (COMPAQ). Purification of the protein sample was monitored at the wavelength of 280 nm using the Unicorn software (version 4.0, Amersham Pharmacia Biotech). The purified protein was eluted using 0.15 M potassium phosphate buffer pH 7.0 with retention time of 45 minutes (at a flow rate of 0.5 ml/min). The purified protein samples were then exhaustively exchanged in deionised water and concentrated using a Centricon (YM10 membrane, Millipore), and were then stored at -80 °C until required. Storing protein samples in buffer was avoided, as storage in buffer appears to affect the spin state of the protein. All proteins used to conduct experiments were FPLC purified.

## **6.4 METHODS FOR PROTEIN ANALYSIS AND CHARACTERISATION**

### **6.4.1 Buffers and solution preparation**

Sodium phosphate (see Appendix A) and potassium phosphate (Appendix A) buffers were used in the pH range 5.5 - 8.5. The ionic strength of this buffer system ranges between 95 - 110 mM depending upon the solution pH. Measurements of aqueous solution pH were taken using a Russell pH-electrode attached to a digital pH-meter (Radiometer, PHM93) and all buffers were filtered using the ultra filtration apparatus (Millipore).

### 6.4.2 SDS-PAGE electrophoresis

All proteins were analysed on 15 % acrylamide gels containing 0.1 % SDS and 4 % polyacrylamide stacking gel. Gels were prepared and run using Mini-Protein II gel systems (Bio-Rad) at a thickness of 0.75 mm. Protein samples were prepared for electrophoresis by the addition of an equal volume of reducing sample buffer (Appendix A) and incubated at 100 °C for three minutes and cooled briefly on ice before being loaded onto the gel. Gels were run in SDS running buffer (Appendix A) at 150 V until the dye-front reached the base of the gel. Gels were stained by soaking in Coomassie Brilliant Blue R250 (Appendix A) for 15 minutes and then destained by soaking in destaining buffer overnight (Appendix A).

### 6.4.3 UV-visible spectroscopy

Routine absorbance measurements and spectra were conducted using a Perkin Elmer Lambda 35 UV-visible spectrophotometer, linked to a Graphics series (G70fmb) Dell computer, or using Lambda 40, linked to a Optiplex (Gx1) Dell computer. Temperature control ( $25.0 \pm 0.1$  °C) was achieved using an internal thermally-jacketed cell holder which was operated in tandem for the Lambda 35 spectrophotometer, whereas temperature control when using Lambda 40 spectrophotometer was achieved using a thermally-jacketed cell holder that was connected to a circulating water bath (NESLAB RTE-200). A Perkin Elmer Lambda 25 UV-visible spectrophotometer was also used to conduct experiments on the reduced form of rsAPX and the rsAPX variants. The Lambda 25 spectrophotometer was linked to an Optiplex (GX620) Dell computer and temperature control was achieved using an internal thermally-jacketed cell holder which was operated in tandem. A typical 270 - 700 nm scan was obtained using a scan speed of 480 nm/minute, acquiring at 0.5 nm intervals and with a 1 nm slit width using a 0.5 ml, 1 ml or 3 ml (10 mm path length) quartz cuvette. Unless otherwise indicated, sample concentrations were determined gravimetrically. Baseline corrections were made against the buffers or solvents used.

#### 6.4.4 Determination of absorption coefficients

The total heme content of a heme protein solution and therefore the absorption coefficient of the heme protein can be determined using the pyridine-haemochromagen method described by Antonini and Brunori (3). An alkaline pyridine solution was prepared from the addition of pyridine (2 ml), 1 M sodium hydroxide (600  $\mu$ l) and distilled water to a final volume of 6 ml. A protein sample with absorbance in the range of 0.3 to 0.9 in the visible region was required to provide the most reliable data; thus the concentration of the protein sample was established by gravimetric dilution and determination of the absorbance at the Soret maximum. Pyridine solution (1.5 ml) was added to the protein solution (500  $\mu$ l of known concentration) to form the pyridine-heme complex. The resulting solution (2 ml) of oxidised haemochromagen (yellow in colour) was divided into two 1 ml aliquots. After five minutes (to enable complete conversion to the haemochromagen), the electronic absorption spectrum was recorded using one of the oxidised aliquots. A single crystal of dithionite was added to the oxidised pyridine-hemochromagen solution and the spectrum of the unstable reduced haemochromagen (scarlet in colour) was recorded immediately. The complete transfer of heme from the protein to pyridine was checked by determining the absorbance at maximum ( $\lambda = 557$  nm) and minimum ( $\lambda = 540$  nm) wavelengths; a ratio of  $A_{557}/A_{540} = 3.5$  is found for protoheme. Absorption coefficients were then calculated knowing the absorption coefficient of the pyridine-protoheme complex ( $\epsilon_{557} = 32.0 \text{ mM}^{-1} \text{ cm}^{-1}$ ) using Equation [6.4]: where A = absorbance of enzyme stock solution, c = concentration of enzyme,  $\epsilon$  = molar extinction coefficient and l is the pathlength of the cuvette. The experiment was repeated on the other aliquot 24 hours later to check reproducibility. Figure [6.2] shows the pyridine hemochrome spectrum of rsAPX

$$A = \epsilon c l \quad \text{(Eq.6.4)}$$

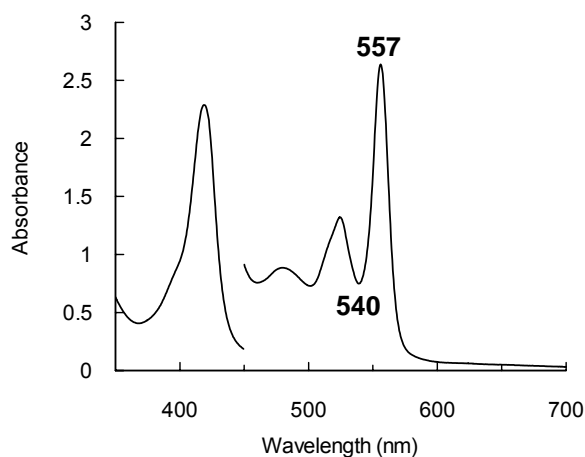


**Figure [6.2]: Electronic spectrum of the reduced pyridine-haemochromagen of rsAPX. The visible region has been multiplied by a factor of five for clarity. The ratio of  $A_{557}/A_{540} = 3.53$ , and therefore indicates a protoheme structure for the protein.**

#### 6.4.5 Ligand-bound derivative spectra

Analytical grade potassium cyanide, sodium fluoride, and sodium azide (Sigma) were dissolved in sodium phosphate buffer (pH 7.0,  $\mu = 0.10$  M) and were filter sterilised using 0.2  $\mu\text{m}$  syringe-top filters (Acrodisc). Spectra of ligand-bound derivatives were obtained by the addition of a small excess of ligand (2  $\mu\text{l}$  of 1 M ligand stock solution, made up in sodium phosphate buffer,  $\mu = 0.10$  M, pH 7.0), to an oxidised solution of rsAPX or variant protein ( $\sim 5$   $\mu\text{M}$ ) equilibrated in sodium phosphate buffer (pH 7.0,  $\mu = 0.10$  M) at 25.0  $^{\circ}\text{C}$ .

The ferrous forms of rsAPX and variants were prepared by the addition of microlitre volumes of fresh sodium dithionite solution to ferric enzyme ( $\sim 8$   $\mu\text{M}$ ) present in anaerobic buffer in an air-tight cuvette until no further change in the spectrum was observed. All solutions were prepared in a glove box (Belle Technology) using anaerobic buffer. The concentration of the sodium dithionite stock was not determined directly, but was used to provide qualitative reduction of the protein samples. The nitric oxide derivatives of rsAPX and W41A were formed by addition of a crystal of potassium nitrite to reduced protein sample ( $\sim 8$   $\mu\text{M}$ ).

### 6.4.6 Ligand binding studies

Equilibrium binding parameters were determined by adding microlitre volumes of the appropriately diluted ligand (cyanide or azide) solutions (made up in sodium phosphate buffer, pH 7.0,  $\mu = 0.1$  M and filter sterilised) using a Hamilton syringe to an air-tight cuvette containing ferric protein ( $\sim 8 \mu\text{M}$ ), which was mixed by inversion and allowed to equilibrate. The UV-visible spectra (270 - 700 nm) were recorded after each addition of ligand. The ligand binding affinity was monitored spectroscopically using absorption at 418 nm and 419 nm for cyanide binding to W41A and rsAPX and the various mutants respectively, and 411.5 nm and 405 nm for azide binding to rsAPX and W41A, respectively.

All solutions required for determining binding parameters of cyanide to ferrous protein were prepared anaerobically in a glove box (Belle Technology) by the addition of microlitre volumes of fresh sodium dithionite solution to an anaerobic solution of ferric protein ( $\sim 8 \mu\text{M}$ ) until no further change in the spectrum was observed. All solutions required for the titration were kept anaerobic by the use of glucose (10 mM, Fisher), glucose oxidase (50  $\mu\text{g/ml}$ , Sigma) and catalase (5  $\mu\text{g/ml}$  Sigma) was also added to remove any  $\text{H}_2\text{O}_2$  generated by the glucose/glucose oxidase system. The same method as described above for the ferric form was used when titrating cyanide into dithionite-reduced protein. The ligand binding affinity was monitored spectroscopically using absorption at 426 nm for cyanide binding to reduced rsAPX and W41A. As a consequence of the high affinity of ferric-rsAPX for cyanide, a non-linear regression analysis using the quadratic equation (Equation [6.5]) was applied to determine the  $K_d$ , where  $[E]$  and  $[L]$  represent the calculated concentrations of total enzyme and total ligand after each addition,  $\Delta A$  and  $\Delta A_\infty$  are the absorbance changes corresponding to the intermediate and saturating ligand concentrations, and  $K_d$  is the equilibrium dissociation constant.

$$\Delta A = \frac{\Delta A_\infty}{2[E]} \{ [E] + [L] + K_d - \sqrt{([E] + [L] + K_d)^2 - 4[E][L]} \} \quad (\text{Eq. [6.5]})$$

Equilibrium dissociation constants for binding of cyanide to ferrous rsAPX, ferric/ferrous W41A and the Asn-71 variants and of azide to ferric rsAPX and W41A,

were calculated using Equation [6.6] in the Grafit 5 software package (Grafit version 5.0.3, Erithacus Software Ltd.):

$$\Delta A = \frac{\Delta A_{\infty} [\text{Free}]}{K_d + [\text{Free}]} \quad (\text{Eq.}[6.6])$$

where  $\Delta A$  and  $\Delta A_{\infty}$  are the absorbance changes corresponding to the intermediate and saturating ligand concentrations,  $[\text{Free}]$  is total concentration of unbound ligand and  $K_d$  is the equilibrium dissociation constant.

#### 6.4.7 Electronic Paramagnetic Resonance (EPR) Spectroscopy

The EPR studies were conducted in collaboration with Dr H. Seward (Department of Biochemistry, University of Leicester) and Dr M. R. Cheesman, in the laboratory supervised by Professor A. J. Thomson (Department of Chemical Sciences and Pharmacy, University of East Anglia, Norwich). Samples were exchanged into sodium phosphate buffer (pH 7.0,  $\mu = 0.10$  M) using a Centricon (Millipore). Glycerol (50 % v/v) was added to the protein sample (final concentration of 300  $\mu\text{M}$ , 200  $\mu\text{l}$  total volume) to obtain quality glasses on freezing for low temperature EPR measurements. X-Band EPR spectra were recorded on a Bruker ER-300D series electromagnet and microwave source interfaced to a Bruker EMX control unit and fitted with an ESR-9 liquid Helium flow cryostat from Oxford Instruments and a dual mode microwave cavity from Bruker (ER-4116DM). [Microwave frequency: 9.67 GHz; microwave power: 2 mW; temperature: 10.7 K; modulation amplitude: 10G]. Quantification of  $S = \frac{1}{2}$  species was carried out by comparison with the spin standard copper ( $\text{Cu}^{2+}$  - EDTA) as described in the literature (4).

## 6.5 STEADY STATE KINETICS

Steady state kinetic measurements were conducted using a Perkin-Elmer spectrophotometer in a fixed wavelength scan mode, acquiring at 0.1 second intervals, monitoring at a wavelength that is dominated by either the reducing substrate or oxidised product over 15 seconds.

### 6.5.1 Measurement of ascorbate and guaiacol activity

The method used to assay APX activity is essentially identical to that reported in the literature (5,6). In a 0.5 ml quartz cuvette (2 mm pathlength) ascorbate (0.1 mM) and rsAPX (25 nM) or variant protein were preincubated (25.0 °C) for 3 minutes in sodium phosphate ( $\mu = 0.10$  M, pH 7.0). The reaction was initiated by the addition of H<sub>2</sub>O<sub>2</sub> (0.1 mM). Oxidation of ascorbate to monodehydroascorbate radical was monitored by obtaining time-dependent spectra of the decrease in absorbance at 290 nm acid ( $\epsilon_{290} = 2.8 \text{ mM}^{-1} \text{ cm}^{-1}$ ) using the Kin-Lab program on spectrophotometer (7). The initial rates obtained from the time-dependent spectra were multiplied by a factor of two to account for the disproportionation of the monodehydroascorbate radical (see Chapter 1, Section 1.5) (6). The above procedure was repeated increasing the ascorbate concentration but maintaining a total volume of 0.5 ml.

Guaiacol stock solution (100 mM) was prepared in sodium phosphate buffer ( $\mu = 0.10$  M, pH 7.0) with 30 % ethanol (8). The oxidation of opaque guaiacol to the red coloured tetraguaiacol was monitored at 470 nm ( $\epsilon_{470} = 22.6 \text{ mM}^{-1} \text{ cm}^{-1}$ ) (9). Guaiacol assays were performed in a 1 ml, 10 mm pathlength quartz cuvette.

Rate of activity was determined by dividing the change in absorbance by the extinction coefficient of the substrate in the case of ascorbate or product in the case of guaiacol. Values for  $k_{\text{cat}}$  were obtained directly from rate ( $\mu\text{M s}^{-1}$ )/[enzyme concentration used in the assay] ( $\mu\text{M}$ ) *versus* substrate concentration plots of the assay data. All kinetic parameters reported are averages of at least three separate experiments, unless stated otherwise.

Steady state turnover of ascorbate by rsAPX exhibits sigmoidal kinetics (Figure [6.3]) which was fitted to the Hill equation (Equation [6.7]):

$$\frac{v}{V_{\max}} = \frac{[S]^n}{K^n + [S]^n} \quad (\text{Eq.}[6.7])$$

where  $v$  is the initial rate,  $V_{\max}$  is the maximum velocity,  $n$  is the level of cooperativity (see below),  $K$  is the substrate concentration at half the maximal rate (defines the affinity of the enzyme for substrate) and  $[S]$  is the substrate concentration.

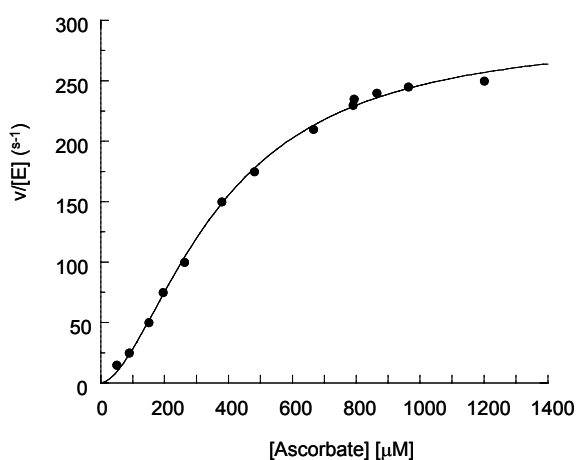


**Figure [6.3]:** Steady state oxidation of ascorbate by rsAPX. Solid line shows a fit of the data to the Hill equation (Equation [6.7]). Conditions: sodium phosphate buffer, pH 7.0,  $\mu = 0.10$  M, 25.0 °C.

The entity  $n$  in the Hill equation, (Equation [6.7]) is more commonly known as the Hill coefficient and can be used to provide an estimate of the number substrate-binding sites on an enzyme. However,  $n$  is now widely used as an index of cooperativity, thus it is thought that multiple binding sites or cooperativity are the cause of the sigmoidal behaviour observed in many enzymes (discussed in Chapter One, Section 1.6.5).

All curve fitting to the Michaelis-Menten equation (Equation [2.1], Chapter 2, Section 2.2.5) or Hill equation were carried out using the KaliedaGraph for Windows software package (KaliedaGraph, version 3.09, Synergy Software).

## 6.6 TRANSIENT STATE KINETICS

Transient state kinetics were performed using a SX.18 MV microvolume stopped-flow spectrometer (Applied Photophysics) fitted with a Neslab RTE-200 circulating water bath ( $5.0 \pm 0.1$  °C). Reported values of  $k_{\text{obs}}$  (sodium phosphate, pH 7.0,  $\mu = 0.10$  M, 5.0 °C) were an average of at least five measurements, conducted in an identical manner to that described in the literature (6). All concentrations reported here are concentrations loaded in the syringes of the stopped-flow.

### 6.6.1 Formation of Compound I

Pseudo-first-order rate constants for the formation of Compound I ( $k_{1,\text{obs}}$ ) were monitored by a decrease in absorbance (corresponding to the formation of Compound I) at 407 nm for rsAPX and 405 nm for W41A in single mixing mode. One syringe of the stopped-flow apparatus contained enzyme (2.0  $\mu\text{M}$ ), which was rapidly mixed with another syringe containing varying concentrations (at least ten-fold in excess) of  $\text{H}_2\text{O}_2$  by the application of 8 mbar of nitrogen gas pressure to both syringes simultaneously at 5.0 °C. Enzyme and  $\text{H}_2\text{O}_2$  solutions were made up in sodium phosphate buffer (pH 7.0,  $\mu = 0.10$  M). The second-order-rate constant  $k_1$ , was determined according to the following equations, Equations [6.8]-[6.10]:



$$d[\text{Compound I}] / dt = k_1[\text{APX}] [\text{H}_2\text{O}_2] \quad (\text{Eq.}[6.9])$$

Under pseudo-first-order conditions:  $[\text{H}_2\text{O}_2] \gg [\text{APX}]$

$$k_{1,\text{obs}} = k_1[\text{H}_2\text{O}_2] \quad (\text{Eq.}[6.10])$$

All kinetic traces were monophasic and were fitted to a single exponential function, (Equation [6.14]), where  $k_{1,\text{obs}}$  was a mean of at least five traces.

Reactions with *tert*-butyl hydroperoxide ( ${}^t\text{BuO}_2\text{H}$ , Avocado Research Chemicals) were conducted in the same manner as described above for  $\text{H}_2\text{O}_2$ , but in

pH 8.3 sodium phosphate buffer ( $\mu = 0.10$  M, Appendix A). Solutions of  ${}^t\text{BuO}_2\text{H}$  were freshly prepared by dilution of a 70 % (v/v) (7.25 M) solution.

### 6.6.2 Reduction of Compound I

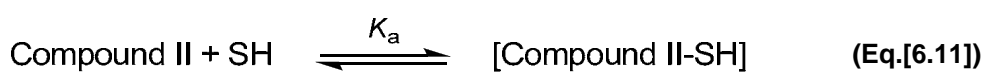
The initial oxidized intermediate, Compound I is reduced by one molecule of ascorbate to yield the second intermediate Compound II. To measure the rate of formation of Compound II a delay time for the formation of Compound I has to be determined, because Compound I is initially formed and then reduced on addition of ascorbate. To determine this delay time (when Compound I formation is complete) enzyme ( $2 \mu\text{M}$ ) was reacted with  $\text{H}_2\text{O}_2$  ( $2 \mu\text{M}$ ) in single mixing mode and the reaction monitored at the Soret (407 nm and 405 nm for rsAPX and W41A, respectively) as when measuring Compound I formation,  $k_1$ . Aging periods of 250 ms and 1000 ms were determined for rsAPX and W41A, respectively.

Pseudo-first-order rate constants for the reduction of Compound I with ascorbate ( $k_{2,\text{obs}}$ ) were collected in sequential mixing mode by mixing enzyme ( $4 \mu\text{M}$ ) with stoichiometric amount of  $\text{H}_2\text{O}_2$  ( $4 \mu\text{M}$ ) in the pre-mixing cell. After a suitable aging period (250 ms and 1000 ms for rsAPX and W41A, respectively), varying concentrations of ascorbate were rapidly mixed with oxidised enzyme solution (Compound I) and reduction was monitored at 409 nm for rsAPX and 414 nm for W41A (isosbestic point between ferric and compound II). All kinetic traces were monophasic and were fitted to a single exponential function, (Equation [6.14]), where  $k_{2,\text{obs}}$  was a mean of at least five traces.

### 6.6.3 Reduction of Compound II

To measure the rate of reduction of Compound II a delay time for the formation of Compound II was determined, because Compound II is initially formed and then reduced on addition of ascorbate. To determine this delay time (when Compound II formation is complete) enzyme ( $4 \mu\text{M}$ ) was reacted with  $\text{H}_2\text{O}_2$  ( $4 \mu\text{M}$ ) in single mixing mode and the reaction monitored at the ferric-compound II isobestic point (409 nm and 414 nm for rsAPX and W41A, respectively) as when measuring Compound I reduction,  $k_2$ . Aging periods of 1000 ms was determined for both rsAPX and W41A.

Sequential mixing mode was used to monitor reduction of Compound II ( $k_{3,obs}$ ) by ascorbate for rsAPX and W41A. One syringe contained enzyme (2  $\mu$ M) which was pre-mixed with stoichiometric amount of  $H_2O_2$  (2  $\mu$ M). After a suitable aging period, (1000 ms for both rsAPX and W41A) varying concentrations of ascorbate were then rapidly mixed with enzyme- $H_2O_2$  solution (Compound II) and reduction was monitored at 427 nm for both rsAPX and W41A (isosbestic point between ferric and Compound I). Kinetic traces collected at low ascorbate concentrations were monophasic and the data were fitted to a single exponential function (Equation [6.14]), however as observed previously (10), kinetic traces collected at high ascorbate concentrations (above ~600 - 800  $\mu$ M) were biphasic and the data were fitted to a two-exponential function (Equation [6.15]). The data for the first phase of the biphasic traces were used together with the data at low ascorbate concentrations to obtain values for  $k_3$  and  $K_d$ . The observed rate constant for reduction of Compound II in both rsAPX and W41A showed saturation kinetics. This non-linear dependence is consistent with the following mechanism, as shown in Equations [6.11]-[6.12]:



From which an expression for  $k_{3,obs}$  can be derived, Equation [6.13]:

$$k_{3,obs} = \frac{k'_3}{1 + K_d/[\text{SH}]} \quad (\text{Eq.}[6.13])$$

Where  $[\text{SH}]$  is the concentration of ascorbate and  $K_d$  the equilibrium dissociation constant for the substrate bound complex ( $K_d = 1/K_a$ ).

An alternative method could be employed to measure the rate of Compound II reduction, according to the method described by Kvaratskhelia *et al* (11). In this case, using the sequential mixing mode of the stopped-flow apparatus, enzyme (4  $\mu$ M) was reacted with an equimolar mixture of  $H_2O_2$  and ascorbate (4  $\mu$ M) to obtain the conventional Compound II directly from the reaction of Compound I with substrate.

After a one second delay, the newly formed Compound II was reduced with varying concentrations of substrate, however both methods yield identical rate constants for the reduction of Compound II by ascorbate.

#### 6.6.4 Data analysis of kinetic transients

Absorbance changes measured at the desired wavelength were relayed to the Archimedes 401-1 microcomputer and all data collected were analysed using non-linear least squares regression analysis using Spectrakinetics software (Applied Photophysics).

Monophasic transient traces were fitted to a single exponential process (Equation [6.14]), to obtain pseudo-first order rate constants,

$$A = Ce^{-k_{\text{obs}} t} + b \quad (\text{Eq.}[6.14])$$

where  $A$  is the absorbance change over time,  $C$  is a constant related to the initial absorbance,  $k_{\text{obs}}$  is the observed rate constant,  $t$  represents the time in seconds and  $b$  is an offset value to account for the non-zero baseline. Transients that were biphasic were fitted to double exponential process, Equation [6.15]:

$$A = C_1(1 - e^{-k_{\text{obsA}}t}) + C_2(1 - e^{-k_{\text{obsB}}t}) + b \quad (\text{Eq.}[6.15])$$

where  $k_{\text{obsA}}$  and  $k_{\text{obsB}}$  are the observed rate constants for the fast and slow phases, respectively,  $C_1$  and  $C_2$  are related to the initial absorbance and  $b$  is an offset value to account for a non-zero baseline. All curve fitting was performed using the Grafit 5 software package (Grafit version 5.0.3, Erithacus Software Ltd).

#### 6.6.5 Analysis of Photodiode array (PDA) data

Time dependent spectra of the various reactions, were performed by multiple wavelength stopped-flow spectroscopy using a photodiode array detector (PDA) and X-SCAN software (Applied Photophysics). Spectral deconvolution was performed by

global analysis and numerical integration methods using PROKIN software (Applied Photophysics).

PDA analysis for formation of the spectral intermediates Compound I and Compound II in rsAPX and W41A were conducted by reaction of enzyme ( $\sim 5 \mu\text{M}$ ) with one equivalent of  $\text{H}_2\text{O}_2$  and monitored over time scales ranging from 3 ms to 1000 s. All solutions were prepared in sodium phosphate buffer (pH 7.0,  $\mu = 0.1 \text{ M}$ ). Similarly, reaction of the Asn-71 variants ( $\sim 5 \mu\text{M}$ ) with  $\text{H}_2\text{O}_2$  (1 to 100 equivalents) was conducted in a similar manner as described for rsAPX and W41A.

PDA analysis for reaction of rsAPX/W41A with  ${}^t\text{BuO}_2\text{H}$  was conducted as described for reaction with  $\text{H}_2\text{O}_2$ , where enzyme (rsAPX/W41A,  $\sim 8 \mu\text{M}$ ) was shot against  ${}^t\text{BuO}_2\text{H}$  solution ( $\sim 4 \text{ mM}$ ) and monitored over time scales ranging from 3 ms to 1000 s. All solutions were prepared in sodium phosphate buffer (pH 8.3,  $\mu = 0.1 \text{ M}$ ).

PDA analysis for formation of ferrous rsAPX and W41A was performed using the SX.18 MV microvolume stopped-flow spectrometer (Applied Photophysics) contained within a glove box (Belle Technology) and fitted to a Neslab RTE-200 circulating water bath ( $5.0 \pm 0.1 \text{ }^\circ\text{C}$ ). Ferric enzyme ( $\sim 5 \mu\text{M}$ ) was shot against fresh sodium dithionite solution to observe formation of the ferrous derivatives of rsAPX and W41A. All solutions were prepared in anaerobic sodium phosphate buffer (pH 7.0,  $\mu = 0.1 \text{ M}$ ).

## 6.7 XANTHINE/XANTHINE OXIDASE METHOD FOR DETERMINATION OF THE FERRIC/FERROUS REDUCTION POTENTIAL

The ferric/ferrous reduction potential for rsAPX and variants were determined by simultaneous reduction with a dye of a known potential according to the method published in the literature (12). The assay contained xanthine ( $300 \mu\text{M}$ , Sigma), xanthine oxidase ( $50 \text{ nM}$ , Sigma), enzyme ( $3 - 4 \mu\text{M}$ ) and the dye phenosafranine (Sigma,  $E_{m,7} = -252 \text{ mV}$ ) (13). Benzyl viologen ( $0.2 \mu\text{M}$ , Sigma) was used in the redox assay for N71A. Potassium phosphate buffer ( $50 \text{ mM}$ , pH 7.0) was made oxygen free by using glucose ( $10 \text{ mM}$ , Fisher), glucose oxidase ( $50 \mu\text{g/ml}$ , Sigma) and catalase ( $5 \mu\text{g/ml}$ , Sigma). Absorbance changes corresponding to reduction of heme were measured at the isosbestic point for phenosafranine ( $407 \text{ nm}$ ); reduction of the dye

was measured at 520 nm where the change due to heme reduction was negligible. Data were fitted to the Nernst Equation (Equation [6.16]) for a single electron process.

$$E = E^{\circ} - \frac{RT}{nF} \ln \left( \frac{[\text{Ox}]}{[\text{Red}]} \right) \quad (\text{Eq.}[6.16])$$

where,  $E$  is the potential of the electrode versus the standard hydrogen electrode (SHE),  $E^{\circ}$  is the standard redox potential,  $R$  is a universal gas constant,  $T$  is the absolute temperature,  $n$  is the number of moles of electrons involved in the reaction,  $F$  is the Faraday constant, and Ox and Red correspond to the concentrations of the oxidised and reduced species, respectively. In all cases, linear Nernst plots for one-electron reduction of heme ( $25 \text{ mV} \ln(E_{\text{ox}}/E_{\text{red}})$ ) and two-electron reduction of dye ( $12.5 \text{ mV} \ln(D_{\text{ox}}/D_{\text{red}})$ ), where  $E_{\text{ox}}$ ,  $E_{\text{red}}$  and  $D_{\text{ox}}$ ,  $D_{\text{red}}$  are the concentrations of oxidised and reduced forms of enzyme and dye, respectively, produced the expected slope of 1 across a wide range of potentials, and the intercept gives a reasonable value for  $\Delta E_{\text{m},7}$  with an error of  $\pm 2 \text{ mV}$ . UV-visible spectra obtained in all experiments were analysed using SPECFIT (14) for singular value decomposition based on factor analysis. All potentials reported are given versus the standard hydrogen electrode (SHE).

## 6.8 X-RAY CRYSTALLOGRAPHY

### 6.8.1 Crystallisation of W41A

The crystallographic data for cyanide and nitric oxide bound rsAPX derivatives were provided by Dr K. H. Sharp (Department of Chemistry, University of Leicester).

Crystals of W41A were obtained using previously published procedures (15). All the screens for the crystallisation of W41A were carried out using the sitting drop method and using 24 well plates (4 x 6 Cryschem plates with 1 ml reservoirs, Hampton Research). The screens were prepared in a temperature controlled room at 19.0 °C. Briefly, sitting drops made up of 2  $\mu\text{l}$  protein solution (10 mg/ml) and 2  $\mu\text{l}$  precipitant solution were allowed to equilibrate with 1 ml of precipitant, 0.10 M Hepes

pH 8.3 and 2.25 M lithium sulphate. The protein solution (10 mg/ml in deionised water) was kept on ice throughout. Protein solution (2  $\mu$ l) was added to the first eight of the small drop wells (4x2). Well solution (2  $\mu$ l) was added to the drop of protein solution, and the first eight wells sealed with clear postal tape making sure there were no air bubbles. The process was then repeated to complete the plate and the screens were left in temperature controlled room at 19.0 °C with no vibrations.

Two weeks after setting up the crystal screens, large crystals emerged. The crystals appeared to be highly ordered as they contained flat surfaces and sharp edges. The best crystals grew to about 150  $\mu$ m long and 75  $\mu$ m in cross-section.

### 6.8.2 Crystal screen trials of Asparagine-71 variants

Crystal screens of the Asp-71 variants placed with, 0.10 M HEPES pH 8.3 and 2.25 M lithium sulphate, were non-productive thus crystallisation conditions were screened using commercially available kits (Wizard I, II and Cryo I, II sparse matrix crystallisation screens, Emerald BioStructures). The screens were prepared in a temperature controlled room at 19.0 °C. The protein solution (10 mg/ml in deionised water) was kept on ice throughout. Each commercial screen solution (700  $\mu$ l) was added to a separate well. The small wells consisted of drops of 1  $\mu$ l of protein and 1  $\mu$ l of well solution.

### 6.8.3 Crystal soaks of W41A

Crystals of the cyanide-bound forms of rsAPX and W41A were obtained by dissolving a few crystals of potassium cyanide in 10 ml of mother liquor (0.1 M HEPES, pH 8.3 and 2.25 M lithium sulphate). During the cyanide soak of W41A the crystal changed colour from deep brown-red to bright red; a similar change was seen in the rsAPX cyanide soaks (16).

Crystals of the nitric oxide-bound heme complexes were obtained by soaking crystals in sodium dithionite in the mother liquor followed by the addition of crystals of potassium nitrite to form nitric oxide *in situ* (17). Both rsAPX and W41A crystals turned pale pink during the nitric oxide soaks (16).

For H<sub>2</sub>O<sub>2</sub> soaks of W41A, crystals were soaked for five minutes in 0.1 M H<sub>2</sub>O<sub>2</sub>, prepared in mother liquor. Effervescence was noticed in the soaks of W41A crystals

with  $\text{H}_2\text{O}_2$  which could be attributed to release of oxygen inferring APX could harbour catalase activity (an assay was performed on rsAPX and W41A to test for catalase activity but the assay proved unsuccessful). The crystals turned a paler red colour during the period of the soak. Similar observations were made during the soaks of rsAPX with  $\text{H}_2\text{O}_2$ , but due to the rapid nature of the reaction no density relating to oxygen bound to the iron was found in the resulting structure (16).

Crystals of ferrous W41A were obtained by soaking crystals for five minutes in a concentrated stock (1 M) of sodium dithionite dissolved in mother liquor.

For  ${}^t\text{BuO}_2\text{H}$  soaks of W41A, crystals were soaked for 15 minutes in 72.5 mM  ${}^t\text{BuO}_2\text{H}$ , prepared in mother liquor. Similar to soaks conducted with  $\text{H}_2\text{O}_2$ , the crystals turned a paler red colour during the period of the soak

The wells were kept covered during the soaking period to prevent evaporation. The crystals were then mounted onto nylon loops before being cryo-cooled in liquid nitrogen and stored until data collection.

UV-visible spectroscopy was used to probe binding of the various ligands used in the soaks described above, under crystallographic conditions (0.1 M HEPES pH 8.3 and 2.25 M lithium sulphate). The spectral changes observed were identical to those observed in sodium phosphate buffer (pH 7.0,  $\mu = 0.1$  M).

#### **6.8.4 Crystallographic data collection and interpretation.**

##### ***6.8.4.1 Crystallographic data collection and interpretation of ferric W41A, $\text{H}_2\text{O}_2$ , cyanide- and nitric oxide-W41A derivatives.***

Diffraction data for the W41A, W41A-cyanide and W41A-nitric oxide structures were collected at beam line ID23-EH1 using an ADSC Quantum-315 detector, whereas data for the W41A- $\text{H}_2\text{O}_2$  soak was collected at beam line ID14-EH4 using an ADSC Quantum-4 detector all at the European Synchrotron Radiation Facility (ESRF, Grenoble, France). Data for the rsAPX-cyanide and rsAPX-nitric oxide complexes were collected at Deutsches Elektronen Synchrotron (DESY, Hamburg) at beam line X-11 using a MAR 165 mm CCD detector. All synchrotron data was collected at 100 K. Data collected at the ESRF was indexed and scaled using MOSFLM (18) and SCALA (19), and the data collected at DESY was indexed and scaled using the HKL programs DENZO and SCALEPACK (20). Using these

programs the space group was determined to be assigned as  $P4_22_12$ . The unit cell dimensions were  $a = 81.8 \text{ \AA}$ ,  $b = 81.8 \text{ \AA}$  and  $c = 75.0 \text{ \AA}$ . In total, 5 % of the data were flagged for the calculation of  $R_{\text{free}}$  and excluded from subsequent refinement. Data collection and processing statistics are shown in Table [2.2].

Dr M. G. Joyce (Department of Biochemistry, University of Leicester) collected and interpreted the data for ferric W41A,  $\text{H}_2\text{O}_2^-$ , cyanide- and nitric oxide-W41A derivatives.

#### **6.8.4.2 Crystallographic data collection and interpretation of ferrous W41A and single-crystal microspectrophotometry**

All diffraction data were collected at the ESRF (Grenoble, France). Beam line ID23-EH1 and an ADSC Quantum-315 detector were used during data collection of dithionite-reduced W41A crystal. Single-crystal microspectrometry and collection of diffraction before and after X-ray reduction of ferric W41A were conducted using beam line ID14-2 and an ADSC Q4 CCD detector. All synchrotron data were collected at 100 K. Crystals were continuously cooled by a cold nitrogen stream from an Oxford Cryosystems 700 series Cryostream. UV-visible absorption spectra of the crystals were recorded in the 500 - 800 nm range using the European Molecular Biology Laboratory (EMBL) online microspectrophotometer (HR2000 CCD detector Ocean Optics). Input light was provided by a deuterium/halogen source (Ocean Optics, DH2000) coupled to custom lenses via a  $100 \text{ \mu m}$  2-UV-SR fibre optic (generating a focal spot of  $25 \text{ \mu m}$ ) and collected from the second lens coupled to a  $600 \text{ \mu m}$  fibre optic. Wherever possible, care was taken to record spectra of the crystal to the same phi position. Spectra of the cryo-cooled crystals remained unchanged during storage. The data were indexed and scaled using MOSFLM (18) and SCALA (19). In total, 5 % of the data were flagged for the calculation of  $R_{\text{free}}$  and excluded from subsequent refinement. Data collection and processing statistics are shown in Table [3.2].

Dr K. Futterer (Department of Biochemistry, University of Birmingham) collected the ferrous W41A crystal data. Data collection at Grenoble using the EMBL online microspectrophotometer was conducted under the supervision of Dr J. McGeehan (EMBL) and Dr P. C. E. Moody (Department of Biochemistry, University of Leicester).

Dr C. L. Metcalfe (Department of Chemistry, University of Leicester) assisted in refinement of the ferrous and X-ray reduced W41A crystal structures.

#### **6.8.4.3 Crystallographic data collection and interpretation of <sup>t</sup>BuO<sub>2</sub>H-W41A and single-crystal microspectrophotometry**

All diffraction data were collected at the ESRF (Grenoble, France). Single-crystal microspectrometry and collection of diffraction data for <sup>t</sup>BuO<sub>2</sub>H-soaked W41A crystal (1.90 Å) was conducted using beam line ID14-2 and an ADSC Q4 CCD detector at 100 K. Crystals were continuously cooled by a cold nitrogen stream from an Oxford Cryosystems 700 series Cryostream. UV-visible absorption spectra of the crystals were recorded in the 500 - 800 nm range using the EMBL online microspectrophotometer (HR2000 CCD detector Ocean Optics). Input light was provided by a deuterium/halogen source (Ocean Optics, DH2000) coupled to custom lenses via a 100 μm 2-UV-SR fibre optic (generating a focal spot of 25 μm) and collected from the second lens coupled to a 600 μm fibre optic. Wherever possible, care was taken to record spectra of the crystal to the same phi position. Spectra of the cryo-cooled crystals remained unchanged during storage.

Data collection at Grenoble using the EMBL online microspectrophotometer was conducted under the supervision of Dr J. McGeehan (EMBL) and Dr P. C. E. Moody (Department of Biochemistry, University of Leicester).

A second data set for <sup>t</sup>BuO<sub>2</sub>H-soaked W41A crystal at higher resolution (1.40 Å) was collected using beam line ID14-1 and an ADSC Q210 CCD detector at 100 K. The data was indexed and scaled using MOSFLM (18) and SCALA (19). In total, 5 % of the data were flagged for the calculation of  $R_{\text{free}}$  and excluded from subsequent refinement. Data collection and processing statistics are shown in Table [4.1]. Professor J. W. R. Schwabe (Department of Biochemistry, University of Leicester) kindly collected the high resolution data (1.40 Å) of the <sup>t</sup>BuO<sub>2</sub>H-soaked W41A crystal.

All figures shown in this thesis were created using PyMOL (21).

## 6.9 HIGH PERFORMANCE LIQUID CHROMATOGRAPHY (HPLC)

HPLC analysis and collection of standards (heme and biliverdin) and protein samples (rsAPX and W41A) before and after treatment with peroxides were conducted on an Agilent Series 1100 binary pump HPLC system fitted with a diode array detector. Samples (100  $\mu$ l) were loaded onto a C18 reverse-phase column (Vydac peptide-protein column, 4.6 mm x 250 mm) and chromatograms were monitored at 398 nm. All solvents were of HPLC grade and were degassed prior to use. Solvents were as follows: A = 0.1 % v/v trifluoroacetic acid (TFA) in 95 % water, 5 % acetonitrile; B = 0.1 % v/v TFA in 80 % acetonitrile, 20 % water. The column was pre-equilibrated with 2 % buffer B and separation (flow-rate of 1 ml/min) was achieved using the following elution gradient: t = 0 minutes, B = 2 %; t = 5 minutes, B = 2 %; t = 40 minutes, B = 70 %, t = 45 minutes, B = 100 % and t = 50 minutes, B = 100 %. The collected fractions were freeze-dried and resuspended in water (100  $\mu$ l) before MALDI-TOF analysis.

Biliverdin and heme, made up in DMSO and potassium hydroxide (0.1 M) solutions, respectively, were diluted into solvent A prior to HPLC analysis. HPLC and mass spectral analysis was conducted immediately after treatment of the proteins with peroxides.

## 6.10 MASS SPECTROMETRY

### 6.10.1 Matrix-Assisted Laser Desorption/Ionisation-Time of Flight (MALDI-TOF) mass spectrometry

Protein samples (rsAPX/W41A) required for MALDI-TOF mass spectrometry were exhaustively exchanged into water using a Centricon (YM10, Millipore) ultrafiltration device (molecular weight cut off 10 kDa) and by centrifugation at 3000 g. The protein samples ( $\sim$ 10 pmol/ $\mu$ l) were then diluted 1:1, 1:10, 1:50, 1:100 with matrix (sinapinic acid, Fluka, 5 mg/ml, in 0.1 % TFA in 1:1 acetonitrile/water). Analysis was carried out as follows: 1  $\mu$ l of the protein/matrix mixture was spotted onto a MALDI target plate using the dried-droplet method (22). The MALDI-TOF mass spectrometer (Voyager-DE STR Biospectrometry Workstation, Applied Biosystems) was calibrated in the range 5000 - 35,000 Da with a protein mass

standard kit (Sequazyme, Applied Biosystems). Spectra of protein samples were acquired in linear mode using external calibration.

MALDI-TOF spectra of heme fragments collected during HPLC analysis were acquired in reflectron mode. Heme containing fragments (1  $\mu$ l) were mixed with matrix, as above ( $\alpha$ -cyano-4-hydroxycinnamic acid, Fluka, 5 mg/ml, 0.1 % TFA in 1:1 acetonitrile/water) for MALDI-TOF mass spectrometry. The MALDI-TOF mass spectrometer for these experiments was calibrated in the range 500 - 6000 Da with a peptide mass calibration kit (Sigma, catalogue number MSCAL2, used according to manufacturer's instructions). MALDI-TOF analysis of the HPLC-purified heme fragments was conducted by Mrs S. Ashra (Protein Nucleic Acid Chemistry Laboratory, University of Leicester). All spectra were an average of 1000 shots and were analysed using Data Explorer software (Applied Biosystems).

### **6.10.2 Electro Spray Ionisation (ESI) mass spectrometry**

Samples of biliverdin, heme, rsAPX and W41A before and after reaction with peroxides were provided to Dr G. Eaton (Department of Chemistry, University of Leicester) for mass spectral analysis, which was carried out using a Micromass Quattro LC electrospray mass spectrometer. The samples were introduced into the instrument via syringe infusion at a flow rate of 10  $\mu$ l/min and the mass spectral analysis was conducted in both positive and negative continuum mode at a rate of 3 spectra/s with the probe voltage set at 2 kV and a cone voltage of 50 or 100 mV. The instrument was calibrated over the range m/z 100 - 1000 using a mixture of polyethylene glycols (PEG), 300, 400, and 600.

**6.11 REFERENCES**

1. Nelson, D. P., and Kiesow, L. A. (1972) *Analytical Biochemistry* **49**, 474-478
2. Dalton, D. A., Diaz del Castillo, L., Kahn, M. L., Joyner, S. L., and Chatfield, J. M. (1996) *Archives of Biochemistry and Biophysics* **328**, 1-8
3. Antinini, M., and Brunori, E. 1971. Hemoglobin and myoglobin and their reactions with ligands, North Holland Publishers, Amsterdam
4. Aasa, R., and Vanngard, T. (1975) *Journal of Magnetic Resonance* **19**, 308-315
5. Mittler, R., and Zilinskas, B. A. (1991) *Plant Physiology* **97**, 962-968
6. Lad, L., Mewies, M., and Raven, E. L. (2002) *Biochemistry* **41**, 13774-13781
7. Asada, K. (1984) *Methods Enzymology* **105**, 422
8. Lad, L., Mewies, M., Basran, J. S., Scrutton, N. S., and Raven, E. L. (2002) *European Journal of Biochemistry* **269**, 3182-3192
9. Santimore, M. (1975) *Canadian Journal of Biochemistry* **53**, 649-657
10. Lad, L. (2001) in *PhD Thesis in Chemistry*, University of Leicester, Leicester
11. Kvaratskhelia, M., George, S. J., and Thorneley, R. N. F. (1997) *Journal of Biological Chemistry* **272**, 20988-21001
12. Efimov, I., Papadopoulou, N. D., McLean, K. J., Badyal, S. K., Macdonald, I. K., Munro, A. W., Moody, P. C. E., and Raven, E. L. (2007) *Biochemistry* **46**, 8017-8023
13. Clark, W. M. (1972) *Oxidation-Reduction Potentials of Organic Systems*, Robert E. Kreiger Publishing Co, Huntington, NY
14. Binstead, R. A., and Zuberbuehler, A. D., Spectrum Software Associates, Chapel Hill, NC

15. Sharp, K. H., Mewies, M., Moody, P. C. E., and Raven, E. L. (2003) *Nature Structural Biology* **10**, 303-307
16. Sharp, K. H. (2004) in *PhD Thesis in Chemistry*, University of Leicester, Leicester
17. Leys, D., Backers, K., Meyer, T. E., Hagen, W. R., Cusanovich, M. A., and Van Beeumen, J. (2000) *Journal of Biological Chemistry* **275**, 16050-16056
18. Leslie, A. G. W. (1992) *Newsletter on Protein Crystallography* **26**, 134-135
19. Collaborative Computational Project, N. (1994) *Acta Crystallography* **D50**, 760-763
20. Otwinoski, Z., and Minor, W. (1997) *Methods Enzymology* **227**, 366-396
21. DeLano, W. L. (2002), DeLano Scientific, San Carlos, CA
22. Kussmann, M., Nordhoff, E., Rahbek-Neilsen, H., Haebel, S., Rossel-Larsen, M., Jakobsen, L., Gobom, J., Mirgorodskaya, E., Kroll-Kirstensen, A., Palm, L., and Roespstorff, P. (1997) *Journal of Mass Spectrometry* **32**, 593-601

## **APPENDIX A**

## **APPENDIX A**

Measurements of the pH of aqueous solutions were taken using a Russell pH-electrode attached to a digital pH-meter (Radiometer, model PHM93) and all buffers used for columns or characterisation were filtered using ultra-filtration apparatus (Millipore).

### **LB MEDIA (Sigma)**

Per litre: LB Broth (21 g) supplemented with glucose (2 g) and made to up to 1 litre with water. Sterilised and allowed to cool ~55 °C before addition of antibiotics ampicillin (100 µg/ml) and kanamycin (30 µg/ml). Antibiotics were filter sterilised using 0.2 µm syringe-top filters (Acrodisc).

### **LB AGAR PLATES**

Per litre: LB Broth (20 g), agar (15 g) supplemented with glucose (2 g) and made up to 1 litre with water. Sterilised and allowed to cool ~55 °C before supplementing with ampicillin (100 µg/ml) for ampicillin plates and kanamycin (30 µg/ml) for ampicillin-kanamycin plates. Antibiotics were filter sterilised using 0.2 µm syringe-top filters (Acrodisc).

### **TE BUFFER (to resuspend primers)**

10 mM Tris (1.21 g) and 1 mM EDTA (0.372 g), pH 8.0 (adjust pH with HCl) made up to 1 litre with water.

### **50x TAE BUFFER (Agarose gel electrophoresis)**

Tris base (2.42 g), glacial acetic acid (37.1 g), 0.5 M EDTA (100 ml) made up to 1 litre with water.

### **DNA GEL MIX**

Agarose (1.4 g), ethidium bromide (20 µl) and TAE buffer (200 ml).

### **REGENERATION BUFFER**

Guanidine hydrochloride (114.6 g) and acetic acid (40 ml) diluted to 200 ml water.

**SONICATION BUFFER**

0.1 M potassium phosphate pH 8.0, 0.3 M potassium chloride.

**WASH BUFFER**

0.1 M potassium phosphate pH 6.0, 0.3 M potassium chloride.

**ELUTION BUFFER**

0.1 M potassium phosphate pH 4.0, 0.3 M potassium chloride.

**FFQ BUFFER**

10 mM potassium phosphate pH 7.0.

**FFQ ELUTION BUFFER**

10 mM potassium phosphate pH 7.0, 0.25 M potassium chloride.

**FPLC BUFFER**

0.15 M potassium phosphate buffer, pH 7.0.

**SODIUM PHOSPHATE BUFFER**

Sodium phosphate buffer pH 7.0,  $\mu = 0.10$  M was prepared by dissolving in water disodium hydrogen orthophosphate anhydrous (3.801 g/l) and sodium dihydrogen orthophosphate anhydrous (2.714 g/l) to a final volume of 1 litre.

Sodium phosphate buffer pH 8.3,  $\mu = 0.10$  M was prepared by dissolving in water disodium hydrogen orthophosphate anhydrous (4.675 g/l) and sodium dihydrogen orthophosphate anhydrous (0.1656 g/l) to a final volume of 1 litre.

**SAMPLE BUFFER**

Dithiothreitol (0.77 g), 10 % sodium dodecyl sulphate (10 ml), 1 M Tris-HCl (1.25 ml, pH 6.8), glycerol (5 ml) and 0.5 % bromophenol blue in ethanol, diluted to 50 ml with water.

**SDS RUNNING BUFFER**

Glycine (14.4 g), Tris-HCL (3 g) and sodium dodecyl sulphate (0.5 g) diluted to 500 ml with water.

**RESOLVING BUFFER**

Tris base (30.3 g) in 100 ml water, adjusted to pH 8.8, plus sodium dodecyl sulphate (0.66 g), made up to 160 ml with water.

**STACKING BUFFER**

Tris base (6.05 g) in 40 ml water, adjusted to pH 6.8, plus sodium dodecyl sulphate (0.4 g), made up to 100 ml with water.

**RESOLVING GEL MIX**

Acrylamide solution (3.25 ml), resolving buffer (1.9 ml) water (2.4 ml), 10 % ammonium persulphate (25  $\mu$ l), TEMED (12.5  $\mu$ l, add TEMED last and proceed immediately).

**STACKING GEL MIX**

Acrylamide solution (325  $\mu$ l), stacking buffer (625  $\mu$ l) water (1.5 ml), saturated bromophenol blue (2  $\mu$ l), 10 % ammonium persulphate (12.5  $\mu$ l), TEMED (6.5  $\mu$ l, add TEMED last and proceed immediately).

**COOMASSIE BRILLIANT BLUE R250**

0.1 % Coomassie blue R-250 in 40 % methanol, 10 % acetic acid made up in water.

**DESTAINING BUFFER**

40 % methanol and 10 % acetic acid made up in water.

**BASIC PYRIDINE SOLUTION**

Pyridine (2 ml), 1 M sodium hydroxide (600  $\mu$ l) and water in a final volume of 6 ml.

**MOTHER LIQUOR FOR CRYSTALLOGRAPHY**

*2.25 M Lithium sulphate and 0.1 M Hepes pH 8.3.*

In 1 ml well reservoir add 900  $\mu$ l of 2.50 M lithium sulphate and then add 100  $\mu$ l of 1 M Hepes pH 8.3 (pH 8.3 is of the 1 M solution of Hepes before addition to the well, which is adjusted by the addition of sodium hydroxide pellets).

**HPLC BUFFER A**

0.1 % Trifluoroacetic acid in 5 % v/v acetonitrile in water (all HPLC grade).

**HPLC BUFFER B**

0.1 % Trifluoroacetic acid in 80 % v/v acetonitrile in water (all HPLC grade).

**N3 BUFFER (QIAGEN)**

Contains guanidine hydrochloride and acetic acid.

**P1 BUFFER (QIAGEN)**

Alkaline buffer that contains RNase, stored at 4 °C.

**P2 BUFFER (QIAGEN)**

Contains sodium hydroxide.

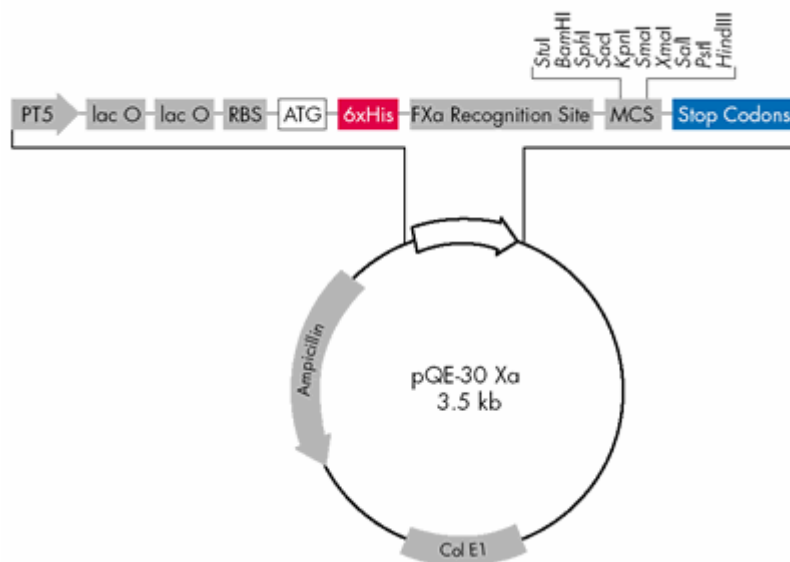
**PB BUFFER (QIAGEN)**

Contains guanidine hydrochloride and isopropanol.

**PE BUFFER (QIAGEN)**

Contains ethanol.

## **APPENDIX B**

**APPENDIX B****Vector pQE-30:****The forward and reverse oligonucleotides used for sequencing.**

**pQE-Forward:** 5'CGG ATA ACA ATT TCA CAC AG 3' ( $T_m = 48\text{ }^\circ\text{C}$ )

**pQE-Reverse:** 5'GTT CTG AGG TCA TTA CTG G 3' ( $T_m = 49\text{ }^\circ\text{C}$ )

## **PUBLICATIONS**

**PUBLICATIONS**

- ❖ **Badyal, S. K.**, Joyce, M. G., Sharp, K. H., Seward, H. E., Mewies, M., Basran, J., Macdonald, I. K., Moody, P. C. E. and Raven, E. L. (2006) Conformational mobility in the active site of a heme peroxidase. *Journal of Biological Chemistry*, 281, 24512 - 24520. **enclosed**
  
- ❖ **Badyal, S. K.**, Metcalfe, C. L., Basran, J., Efimov, I., Moody, P. C. E. and Raven, E. L. (2008) Iron oxidation state modulates active site structure in a heme peroxidase. *Biochemistry*, 47, 4403 - 4409. **enclosed**
  
- ❖ Macdonald, I. K., **Badyal, S. K.**, Ghamsari, L., Moody, P. C. E. and Raven, E. L. (2006) The interaction of ascorbate peroxidase with substrates: a mechanistic and structural analysis. *Biochemistry*, 45, 7808 - 7817.
  
- ❖ Pipirou, Z., Bottrill, A. R., Metcalfe, C. L., Mistry, S. C., **Badyal, S. K.**, Rawlings, B. J., and Raven, E. L. (2007) Autocatalytic formation of a covalent link between Trp41 and the heme in ascorbate peroxidase. *Biochemistry*, 46, 2174 - 2180.
  
- ❖ Efimov, I., Papadopoulou, N. D., McLean, K. J., **Badyal, S. K.**, Macdonald, I. K., Munro, A. W., Moody, P. C. E. and Raven, E. L. (2007) The redox properties of ascorbate peroxidase. *Biochemistry*, 46, 8017 - 8023.
  
- ❖ Efimov, I., Metcalfe, C. L., **Badyal, S. K.**, Moody, P. C. E. and Raven, E. L. (2008) Proton delivery in ascorbate peroxidase. *In press*

# Conformational Mobility in the Active Site of a Heme Peroxidase\*

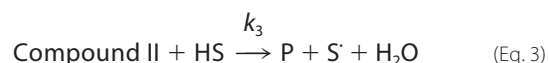
Received for publication, March 20, 2006, and in revised form, June 6, 2006 Published, JBC Papers in Press, June 7, 2006, DOI 10.1074/jbc.M602602200

Sandip K. Badyal<sup>‡</sup>, M. Gordon Joyce<sup>§</sup>, Katherine H. Sharp<sup>‡</sup>, Harriet E. Seward<sup>§</sup>, Martin Mewies<sup>‡</sup>, Jaswir Basran<sup>§</sup>, Isabel K. Macdonald<sup>‡</sup>, Peter C. E. Moody<sup>§</sup>, and Emma Lloyd Raven<sup>†1</sup>

From the <sup>‡</sup>Department of Chemistry, Henry Wellcome Building, University of Leicester, University Road, Leicester LE1 7RH, United Kingdom and <sup>§</sup>Department of Biochemistry and Henry Wellcome Laboratories for Structural Biology, Henry Wellcome Building, University of Leicester, Lancaster Road, Leicester LE1 9HN, United Kingdom

Conformational mobility of the distal histidine residue has been implicated for several different heme peroxidase enzymes, but unambiguous structural evidence is not available. In this work, we present mechanistic, spectroscopic, and structural evidence for peroxide- and ligand-induced conformational mobility of the distal histidine residue (His-42) in a site-directed variant of ascorbate peroxidase (W41A). In this variant, His-42 binds “on” to the heme in the oxidized form, duplicating the active site structure of the cytochromes *b* but, in contrast to the cytochromes *b*, is able to swing “off” the iron during catalysis. This conformational flexibility between the on and off forms is fully reversible and is used as a means to overcome the inherently unreactive nature of the on form toward peroxide, so that essentially complete catalytic activity is maintained. Contrary to the widely adopted view of heme enzyme catalysis, these data indicate that strong coordination of the distal histidine to the heme iron does not automatically undermine catalytic activity. The data add a new dimension to our wider appreciation of structure/activity correlations in other heme enzymes.

The heme peroxidase enzymes catalyze H<sub>2</sub>O<sub>2</sub>-dependent oxidation of a range of substrates through a mechanism that, in all cases, involves formation of an oxidized ferryl intermediate (known as Compound I; see Equation 1) that is subsequently reduced by substrate (Equations 2 and 3) (1, 2). In the majority of cases, reduction of Compound I occurs by two successive single-electron transfer steps, as follows (where P = peroxidase, HS = substrate, S<sup>•</sup> = 1-electron oxidized form of substrate).



Structural information is available for a number of heme peroxidase enzymes, and in all cases the heme iron is poised in a 5- or 6-coordinate environment with the sixth ligand provided by a weakly coordinated water molecule. This differs from the heme coordination geometry in other noncatalytic heme proteins that do not require binding of an exogenous ligand at the metal site. The classic example is the cytochromes, which typically have a strong endogenous protein ligand at the sixth site (usually His or Met) and no vacant coordination site for iron-catalyzed chemistry to occur. The prevailing view that has emerged, therefore, is that the catalytic enzymes (which include the heme peroxidases but also embraces other, more complex heme enzymes such as heme oxygenase, the cytochrome P450s, and cytochrome *c* oxidase) usually contain 5-coordinate or weakly 6-coordinate heme groups that allow facile reaction with substrate, whereas the electron transfer proteins, for example the cytochromes, have no vacant site at the metal ion for catalysis to occur.

In line with the above considerations, there are no known examples of a genuine heme peroxidase with bis-histidine ligation, but there are a few examples in the literature of different heme peroxidases, or site-directed variants thereof, in which coordination of the distal histidine residue has been proposed on the basis of spectroscopic studies (3–8). These examples include: the W51A (7) and D235N (6) variants of cytochrome *c* peroxidase; thermally inactivated manganese peroxidase (4); and manganese peroxidase at alkaline pH (8). Removal of the ligands coordinating to the bound K<sup>+</sup>-site in ascorbate peroxidase also leads to formation of a low-spin species (3). In none of these cases has unambiguous structural information been obtained, however. In this work, we present the first crystallographically defined example of a functional peroxidase enzyme with bis-histidine ligation in the W41A variant of ascorbate peroxidase. This variant duplicates the heme coordination geometry of the cytochromes *b* in the oxidized form but remains fully competent for formation of the catalytic Compound I and Compound II intermediates, as well as for sub-

\* This work was supported by Project Grants 91/B19083 and B11469 and a studentship from the Biotechnology and Biological Sciences Research Council (to S. K. B.) and by a fellowship from The Leverhulme Trust (to E. L. R.). The costs of publication of this article were defrayed in part by the payment of page charges. This article must therefore be hereby marked “advertisement” in accordance with 18 U.S.C. Section 1734 solely to indicate this fact.

The atomic coordinates and structure factors (code 2GGN, 2GHC, 2GHD, 2GHE, 2GHH, 2GHK) have been deposited in the Protein Data Bank, Research Collaboratory for Structural Bioinformatics, Rutgers University, New Brunswick, NJ (<http://www.rcsb.org/>).

<sup>1</sup> To whom correspondence should be addressed. Tel.: 44-116-229-7047; Fax: 44-116-252-2789; E-mail: emma.raven@le.ac.uk.

strate oxidation, by means of a reaction mechanism in which a conformationally mobile ligand (His-42) binds "on" and then swings "off" the iron during catalysis. This switch between the on and off forms is triggered by reaction with hydrogen peroxide (or other ligands) and, under catalytic conditions, is fully reversible, allowing essentially complete activity to be maintained. These data indicate that strong coordination of the distal histidine residue to the heme iron does not automatically undermine peroxidase activity.

## EXPERIMENTAL PROCEDURES

**Materials**—L-Ascorbic acid (Aldrich), guaiacol (Sigma), and the chemicals used for buffers (Fisher) were of the highest analytical grade (more than 99% pure) and were used without further purification. Hydrogen peroxide solutions were freshly prepared by dilution of a 30% (v/v) solution (BDH Chemicals); exact concentrations were determined using the published absorption coefficient ( $\epsilon_{240} = 39.4 \text{ M}^{-1} \text{ cm}^{-1}$  (9)). Aqueous solutions were prepared using water purified through an Elgastat Option 2 water purifier, which itself was fed with deionized water. All pH measurements were made using a Russell pH-electrode attached to a digital pH-meter (Radiometer Copenhagen, model PHM 93).

**Mutagenesis and Protein Purification**—Site-directed mutagenesis on recombinant soybean cytosolic APX (rsAPX)<sup>2</sup> was performed according to the QuikChange<sup>TM</sup> protocol (Stratagene Ltd., Cambridge, UK). Two oligonucleotides encoding the desired mutation were synthesized and purified (Invitrogen). For W41A, the primers were: 5'-GCT-CCGTTTGGCAGCGCACTCTGCTGGAACC-3' (forward primer) and 3'-GGTTCAGCAGAGTGCCTGCCAACGGAGC-5' (reverse primer). DNA sequencing of the entire coding region using an Applied Biosystems 3730 DNA analyzer was used to confirm the desired mutation and the absence of spurious mutations.

Bacterial fermentation of cells and purification of rsAPX and W41A was carried out according to published procedures (10, 11). Enzyme purity was assessed by examination of the  $A_{\text{solet}}/A_{280}$  value; in all cases an  $A_{\text{solet}}/A_{280}$  value of  $>1.7$  for rsAPX and W41A was considered pure. Enzyme purity was also assessed using SDS-PAGE, and the preparations were judged to be homogeneous by the observation of a single band on a Coomassie Blue-stained reducing SDS-polyacrylamide gel. Enzyme concentrations for the W41A mutant were determined using the pyridine hemochromagen method (12); an absorption coefficient of  $\epsilon_{405} = 125 \text{ mM}^{-1} \text{ cm}^{-1}$  was determined for W41A. Enzyme concentrations of rsAPX were determined using the  $\epsilon_{407} = 107 \text{ mM}^{-1} \text{ cm}^{-1}$  (13).

**Mass Spectrometry**—The integrity of the tryptophan mutant was confirmed by MALDI-TOF mass spectrometry. A 10 pmol/ $\mu\text{l}$  stock of the W41A mutant was made up in water and 0.5  $\mu\text{l}$  of the 1:1 protein/matrix mixture (sinapinic acid (5 mg/ml) in 1:1 acetonitrile/water, 0.1% trifluoroacetic acid) was spotted onto a MALDI target plate using the drying droplet method. The MALDI-TOF mass spectrometer (Applied Bio-

systems) was calibrated in the range of 5000 to 35,000 Da with a protein mass standard kit (Sequazyme, Applied Biosystems). Spectra were accumulated in the same mass range using an average of at least 250 laser shots. The spectra were analyzed using Data Explorer software (Applied Biosystems). The MALDI-TOF mass spectrum of W41A gives a mass of  $28,209.36 \pm 0.05\%$  Da (calculated mass for W41A = 28,203.74 Da), indicating that no posttranslational modification has occurred.

**Steady-state Kinetics**—Steady-state measurements (sodium phosphate, pH 7.0,  $\mu = 0.1 \text{ M}$ , [enzyme] = 25 nM, 25 °C) were carried out according to published protocols (14). Oxidation of ascorbate was monitored at 290 nm ( $\epsilon_{290} = 2.8 \text{ mM}^{-1} \text{ cm}^{-1}$ ) (15) and initial rates were multiplied by a factor of 2 to account for the fast disproportionation ( $k \approx 10^6 \text{ M}^{-1} \text{ s}^{-1}$ ) of the monodehydroascorbate radical to ascorbate and dehydroascorbate (16). For oxidation of guaiacol, stock solutions (100 mM) were prepared in sodium phosphate buffer containing 30% ethanol (17), and oxidation to tetraguaiacol was monitored at 470 nm ( $\epsilon_{470} = 22.6 \text{ mM}^{-1} \text{ cm}^{-1}$  (17)). Values for  $k_{\text{cat}}$  were calculated by dividing the maximum rate of activity ( $\mu\text{M}^{-1} \text{ s}^{-1}$ ) by the micromolar concentration of the enzyme. Values for  $K_m$  were determined by a fit of the data to the Michaelis-Menten equation using a nonlinear regression analysis program (Kalieda-Graph, version 3.09, Synergy Software). All reported values are the mean of three independent assays.

**Transient-state Kinetics**—Transient-state measurements were performed using an SX.18MV microvolume stopped-flow spectrophotometer (Applied Photophysics) fitted with a Neslab RTE-200 circulating water bath ( $\pm 0.1$  °C). Reported values of  $k_{\text{obs}}$  are an average of at least five measurements. Individual traces were monophasic in all cases. All kinetic data were analyzed using nonlinear least squares regression analysis on an Archimedes 410-1 microcomputer (Applied Photophysics) using Spectrakinetics software. All curve fitting was performed using the Grafit 5 software package (Grafit version 5.0.3, Erithacus Software Ltd.). Pseudo-first-order rate constants for the formation of Compound I ( $k_{1,\text{obs}}$ ) were monitored by a decrease in absorbance (corresponding to the formation of Compound I) at 407 nm for rsAPX and 405 nm for W41A in single mixing mode by mixing enzyme (1  $\mu\text{M}$ ) with various concentrations of  $\text{H}_2\text{O}_2$ .

Multiple wavelength absorption studies were carried out using a photodiode array detector and X-SCAN software (Applied Photophysics). Spectral deconvolution was performed by global analysis and numerical integration methods using PROKIN software (Applied Photophysics).

**EPR Spectroscopy**—EPR spectra ( $[\text{W41A}] = 300 \mu\text{M}$ ) were recorded in sodium phosphate buffer (pH 7.0,  $\mu = 0.10 \text{ M}$ ) and glycerol (50% v/v). X-Band EPR spectra were recorded on a Bruker ER-300D series electromagnet and microwave source interfaced to a Bruker EMX control unit and fitted with an ESR-9 liquid helium flow cryostat from Oxford Instruments and a dual mode microwave cavity from Bruker (ER-4116DM).

**Crystal Growth and Structure Determination**—Crystals of rsAPX and the W41A mutant were obtained using the previously published procedures (18). Crystals of the cyanide-bound forms of rsAPX and the W41A mutant were obtained by dis-

<sup>2</sup> The abbreviations used are: APX, ascorbate peroxidase; rsAPX, recombinant soybean cytosolic ascorbate peroxidase; sh, shoulder; MALDI, matrix-assisted laser desorption ionization; TOF, time-of-flight.

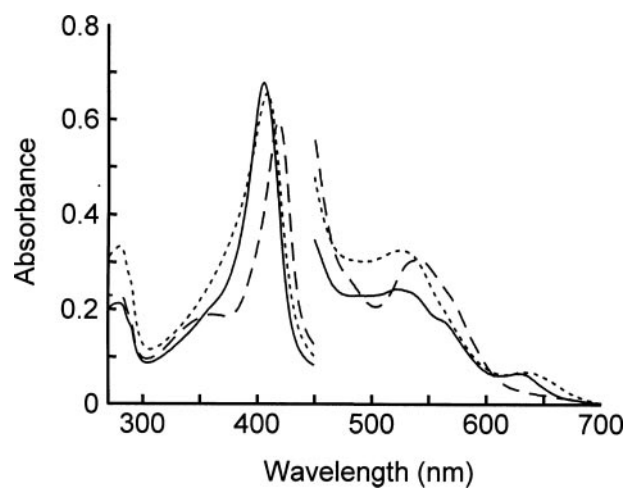


FIGURE 1. Electronic spectrum of ferric rsAPX (dotted line), ferric W41A (solid line), and cyanide-bound W41A (dashed line). The visible region has been multiplied by a factor of 5. Sample conditions: sodium phosphate, pH 7.0,  $\mu = 0.10$  M, 25.0 °C.

solving a few crystals of potassium cyanide in 10 ml of mother liquor (0.1 M HEPES, pH 8.3, and 2.25 M lithium sulfate). Crystals of the NO-bound heme complexes were obtained by soaking crystals in sodium dithionite in the mother liquor followed by the addition of crystals of potassium nitrite, which reacts with excess dithionite to produce nitric oxide (19). For  $\text{H}_2\text{O}_2$  soaks of W41A, crystals were soaked in 0.1 M  $\text{H}_2\text{O}_2$ , left for 5 min, and then frozen in liquid nitrogen. The heme coordination geometry in cytochrome *c* peroxidase is known to be sensitive to the presence of noncoordinating anions (e.g. phosphate, nitrate; see for example, Refs. 6, 7, and 20–23). These anions were not used in the crystallization experiments reported here. Glycerol also was not used in the crystallization studies.

Diffraction data for W41A and the NO- and cyanide-bound forms were collected at beamline ID23-EH1 using an ADSC Quantum-315 detector, whereas data for the W41A- $\text{H}_2\text{O}_2$  soak was collected at beamline ID14-EH4 using an ADSC Quantum-4 detector all at the ESRF, Grenoble. Data for the rsAPX-NO and rsAPX-CN complexes were collected at DESY (Hamburg) at beamline X-11 using a MAR 165 mm CCD detector. All synchrotron data were collected at 100 K. Data collected at the ESRF was indexed and scaled using MOSFLM (24) and SCALA (25), and data collected at DESY was indexed and scaled using the HKL programs DENZO and SCALEPACK (26). Data collection and processing statistics are shown in Table 1; 5% of the data were flagged for the calculation of  $R_{\text{free}}$  and excluded from subsequent refinement. The structures were refined from a model derived from the 1.45-Å rsAPX-ascorbate complex (Protein Data Bank accession code 1OAF) by the removal of bound ligand and water molecules. Several cycles of refinement using REFMAC5 (27) from the CCP4 suite (25) and manual rebuilding of the protein model using COOT (28) followed by the addition of water molecules were carried out until the  $R_{\text{free}}$  and  $R_{\text{factor}}$  values converged. In total, six crystal structures and diffraction data have been deposited with the following identifiers: Protein Data Bank codes 2GGN (ferric W41A), 2GHC (W41A-NO complex), 2GHD (W41A-CN complex), 2GHE (W41A- $\text{H}_2\text{O}_2$  soak), 2GHH (rsAPX-NO complex), and

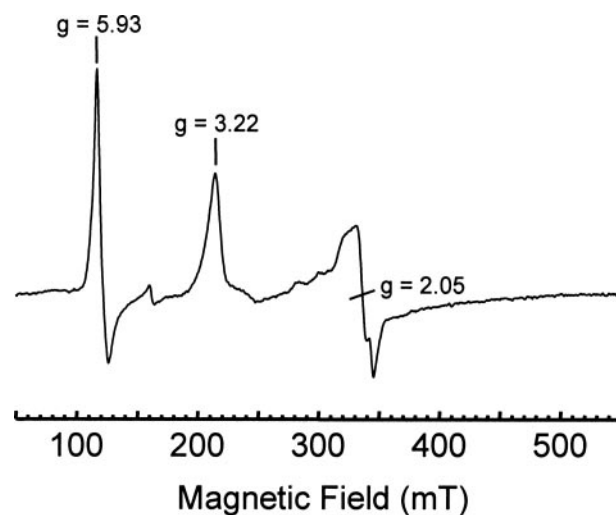


FIGURE 2. EPR spectrum of ferric W41A. Conditions: [enzyme] = 300  $\mu\text{M}$ , sodium phosphate, pH 7.0,  $\mu = 0.10$  M + glycerol (50% v/v), microwave frequency = 9.67 GHz, microwave power = 2 milliwatts, temperature = 10.7 K, modulation amplitude = 10 G.

2GHK (rsAPX-CN complex). The final refinement statistics of all structures are presented in Table 1.

## RESULTS AND DISCUSSION

**Heme Coordination Geometry**—The electronic spectrum of the ferric derivative of W41A is shown in Fig. 1. The spectrum ( $\lambda_{\text{max}}/\text{nm}$  ( $\epsilon/\text{mM}^{-1} \text{cm}^{-1}$ ) = 405 (125), 525, 564, 630) differs from that of the wild type enzyme ( $\lambda_{\text{max}}/\text{nm}$  ( $\epsilon/\text{mM}^{-1} \text{cm}^{-1}$ ) = 407 (107), 525,  $\approx$ 630 (11); Fig. 1) and shows a peak in the visible region (564) that is consistent with the presence of low-spin heme. (The corresponding W41A variant in pea cytosolic APX was also examined (data not shown); in this variant similar wavelength maxima are observed but the Soret band is shifted to 412 nm.) The high-spin peak at  $\approx$ 630 nm in the wild type enzyme is still visible in the variant (Fig. 1). No evidence for the formation of (low-spin) hydroxide-bound heme was observed at alkaline pH (data not shown); hence, the low-spin species was tentatively assigned as arising from coordination of an (internal) protein ligand.

Reaction of ferric W41A with various noncatalytic ligands is informative because it allows us to assess whether the proposed protein ligand is reversibly or irreversibly bound to the metal. Addition of potassium cyanide to the ferric derivative of W41A leads to a spectrum in which complete formation of low-spin heme is now observed ( $\lambda_{\text{max}}/\text{nm}$  = 418, 540, 561<sup>sh</sup>; Fig. 1). This suggests that addition of a strong exogenous ligand leads to displacement of the existing (internal) ligand. As shown below, the crystal structure of the cyanide-bound derivative of W41A confirms this observation. Additionally, we have observed that NO binds to the reduced heme ( $\lambda_{\text{max}} = 417, 541, 574$  nm); the crystal structure of the NO-bound derivative also confirms that His-42 is displaced (see below).

EPR spectroscopy provides further evidence in support of a low-spin heme species (Fig. 2). The EPR spectrum of ferric W41A is dominated by a rhombic low-spin species with observed *g*-values of 3.22 and 2.05 (the third feature is too broad to be observed). A second, minor component with *g*-values of

5.67 and 1.99 is consistent with an axial, high-spin species. The low-spin species is the majority species at 10 K and is consistent with bis-histidine ligation; the  $g$ -values are consistent with an orientation in which the imidazole planes are not parallel to each other. Neither species resembles those observed in the

EPR spectrum of the wild type enzyme, which has a rhombic high-spin species ( $g = 6.04, 5.27, \text{ and } 1.98$ ) and a small amount of rhombic low-spin heme ( $g = 2.69, 2.21, \text{ and } 1.79$ ) (13, 29). A minor low-spin rhombic species ( $g_z = 2.95$ , as a shoulder on the  $g = 3.22$  feature) and the positive lobe of  $g_y$  feature ( $g_y = 2.30$ )

in W41A are likely to arise from a histidine/histidine-ligated heme in which the imidazole planes are parallel to each other (note that there is also evidence for multiple conformations of the proximal histidine in the crystal structure of the cyanide-bound form of W41A; see above).

*X-ray Crystallography of W41A and Its Cyanide- and NO-bound Derivatives*—The crystal structure of the cyanide-bound derivative of W41A (Fig. 3 and Table 1) confirms the observations made in solution. In this structure (Fig. 3B), which closely maps onto that for the cyanide-bound form of rsAPX (Fig. 3A), the iron is ligated by the cyanide ligand and the nitrogen of the bound ligand is hydrogen-bonded (2.8 Å) to N $^{\epsilon}$  of His-42 (2.5 Å in rsAPX). For the W41A-CN complex, the electron density observed for the proximal His-163 residue is consistent with two orientations of this side chain (Fig. 3B). One orientation has His-163 hydrogen-bonded to Asp-208 (3.3 Å) as for rsAPX (3.1 Å); the other orientation has His-163 hydrogen-bonded (2.8 Å) to the backbone carbonyl of Ser-160 (3.8 Å in rsAPX). In the rsAPX-CN structure a single conformation of His-163 is observed; however, the data are to lower resolution (2.0 Å compared with 1.4 Å), and a second orientation of the

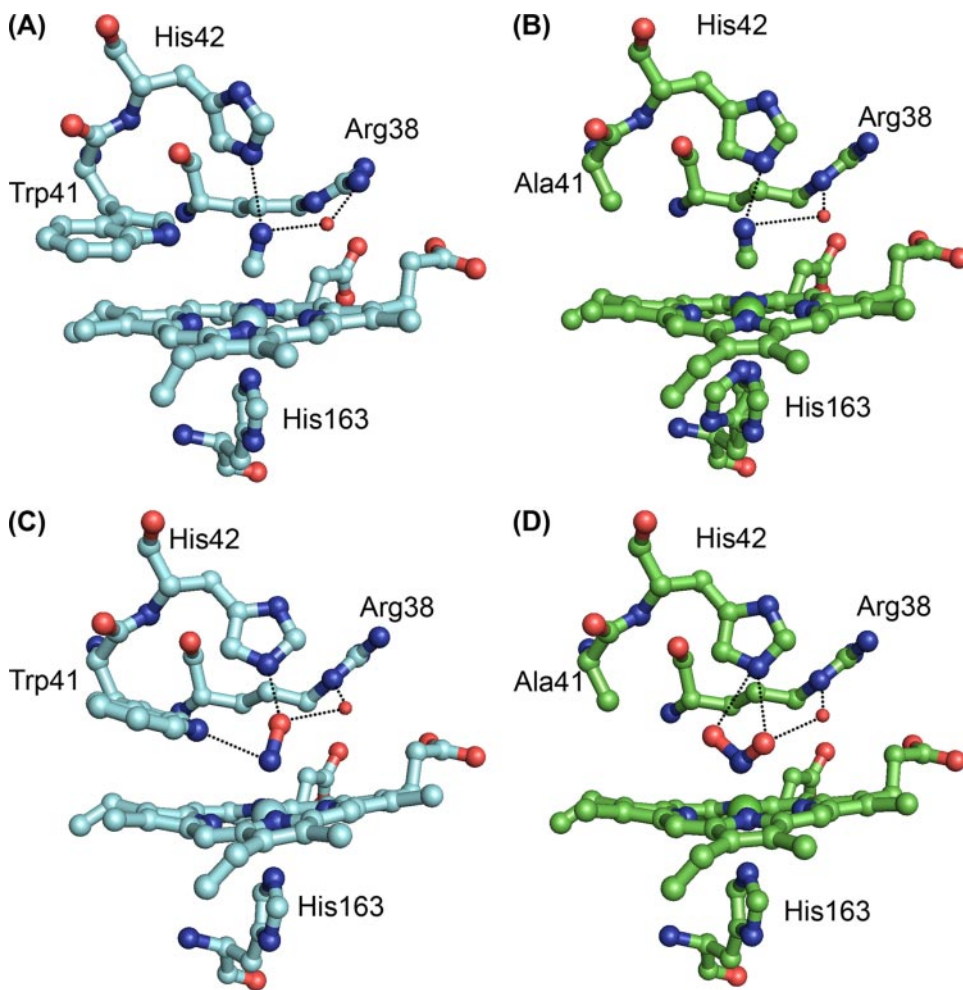


FIGURE 3. *A* and *B*, structures of the cyanide-bound complexes of rsAPX (*A*) and W41A (*B*) showing coordination of the diatomic ligand to the heme. For W41A, there are two orientations of His-163 observed. *C* and *D*, structures of the NO-bound complexes of rsAPX (*C*) and W41A (*D*) in the region of the active site. The loss of the indole of Trp-41 in W41A allows the NO molecule to adopt two orientations. Hydrogen bonds are shown as black dotted lines. Water molecules are shown as red spheres. This figure was created using PyMOL (40).

TABLE 1

Data collection and refinement statistics

r.m.s.d., root-mean-square deviation; PDB, Protein Data Bank. Values for outer shells are given in parentheses.

Statistics	W41A	W41A-CN	rsAPX-CN	W41A-NO	rsAPX-NO	W41A-H <sub>2</sub> O <sub>2</sub>
<b>Data collection</b>						
Resolution (Å)	28.88-1.35	36.81-1.4	58-2.00	45.88-1.25	18.86-2.01	28.99-1.75
Outer shell	(1.42-1.35)	(1.436-1.4)	(2.07-2.0)	(1.32-1.25)	(2.064-2.01)	(1.84-1.75)
Total observations	599,082	248,232	58,820	299,270	59,132	360,725
Unique observations	56,193	52,940	15,798	69,773	16,455	26,381
$I/\sigma I$	17.8 (4.0)	13.3 (3.1)	15.9 (2.98)	12.8 (3.9)	15.8 (3.12)	30.6 (11.6)
$R_{\text{merge}}$	0.097	0.088	0.052	0.107	0.051	0.059
Completeness	99.4 (99.9)	92.8 (96.6)	95.22 (95.7)	98.6 (99.9)	97.32 (95.9)	99.8 (100)
Multiplicity	10.7	4.7	3.7	4.3	3.6	13.7
<b>Refinement</b>						
$R_{\text{factor}}$	0.190	0.206	0.187	0.189	0.183	0.179
$R_{\text{free}}$	0.205	0.229	0.235	0.207	0.258	0.220
r.m.s.d. angle (°)	1.086	1.110	1.290	1.049	1.457	1.188
r.m.s.d. bonds (Å)	0.007	0.008	0.012	0.006	0.015	0.011
PDB accession code	2GGN	2GHD	2GHK	2GHC	2GHH	2GHE

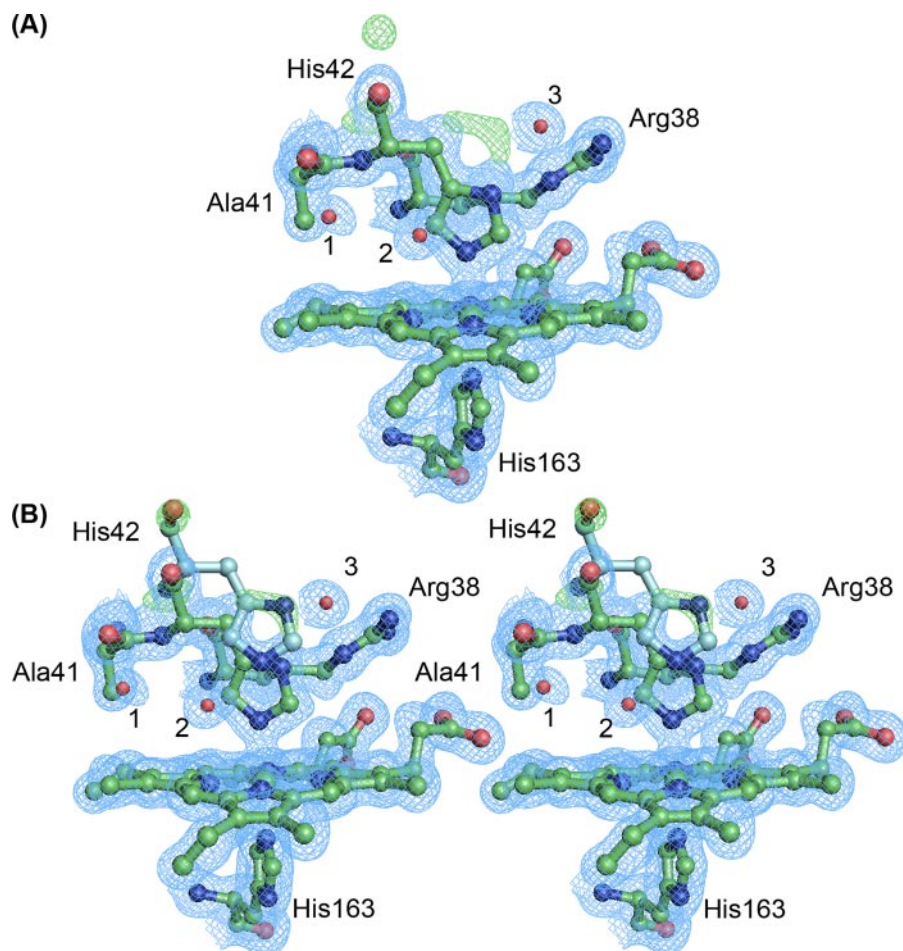


FIGURE 4. *A*, the active site of ferric W41A, showing the coordination of His-42 to the iron. SigmaA-weighted  $2F_o - F_c$  electron density at  $1\sigma$  is shown in blue, and sigmaA-weighted  $F_o - F_c$  electron density at  $3\sigma$  is shown in green. The positive  $F_o - F_c$  electron density in green overlays with the position of His-42 in the structure of rsAPX. Water molecules are shown as red spheres. *B*, stereo view of a structural alignment of the orientation of His-42 in rsAPX (in blue, Protein Data Bank code 1OAG) with the active site in W41A (in green). Water molecules are shown as red spheres for W41A. This figure was created using PyMOL (40).

proximal histidine may not be observed because of the large effect of the heme electron density.

The crystal structure of the NO-bound derivative of W41A also confirm that His-42 is displaced (Fig. 3D). In this case, and in contrast to rsAPX-NO (Fig. 3C), removal of the hydrogen bond to Trp-41 means that the NO ligand now adopts two conformations.

To clarify the nature of the low-spin heme in ferric W41A, diffraction data to 1.75 Å were obtained (Fig. 4 and Table 1). W41A is very similar in its overall structure to the wild type protein; the root-mean-square deviation between C $\alpha$  positions (residues 2–249) for this structure and ferric rsAPX is 0.260 Å (determined using LSQKAB (30)). The structure of W41A shows that space previously occupied by the Trp side chain is now filled by two water molecules (labeled 1 and 2 in Fig. 4A). Although the overall structure and most of the active site structure is similar to rsAPX, there are local changes in protein conformation around His-42 (Fig. 4B). Hence, the main chain of His-42 moves toward the heme in W41A such that N $\epsilon$  of His-42 is now within bonding distance (2.3 Å, compared with 5.5 Å in rsAPX) of the iron. We refer to this as the “on” form. A further water molecule (labeled 3 in Fig. 4A) is located in the region that

was previously occupied by His-42. The Fe-N $\epsilon$ (His-163) distance is essentially identical in both W41A and rsAPX (2.1 and 2.0 Å, respectively). This new histidine ligand replaces a water molecule that is bonded to the iron in the wild type protein (2.1 Å). This movement of the main chain of His-42 toward the heme in the on form and the subsequent alteration in heme geometry are the consequences of the removal of the bulky Trp-41 residue, which allows the His-42 side chain to ligate to the iron.

Examination of the electron density for W41A around His-42 indicates that there is positive  $F_o - F_c$  density above His-42 and also close to the main chain of His-42 (carbonyl oxygen; Fig. 4). This density overlays with the orientation of His-42 in rsAPX and is consistent with the presence of a minority (presumed high-spin) heme species in which His-42 is not ligated. There are two explanations of this observation. First, the spectroscopic data presented above are also consistent with some high-spin heme in the ferric form; in this case, the residual electron density would arise from a mixed population of high- and low-spin iron in the crystal. Second, although we used ferric enzyme in our experiments, we recognize that

partial reduction of heme is possible during data collection (31). The electronic spectrum of ferrous W41A shows maxima ( $\lambda_{\max}/\text{nm} = 428, 556, 581$ ) that are similar to those for rsAPX ( $\lambda_{\max}/\text{nm} = 431, 555, 585$ ) and are not consistent with bis-histidine ligation, indicating that dissociation of His-42 probably occurs on reduction. In this case, the residual electron density would arise from partial reduction of the heme during data collection. We were not able to obtain crystallographic data for the ferrous W41A derivative. Whatever the origin of the residual density, the important feature is that the data clearly indicate that His-42 is flexible and can adopt more than one conformation.

**Reactivity toward  $H_2O_2$** —The data presented above indicated that, although the heme is largely 6-coordinate and low-spin in ferric W41A (with two strong histidine ligands), His-42 is not irreversibly bound to the heme and may dissociate under certain conditions. We refer to this dissociated form as the “off” form. If this is the case, then reaction with  $H_2O_2$  and turnover of substrate may still be possible. Because there is, to our knowledge, no unambiguous example of a crystallographically defined bis-histidine-ligated peroxidase in the literature, it was of critical interest to establish whether strong axial ligation,

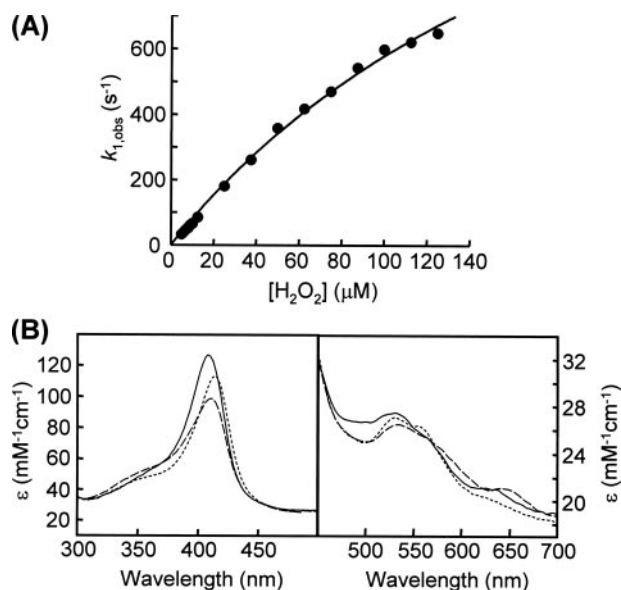
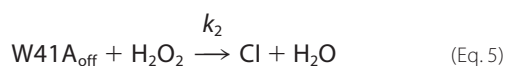


FIGURE 5. A, plot of observed rate constant,  $k_{1,obs}$ , versus  $[H_2O_2]$  for the reaction of W41A with hydrogen peroxide (sodium phosphate buffer, pH 7.0,  $\mu = 0.10$  M, 25.0 °C). The solid line is a fit of the data to Equation 3. B, spectra of reaction intermediates, obtained using photodiode array, from reaction of ferric W41A with  $H_2O_2$ . Solid line, ferric W41A; dashed line, Compound I; dotted line, Compound II (pH 7.0, 5.0 °C,  $[W41A] = 3 \mu M$ ,  $[H_2O_2] = 3 \mu M$ ).

analogous to that observed for example in the cytochromes *b*, would preclude reaction with  $H_2O_2$ .

Rate constants for Compound I formation in W41A were determined under pseudo-first-order conditions ( $[H_2O_2] = 10\text{--}125 \times [W41A]$ ). The W41A variant was shown to be competent for formation of Compound I under these conditions, albeit at a lower rate, as evidenced by a decrease in absorbance at 405 nm. These changes in absorbance duplicate those observed for rsAPX (11). Observed rate constants for this process,  $k_{1,obs}$ , showed a clearly nonlinear dependence on the concentration of hydrogen peroxide (Fig. 5A). This is in contrast to the data for rsAPX, in which a linear dependence on  $[H_2O_2]$  is observed in the experimentally accessible concentration range ( $k_1 = (3.3 \pm 0.1) \times 10^7 \text{ M}^{-1} \text{ s}^{-1}$  (11)). The nonlinear dependence is consistent with a mechanism that requires a conformational change of the protein, proposed to be conversion between the on and off forms, prior to reaction with  $H_2O_2$ , as shown in Equations 4 and 5 (CI = Compound I).



In the presence of excess  $H_2O_2$ , the observed rate constant,  $k_{1,obs}$ , can be expressed as follows (Equation 6).

$$k_{1,obs} = \frac{k_1 k_2 [H_2O_2]}{k_{-1} + k_2 [H_2O_2]} \quad (\text{Eq. 6})$$

A fit of these data for W41A to Equation 6 (Fig. 5A) yields values for the limiting first-order rate constant,  $k_1$ , of  $2370 \text{ s}^{-1}$  and the

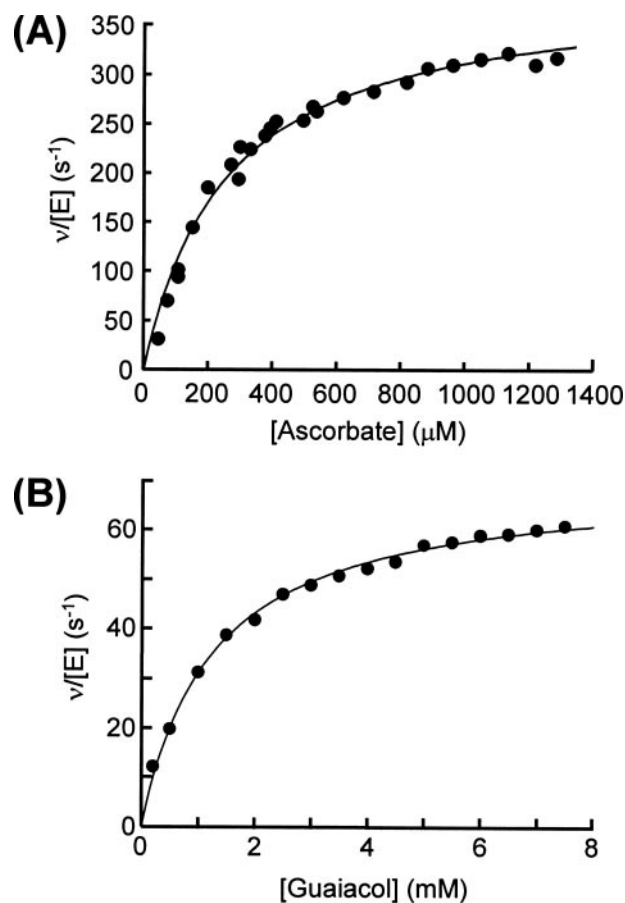


FIGURE 6. Steady state oxidation of l-ascorbate (A) and guaiacol (B) by W41A (pH 7.0, 25.0 °C). The solid lines are a fit of the data to the Michaelis-Menten equation.

composite second order rate constant,  $k_1 k_2 / k_{-1}$ , of  $6.6 \times 10^6 \text{ M}^{-1} \text{ s}^{-1}$ .

In separate experiments, the reaction of W41A with  $H_2O_2$  was studied using photodiode array detection (Fig. 5B). Data collected over a period of 500 ms were best-fitted to a two-step model ( $A \rightarrow B \rightarrow C$ , as shown previously for rsAPX (11)), where *A* is ferric W41A, *B* is Compound I, and *C* is Compound II. Spectra for the Compound I ( $\lambda_{max}/nm = 410, 530, 569^{sh}, 640$ ) and Compound II ( $\lambda_{max}/nm = 414, 530, 560^{sh}$ ) intermediates are in agreement with those observed for rsAPX ( $\lambda_{max}/nm = 409, 530, 569^{sh}$ , and 655 for Compound I and  $\lambda_{max}/nm = 417, 529$ , and  $560^{sh}$ ; this work and Ref. 11). Formation of Compound I (*i.e.*  $A \rightarrow B$ ) for W41A occurs with an observed rate constant ( $k_{1,obs}$ ) of  $26 \pm 0.2 \text{ s}^{-1}$ , which is  $\sim 10$ -fold slower than for rsAPX ( $k_{1,obs} = 218 \pm 2.6 \text{ s}^{-1}$ ). Formation of Compound II (*i.e.*  $B \rightarrow C$ ) occurs with similar rate constants for both W41A and rsAPX ( $k_{2,obs} = 3.8 \pm 0.05$  and  $2.7 \pm 0.1 \text{ s}^{-1}$ , respectively). These data clearly indicate that reaction of ferric W41A with  $H_2O_2$  leads to the formation of genuine Compound I and Compound II intermediates, as observed for rsAPX, and suggest that conformational rearrangement of the protein is involved during catalysis.

**Reactivity toward Substrates**—The W41A variant was also shown to be competent for oxidation of two types of substrate. In addition to its physiological substrate (ascorbate), APX is known to oxidize other aromatic substrates that are typical of the class II and III peroxidases (32). The binding site for these

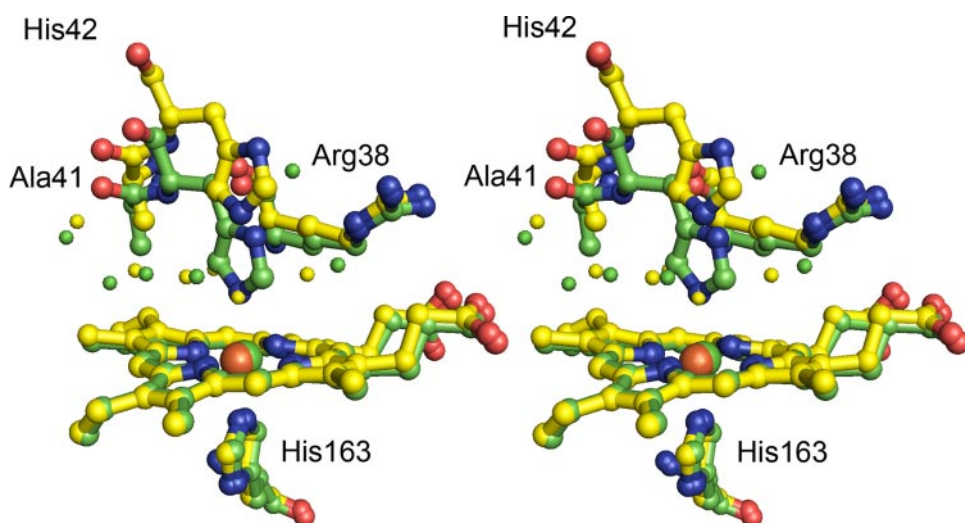


FIGURE 7. Overlay of the structures of ferric W41A (green) and ferric W41A after reaction with  $\text{H}_2\text{O}_2$  (yellow). Water molecules in the two structures are shown in green and yellow, respectively. The orientation of His-42 after reaction with  $\text{H}_2\text{O}_2$  (yellow) overlays with that of rsAPX (see Fig. 4B). This figure was created using PyMOL (40).

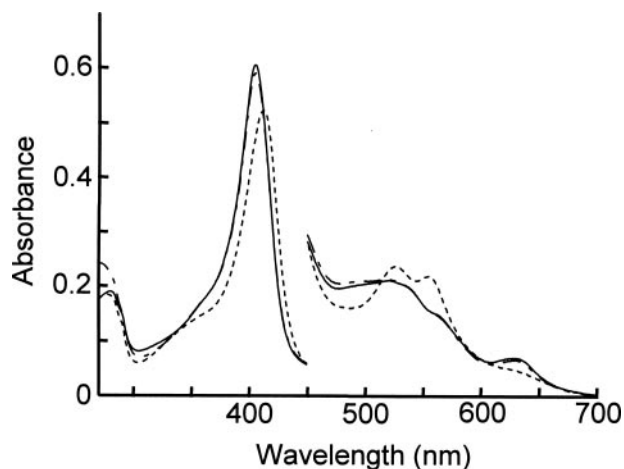


FIGURE 8. Electronic spectra of ferric W41A prior to the addition of  $\text{H}_2\text{O}_2$  (solid line) and ferric W41A immediately after reaction with 1 equivalent of  $\text{H}_2\text{O}_2$  (dashed line) and after reaction with 1 equivalent of  $\text{H}_2\text{O}_2$  followed by the addition of 1 equivalent of ascorbate (dashed-dotted line). The visible region has been multiplied by a factor of 5 (sodium phosphate, pH 7.0,  $\mu = 0.10 \text{ M}$ ,  $25.0^\circ\text{C}$ ).

two types of substrate differs: ascorbate binds close to the heme 6-propionate (at the so-called  $\gamma$ -heme edge (18)), and aromatic substrates are thought to bind close to the  $\delta$ -heme edge (33, 34). For ascorbate oxidation by W41A, steady state data obeyed Michaelis kinetics (Fig. 6A), and the following values were obtained:  $k_{\text{cat}} = 371 \pm 7.8 \text{ s}^{-1}$ ,  $K_m = 254 \pm 16 \mu\text{M}$ ,  $k_{\text{cat}}/K_m = 1.46 \mu\text{M}^{-1} \text{ s}^{-1}$ . The corresponding values for rsAPX were:  $k_{\text{cat}} = 272 \text{ s}^{-1}$ ,  $K_m = 389 \mu\text{M}$ ,  $k_{\text{cat}}/K_m = 0.69 \mu\text{M}^{-1} \text{ s}^{-1}$  (11).<sup>3</sup>

For oxidation of guaiacol by W41A (Fig. 6B), fitting of the data to the Michaelis-Menten equation gives  $k_{\text{cat}} = 78 \pm 2 \text{ s}^{-1}$ ,  $K_m = 1.3 \pm 0.09 \text{ mM}$  and  $k_{\text{cat}}/K_m = 61 \text{ mM}^{-1} \text{ s}^{-1}$  (rsAPX:  $k_{\text{cat}} = 68 \text{ s}^{-1}$ ,  $K_m = 12.9 \text{ mM}$ ,  $k_{\text{cat}}/K_m = 5.3 \text{ mM}^{-1} \text{ s}^{-1}$  (11)). Hence, ascorbate oxidation is largely unaffected by the

<sup>3</sup> For rsAPX, data for oxidation of ascorbate did not obey Michaelis kinetics, and these data were fitted to the Hill equation instead to extract values for  $k_{\text{cat}}$  and  $K_m$  (11).

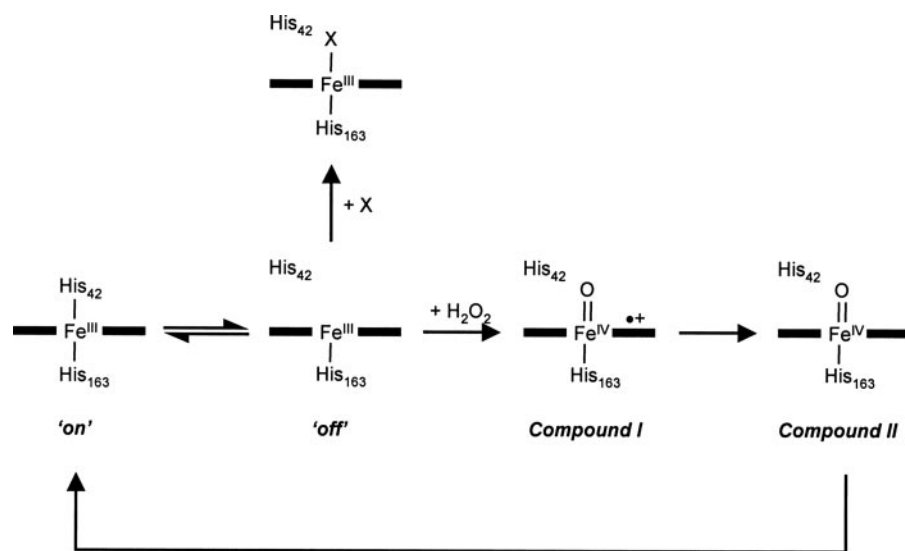
mutation, but for guaiacol an  $\approx 10$ -fold increase in affinity of the enzyme for the aromatic substrate was observed. This almost certainly arises from the presence of a larger hydrophobic pocket that has been created by removal of the bulky Trp-41 residue. We note that Trp-41 has also been implicated in binding of the aromatic substrate analogue salicylhydroxamic acid close to the  $\delta$ -heme edge (33), and these data therefore provide further evidence for binding of aromatic substrates at this site.

*Structural Evidence for Mobility of His-42 during Catalysis*—The spectroscopic, crystallographic, and kinetic data presented above allow three major conclusions to be drawn. (a) Removal of Trp-41 leads

to increased conformational mobility around the active site. This makes His-42 more mobile such that it now coordinates to the heme in the ferric derivative of W41A (the on form). (b) The inherent flexibility of His-42 means that it may dissociate from the heme under certain conditions (the off form), for example in the presence of a strong exogenous ligand (e.g. cyanide, NO). (c) This switch between the on and off forms is also used during catalysis through a mechanism that involves dissociation of His-42 on reaction with  $\text{H}_2\text{O}_2$  and subsequent oxidation of substrate through the normal catalytic route.

We sought more explicit information on the conformational mobility of His-42 during catalysis. Hence, we conducted an experiment in which crystals of ferric W41A were soaked in  $\text{H}_2\text{O}_2$  (100 mM) for 5 min and then frozen immediately in liquid nitrogen. The overall structure of  $\text{H}_2\text{O}_2$ -soaked W41A, including most of the active site region, is very similar to both ferric W41A (root-mean-square deviation between  $\text{C}\alpha$  positions is  $0.179 \text{ \AA}$ ) and to ferric rsAPX ( $0.10 \text{ \AA}$ ), but in comparison with the ferric W41A structure there are local changes in conformation around His-42 (Fig. 7). Hence, His-42 now swings off the iron to occupy a position that is identical to that observed in the ferric rsAPX structure. Clear electron density is observed directly above the iron in a region that for ferric rsAPX (18), as well as for other peroxidases, has been assigned as a water molecule; we have also assigned this density as arising from a water molecule (Fig. 7). The distance between the iron and this distal water molecule is very similar ( $2.2 \text{ \AA}$ ) to that observed in ferric rsAPX ( $2.1 \text{ \AA}$ ).

*Examination of Catalytic Intermediates*—The heme geometry observed in the structure of  $\text{H}_2\text{O}_2$ -soaked W41A, in which His-42 swings off the heme, is different from the majority of low-spin species observed spectroscopically at both room temperature (electronic spectra) or cryogenic temperature (EPR spectra) or from that observed in the crystal structure of the ferric derivative (see above). For this reason we carried out solution experiments, on a timescale identical to that of the crystallography experiments, to authenticate the nature of the heme



SCHEME 1. Depicts the species observed in this work, showing His-42 in the on and off forms. X represents an external ligand (e.g. CN). Conversion of Compound II back to the on form occurs either in the presence of substrate (i.e. during turnover) or, more slowly, in the absence of substrate.

species observed. Hence, ferric W41A was reacted with  $\text{H}_2\text{O}_2$  (varied from 1–100 equivalents) and the spectrum collected immediately. This spectrum (Fig. 8), shows clear evidence for formation of a Compound II intermediate, as observed for W41A in the transient kinetic experiments (Fig. 5B). This Compound II species persisted for >15 min for W41A; subsequent reduction by ascorbate gave a spectrum that was essentially identical to the original ferric low-spin heme species (i.e. predominantly bis-histidine ligated) (Fig. 8).<sup>4</sup> This is interpreted as evidence for reversibility between the on and off forms and is consistent with the steady state data presented above. No evidence for the presence of majority high-spin heme was observed under any conditions; high-spin heme is easily identifiable because ferric (water-bound) rsAPX has a clear spectroscopic signature (see above) that is not observed for W41A.

These data provide clear evidence for reversible switching between the on and off forms and are in agreement with the mechanism proposed above and with the crystallographic data. In the light of these data, and because no evidence for a predominantly high-spin (water-bound) heme was observed spectroscopically, the crystallographic data presented in Fig. 7 are most sensibly rationalized as arising from a Compound II-derived structure. The iron-oxygen bond, at 2.2 Å, is longer than those previously reported for other Compound II intermediates (reported as 1.87 Å (35), 1.92 Å (36), 1.82 Å (37), 1.8 Å (31)), which may reflect the fact that partial conversion back toward the on form, as observed spectroscopically, has occurred.

**Conclusions**—Collectively, the spectroscopic, mechanistic, and crystallographic data presented here illustrate that removal of Trp-41 in ascorbate peroxidase leads to increased internal mobil-

ity of His-42 and clearly indicate that this residue can ligate to the heme in the oxidized derivative. The major findings are summarized in Scheme 1. Contrary to expectation, strong coordination of His-42 to the iron to form a bis-histidine-ligated heme does not preclude reaction with  $\text{H}_2\text{O}_2$  because His-42 is conformationally mobile and can reversibly interconvert between on and off forms to allow reaction with peroxide to occur normally. In this sense, W41A is able to act as a *bona fide* peroxidase, because substrate binding at both the  $\gamma$ -heme edge (for ascorbate) and the  $\delta$ -heme edge (for aromatic substrates) is still possible. More generally, any alteration in peroxidase structure that allows increased mobility of His-42, either through removal of the hydrogen bonding interaction between

His-42 and Asn-71 or by removal of steric bulk in the heme cavity (near Trp-41), should encourage conversion to cytochrome *b*-type geometry. Introduction of bulk on the distal side (e.g. by replacement of Asn-71 with a more bulky residue) may have the same effect by pushing His-42 toward the iron.

These results provide a new perspective on the widely held view of heme enzyme catalysis in which strong axial ligation, as exemplified most famously in the cytochromes, is presumed to inhibit reaction with ligands at the heme iron. We note that reversible coordination of the distal histidine is also possible in some hemoglobins (38) and some heme-based sensors (39), indicating that a similar mechanism for heme-catalyzed biological activity might be used more widely in other, more complex heme enzymes.

**Acknowledgments**—We thank Kuldip Singh for technical assistance. We are grateful to Professor Andrew Thomson and Dr. Myles Cheesman for the use of EPR facilities and to Dr. Clive Metcalfe for collection of preliminary mass spectrometry data. Dr. Sharad Mistry, Dr. Andrew Bottrill, and Shairbanu Ashra are also acknowledged for assistance with MALDI data collection. We also thank Dr. David Leys and Dr. Alexandre R. Gingras for synchrotron data collection and Nicholas Putz for assistance with graphics.

## REFERENCES

1. Everse, J., Everse, K. E., and Grisham, M. B. (1991) *Peroxidases in Chemistry and Biology*, Vol. 1 and 2, CRC Press, Boca Raton, FL
2. Dunford, H. B. (1999) *Heme Peroxidases*, John Wiley, Chichester, United Kingdom
3. Cheek, J., Mandelman, D., Poulos, T. L., and Dawson, J. H. (1999) *J. Biol. Inorg. Chem.* **4**, 64–72
4. Sutherland, G. R. J., Zapanta, S., Tien, M., and Aust, S. D. (1997) *Biochemistry* **36**, 3654–3662
5. Smulevich, G., Miller, M. A., Kraut, J., and Spiro, T. G. (1991) *Biochemistry* **30**, 9546
6. Vitello, L. B., Erman, J. E., Miller, M. A., Mauro, J. M., and Kraut, J. (1992)

<sup>4</sup>In separate control experiments in the absence of ascorbate (data not shown), the spectrum of Compound II decayed over approximately 60 min to a species that resembles the original low-spin ferric form but that had a slightly lower absorbance in the Soret region (probably because of partial heme degradation over long timescales). No dominant high-spin heme signature was observed.

## Conformational Mobility in a Heme Peroxidase

- Biochemistry* **31**, 11524–11535
- Turano, P., Ferrer, J. C., Cheesman, M. R., Thomson, A. J., Banci, L., Bertini, I., and Mauk, A. G. (1995) *Biochemistry* **34**, 13895–13905
  - Youngs, H. L., Moenne-Loccoz, P., Loefer, T. M., and Gold, M. H. (2000) *Biochemistry* **39**, 9994–10000
  - Nelson, D. P., and Kiesow, L. A. (1972) *Anal. Biochem.* **49**, 474–478
  - Metcalf, C. L., Ott, M., Patel, N., Singh, K., Mistry, S. C., Goff, H. M., and Raven, E. L. (2004) *J. Am. Chem. Soc.* **126**, 16242–16248
  - Lad, L., Mewies, M., and Raven, E. L. (2002) *Biochemistry* **41**, 13774–13781
  - Antonini, M., and Brunori, E. (1971) *Hemoglobin and Myoglobin and Their Reactions with Ligands*, North Holland Publishers, Amsterdam
  - Jones, D. K., Dalton, D. A., Rosell, F. L., and Lloyd Raven, E. (1998) *Arch. Biochem. Biophys.* **360**, 173–178
  - Mittler, R., and Zilinskas, B. A. (1991) *Plant Physiol.* **97**, 962–968
  - Asada, K. (1984) *Methods Enzymol.* **105**, 422–427
  - Kelly, G. J., and Latzko, E. (1979) *Naturewissenschaften* **66**, 617–618
  - Santimone, M. (1975) *Can. J. Biochem.* **53**, 649–657
  - Sharp, K. H., Mewies, M., Moody, P. C. E., and Raven, E. L. (2003) *Nat. Struct. Biol.* **10**, 303–307
  - Leys, D., Backers, K., Meyer, T. E., Hagen, W. R., Cusanovich, M. A., and Van Beeumen, J. J. (2000) *J. Biol. Chem.* **275**, 16050–16056
  - Ferrer, J. C., Turano, P., Banci, L., Bertini, I., Morris, I. K., Smith, K. M., Smith, M., and Mauk, A. G. (1994) *Biochemistry* **33**, 7819–7829
  - Vitello, L. B., Huang, M., and Erman, J. E. (1990) *Biochemistry* **29**, 4283–4288
  - Vitello, L. B., Erman, J. E., Miller, M. A., Wang, J., and Kraut, J. (1993) *Biochemistry* **32**, 9807–9818
  - Erman, J. E., Vitello, L. B., Miller, M. A., Shaw, A., Brown, K. A., and Kraut, J. (1993) *Biochemistry* **32**, 9798–9806
  - Leslie, A. G. W. (1992) *Joint CCP4 + ESF-EAMCB Newsletter on Protein Crystallography*, No. 26
  - Collaborative Computational Project (1994) *Acta Crystallogr. Sect. D Biol. Crystallogr.* **50**, 760–763
  - Otwinoski, Z., and Minor, W. (1997) *Methods Enzymol.* **227**, 366–396
  - Murshudov, G. N., Vagin, A. A., and Dodson, E. J. (1997) *Acta Crystallogr. Sect. D Biol. Crystallogr.* **53**, 240–255
  - Emsley, P., and Cowtan, K. (2004) *Acta Crystallogr. Sect. D Biol. Crystallogr.* **60**, 2126–2132
  - Gadsby, P. M., and Thomson, A. J. (1990) *J. Am. Chem. Soc.* **112**, 5003–5011
  - Kabsch, W. (1976) *Acta Crystallogr. Sect. A* **32**, 922–923
  - Berglund, G. I., Carlsson, G. H., Smith, A. T., Szoke, H., Henriksen, A., and Hajdu, J. (2002) *Nature* **417**, 463–468
  - Raven, E. L. (2003) *Nat. Prod. Rep.* **20**, 367–381
  - Sharp, K. H., Moody, P. C. E., Brown, K. A., and Raven, E. L. (2004) *Biochemistry* **43**, 8644–8651
  - Burse, E. H., and Poulos, T. L. (2000) *Biochemistry* **39**, 7374–7379
  - Bonagura, C. A., Bhaskar, B., Shimizu, H., Li, H., Sundaramoorthy, M., McRee, D. E., Goodin, D. B., and Poulos, T. L. (2003) *Biochemistry* **42**, 5600–5608
  - Hersleth, H. P., Dalhus, B., Gorbitz, C. H., and Andersson, K. K. (2002) *J. Biol. Inorg. Chem.* **7**, 299–304
  - Green, M. T., Dawson, J. H., and Gray, H. B. (2004) *Science* **304**, 1653–1656
  - Trent, J. T., III, and Hargrove, M. S. (2002) *Trends Plant Sci.* **8**, 387–393
  - Sasakura, Y., Yoshimura-Suzuki, T., Kurokawa, H., and Shimizu, H. (2006) *Acc. Chem. Res.* **39**, 37–43
  - DeLano, W. L. (2002) *The PyMOL Molecular Graphics System*, DeLano Scientific, San Carlos, CA

Iron Oxidation State Modulates Active Site Structure in a Heme Peroxidase<sup>†,‡</sup>Sandip K. Badyal,<sup>§</sup> Clive L. Metcalfe,<sup>§</sup> Jaswir Basran,<sup>||</sup> Igor Efimov,<sup>§</sup> Peter C. E. Moody,<sup>||</sup> and Emma Lloyd Raven<sup>\*:§</sup>

Department of Chemistry, Henry Wellcome Building, University of Leicester, University Road, Leicester LE1 7RH, England, U.K., and Department of Biochemistry and Henry Wellcome Laboratories for Structural Biology, Henry Wellcome Building, University of Leicester, Lancaster Road, Leicester LE1 9HN, England, U.K.

Received November 27, 2007; Revised Manuscript Received February 14, 2008

**ABSTRACT:** We have previously shown [Badyal, S. K., et al. (2006) *J. Biol. Chem.* 281, 24512–24520] that the distal histidine (His42) in the W41A variant of ascorbate peroxidase binds to the heme iron in the ferric form of the protein but that binding of the substrate triggers a conformational change in which His42 dissociates from the heme. In this work, we show that this conformational rearrangement also occurs upon reduction of the heme iron. Thus, we present X-ray crystallographic data to show that reduction of the heme leads to dissociation of His42 from the iron in the ferrous form of W41A; spectroscopic and ligand binding data support this observation. Structural evidence indicates that heme reduction occurs through formation of a reduced, bis-histidine-ligated species that subsequently decays by dissociation of His42 from the heme. Collectively, the data provide clear evidence that conformational movement within the same heme active site can be controlled by both ligand binding and metal oxidation state. These observations are consistent with emerging data on other, more complex regulatory and sensing heme proteins, and the data are discussed in the context of our developing views in this area.

The iron-containing heme group is used widely in biology. Traditionally, heme-containing proteins have been categorized into the oxygen transport proteins (the globins), the electron transfer proteins (the cytochromes), and the catalytic heme-containing enzymes (e.g., the P450s, peroxidases, etc.). This categorization conveniently differentiated the noncatalytic electron transfer proteins from the transport proteins and the catalytic enzymes, and it became clear that at least part of this differentiation arose from differences in heme coordination geometry. Hence, the electron transfer proteins contain six-coordinated heme groups, as a means of facilitating rapid electron transfer, whereas the transport proteins and the catalytic enzymes are most often found as five-coordinate or weakly six-coordinate heme structures to allow ligand binding or catalysis at the sixth site. Over the past several years, a few examples emerged in the literature of heme proteins that did not fit this categorization. This was because these proteins actually switched their heme coordination geometry through conformational rearrangements of the protein structure. Examples include cytochrome *c* (1), *Chlamydomonas* hemoglobin (2), cytochrome *cd*<sub>1</sub> (3), the diheme cytochrome *c* peroxidase (4), the heme chaperone

protein CcmE (5), and leghemoglobin (6). The trigger for these conformational rearrangements appeared to be, variously, pH, the oxidation state of the iron, and the binding of ligands, substrate, or other (noncatalytic) metal ions. Although these documented examples were significant in their own right, their collective significance was not immediately apparent. This was in part because a functional basis for the ligand switch could not be identified in all cases. Later, further examples of conformational rearrangements in other regulatory heme proteins linked to, for example, gas-sensing processes, signaling, and gene transcription were published (see ref 7 for a recent review). It was only then that it started to become clear that conformational rearrangements associated with the heme group, its ligands and/or substrates, and its oxidation state might actually be used more widely as a means of regulation and/or sensing in biology.

Currently, therefore, it appears that at least some heme protein architectures are intrinsically mobile, that this mobility can be triggered by redox changes or ligand–substrate binding, and that this trigger is used, in certain cases, as a link to more complex downstream biological processes. What we do not yet know is whether conformational mobility is a more general characteristic of other heme protein structures and whether these triggering mechanisms are more generally accessible in other protein structures. In this context, we have recently reported (8) an example of a six-coordinate heme peroxidase (W41A variant of ascorbate peroxidase) which has bis-histidine coordination, like a cytochrome, but that is catalytically active because the distal histidine reversibly dissociates to form a five-coordinate heme in response to binding of hydrogen peroxide. In this work, we show that this conformational movement is also triggered by a change in oxidation state. The implications of these observations are

<sup>†</sup> This work was supported by grants from the BBSRC (Grants BB/C00602X/1, BB/C001184/1, and IIP0206/009, and a studentship to S.K.B.) and ESRF Proposal MX-635.

<sup>‡</sup> PDB accession codes for the protein structures reported in this paper are as follows: 2VNZ (ferrous W41A), 2VO2 (low-dose W41A), and 2VNX (high-dose W41A).

\* To whom correspondence should be addressed. Telephone: +44 (0)116 2297047. Fax: +44 (0)116 2522789. E-mail: emma.raven@le.ac.uk.

<sup>§</sup> Department of Chemistry, University of Leicester.

<sup>||</sup> Department of Biochemistry and Henry Wellcome Laboratories for Structural Biology, University of Leicester.

discussed in terms of our evolving understanding of the role of heme in biological regulation and sensing.

## EXPERIMENTAL PROCEDURES

**Materials.** Sodium dithionite, sodium azide, and potassium cyanide were purchased from Sigma-Aldrich, and the chemicals used for buffers (Fisher) were of the highest analytical grade (>99% pure) and were used without further purification. Aqueous solutions were prepared using water purified through an Elgastat Option 2 water purifier, which itself was fed with deionized water. All pH measurements were made using a Russell pH electrode attached to a digital pH meter (Radiometer Copenhagen, model PHM 93).

**Protein Expression and Purification.** Bacterial fermentation of cells and purification of rsAPX<sup>1</sup> and W41A were carried out according to published procedures (8, 9). Purified samples of rsAPX and W41A exhibited wavelength maxima at 407 (107), 525, and ≈630 nm and 405 (125), 525, 564, and ≈630 nm, respectively, as reported previously (8, 10). Enzyme concentrations for rsAPX and W41A were determined using the following absorption coefficients:  $\epsilon_{407} = 107 \text{ mM}^{-1} \text{ cm}^{-1}$  (10) and  $\epsilon_{405} = 125 \text{ mM}^{-1} \text{ cm}^{-1}$  (8), respectively.

**Electronic Absorption Spectroscopy.** Spectra were collected using a Perkin-Elmer Lambda 25, 35, or 40 spectrophotometer, linked to a PC workstation running UV-Winlab. Ferrous forms of rsAPX and W41A were prepared by the addition of microliter volumes of a fresh sodium dithionite solution to the ferric enzyme (~8  $\mu\text{M}$ ) present in anaerobic buffer in an airtight cuvette until no further change in the spectrum was observed. All solutions were prepared in a glovebox (Belle Technology) using anaerobic buffer.

**Titrations with Anionic Ligands.** Equilibrium binding parameters were determined by adding microliter volumes of the appropriately diluted ligand (cyanide or azide) solutions (made up in sodium phosphate buffer, pH 7.0,  $\mu = 0.1 \text{ M}$ , and filter-sterilized) using a Hamilton syringe to an airtight cuvette containing ferric protein, which was mixed by inversion and allowed to equilibrate. The UV-visible spectra (270–700 nm) were recorded after each addition of ligand. The ligand binding affinity was monitored spectroscopically using absorption at 418 nm for cyanide binding to rsAPX and W41A and 411.5 and 405 nm for azide binding to rsAPX and W41A, respectively.

All solutions for determining parameters for binding of cyanide to ferrous protein were prepared anaerobically in a glovebox, by the addition of microliter volumes of a fresh sodium dithionite solution to an anaerobic solution of ferric protein (~8  $\mu\text{M}$ ) until no further change in the spectrum was observed. All solutions required for the titrations were kept anaerobic by the use of glucose (Fisher, 10 mM), glucose oxidase (Sigma, 50  $\mu\text{g}/\text{mL}$ ), and catalase (Sigma, 5  $\mu\text{g}/\text{mL}$ ). The same method that was described above for the ferric form was used for the titration of cyanide into dithionite-reduced protein. The ligand binding affinity was monitored spectroscopically using absorption at 426 nm for cyanide binding to reduced rsAPX and W41A. As a consequence of the high affinity of ferric rsAPX for cyanide,

a nonlinear regression analysis using eq 1 was applied to determine the  $K_d$

$$\Delta A = \frac{\Delta A_{\infty}}{2[E]} \{ [E] + [L] + K_d - [(E) + [L] + K_d]^2 - 4[E][L] \}^{1/2} \quad (1)$$

where [E] and [L] represent the calculated concentrations of total enzyme and total ligand after each addition, respectively,  $\Delta A$  and  $\Delta A_{\infty}$  are the absorbance changes corresponding to the intermediate and saturating ligand concentrations, respectively, and  $K_d$  is the equilibrium dissociation constant.

Equilibrium dissociation constants for binding of cyanide to ferrous rsAPX and ferric/ferrous W41A, and of azide to ferric rsAPX and W41A, were calculated using eq 2 in Grafit 5 (Grafit version 5.0.3, Erithacus Software Ltd.):

$$\Delta A = \frac{\Delta A_{\infty}[\text{free}]}{K_d + [\text{free}]} \quad (2)$$

where  $\Delta A$  and  $\Delta A_{\infty}$  are the absorbance changes corresponding to the intermediate and saturating ligand concentrations, respectively, [free] is total concentration of unbound ligand, and  $K_d$  is the equilibrium dissociation constant.

**Transient-State Kinetics.** Transient-state measurements were performed using an SX.18MV microvolume stopped-flow spectrophotometer (Applied Photophysics) contained within a glovebox (Belle Technology) and fitted to a Neslab RTE-200 circulating water bath ( $5 \pm 0.1 \text{ }^{\circ}\text{C}$ ). Multiple-wavelength absorption studies were carried out using a photodiode array detector and X-SCAN (Applied Photophysics Ltd.). Spectral deconvolution was performed by global analysis and numerical integration methods using PROKIN (Applied Photophysics Ltd.).

**Crystal Growth and Structure Determination.** Crystals of W41A were obtained using previously published procedures (11). Crystals of ferrous W41A were obtained by soaking crystals for 5 min in a fresh solution of sodium dithionite dissolved in mother liquor [0.1 M Hepes (pH 8.3) and 2.25 M lithium sulfate]. All crystals were flash-frozen and then cryocooled in liquid nitrogen and stored for data collection.

All diffraction data were collected at ESRF (Grenoble, France) for dithionite-reduced W41A using beam line ID23-EH1 (0.873 $\text{\AA}$ ) and an ADSC Quantum-315 detector. Single-crystal microspectrometry and collection of diffraction before and after X-ray reduction of ferric W41A used beamline ID14-2 (0.933 $\text{\AA}$ ) and an ADSC Q4 CCD detector. All synchrotron data were collected at 100 K. The data were indexed and scaled using MOSFLM (12) and SCALA (13). Crystals were continuously cooled by a cold nitrogen stream from an Oxford Cryosystems 700 series cryostream. UV-visible absorption spectra of the crystals were recorded in the 500–800 nm range using the EMBL online microspectrophotometer (HR2000 CCD detector Ocean Optics). Input light was provided by a deuterium/halogen source (Ocean Optics, DH2000) coupled to custom lenses via a 100  $\mu\text{m}$  2-UV-SR fiber optic (generating a focal spot of 25  $\mu\text{m}$ ) and collected from the second lens coupled to a 600  $\mu\text{m}$  fiber optic. Wherever possible, care was taken to record spectra of the crystal to the same  $\varphi$  position. Spectra of the cryocooled crystals remained unchanged during storage.

<sup>1</sup> Abbreviations: APX, ascorbate peroxidase; rsAPX, recombinant soybean cytosolic ascorbate peroxidase.

Table 1: Data Collection and Refinement Statistics<sup>a</sup>

	ferrous	low-dose	high-dose
Data Collection			
PDB entry	2VNZ	2VO2	2VNX
space group	<i>P4</i> <sub>2</sub> <i>2</i> <sub>1</sub> <i>2</i>	<i>P4</i> <sub>2</sub> <i>2</i> <sub>1</sub> <i>2</i>	<i>P4</i> <sub>2</sub> <i>2</i> <sub>1</sub> <i>2</i>
unit cell dimensions (Å)			
<i>a</i> = <i>b</i>	81.78	82.06	82.00
<i>c</i>	75.24	75.63	75.57
resolution (Å)	45.83–1.30 (1.39–1.30)	46.03–2.00 (2.11–2.00)	37.80–1.60 (1.69–1.60)
total no. of observations	649696 (94551)	63697 (9264)	352976 (49343)
no. of unique reflections	63112 (9091)	17935 (2570)	34661 (4988)
<i>I</i> / <i>σ</i> <i>I</i>	21.6 (4.3)	6.2 (0.9)	19.5 (3.1)
<i>R</i> <sub>merge</sub>	0.09 (0.45)	0.026 (0.138)	0.086 (0.66)
completeness (%)	99.9 (100)	99.7 (100)	100 (100)
Refinement Statistics			
<i>R</i> <sub>work</sub>	0.182	0.174	0.175
<i>R</i> <sub>free</sub>	0.199	0.236	0.209
root-mean-square deviations from ideal			
bonds (Å)	0.006	0.016	0.010
angles (deg)	1.117	1.507	1.152

<sup>a</sup> Values in parentheses are for the outer shell.

Data collection and processing statistics are listed in Table 1; 5% of the data was flagged for the calculation of *R*<sub>free</sub> and excluded from subsequent refinement. The structures were refined from the 1.35 Å ferric W41A structure (Protein Data Bank entry 2GGN). Several cycles of refinement using REFMAC5 (14) from the CCP4 suite (13) and manual rebuilding of the protein model using COOT (15) followed by the addition of water molecules were carried out until the *R*<sub>free</sub> and *R*<sub>factor</sub> values converged. The final refinement statistics are presented in Table 1.

## RESULTS AND DISCUSSION

**Spectra of Ferric and Ferrous Derivatives.** The electronic spectra of the ferric and ferrous derivatives of rsAPX and W41A are shown in Figure 1. The spectrum of the ferric derivative of W41A [ $\lambda_{\text{max}} = 405$  ( $\epsilon = 125 \text{ mM}^{-1} \text{ cm}^{-1}$ ), 525, 564, and 630 nm] (8) shows a peak in the visible region (564 nm) that is consistent with the presence of low-spin heme (Figure 1B). This distinguishes it clearly from the spectrum of ferric rsAPX (Figure 1A) in which no low-spin peaks are observed [ $\lambda_{\text{max}} = 407$  ( $\epsilon = 107 \text{ mM}^{-1} \text{ cm}^{-1}$ ), 525, and  $\approx 630$  nm ( $\epsilon = 16 \text{ mM}^{-1} \text{ cm}^{-1}$ )]. For W41A, the low-spin component has been shown, crystallographically, to derive from coordination of the distal histidine (His42) to the ferric heme (8). In contrast, the spectra of the ferrous derivatives of rsAPX and W41A (Figure 1A,B) are similar to each other ( $\lambda_{\text{max}} = 430, 555,$  and 583 nm for rsAPX;  $\lambda_{\text{max}} = 428, 556,$  and 581 nm for W41A), with both spectra consistent with a reduced heme species. As reduced rsAPX is five-coordinate, this suggests that in the dithionite-reduced form of W41A the His42 ligand dissociates from the iron.

**Ligand Binding to Ferric and Ferrous Derivatives.** Complete formation of low-spin ferric heme is observed upon addition of cyanide to both ferric rsAPX [ $\lambda_{\text{max}} = 419, 536,$  and 563<sup>sh</sup> nm (data not shown)] and W41A [ $\lambda_{\text{max}} = 418, 540,$  and 561<sup>sh</sup> nm (Figure 1C)]. This is consistent with binding of cyanide at the sixth coordination site, as confirmed crystallographically in both cases (8). Addition of azide to ferric rsAPX and W41A leads to a predominantly low-spin ferric heme species with some high-spin character [ $\lambda_{\text{max}} = 412, 528^{\text{sh}}, 562^{\text{sh}},$  and 630 nm for rsAPX;  $\lambda_{\text{max}} = 415, 538^{\text{sh}},$

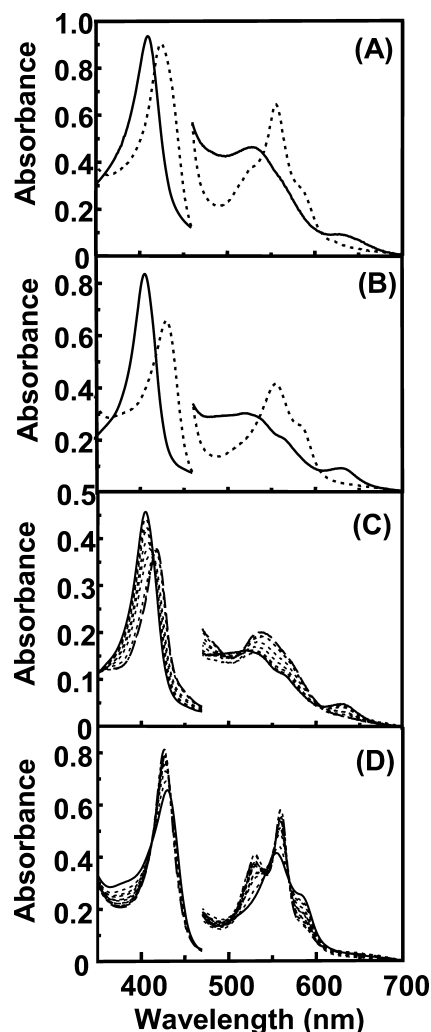


FIGURE 1: Electronic spectra of (A) rsAPX and (B) W41A, showing the ferric (solid line) and ferrous (dashed line) species. The ferrous spectra were obtained by addition of dithionite. (C and D) Selected spectra collected during titration of (C) ferric W41A (3.6  $\mu\text{M}$ ) and (D) ferrous W41A (6.8  $\mu\text{M}$ ) with cyanide. Intermediate spectra between the initial spectrum (solid line) and the final saturated spectrum (dashed line) are shown as dotted lines. Sample conditions: enzyme, sodium phosphate, pH 7.0,  $\mu = 0.1 \text{ M}$ , 25 °C. The visible region has been multiplied by a factor of 5 in all cases.

Table 2: Equilibrium Dissociation Constants for Binding of Cyanide and Azide to rsAPX and W41A<sup>a</sup>

	rsAPX		W41A	
	ferric	ferrous	ferric	ferrous
cyanide	0.73 ± 0.075 μM	0.31 ± 0.025 mM	20 ± 0.75 μM	1.5 ± 0.17 mM
azide	0.40 ± 0.019 mM	–	3.8 ± 0.091 mM	–

<sup>a</sup> Sample conditions: sodium phosphate, pH 7.0,  $\mu = 0.1$  M, 25 °C.

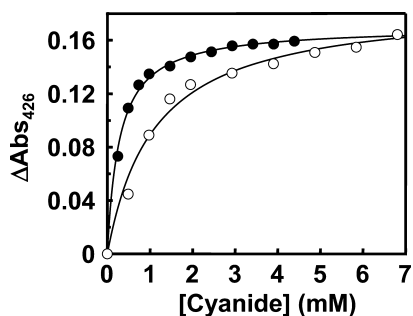


FIGURE 2: Plot of the absorbance change at 426 nm vs total cyanide concentration for binding to ferrous rsAPX (●) and ferrous W41A (○). The solid line is a fit of the data to eq 2.

562<sup>sh</sup>, and 630 nm for W41A (data not shown)]. Similarly, addition of potassium cyanide to ferrous rsAPX and W41A leads to formation of a low-spin species in both cases [ $\lambda_{\max} = 426, 529,$  and  $560$  nm for rsAPX (data not shown);  $\lambda_{\max} = 426, 530,$  and  $560$  nm for W41A (Figure 1D)].

Equilibrium binding constants (Table 2 and Figure 2) obtained from the data given above showed large differences in the binding affinity between the ferric forms of rsAPX and W41A, with  $K_d$  values for binding of cyanide and azide  $\approx 30$ - and  $\approx 10$ -fold lower, respectively, for W41A than those for rsAPX. This can be rationalized by the different coordination geometries in the two proteins: rsAPX contains a weakly bound water molecule at the sixth coordination position, whereas in W41A, the distal histidine binds to the heme at the sixth site. In contrast, binding constants for binding of cyanide to the ferrous form are closely matched for both rsAPX and W41A (Table 2). This is consistent with the electronic spectra of the ferrous forms of the two proteins and indicates that the coordination geometry is similar in both cases.

**Crystallography.** The crystal structure of ferric W41A [Figure 3A (8)] indicated that His42 was within bonding distance (2.3 Å, compared to 5.5 Å in rsAPX) of the iron, to give six-coordinate heme. We have called this the “on” form (8). The crystal structure of the dithionite-reduced form of W41A (Figure 3B and Table 1) reveals that His42 is no longer bound to the iron and shows a water molecule in the active site (Fe–O distance of 2.12 Å). Although the overall structure of ferrous W41A is similar to that of ferric W41A, there are changes in conformation around His42. Hence, the main chain of His42 in ferrous W41A has moved away from the heme to a position analogous to that of His42 in the structure of ferric rsAPX. We have referred to this conformation of His42 as the “off” form. For dithionite-reduced W41A, there is no additional density directly above the iron that correlates to the histidine being ligated to the iron (i.e., in the on form); the only density is for the water molecule as described above.

Reduction of the heme is also possible during collection of crystallographic data (see, for example, refs 17–20), and

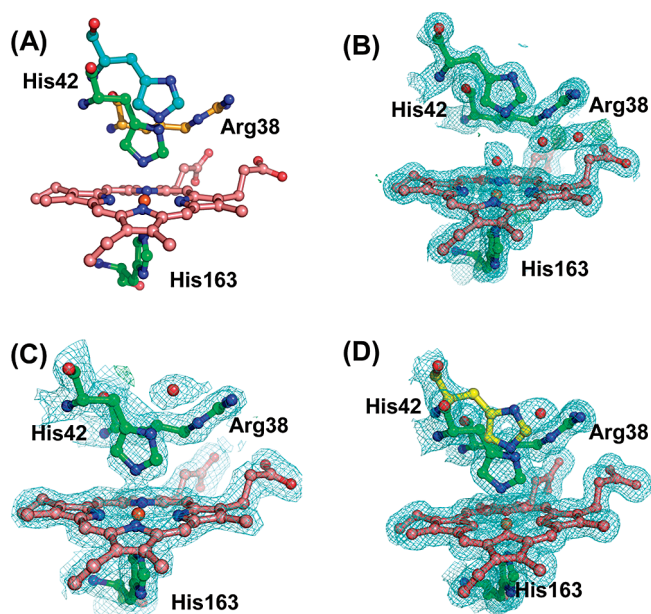


FIGURE 3: (A) Structural alignment of the active sites of rsAPX (blue, Protein Data Bank entry 1OAG) and W41A (green), showing the orientation of His42 in the off and on positions, respectively. Arg38 is highlighted in yellow. (B) Structure of W41A after reduction by dithionite, showing His42 in the off position. (C) Structure of W41A after exposure to low-intensity irradiation. (D) Structure of W41A after exposure to high-intensity irradiation showing the dual occupancy of His42. The  $\sigma_A$ -weighted  $2F_o - F_c$  electron density at  $1\sigma$  is colored blue. The off position of His42 is colored yellow (modeled with an occupancy of 0.3), and the on position of His42 is colored green (modeled with an occupancy of 0.7). This figure was created using PyMOL (30). Water molecules are shown as red spheres in all cases.

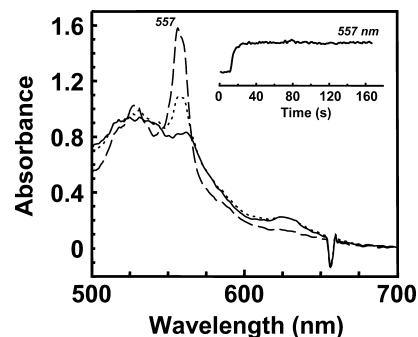
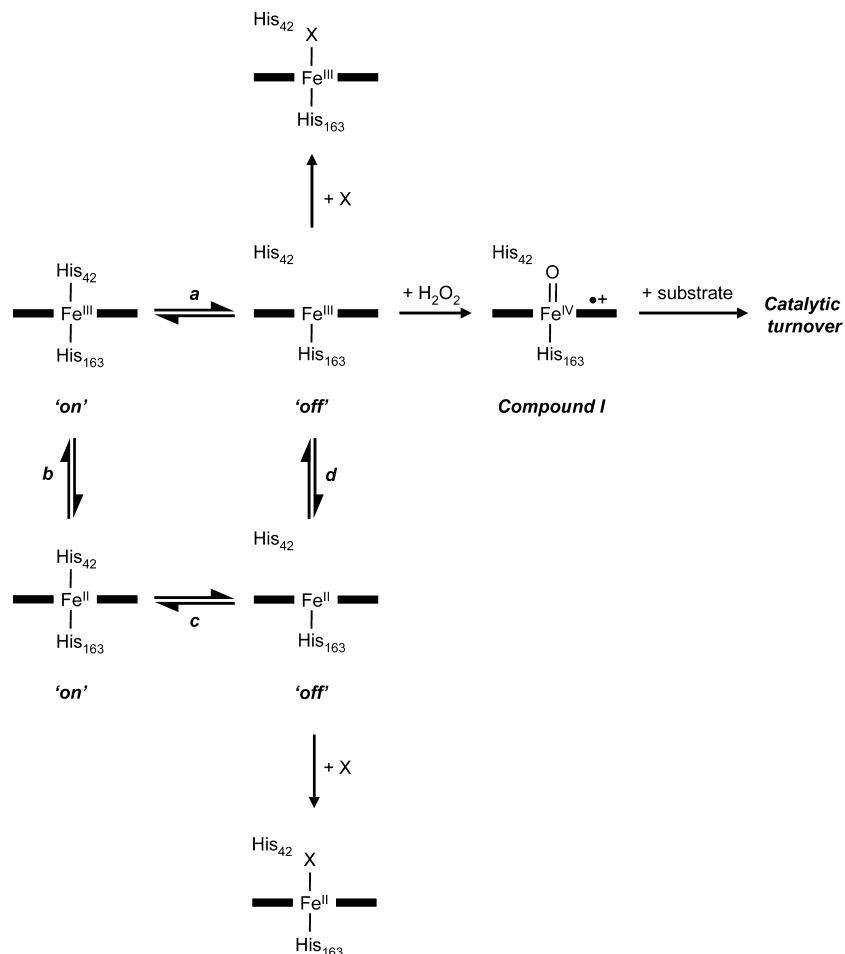


FIGURE 4: Changes in the absorption spectrum (100 K) of a crystal of ferric W41A (solid line) on exposure to small (dotted line) and large (dashed line) X-ray doses. The inset is a plot showing the time-dependent changes in absorbance at 557 nm on exposure of the crystal to a high-intensity X-ray beam.

we used this to obtain further structural evidence for movement of His42 between the on and off positions. The structures of a crystal of ferric W41A determined after exposure to an attenuated-low intensity X-ray source (low-dose) and the full-intensity unattenuated X-ray source (high-dose) are shown in panels C and D of Figure 3, respectively.

Scheme 1: Species Observed in This and Previous (8) Work, Showing the Mobility of His42 during Catalysis and Reduction<sup>a</sup>

<sup>a</sup> Step a shows the equilibrium between the on and off forms of the ferric protein. This form has been previously shown (8) to bind both exogenous ligands and to be catalytically active (reaction with H<sub>2</sub>O<sub>2</sub>), as shown herein. Step b represents the reduction of ferric W41A to an initial low-spin ferrous form, which is the likely route in the X-ray beam. Step c represents subsequent loss of His42 from this initial low-spin ferrous intermediate; this form can also bind exogenous ligands. Step d shows the reoxidation of the ferrous off form to the ferric form. On reaction with dithionite in solution, step b followed by c is possible, but an alternative mechanism in which reduction of the ferrous form with dithionite involves prior dissociation of His42 from the heme before reduction (step a followed by step d) is also possible.

The structure for the low-dose sample (Figure 3C) is similar to that of pure ferric W41A (Figure 3A), in which His42 is in the on position and within bonding distance (2.3 Å) of the iron, and there is no additional density above the heme corresponding to the off position. In contrast, for the high-dose structure, there is positive  $F_o - F_c$  density above His42, near the main chain of His42 and close to the off position. This second conformation [which is not observed at low X-ray doses (Figure 3C)] was refined placing His42 in an orientation identical to that of His42 in dithionite-reduced ferrous W41A (Figure 3B). The occupancies of the two conformations were estimated to be 0.3 for the off form and 0.7 for the on form and included in the final stages of refinement; the resulting electron density is shown in Figure 3D. Thus, on exposure to the high-dose beam, the ferric W41A crystal is being reduced and His42 is observed to partially move away from the iron on reduction.

In parallel experiments, single-crystal microspectrophotometry was used to monitor changes in the electronic spectrum of the ferric W41A crystal that correspond to the structures presented in Figure 3. The initial spectrum of the ferric W41A crystal at 100 K (Figure 4) before exposure to the beam is the same as that observed in solution at room

temperature (Figure 1B). This indicates that the species in solution and in the crystal are similar and demonstrates that freezing and crystallization effects are not responsible for the conformational movement. [In fact, we note that the bond in the on form (2.3 Å) is longer than usual for an iron-histidine bond, which accounts for the 630 nm (high-spin) band in the visible region at both room temperature and 100 K and suggests that His42 is quite weakly coordinated.] When the ferric W41A crystal was exposed to a low-intensity beam, an increase in absorbance at 557 nm [close to the absorption maximum for the ferrous derivative (Figure 1)] was observed (Figure 4). Note, however, that no additional density was observed for His42 in the off position in the corresponding structure of this species (Figure 3C), indicating that under these conditions His42 is not yet dissociated from the iron even though a significant population of the heme groups have been reduced by the beam, as evidenced by the change in absorbance at 557 nm. On exposure of the ferric W41A crystal to a high-intensity X-ray beam, much larger increases in absorbance at 557 nm are observed over time (Figure 4 and inset) so that the final spectrum after data collection resembled that of a ferrous bis-histidine (low-spin) heme species, such as

cytochrome *b*<sub>5</sub> (21). The structure that corresponds to this reduced spectrum (Figure 3D) clearly shows His42 still within bonding distance of the iron, but there is additional density above His42 in the off position. Reduction of the ferric crystal was complete within ~40 s at 100 K (Figure 4 inset). Significantly, the final spectrum after 40 s is different from that obtained when W41A is chemically reduced by dithionite (Figure 1B). This is interpreted as evidence that reduction of ferrous W41A in the beam at 100 K leads to an initial reduced, bis-histidine species which presumably then decays back to a species that is the same as that observed when W41A is reduced with dithionite in solution. In transient-state kinetic experiments (photodiode array stopped flow, 5 °C), there was no evidence of the presence of a bis-histidine ligated ferrous heme protein in solution on reaction of W41A with dithionite (data not shown), and we assume that at this temperature the conformational rearrangements occur more rapidly so that the reduced, bis-histidine species decays too quickly for detection by stopped flow.

**Wider Implications.** There are relatively few examples of crystallographically defined conformational changes in heme proteins. In previous work (8), we showed that the coordination geometry in W41A was variable so that His42 binds onto the heme in the oxidized form but that addition of peroxide triggered a conformational change that led to displacement of His42 so that essentially complete catalytic activity was maintained. This ran counter to widely adopted views of heme enzyme catalysis, because it showed that strong coordination of His42 to the heme does not, automatically, undermine catalytic activity.

The data presented above show that a conformational movement within the protein structure can also be triggered by a change in the oxidation state of the iron, and we present crystallographic evidence to show dissociation of His42 on reduction. The major findings are summarized in Scheme 1. On the basis of the data presented, we propose a mechanism for reduction that involves initial formation of a reduced, bis-histidine-ligated species that subsequently decays by dissociation of His42 from the heme. What is clear is that conformational mobility can be induced within the same protein structure either by ligand (peroxide) binding (8) or by reduction of the heme. As noted above, other examples of conformationally mobile heme protein structures have appeared sporadically (for example, refs 1–5 and 22). Collectively, we interpret this as evidence that these protein structures are intrinsically mobile and that this might be a feature of other heme protein structures that is used more widely than previously realized.

These observations chime with our developing views on the wider role of heme in biological systems because it is now becoming clear that the role of heme is not restricted to its involvement as a prosthetic group in specific proteins and enzymes but that it is also involved in various regulatory processes, including gas sensing, control of gene transcription, and modulation of ion channels. The limited information that is currently available seems to suggest that the trigger for these regulatory processes is similarly controlled either by ligand binding or by the oxidation state of the iron and that either of these events is used to initiate downstream conformational rearrangements of the protein architecture either at the active site or beyond. Examples include ligand binding to the heme-regulated inhibitor kinase (23) and the

heme sensor HemAT (24), and reduction of the iron in the heme-regulated phosphodiesterase from *Escherichia coli* (25) and in *CooA* (26, 27). Similar mechanisms might also apply to gas-responsive transcription factor NPAS2 (28), heme-binding transcription factor Hap1 (29), and heme-based sensor FixL (30).

## ACKNOWLEDGMENT

We thank Dr. John McGeehan for support in using the microspectrophotometer on ID14-2. We are grateful to Dr. Klaus Futterer for collection of the ferrous W41A crystal data. We also thank Dr. Louise Fairall and Dr. Alexandre R. Gingras for assistance with graphics.

## REFERENCES

- Rosell, F. I., Ferrer, J. C., and Mauk, A. G. (1998) Proton-Linked Protein Conformational Switching: Definition of the Alkaline Conformational Transition of Yeast Iso-1-ferricytochrome c. *J. Am. Chem. Soc.* *120*, 11234–11245.
- Das, K. T., Couture, M., Lee, H. C., Peisach, J., Rousseau, D. L., Wittenberg, B. A., Wittenberg, J. B., and Guertin, H. (1999) Identification of the Ligands to the Ferric Heme of *Chlamydomonas* Chloroplast Hemoglobin: Evidence for Ligation of Tyrosine-63 (B10) to the Heme. *Biochemistry* *38*, 15360–15368.
- Williams, P. A., Fulop, V., Garman, E. F., Saunders, N. F. W., Ferguson, S. J., and Hajdu, J. (1997) Haem ligand-switching during catalysis in crystals of a nitrogen cycle enzyme. *Nature* *389*, 406–412.
- Dias, J. M., Alves, T., Bonoifacio, C., Pereira, A. S., Trincao, J., Bougeois, D., Moura, I., and Romano, M. (2004) Structural Basis for the Mechanism of Ca<sup>2+</sup> Activation of the Di-Heme Cytochrome c Peroxidase from *Pseudomonas nautica* 617. *Structure* *12*, 961–973.
- Uchida, T., Stevens, J. M., Daltrop, O., Harvat, E. M., Hong, L., Ferguson, S. J., and Kitagawa, T. (2004) The interaction of covalently bound heme with the cytochrome c maturation protein CcmE. *J. Biol. Chem.* *279*, 51981–51988.
- Patel, N., Jones, D. K., Cheesman, M. R., Thomson, A. J., and Raven, E. L. (2002) Leghaemoglobin: A model for the investigation of haem protein axial ligation. *Inorg. Chim. Acta*, 303–309.
- Poulos, T. L. (2007) The Janus nature of heme. *Nat. Prod. Rep.* *24*, 504–510.
- Badyal, S. K., Joyce, M. G., Sharp, K. H., Seward, H. E., Mewies, M., Basran, J., Macdonald, I. K., Moody, P. C. E., and Raven, E. L. (2006) Conformational mobility in the active site of a heme peroxidase. *J. Biol. Chem.* *281*, 24512–24520.
- Metcalfe, C. L., Ott, M., Patel, N., Singh, K., Mistry, S. C., Goff, H. M., and Raven, E. L. (2004) Autocatalytic formation of green heme: Evidence for H<sub>2</sub>O<sub>2</sub>-dependent formation of a covalent methionine-heme linkage in ascorbate peroxidase. *J. Am. Chem. Soc.* *126*, 16242–16248.
- Jones, D. K., Dalton, D. A., Rosell, F. I., and Raven, E. L. (1998) Class I heme peroxidases: Characterization of soybean ascorbate peroxidase. *Arch. Biochem. Biophys.* *360*, 173–178.
- Sharp, K. H., Mewies, M., Moody, P. C. E., and Raven, E. L. (2003) Crystal structure of the ascorbate peroxidase-ascorbate complex. *Nat. Struct. Biol.* *10*, 303–307.
- Leslie, A. G. W. (1992) Recent changes to the MOSFLM package for processing film and image plate data. *Joint CCP4 + ESRF-EMCB Newsletter on Protein Crystallography* *26*, 134–135.
- Collaborative Computational Project Number 4 (1994) The CCP4 suite: Programs for protein crystallography. *Acta Crystallogr. D50*, 760–763.
- Murshudov, G. N., Vagin, A. A., and Dodson, E. J. (1997) Refinement of Macromolecular Structures by the Maximum-Likelihood Method. *Acta Crystallogr. D53*, 240–255.
- Emsley, P., and Cowtan, K. (2004) *Acta Crystallogr. D60*, 2126–2132.
- Lad, L., Mewies, M., and Raven, E. L. (2002) Substrate Binding and Catalytic Mechanism in Ascorbate Peroxidase: Evidence for Two Ascorbate Binding Sites. *Biochemistry* *41*, 13774–13781.
- Berglund, G. I., Carlsson, G. H., Smith, A. T., Szoke, H., Henriksen, A., and Hajdu, J. (2002) The catalytic pathway of horseradish peroxidase at high resolution. *Nature* *417*, 463–468.

18. Hersleth, H. P., Dalhus, B., Gorbitz, C. H., and Andersson, K. K. (2002) An iron hydroxide moiety in the 1.35 angstrom resolution structure of hydrogen peroxide derived myoglobin compound II at pH 5.2. *J. Biol. Inorg. Chem.* 7, 299–304.
19. Schlichting, I., Berendzen, J., Chu, K., Stock, A. M., Maves, S. A., Benson, D. E., Sweet, R. M., Ringe, D., Petsko, G. A., and Sligar, S. G. (2000) The catalytic pathway of cytochrome P450cam at atomic resolution. *Science* 287, 1615–1622.
20. Hersleth, H. P., Uchida, T., Rohr, A. K., Teschner, T., Schunemann, V., Kitagawa, T., Trautwein, A. X., Gorbitz, C. H., and Andersson, K. K. (2007) Crystallographic and spectroscopic studies of peroxide-derived myoglobin compound II and occurrence of protonated Fe<sup>IV</sup>O. *J. Biol. Chem.* 282, 23372–23386.
21. Ozols, J., and Strittmatter, P. (1964) The Interaction of Porphyrins and Metalloporphyrins with Apocytochrome b<sub>5</sub>. *J. Biol. Chem.* 239, 1018–1023.
22. Patel, N., Seward, H. E., Svensson, A., Gurman, S. J., Thomson, A. J., and Raven, E. L. (2003) Exploiting the conformational flexibility of leghemoglobin: A framework for examination of heme proetin axial ligation. *Arch. Biochem. Biophys.* 418, 197–204.
23. Igarashi, J., Sato, A., Kitagawa, T., Yoshimura, T., Yamauchi, S., Sagami, I., and Shimizu, T. (2004) Activation of Heme-regulated Eukaryotic Initiation Factor 2 $\alpha$  Kinase by Nitric Oxide Is Induced by the Formation of a Five-coordinate NO-Heme Complex. *J. Biol. Chem.* 279, 15752–15762.
24. Pinakoulaki, E., Yoshimura, H., Daskalakis, V., Yoshioka, S., Aono, S., and Varotsis, C. (2006) Two ligand-binding sites in the O<sub>2</sub>-sensing signal transducer HemAT: Implications for ligand recognition/discrimination and signaling. *Proc. Natl. Acad. Sci. U.S.A.* 103, 14796–14801.
25. Kurokawa, H., Lee, D. S., Watanabe, M., Sagami, I., Mikami, B., Raman, C. S., and Shimizu, T. (2004) A redox controlled molecular switch revealed by the crystal structure of a bacterial heme PAS sensor. *J. Biol. Chem.* 279, 20186–20193.
26. Lanzilotta, W. N., Schuller, D. J., Thorstensson, M. V., Kerby, R. L., Roberts, G. P., and Poulos, T. L. (2000) Structure of the CO sensing transcription activator CooA. *Nat. Struct. Biol.* 7, 876–880.
27. Nakajima, H., Honma, Y., Tawara, T., Kato, T., Park, S. Y., Miyatake, H., Shiro, Y., and Aono, S. (2001) Redox Properties and Coordination Structure of the Heme in the CO-sensing Transcriptional Activator CooA. *J. Biol. Chem.* 276, 7055–7061.
28. Dioum, E. M., Rutter, J., Tuckerman, J. R., Gonzalez, G., Gilles-Gonzalez, M.-A., and McKnight, S. L. (2002) NPAS2: A gas-responsive transcription factor. *Science* 298, 2385–2387.
29. Lan, C., Lee, H. C., Tang, S., and Zhang, L. (2004) A novel mode of chaperon action. *J. Biol. Chem.* 279, 27607–27612.
30. Gilles-Gonzalez, M. A., and Gonzalez, G. (2005) Heme-based sensors: Defining characteristics, recent developments, and regulatory hypotheses. *J. Inorg. Biochem.* 99, 1–22.

BI702337N